National Institute of Materials Physics

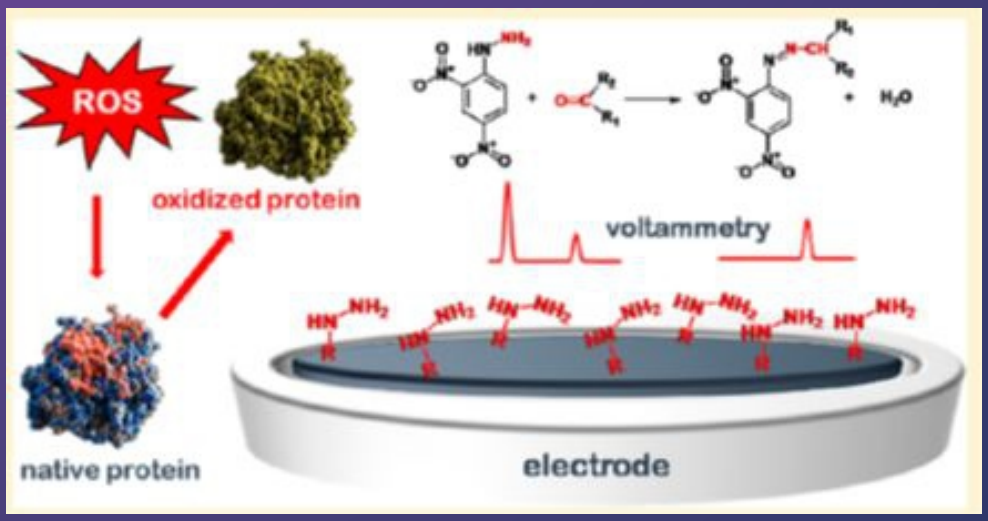

2019

Annual Report

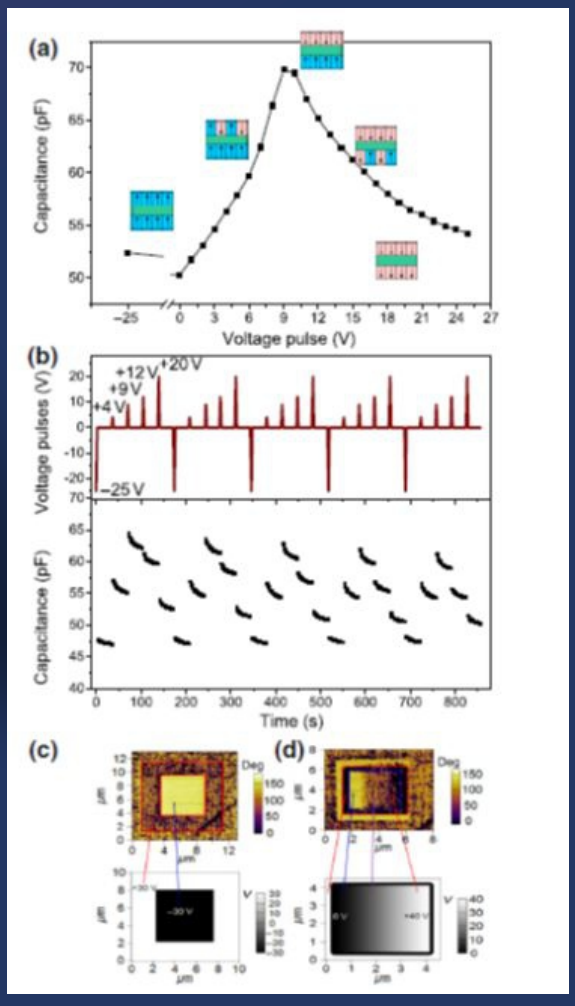

www.infim.ro

National Institute of Materials Physics

Institutul Național de Cercetare-Dezvoltare pentru Fizica Materialelor

COVER IMAGE

Upper image: T.A. Enache, E. Matei, V.C. Diculescu, Anal. Chem. 91, 1920–1927 (2019)

Lower image: A.G. Boni et all., Physical Review Applied 12, 024053 (2019)

Directorate

General Director: **Dr. Ionuț Marius ENCULESCU**

Scientific Director: **Dr. Lucian PINTILIE**

Economic Director: **Ec. Gabriela IVĂNUȘ**

National Institute of Materials Physics
405A Atomistilor Street, PO BOX MG-7, Măgurele, Ilfov, România

Phone: + 4 021 369 01 85
Fax: + 4 021 369 01 77

Email

Dr. I. ENCULESCU: director@infim.ro
Dr. L. PINTILIE: pintilie@infim.ro

Website

www.infim.ro

Contents

Foreword

2019 was no better than 2018 and the R&D sector suffered, again, of lack of predictability and insufficient funding. Only about 70 % from the allocated budget was actually consumed thus the rectification was again negative for R&D.

A new Core Program has started for a period of 4 years (2019-2022). New competitions were organized, the second round, at 3 years after first round. NIMP has submitted an impressive number of projects proposals: 103 for Experimental Demonstrative Projects (68 as coordinator and 35 as partner); 23 for Young Team Projects; 23 for Post-doctoral Projects; 7 for Transfer to Economy Project (as partner). Other projects proposals were submitted to Programs as ERC grants, Norway grants, M-ERA NET, IFA-CERN, H2020. However, the expected success rate is, on average, around 10 %. Even though NIMP has, as demonstrated before, a success rate double than average, it is not enough to sustain the human resources and infrastructure.

Although the funding sources were scarce, NIMP has managed to survive for another year, continuing to publish articles in reputed journals. At the end of the year the cumulated impact factor was nearly 680, with about 185 publications in journals indexed on main databases Web of Science and Scopus. Thus resulting that the average impact factor of the journals is well over 3.

The 4th edition of International Workshop of Materials Physics (May 2019), was organized. The topic for the 2019 edition was dedicated to energy, with a special focus on topics such as: photovoltaics (novel photo-effects, halide perovskites, new architectures for solar cells, etc.), energy harvesting (piezo, pyro, thermoelectric), fusion, energy storage, energy transport, and other similar topics. Aspects related to modeling, fabrication, characterization were presented and discussed.

The change in Government at the end of 2019 troubled again the research sector. The expectations for 2020 are worse, with a lower allocated budget than in 2019, and with expected reduction of funding for Core Programs. This will have a negative impact on the financial predictability and on the stability of the human resources.

NIMP Management Team

LABORATORIES AND GROUPS

Structure

The National Institute of Materials Physics is structured in 5 Laboratories with 9 research groups.

Laboratory 10 "Multifunctional Materials and Structures Laboratory"

Group name

Functional nanostructures

Group leader

Ionut-Marius Enculescu

Team

7 CS1, 2 CS2, 6 CS3, 3 CS, 13 ACS, 1 technician

Main research directions

The group deals with nanostructures and nanostructured materials preparation and development of applications. Both chemical/ electrochemical (chemical bath deposition, electrochemical deposition with and without a template, chemical vapor deposition) and physical (sputtering, thermal evaporation in vacuum, electrospinning and forcespinning) methods are employed for nanostructures and nanostructured materials preparation. Different types of materials are used, including here metals, metal oxides, organometalic compounds and polymers. The nanostructures developed by this approach are used as building blocks for different types of functional devices (transistors or diodes, biosensors, actuators).

Nanostructures and devices based on nanostructures – physical and chemical methods are employed for preparing nanostructures.

Electrochemical or chemical deposition are used for preparing nanowires of zinc oxide with diameters down to 10 nm. Thermal oxidation of metal foils is used for obtaining metal oxide nanowires with diameters down to 20 nm. Further, the nanowires can be employed as building blocks for electronic devices such as diodes and transistors using microlithographic (photolithography and electron beam lithography). Devices complexity can be employed (e.g. core shell devices can be fabricated) by covering the nanowires with thin films employing methods such as sputtering or thermal evaporation. Chemical vapor deposition is employed for preparing thin nanostructured films such as metallic oxides or graphene.

Materials for applications in optics, optoelectronics and photonics for devices which include diodes and transistors for light emitting applications, glasses or modular composition fibers for photonic applications.

Biosensors and biomedical devices based on nanostructures or on devices containing nanostructures as building blocks.

Nanostructures and nanostructured materials can be exploited succesfully in biosensors, mainly due to the high specific surface but also due to other secific functionalities induced by the low dimensionality. Electrochemical sensors are developed based on nanostructured materials and are functionalized with different types of biomolecules in such a way in which both the desired sensitivity and selectivity are obtained. In this context different types of substrates and configurations of functionalization are investigated with the goal of optimizing devices' performances. Novel applications are taken into account including wearable sensors for physiologic parameters monitoring.

Submicrometer fibres; biomimetic devices based on microfiber web electrodes. In our group, methods of fabricating polymer submicrometric fibers were developed namely by electrospinning and forcespinning. By further functionalization transparent and flexible electrodes based on metal covered polymer fiber webs are obtained. These electrodes can be applied on a wide range of substrates including here materials such as textiles and paper and can become the functional element of devices such as biosensors or for applications such as artificial muscles. Functionality can be increased by covering with electroactive polymers, leading to devices with highly superior performances when compared to classic architectures.

Biocompatible materials represent another research direction of the group, several approaches being developed, including both biopolymeric fibers (collagen or celulose), natural membranes (egg shell membrane) or nanostructured materials such as hydroxiapatite.

Further functionalization includes covering with different compounds or nanostructures or doping and leads to multiple fields of applications, the main one being that of medical devices.

The research directions presented in the group are mostly interconnected for developing devices with direct applications. Equipment for fabricating fibers by means of electrospinning and forcespinning were designed and developed in the group with the support of the engineers from the applications department.

Relevant infrastructure

The groups' activity is based on several chemistry and electrochemistry laboratories dedicated to different types of applications. For obtaining the desired nanostructures or nanostructured materials several chemistry and electrochemistry laboratories are used including specific equipment such as chemistry hoods, ovens, potentiostats and so on.

Clean room equipment is essential for devices fabrication:

Electron beam nanolithography equipment with Raith Elphy systems with laser interpherometers and Hitachi S3400 and Zeiss Merlin Compact electron microscopes;EVG 620 NT equipment with nanoimprint capabilities;

CVD equiment for preparation of carbon based nanostructures;CVD equipment for semiconducting materials deposition;

Laboratory for optical characterization including UV – vis absorption spectrometers (Carry 5 and Perkin Elmer 35), photoluminescence spectrometers (Edinburgh and Perkin Elmer LS55), near field photoluminescence microscope, plasmonic resonance spectrometer with potentiostat;

Liquid chromatography equipment with mass spectroscopy;Laboratory for biocompatibility testing including cell culture, flux citometry, fluorescence microscope.

Services

Scanningelectronmicroscopycharacterization of materials (micromorphology, composition)

Optical characterization by means of optical spectroscopy

Development of equipment for producing micrometric and submicrometric fibers by means of electrospinning and forcespinning;

Results

45 papers published; 3 patent applications; 1 MERA NET approved project (Dr. Monica Enculescu).

A wearable pH sensor was developed for sweat monitoring, sensor based on submicrometric fiber webs. Device's sensitivity is comparable to other macroscopic devices whilst allowing characterization of this important parameter on quantities of nanoliters of analite.

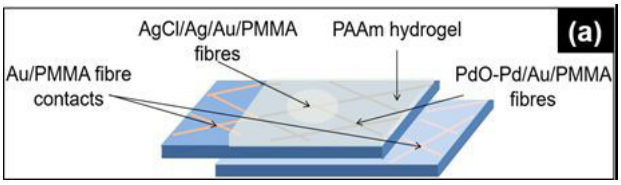

A photodiode was developed based on a core shell nanowire with the core fabricated by thermal oxidation and further covered with the shell by employing sputtering. The electrical contacts were obtained by lithographic methods allowing the fabrication of devices with a diameter of only 60 nm.

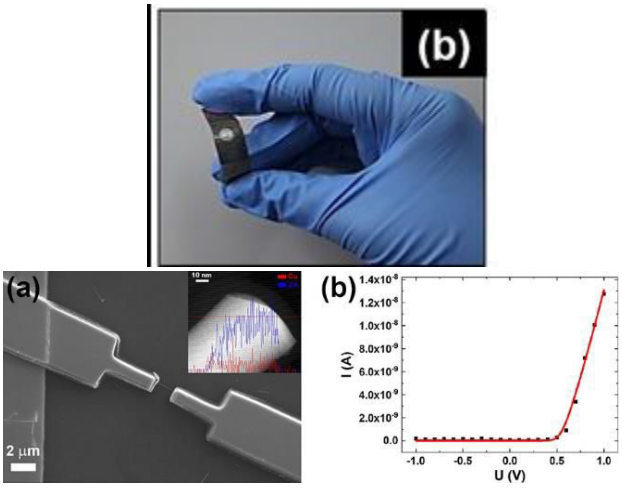

Group name

Group of Complex Heterostructures and Oxide Materials with Perovskite structure (CHetOMaP)

Group Leader

Lucian Pintilie, PhD, Senior Researcher rank 1

Team

CHetOMaP group has, at present, 38 members, 35 with permanent contract and 3 with short term contracts. Of the 35 members with permanent contracts, 6 are Senior Researchers rank 1 (CS1), 3 are Senior Researchers rank 2 (CS2), 11 are Senior Researchers rank 3 (CS3), 4 are Senior Researchers (CS), 5 are Junior Researchers (assistant researchers or ACS), and 5 are sub-engineers or technicians. There are 24 holders of PhD title, 4 PhD students and 1 PhD supervisor.

Main research directions

Ferroelectric materials and related structures for electronic, optoelectronic and sensing applications (including non-volatile memories, UV and IR detectors, piezoelectric devices);

Materials and structures for photovoltaic conversion and light/particle detection (including perovskite solar cells and Si particle detectors);

Bio-compatible materials and other materials with potential applications in medicine or life sciences.

Relevant infrastructure

The group has an extensive infrastructure, covering various methods of material preparation, thin film deposition, and complex physico-chemical characterization.

Relevant infrastructure

PLD (pulsed lase deposition) work station with (**Fig. 1**): 2 deposition chambers, each with 4 target carousel, sample heater up to 1000 K, fluence control, vacuum system and control of working gases pressure; one chamber has high pressure RHEED; a KrF excimer laser with 248 nm wavelength, 10 Hz repetition rate and maximum 700 mJ energy. One chamber is used to deposit ferroelectric layers from materials with perovskite structure and other simple metal oxides (ZnO, HfO_2), and the other chamber is used to deposit superconductor materials.

Matrix assisted pulsed laser deposition (MAPLE): 1 deposition chamber with 2 frozen and 2 solid targets; sample holder heated up to 800 K; a KrF excimer laser with 248 nm wavelength, 10 Hz repetition rate and maximum 700 mJ energy. This machine is used for example, to deposit nanoparticles from frozen suspensions in a dielectric matrix.

RF sputtering equipment (with 4 confocal magnetron sputtering for 2 inch targets, and 1 central magnetron sputtering with 3-inch target, see (**Fig. 2**).

Chemistry laboratory, with various spin-coaters, annealing furnaces, glove boxes and other laboratory equipment for preparation of nanopowders and thin films.

X-ray diffraction equipment for thin films (XRD) from Rigaku (**Fig. 3**), and other two older machines from Bruker, one for powders and one for thin films. Thes are used for structural characterization, allowing identification of crystalline phases, crystalline strain, quality of epitaxy, etc.

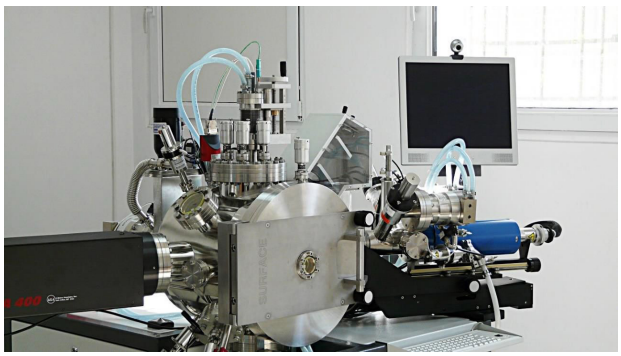

Fig. 1. *PLD work station-the chamber for deposition of ferroelectric thin films.*

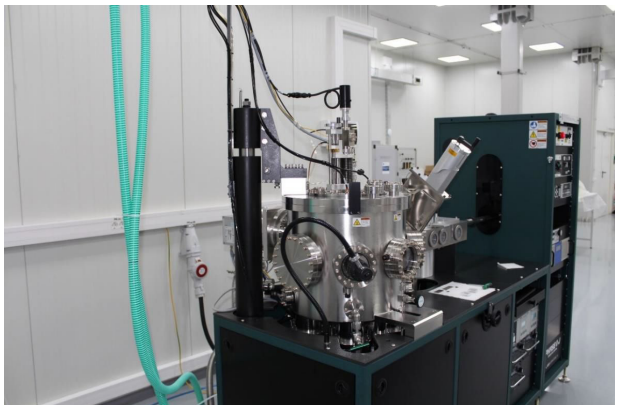

Fig. 2. *RF magnetron sputtering equipment.*

Fig. 3. *XRD equipment for thin film characterization, produced by Rigaku.*

Laboratory for electrical measurements (see **Fig. 4**), including: 2 Lake Shore cryo-probers, one with vertical magnetic field up to 2.5 T, and one with horizontal magnetic field up to 1.5 T, each having at least 3 micro-manipulated arms with contact needles allowing electrical measurements from liquid helium to 425 K with various electric fields and illumination conditions; several close cycled cryostats for measurements between 10 K and 400 K; DLTS system for trap investigation; set-up for pyroelectric measurements; ferritester from AiXACCT; various instruments to measure low currents, high resistance; RLC bridges. This lab is used to perform complex investigation of the electrical properties (hysteresis loops, C-V and I-V characteristics, impedance spectroscopy; thermally stimulated currents, etc.).

Laboratory for testing solar cells, with 1 SUN solar simulator and other accessories.

Laboratory for characterization of materials for microwave devices, as well as laboratory models of microwave devices, including: 1) Vector Network Analyzer PNA 8361° from Agilent (0,01 - 67 GHz) for two-ports complex S parameters. The instrument is also used for material characterization. It uses electronic calibrator Agilent N4694-60001 in range 10 MHz – 67 GHz. For access, 1.9 mm, 2.9 mm, 2.4mm, 3.5 mm, SMA or N connectors or adaptors are used. 2) Vector Network Analyzer PNA-X N5245A from Agilent (0,1 – 50 GHz standalone) with 4 ports and dual sources. It allows the measurements of such non linear parameters as the X parameters. By using the millimeter wave extensions, the system covers a wide frequency band up to 500 GHz, unique in South-Eastern Europe. Each extension pair allows the measurement of two-ports parameter of waveguide devices. The millimeter wave extensions are from OML (N5260A V10 VNA2, WR-10, 75-110 GHz; N5260A V06 VNA2, WR-06, 110-170 GHz; N5260A V05 VNA2, WR-05, 140-220 GHz; N5260A V03 VNA2, WR-03, 220-325 GHz; N5260A V02.2 VNA2, WR-02.2, 325-500 GHz). 3) Anechoic chamber with internal dimensions 3040 mm x 4100 mm x 2800 mm. 4) Microprobe station for direct on wafer measurements of two-ports in the frequency range 0.1 - 67 GHz by using probes GSG with 150 m si 100 m pitch. 5) TDS THz spectrometer from Aispec.

Laboratory for optical spectroscopies including a spectroscopic ellipsometer and FTIR.

The group has access to other infrastructures located at NIMP, through collaborative research activities, such as: TEM and SEM equipment; XPS characterization (including at Elettra Synchrotron Trieste); magnetic measurements (SQUID, PPMS); other optical spectroscopies (Raman, UV-Vis-NIR, luminescence); clean room facility; small bio-laboratory for testing bio-materials.

Fig. 4. *Laboratory for electrical characterization of dielectric, ferroelectric and semiconductor materials and related structures.*

Services

Material preparation (bulk ceramics, thin films deposition by various techniques) Trap investigation by DLTS and TSC Electric characterization of materials on a wide temperature range, under electric and magnetic fields.

Investigation of pyroelectric properties.

Fabrication and characterization of erovskite solar cells.

Characterization of microwave, millimeter waves and Terahertz materials and devices.

Biocompatible coatings for implants.

Realization and characterization of catalytic materials AFM/PFM characterization.

Results

14 on-going projects in 2019 (12 will continue in 2020); 21 project proposals submitted in 2019.
51 published papers (28 in Q1; 15 in Q2; 9 only with authors from the group); 8 patent request or other form of intellectual property rights, 3 granted patents.

Multi-layers are formed by alternating ferroelectric and insulating films so that the structure starts and ends with a ferroelectric film. It was found that such structures present: multiple polarization states, therefore can be used to dramatically increase the memory density from only 2 states in classic ferroelectric memories to 2^n in multilayers, with n being the number of ferroelectric layers in the structure; the memory state can be read non-destructively by measuring the capacitance, resulting 2^{n-1} independent capacitance states; logic memories can be performed with the multi-layer structure, and the final result can be stored in the same cell, concluding the new structure acts as a memcapacitor (see **Fig. 5**).

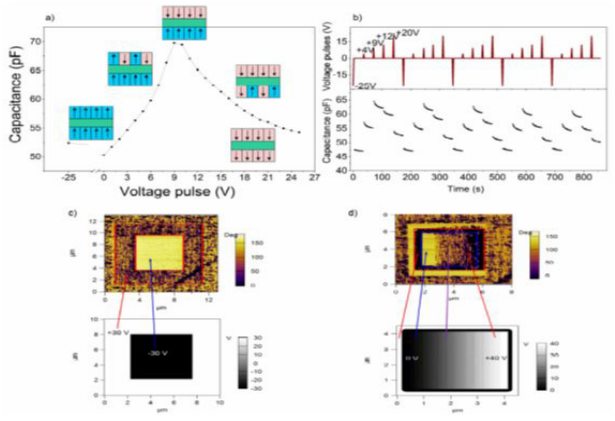

Fig. 5. *Tri-layer ferroelectric-insulator-ferroelectric structure acting as memcapacitor (PHYSICAL REVIEW APPLIED 12, 024053 (2019)).*

Laboratory 20 "Magnetism and Superconductivity"

Group name

Electronic Correlations and Magnetism

Group leader

Victor Kuncser

Team

3 CSI, 3 CSII, 8 CSIII, 2 CS, 4 ACS, 1 IDT3, 1 engineer, 1 technician.

Main research directions

It envisages the domain of magnetic and magneto-functional materials for actuator and sensoristic applications. The research process covers all stages, from preparation (bulk materials, thin films or nanostructures) to structural and electronic characterization, completed with a deep analysis of magnetic properties and functionalities mediated by magnetic reconfiguration controlled by temperature, magnetic and electric fields, applied or from interface interactions. The research is focused especially on the study of 0D,1D and 2D nanostructures. In the case of magneto-functional structures, magnetic systems of nanoparticles, thin films and multilayers, materials for colossal magnetoresistance (CMR), giant magnetoresistance (GMR) and tunnelling magnetoresistance (TMR), soft and hard magnetic materials, Heusler compounds with spin polarization, heterogeneous multiferroic systems, magneto-caloric materials, diluted magnetic oxides/semiconductors, thermo-electric systems, etc. are envisaged. In addition, bulk materials, advanced hybrid systems and composites / nanocomposites destined to operate in extreme conditions such as the ones in fusion and fission reactors, particle accelerators and in space, are investigated. Aspects related to the effect of explosions on various materials in correlation with specific parameters of the shock waves are also considered. Interactions at the interface and functionalities induced by them in nanostructured hybrid systems such as soft magnet / hard magnet (exchange-spring), ferromagnet/antiferromagnet (exchange-bias), ferromagnet-ferroelectric (magneto-electric coupling) represent another field of interest related to fundamental and applicative aspects of smart multi-functional systems. In specific cases, the experimental studies are completed by theoretical studies approaching electronic configurations based on Density functional theory (DFT) and magnetic configurations based on finite-element simulation programs.

Relevant infrastructure

Among important research equipment, considering preparation facilities as well as characterization ones, the following can be listed: spark plasma sintering, microwave sintering and melt spinning equipment, nanoparticle preparation systems by hydrothermal / solvothermal synthesis in autoclave and centrifugation for separation by sizes), RF/DC sputtering deposition system for magnetic thin films and multilayers with 4 sources and base pressure in the range of 10^{-9} mbar, facility for inducing thermal transfer in radiofrequency magnetic field to determine specific absorption rates in dispersed nanoparticle systems, thermogravim etric and differential scanning calorimetry systems, Vibrating Sample Magnetometry system in magnetic fields up to 9 Tesla, Mossbauer spectrometers with different accessories to perform measurements at variable temperatures (4.5 K –1000 K) and in applied fields, via the detection of gamma radiation / X- rays / conversion electrons (the only group in Romania active in Mossbauer Spectroscopy), complex system for measurements of physical properties (PPMS) with magnetic fields up to 14 Tesla and a SQUID type magnetometer working in 7T down to 2K from Quantum Device with the corresponding facility for liquid He production (18 l /24 h).

Magnetic texturing of thin films is investigated by vectorial MOKE magnetometry. For the high temperature domain, the laboratory possesses a Laser Flash Analyzer system that allows the determination of thermal diffusivity, specific heat and thermal conductivity of the volume materials or multilayers (3 layers, including liquids) in the range 25-1100^0 C, a dilatometer (Netzsch 402 C, 2015) to determine thermal expansion coefficients (25-1600^0 C) and an equipment (Netzsch, Nemesis 2015) to determine electrical conductivity and Seebeck coefficient (25-800^0 C). In order to determine the composition in bulk / powder systems, an X-ray fluorescence device is available, as for very low concentrations/quantities, the group possesses an inductively coupled plasma mass spectrometer (ICP-MS), with an extension for thin film analysis by laser ablation (LA), the last one being aquired in 2019, in collaboration with Laboratory 10.

Fig. 1. *ICP-MS with LA for thin films (upper left)*

Mossbauer spectrometers with closed circuit He cryostats (lower left) and SQUID device – Quantum Design, of high sensitivity (right).

Available services

Preparation of metallic and intermetallic compounds in the geometry of thin films, ribbons or bulk.

Synthesis of materials that are important for applications using state-of-the-art powder metallurgy techniques.

Lyophilisation from freezed materials.

Treatment of powders and thin films at high pressures and temperatures in non-corrosive gas atmosphere (hydrogen, nitrogen, methane, carbon dioxide, helium) and measurement of the formation kinetics and thermodinamics of the materials obtained by gas-solid reaction.

High sensitivity magnetometry to characterize the magnetic properties of the elements (bulk, powders and nano-powders, ribbons and nanocomposites, 0-, 1- and 2-dimensional nanostructures).

Characterization of the thermodynamic and transport properties (thermal, electric) of the materials.

Determination of the Debye temperature, specific heat and entropy variation of solid materials in the temperature range of 2-300 K and in a magnetic field between 0 and 14 T.

Determination of thermal conductivity of solid materials in the temperature range of 2-300 K and in a magnetic field between 0 and 14 T.

Complex characteristics and specific properties of materials with iron evidenced by powerful nuclear gamma resonance investigation methods (Mossbauer spectroscopy).

Specific temperature-dependent properties evidenced by modern differential thermal analysis methods, differential calorimetry and mass spectrometry.

Atomistic simulation within the density functional theory (DFT) of the materials for advanced applications and finite element micromagnetic modelling.

Activity and Results

In 2019, the group had 3 ongoing national research projects (excepting the Core Programe), as coordinator (1 Solutions, 1 PCCCDI, 1 Ideas), with important additional contributions to other 3 national projects. Members of the group also account for 4 international projects (1 EUROATOM, 1 EIT and 2 bilateral cooperations), additionally contributing to other 2 projects of POC type. In parallel, some services were provided within 3 economical contracts.

Within the same interval, 21 papers were published (15 having main authors from the group) and other 8 papers were accepted for publication. A number of 3 patent / utility models applications were submitted.

Among the results of the group obtained in 2019 (others than those presented in selected results) one may note the results related to the investigations of materials for operating in extreme conditions and, respectively, the focus on specific magneto-functionalities of thin films based on iron (Fe) and a rare earth (RE) elements.

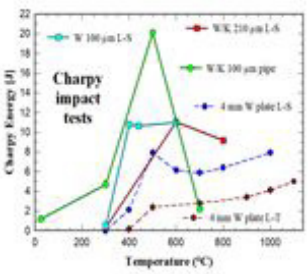

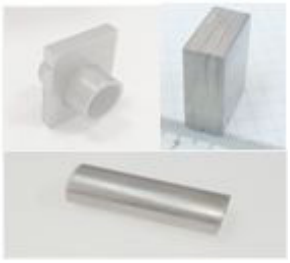

In the WPMAT work performed in EUROfusion consortium frame, the group is involved in the development and characterization of materials for applications in extreme conditions like those expected in thermo-nuclear fusion reactors. In 2019, important results were obtained concerning W-laminates materials. These layered composites aim to transfer the excellent mechanical properties of W foils (produced by cold severe plastic deformation)

to bulk materials which can be used both as armour or structural materials in a fusion reactor like DEMO.

The composites produced in NIMP by our recently developed FAST joining technology have reached record values in Charpy impact tests, both for standard and pipe formed specimens.

Intermetallic thin films of type Fe-RE (with or without bohrium addition) can be strictly controled from the point of view of structural and magnetic properties by the type and content of rare earth.

By adequately choosing those parameters, random magnetic anisotropy phenomena can be induced (the case of RE ions with single ion magnetic anisotropy in amourphous structure), as well as numerous specific magneto-functionalities (the case of isotropic RE ions that couple antiferromagnetically with Fe).

Therefore, it was proved that in the case of Fe1-xGdx type amorphous systems, where x varies around the magnetic compression point (the concentration at which the magnetic moment per unit formula of Fe equals the one of Gd), significant variations of the magneto-optic effects in very narrow concentration ranges (x=0.79 left, x=0.85 right in the bottom **Figure**) can be obtained as well as respectively, atypical magneto-resistive effects, with monothonic variations of the resistance versus the applied field (middle).

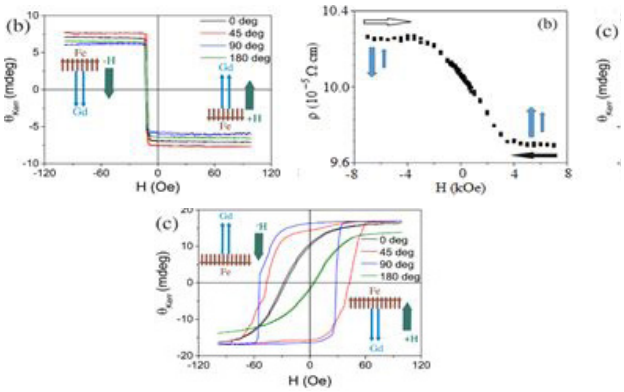

Group name

Superconductivity Group

Group leader

Adrian Crisan, Ph.D., D.Sc.

Team

2 CSI, 1 CSII, 2 CSIII, 1 CS, 1 ACS, 2 technical staff

Main research directions

Fundamental and applied research on superconductivity, mainly targeting materials with superconducting properties with potential for practical applications; studies of vortex matter, dynamics and pinning; nano-engineering of artificial pinning centres for high-magnetic field applications. Exploration of fields of applicability of these materials and related ones considering, beyond superconductivity, other that may be important for applications, such as mechanical, biological, optical, etc.

Activity

The group has a rich research activity dating back to 1973 and is included in the EU White Paper on Superconductivity since 2008.

The group aims to capitalize on the experience gained in superconductivity, both from fundamental and applicative point of views, on various superconducting materials, as well as other materials for new applications where properties other than superconductors are the defining ones: mechanical, optical, biodegradation.

The studied materials are mainly cuprate high temperature superconductors Y(rare earth) $Ba_2Cu_3O_7$ (RE123) with nano-engineered pinning centres, Bi- and La- based superconducting cuprates, MgB_2 (with various additions for increasing pinning properties), iron-based pnictide and chalcogenide multicomponent superconductors and low temperature (classic) metallic and intermetallic superconductors. Other materials of interest are CeO_2, $SrTiO_3$, LiPdPtB, PdO, boron/carbide composites, selected steels, and archaeological ceramic materials.

Most of the materials are obtained in the laboratory in various morphologies: powders, polycrystalline bulk samples, single crystals, wires/tapes, nanostructures, heterostructures and nano-composites. The group uses advanced techniques for obtaining or processing materials: conventional powder synthesis in a controlled atmosphere, cryochemistry or energy milling, crystal growth in flux or by melting zone, growth of thin films by laser ablation, sintering by Spark Plasma, lamination, arc melting, etc. The equipment for fabrication of above-mentioned materials is available in the Laboratory of Magnetism and Superconductivity (LMS) of which the Superconductivity Group is a member.

The materials are characterized mainly from the viewpoint of superconducting properties, at temperatures down to 1.8 K, maximum magnetic field 14 T, and at frequencies up to 10 kHz, using high-performance equipment available in our laboratory: *Quantum Design* Physical Properties Measurement System (PPMS), *Quantum Design* SQUID Magnetic Properties Measurement System (MPMS), *Cryogenic* Vibrating Sample Magnetometer (VSM). Mechanical properties are determined in quasistatic regime up to 1700 ^{0}C, using a recently-acquired equipment (INSTRON). Other measurements (structural, microstructural, chemical, bio, degradation) are performed using equipment available in our institute and/or in collaboration with other groups, from Romania or from other countries (Japan, France, Brazil, Russia, Ukraine, Italy, Germany, China, UK, Norway).

Advanced analysis of superconducting properties aims in particular to determine vortex phase diagrams vortex dynamics and vortex pinning. The group has internationally recognized fundamental contributions in these directions.

Temperature dependence of magnetization and resistivity, isothermal hysteresis magnetization and magnetic relaxation, current-voltage characteristics, bulk pinning force and pinning potential etc. are analysed within the existing theoretical models or using recognized practical and theoretical methodologies developed by a few members of the group, for example pinning potential determined from frequency-dependent AC susceptibility response, or the use of normalized magnetic relaxation rate to determine the cross-over between elastic and plastic vortex creep, and various field-m and temperature-dependent creep exponents.

The group develops materials and technologies for a number of applications: superconducting thin layers and coated conductors from high critical temperature cuprates containing nano-engineered pinning centres; superconducting MgB_2 wires/tapes in metallic sheath; MgB_2-based magnetic storage devices, magnetic concentrators and magnetic shieldings; MgB_2-based powders, coatings and bulks for biomedical applications; boron-based super-hard materials for tools and extreme high temperature applications, integrated multifunctional devices.

Relevant infrastructure

Among the most important research equipment used within the group are: spark plasma sintering installation, microwave field sintering installation, thin film / two-dimensional hetero-structure deposition system by pulsed laser ablation, melt zone furnace for crystal growths with ultra-intense illumination (*Crystal Systems Corp.*, Japan), systems for thermogravimetric measurements, *Quantum Design* (USA) Physical Properties Measurement System (PPMS), *Quantum Design* (USA) SQUID Magnetic Properties Measurement System (MPMS), *Cryogenic* (UK) Vibrating Sample Magnetometer (VSM), dilatometer (Netzsch 402^0 C) for determining the coefficients of thermal expansion.

For compositional analysis in bulk / powder systems, an X-ray fluorescence device and inductive coupled plasma mass spectrometer (ICP-MS) are used.

Within the group there is a pressure equipment for mechanical measurements, a complex system for corrosion measurements and a rolling machine with flat and profiled rolls.

Spark PLASMA sintering plant used to obtain high density bulk materials.

Services

Preparation / processing by various echniques of powders, single-crystals, thin films / heterostructures / nanostructures, bulks, composites.

Magnetic and transport measurements on superconducting materials.

Analysis of experimental data obtained on superconductors with the determination and modelling of critical parameters (critical temperature, critical current density, irreversibility field, pinning force and pinning mechanisms, trapped field, vortex pinning energies, Debye temperature, and others).

Mechanical measurements in quasistatic regime up to 1700 ^{0}C (bending / compression of hard materials).

Analysis of mechanical properties and correlation with fractography aspects.

Targets fabrication for thin layer deposition;

Results

In 2019 there were published 13 ISI articles (8 with first/corresponding author) and 4 book chapters (3 with first/corresponding author). Also 2 patent applications were submitted in 2019.

In 2019 the group had the following projects in progress (as coordinator): EU Operational Programme Competitiveness Program-Attracting Experienced Researchers from Abroad POC 37_697 no. 28 / 01.09.2016 “Rare-Earths- and Boron-based Advanced Special Materials” (REBMAT); European Research Area-M 74/2017 BIOMB, COST Action “Nanoscale Coherent Hybrid devices for Superconducting Devices” (NanoCohybri).

Among the results of the group in 2019 that are not encased in the 2019 Report of the institute we mention the detection and explanation of extremely high activation vortex energies at small relaxation times in superconductors in mixed state, even in the vicinity of the DC irreversibility line. Short-time relaxation was obtained from the AC magnetic response of samples with known vortex pinning microstructure in detail, such as the one presented in (a) for YBCO layers with barium zirconate (BZO) nano-rods, having a critical temperature $T_C \sim 89.2$ K, deposited on STO substrates decorated with Ag nanodots. In (a) BZO (1) nanorods are distinguished between YBCO columns (2) and BZO nanoparticles (3).

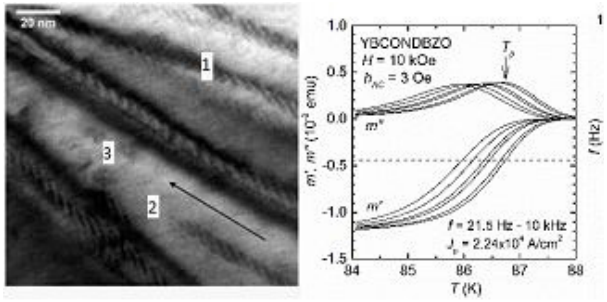

(a) (b)

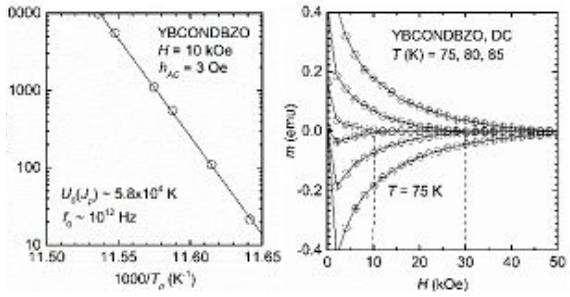

(c) (d)

Frequency-dependent AC magnetic response shown in (b) reveals maxima of imaginary (out-of-phase) component m" at peak temperatures T_p when the AC critical state reaches the centre of the sample, with a current Jp induced in the sample. From the slope in the Arrhenius representation on ln(f) vs. 1 / T_p, where f is the frequency, shown in (c), is straightforward to estimate the activation energy at low temperatures U_{AC} (0, Jp). For a magnetic field H = 10 kOe, U_{AC} (0, J_p) resulted to be approximately $5.8x10^4$ K. Using the formula $U_{AC}(T, J_p) = U_{AC}(0, J_p)$ $(1 - T/T_c)$ we determined an activated energy at T = 85 K of 2731 K (in K, taking Boltzmann constant 1). This is an unexpectedly high value considering that for H = 10 kOe and T = 85 K the sample reached the irreversibility line, above which the vortex pinning centers are practically inactive for long periods (DC case), as shown in (d). Through the laborious measurements described in (High Vortex Activation Energy in the AC Magnetic Response of Superconductors close to the DC Irreversibility Line L. Miu; I. Ivan; AM Ionescu; A. Crisan; D Miu; T. Petrisor; eds. P. Mele, P. Badica et al, Springer, ch 6 in Superconductivity from materials science to practical applications, 2019, pp. 303-324), i.e by estimating the hopping distance for vortices, we concluded that this is much larger than the average distance between the pinning centers. The origin of the very high activation energies at short times was explained by us due to the excessive viscosity of the vortex system, caused by the presence of active pinning centers at short times, due to the fact that when the hopping distance exceeds the average separation between the pinning centers, the renormalization of the pinning potential due to thermal fluctuations is incomplete.

Thus, the activation energy of vortices at short times is described by

$$U_{AC} = \phi 0 L_{eff} l_h^- (J_d - J),$$

where ϕ_0 is the magnetic flux, L_{eff} is the effective vortex length, (l_h) is the average hopping distance, and J_d is the critical current.

Laboratory 30 "Nanoscale Condensed Matter"

Group name
Theoretical Physics
Group leader
Valeriu Moldoveanu (SR 1)
Team
8 permanent positions (2 CSI, 1 CSII, 2 CSIII, 1 JR, 2 ACS) .

Main research directions

Topological features of 2D materials and transport properties of 2D lattices.

Open quantum emitters and nano-electromechanical systems.

Results and funding

Publications: 7 papers (2 Phys. Rev. B, 1 invited review paper Entropy Journal, 2 Phys. Stat. Solidi B, 1 Annalen der Physik, 1 Beilstein Journal of Nanotechnology).

Projects: PCE 3/2017 "Electron-vibron coupling effects in nano-electromechanical systems" (PI V. Moldoveanu), PCE 201/2017 "Spontaneous symmetry breaking and dissipative processes in single quantum dot lasers. Lasing as a phase transition" (PI P. Gartner).

Selected results

Back-action effects in cavity-coupled quantum conductors. We investigated the electronic transport through a pair of distant nanosystems embedded in a single-mode cavity. We propose two settings which exhibit clear effects of the coupling between the two conductors via cavity photons. A steady-state effect consists of the removal of a Coulomb blockade from one subsystem when a current passes through the second subsystem. In a second setup we show that the photon-induced correlations provide information on the initial state of a closed subsystem by looking at the transient current which passes through a neighbor open subsystem. The results are published in Phys. Rev. B 100, 125416 (2019).

Spontaneous symmetry breaking in the laser transition. The instability of the laser systems to symmetry-breaking infinitesimal perturbations was studied theoretically. It is shown that the laser transition is similar to equilibrium phase transitions. Also, we prove that the mechanism of the spontaneous symmetry breaking is connected to the existence of a sharp laser transition, with a well defined threshold point. Moreover, the spontaneous symmetry breaking takes place when the system is in the lasing phase, and only then. As examples we discussed i) the case of a single, two-level emitter embedded in a cavity and interacting resonantly with its photon mode and ii) a chain of such cavities. The results are published in Phys. Rev. B 99, 115313 (2019).

Group name

Group of Nanomaterials and Nanostructures based on SiGeSn

Group leader

Dr. Ana-Maria Lepadatu

Team

6 senior researchers (3 CSI, 1 CSII, 2 CSII); 1 post-doc (1 junior researcher); 2 PhD students (2 ACS); 1 technician

Main research directions

Frontier research in condensed matter physics at nanoscale and in science of advanced materials of structures with nanocrystals (NCs) based on SiGeSn, 2D materials based on transition metal dichalcogenides (2D-TMD) and structures based on ferroelectric HfO_2:

- study of optical, electrical, photoelectrical, ferroelectric and charge storage properties

- strain and defects studies for improving the above mentioned properties

Advanced materials for industry with global impact (fields of Eco-Nanotechnologies and Advanced Materials, Information and Communication Technology, Security, Energy, New and Emerging Technologies) for micro-, opto- and nanoelectronics applications and sensors for health and environment applications:

- films and multilayered structures with NCs based on SiGeSn embedded in dielectric matrices (SiO_2, TiO_2, HfO_2, Al_2O_3, Si_3N_4) photosensitive in SWIR, with ferroelectric and charge storage properties

- 2D-TMD based materials and heterojunctions with electro-optic properties

Applied research and experimental development for environment, security, space, health and internet of things applications using the above mentioned materials (fields of Eco-Nanotechnologies and Advanced Materials, Information and Communication Technology, Security, Energy, New and Emerging Technologies); fabrication of devices – demonstrators up to TRL 5: electronic and photoelectric nonvolatile memories, dosimeters, optical sensors for monitoring the slippery road conditions (wet and icy in respect to dry asphalt), SWIR photodetectors.

Relevant infrastructure

SiGeSn Group research infrastructure consists mainly of: magnetron sputtering equipment (10^{-8} Torr high vacuum) for deposition of thin films and multilayer structures, equipped with in situ analysis techniques consisting of Auger electron surface spectroscopy – AES and low-energy electron diffraction – LEED, as well as real time *in situ* ellipsometric monitoring and profilometer for measuring thicknesses; rapid thermal processing (RTP) system for thermal annealing (RTA), oxidation (RTO) and nitration (RTN); three independent temperature zone horizontal split tube furnace for thermal annealing and physical vapor deposition (PVD); two set-ups for electrical (including ferroelectric and charge storage) and photoelectrical measurements; set-up for Hall effect and magnetoresistance measurements.

Magnetron sputtering equipment for deposition of thin films and multilayer structures, equipped with in situ analysis techniques consisting of Auger electron surface spectroscopy – AES and low-energy electron diffraction – LEED, as well as real time in situ ellipsometric monitoring.

Rapid thermal processing - RTP system (left); Three independent temperature zone horizontal split tube furnace (right).

Set-ups for electrical (including ferroelectric & charge storage) and photoelectrical measurements (left); Hall effect and magnetoresistance measurements (right).

Services

Deposition of semiconductor thin films and multilayer structures by magnetron sputtering: dielectrics (SiO_2, TiO_2, ZrO_2, HfO_2, Al_2O_3, Si_3N_4) and semiconductors (Si, Ge, SiGe, SiGeSn) on heated substrates or on substrates mantained at room temperature

Rapid thermal annealing (RTA) and controlled oxidations (RTO) in the rapid thermal processing - RTP system (up to 3-inch silicon wafer) at 200 – 1250^{0}C with ramp rates up to 200^{0}C/s, in gas flow (N_2, O_2, Ar si H_2) and thermal annealing in the three independent temperature zone horizontal split tube furnace at temperatures up to 1200 °C in vacuum or Ar, N_2 flow

Electrical characterization in dark and under illumination and Hall investigations by measurements and modelling of experimental curves:

- current-voltage (I – V) at different temperatures T, in DC and AC regime
- capacitance-voltage (C – V), capacitance-frequency (C – *f*) and capacitance-time (C – t)
- polarization-voltage (P – V)
- I – T and R – T at different bias voltages
- Photocurrent spectra (I – λ) under modulated and continuous light regime
- Hall measurements: V-I characteristics for different applied currents, magnetic fields and T

Results

In 2019 SiGeSn Group has coordinated 5 national projects (PCE 122/2017-19, TE 30/2018-20, TE 19/2018-21, PD 39/2018-20, NIMP group coordinator partner in PCCF 7/2018-22) and 1 international project (GESNAPHOTO/2016-19); published 9 ISI articles (Sci. Rep., ACS Appl. Nano. Mater., Nanotechnology – 2, Appl. Surf. Sci. – 2, Beilstein J. Nanotech. – 2, Rom. Rep. Phys.) and 2 IEEE proceedings papers; filed 1 patent application OSIM no. A 00772/2019. 3 patent applications were also published in the 2019 Official Industrial Property Bulletins of OSIM (RO133299-A0, RO133300-A0, RO133227-A0). The team members participated to 6 international conferences (EMRS – France, ICASS – Italy, GraFOx – Italy, EuroNanoForum – Bucharest, IBWAP – Constanta, CAS – Sinaia) with 11 contributions from which 1 invited lecture, 3 oral presentations and 7 posters. Also, the group received distinctions at invention fairs held in 2019, i.e. EuroInvent (Diploma of Excellence) and ProInvent (Diploma of Excellence and ProInvent Medal).

Trilayer structures based on Ge nanoparticles (NPs) embedded in HfO_2 for nonvolatile memories.

Obtaining nonvolatile memories with enhanced performance (6 V memory window) due to the cumulative contribution of Ge NPs charge storage centers and ferroelectric HfO_2 matrix.

Fabrication of dosimeter with high sensitivity (0.8 mV/Gy) to α particle irradiation at low doses (< 50 Gy), based on the mentioned nonvolatile memories.

VIS-SWIR photosensitive films and multilayer structures with SiGeSn-based nanocrystals (NCs) embedded in SiO_2, deposited by magnetron sputtering.

Fabrication of photodetectors with Ge NPs in SiO_2 with high responsivity (2.42 AW^{-1}) and quantum efficiency (445%), the Ge-NPs:SiO_2 films being deposited on heated substrates.

Increasing of photosensitivity of photodiodes based on SiO_2/SiGe/SiO_2/Si multilayers by hydrogen plasma annealing (in collaboration with Reykjavik University, School of Science and Engineering, Iceland in the frame of M-Era.NET PhotoNanoP project).

Elucidating the processes of GeSn NCs formation in SiO_2 – modelling.

Fabrication of photodiodes with GeSn NCs in SiO_2 having spectral response in VIS-SWIR up to 2.5 μm.

Group name

Group of Surface and Interface Science

Group leader

Cristian Mihail Teodorescu, PhD, Habil.,
Senior Scientist I

Team

1 CSI, 5 CSII, 7 CS III, 4 CS, 5 ACS, 1 Engineer, 3 Technicians.

Main research direction

Surface science, ferroelectrics, catalysis, magnetic materials, epitaxy.

Experimental setups

Experimental surface science setup, comprised by: (i) molecular beam epitaxy, with *in situ* analysis by low energy electron diffraction (LEED), reflection high energy electron diffraction (RHEED), Auger electron spectroscopy (AES), sample preparation by ion sputtering, annealing, plasma source, Knudsen cells, electron bombardment evaporators, residual gas analysis; (ii) an installation for scanning tunneling microscopy and spectroscopy (STM–STS), at variable temperature; (iii) an installation for angle- and spin-resolved photoelectron spectroscopy, allowing X-ray photoelectron spectroscopy (XPS), photoelectron diffraction (PED, XPD), angle-resolved ultraviolet photoelectron spectroscopy (ARUPS) also with spin resolution. Actually, this cluster is delocalized on the SuperESCA beamline at the Elettra synchrotron radiation facility in Trieste, Italy and is available for external users, fed with synchrotron radiation with continuous spectrum with energy between 90–1200 eV. Outside the beamtime allocated by Elettra, photoemission can still be performed by using monochromated Al K_α (1486.7 eV)/ Ag L_α (2984.3 eV) radiation and high power UV lamp (300 W) with He I (21.2 eV) and He II (40.8 eV) radiation. Manufacturer: Specs, Germany.

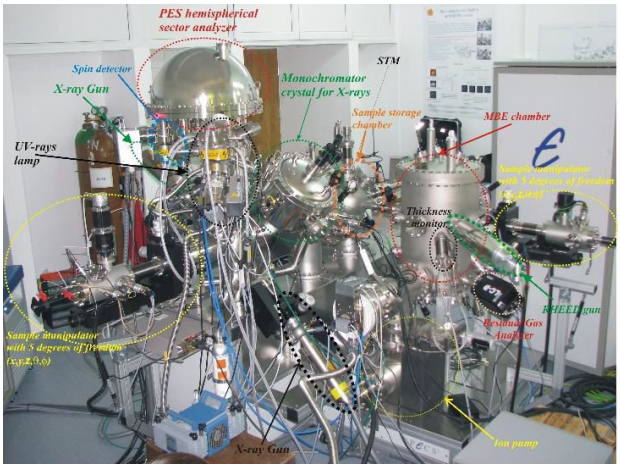

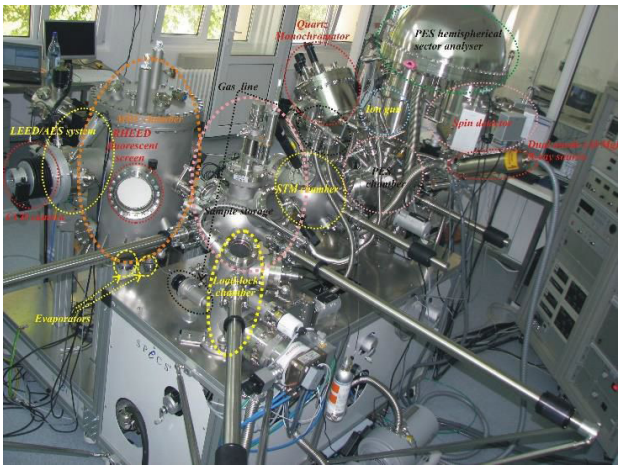

Experimental cluster comprising (i) a molecular beam epitaxy (with in situ LEED, RHEED and AES analyses), sample preparation (sputtering, annealing, Knudsen cells, e-beam evaporators), residual gas analysis, gas cabinet; (ii) a chamber for scanning tunneling microscopy and spectroscopy (STM – STS); (iii) chamber for photoelectron spectroscopy (XPS, UPS). Available excitation sources: monochromated Al K_α radiation (1486.7 eV), dual Al K_α (1486.7 eV) / Mg K_α (1253.6 eV) anode, UV lamp with He I (21.2 eV) radiation. Manufacturer: Specs, Germany.

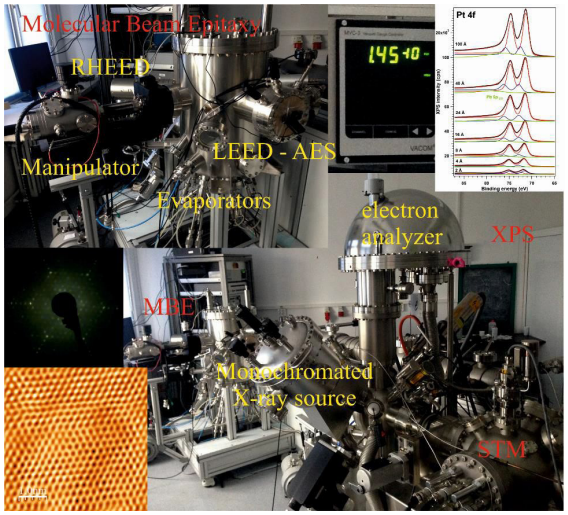

Automated installation for XPS with spatial resolution (2μ m) coupled to a reaction cell for online studies of surface reactions at high temperatures and pressures (1000 °C, 4 bar), with gas cabinet with 4 ways. Excitation sources: monochromated Al K_{α} (1486.7 eV), dual Al K_{α} (1486.7 eV) / M gK_{α} (1253.6 eV) anode. Manufacturer: Kratos Analytical, U. K.

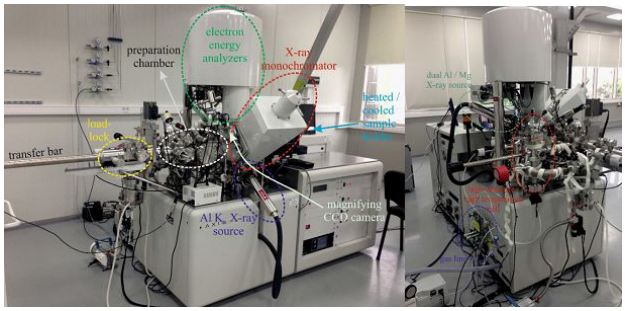

Installation for low energy electron microscopy (LEEM) and photoemission electron microscopy (PEEM). Available techniques: (i) dark or bright field LEEM with 4 nm lateral resolution; (ii) PEEM using excitation with Hg lamp or with UV lamp with He I and He II radiation, lateral resolution 15 nm; (iii) mirror electron microscopy; (iv) micro-LEED (with m lateral resolution); ***k***-space mapping with sub-micrometer lateral resolution (vi) Possibility to follow in real time LEEM, PEEM, MEM, LEED during thermal treatment, ion bombardment, thin film growth. Manufacturer: Specs, Germany.

Setup for laboratory extended X-ray absorption fine structure (EXAFS). Excitation: Mo $K_{\alpha 1}$ (17479.34 eV), W $L_{\alpha 1}$ (8397.6 eV), power 3 kW (40 kV, 75 mA); monochromators Ge(220), Ge(400), Ge(840); detectors: proportional or scintillators, measurements in transmission or fluorescence, simulation and analysis software. Manufacturer: Rigaku, Japan.

Chemistry laboratory, with basic instrumentation: glassware, balances, ultrasonic shafts, vortex, water distillation, pressure reactors, heating and stirring systems, photocatalytic reactions, vacuum stove (Memmert), rotvapor (Heidolph), etc. Dedicated to catalyst preparation and performance evaluation for oxidation, hydrogenation, coupling reactions etc. The laboratory is assisted by: (a) Analytical methods for chemical compound identification (gas chromatography coupled to mass spectroscopy GC-MS QP2010 Ultra, manufactured by Shimadzu, Japan). This equipment uses two injectors, two detectors (MS and BID), pressure valve for real time analysis, auto-sampler, detects gaseous compounds or volatile liquids. (b) Analysis system for materials characterization, using cumulative characterization techniques, such as temperature programmed desorption, reduction or oxidation (TPD, TPR, TPO), pulsed chemisorption, nitrogen physisorption (Brunauer-Emmett-Teller BET) for pore size analysis. (c) Raman spectroscopy (AvaRaman 532) and UV-Vis-NIR spectro-photometry (AvaSpec-ULS 2048 L-RS-USB2) used for reaction follow-up, product identification, detection and characterization of nanoparticles in suspension. Irradiation sources: 532 nm laser for Raman spectroscopy and Xe source with emission 200 – 1100 nm, for the UV-Vis-NIR spectro-photometer. The latter is equipped with an integrating sphere with 80 mm internal diameter and flux cell analysis with transverse Swagelok feedthroughs and two collimating lenses UV-Vis-NIR; maximum temperature 80 ^{0}C, maximum pressure 10 bar.

Services

Photoelectron spectroscopy-based techniques: X-ray photoelectron spectroscopy (XPS) and diffraction (XPD), ultraviolet photoelectron spectroscopy (UPS), angle-resolved UPS (ARUPS), spin-resolved ARUPS.

Auger electron spectroscopy (AES) and diffraction (AED).

Low energy electron diffraction (LEED) and reflection high energy electron diffraction (RHEED) characterization of surfaces.

Scanning tunneling microscopy (STM) and spectroscopy (STS) at variable temperature.

Sample depth profiling by ion sputtering assisted by XPS or AES.

Surface cleaning and synthesis of epitaxial thin films by molecular beam epitaxy (MBE).

Thermally-programmed desorption of molecules from surfaces by residual gas analysis (RGA).

Low energy electron microscopy (LEEM) and photoemission electron microscopy (PEEM), micro-LEED and micro-ARUPS.

Extended X-ray absorption fine structure (EXAFS).

Positron annihilation-induced Auger electron spectroscopy (PAES).

Results

53 papers in ISI-ranked journals, 6 patent applications.

Epitaxial growth of Ag(111) on Si(111) 7X7. This growth was performed up to thick layers (30 nm) in view of the cheap synthesis of single crystal Ag(111) substrates for growth of 2D systems. In the **Figure** below (a, b) represent XPS spectra confirming layer-by-layer growth, (c, d) are LEED images pointing long range order and (e) is a STM image of the 30 nm Ag(111) film exhibiting good surface morphology. Ref. A.E. Bocîrnea, R.M. Costescu, N.G. Apostol, C.M. Teodorescu, Appl. Surf. Sci. 473, 433–441 (2019).

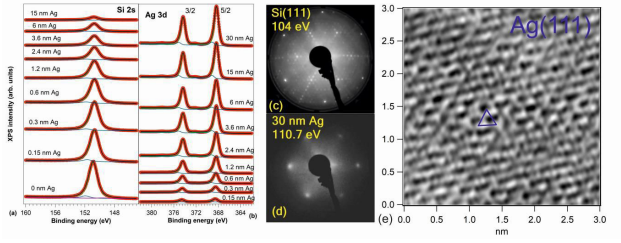

Origin and sense of resistance hysteresis in graphene-like layers grown on ferroelectric surfaces

sp^2 graphene-like layers were synthesized on atomically clean lead zirco-titanate (001) in a dedicated setup for *in situ* surface analysis together with electrical measurements for different substrate polarizations (I, below). Characterization was performed by high resolution XPS (II) allowing to deride carbon coverage and electronic structure of graphene-like layers, near-edge absorption fine structure (NEXAFS, III) allowing one to derive the percentage of in-plane sp^2 bonds, STM (IV) and resistance measurements vs. voltages applied on the ferroelectric (V). Layers with thicknesses of 1 monolayer (1 ML) or below, exhibit 'anti-hysteretic' behavior, while starting with 2 ML, the 'normal' hysteresis is obtained. The explanation proposed takes into account combined transport through graphene-like layers and the ferroelectric material near surface, when accumulated charge carriers are available due to some orientations of the ferroelectric polarization. Ref. N.G. Apostol, D. Lizzit, G.A. Lungu, P. Lacovig, C.F. Chirilă, L. Pintilie, S. Lizzit, C.M. Teodorescu, RSC Adv. 10, 1522–1534 (2020).

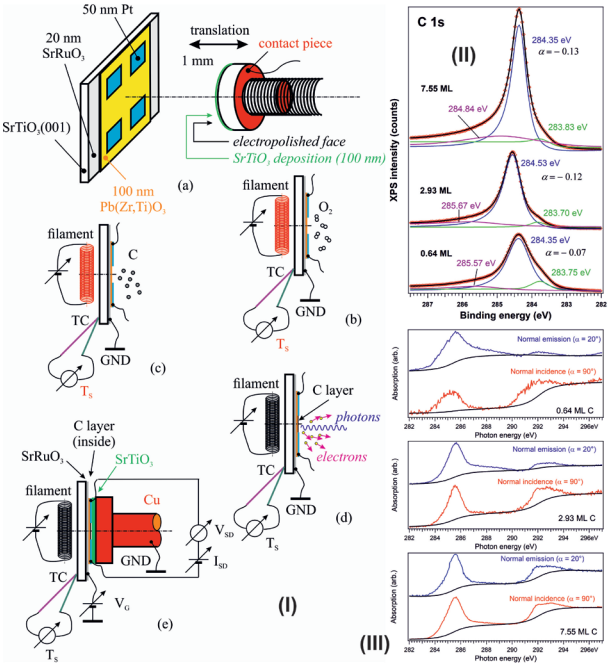

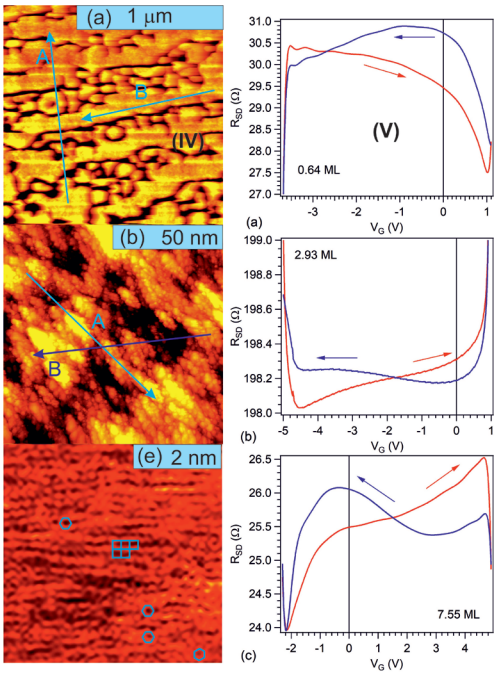

Laboratory 40 "Optical processes in nanostructured materials"

Group name

Group of Optical Processes in Nanostructured Materials

Group leader

Dr. Mihaela Baibarac

Team

3 CSI , 6 CSII, 3 CSIII, 6 CS, 14 ACS, 1 technician

Main research directions

Optical properties of composite materials based on macromolecular compounds and carbon nanoparticles (graphene, including graphene oxide and reduced graphene oxide, carbon nanotubes, fullerene) and phosphorene, respectively, for applications in the field of eco-nanotechnologies, health and energy storage (supercapacitors, rechargeable batteries).

Optical properties of the inorganic micro/nano-particles for applications in the field of heritage and optoelectronic.

Relevant infrastructure

i) an UV-VIS-NIR spectrophotometer, Lambda 950 model, from Perkin Elmer; ii) a FTIR spectrophotometer, Vertex 80 model, from Bruker, iii) a FTRaman spectrophotometer, RFS 100 S model, from Bruker; iv) a Fluorolog FL-3.2.2.1 model with upgrade for the NIR range, from Horiba Jobin Yvon, v) a triple Raman spectrophotometer T64000 model, from Horiba Jobin Yvon, equipped with the lasers for the excitation in visible range; vi) a FTIR imaging microscope SPOTLIGHT 400 from Perkin Elmer, vii) a thermoluminescence reader Harshaw TLD 3500, viii) a system for photoconductivity and I-V characteristics; ix) a Scanning Near Field Optical Microscope (Multiview 4000 SNOM/SPM system from Nanonics) coupled with Atomic Force Microscope (AFM), x) Fluoromax 4P with quantum efficiency and colorimetry options, for luminophores characterization, xi) system to measure surface/interfacial tension, contact angle and density; xii) Langmuir-Blodgett instruments, KSV 2000 system and KSV 5003 model; xiii) a potentiostat/galvanostat, Voltalab 80, from Radiometer Analytical; xiv) multi-channel potentiostat/galvanostat, Origaflex model, from Origalys; xv) equipment for deposition by vacuum evaporation of organic materials; xvi) broadband dielectric spectroscopy system from Novocontrol; xvii) an infrared spectro-microscope, Carry 600, from Agilent Scientific; xviii) a surface plasmons resonance (SPR) equipment from Reichert; xix) Hybrid Magnetron Sputtering – Pulsed Laser Deposition equipment for thin films and xx) Physical Vapor Transport equipment for transition metal dichalcogenides.

Services

The economic contract with S.C. Intelectro Iasi S.R.L. which aimed at highlighting the physico-chemical properties of nanostructured inks, the main analyzes being performed by UV-VIS and IR absorption spectroscopy, Raman scattering and viscosimetry.

Surface Plasmon Resonance equipment from Reichert

Infrared spectro-miscroscope, Cary 600 from Agilent Technologies

Physical Vapor Transport equipment for transition metal dichalcogenides

Hybrid Magnetron Sputtering – Pulsed Laser Deposition equipment for thin films

Results

At the 5 national projects that were in progress (POC 58/2016 - project director Dr. M. Baibarac, PCCDI38 / 2018 - project responsible Dr. M. Baibarac, PCCDI44 / 2018 - project responsible Dr. M. Baibarac , PN-III-P1-1.1-TE-2016-1997 - project director Dr. A. Velea, PCCDI52 / 2018 - project responsible Dr. CE Secu) have won the following 4 international projects EEA Grant / 2019 - project director Dr. O. Rasoga, M-ERANET-2D-SPIN-MED/ 2019 - project director Dr. A. Velea, MNET18/ADMA3454 - project director Dr. M. Baibarac and JINR-Theme: 04- 4-1121-2015 - project responsible Dr. I. Zgura.

2 patent applications (no. a 2019 00516/ 28/08/2019; no. a2019 00738/13.11.2019) and an experimental model were submitted to OSIM and.

34 articles were published in ISI journals from which 14 are in Q1 rank, 11 in Q2 rank, 6 in Q3 rank and 2 in Q4 rank.

The highlighting by the Raman scattering and photoluminescence (PL) studies of the adsorption processes of 1, 4-phenylene diisothiocyanate (PDITC) onto the graphene oxide (GO) sheets functionalized with polydiphenylamine (PDPA) in doped state (Sci. Rep. 9, 11968, 2019). In this context, two samples types were used. One resulted by the interaction in solid state phase of PDITC with GO and another prepared by the drop casting when a deposition of PDITC onto the PDPA functionalized GO sheets was reported. The interaction in solid state phase of PDITC with GO results in an intercalation process of the organic compound between GO layers and the generation of the o-thiocarbamate groups, which induces.

An increasing in the intensity of the PDITC Raman lines localized in the spectral ranges: 400–800 and 1000–1300 cm^{-1}.

A variation of the ratio between the intensities of the Raman lines at 1585 and 1602 cm^{-1} accompanied by an up-shift of the second line and iii) a down-shift of the PL band of PDTIC from 502 to 491 nm. Using cyclic voltammetry, an electrofunctionalization of the GO sheets with PDPA doped with H3PMo12O40 heteropolyanions occurs, as demonstrated by Raman scattering and FTIR spectroscopy. The presence of the amine groups in the molecular structure of the doped PDPA functionalized GO layers induces a chemical adsorption of PDITC on this platform, when the thiourea groups appear simultaneously with o-thiocarbamate groups.

The highlighting, by photoluminescence (PL) and UV-VIS absorption spectroscopy, of the influence of the UV light on folic acid (FA) in the presence of the phosphate buffer (PB) solutions (Sci. Rep. 9, 14278, 2019). We have demonstrated that a complementary method to UV-VIS absorption spectroscopy for the assessing of the photo-degradation process of FA in PB solutions can be PL. The PL band intensity of FA, localized in the 375–600 nm spectral range, was dependent on the PB solution pH. The FA PL band intensity increased as an increasing of the UV irradiation time takes place in the case of the FA-PB solutions having pH values equal to 6.4 and 5.4.

Under emission wavelength of 500 nm, a change in the position of the FA photoluminescence excitation (PLE) band when the FA-PB solution pH is changed from 7 to 5.4 is reported as the irradiation time increased to 317 min. These variations were explained by taking into account the formation of two photo-degradation products, i.e. pterine-6-carboxylic acid and p-amino-benzoyl-L-glutamic acid, as shown by IR spectroscopy. Our UV-VIS spectroscopy and PL studies demonstrate that the presence of various excipients in commercial pharmaceutical tablets does not affect the photodegradation process of FA in PB solutions.

Laboratory 50 "Atomic Structures and Defects in Advanced Materials (LASDAM)"

Group name

Atomic Structures and Defects in Advanced Materials

Group leader

Dr. Corneliu Ghica

Team

LASDAM counts 29 research and technical personnel including: 17 Senior Researchers (5 CSI, 3 CSII, 8 CSIII, 1 CS), 5 ACS (4 PhD students, 1 MSc student) and 7 technical staff (4 engineers and 3 technicians).

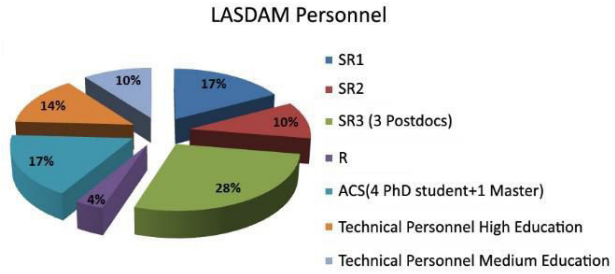

Main research directions

In-depth study of the microstructural properties of advanced materials such as nanostructures (powders, nanowires), thin films, ceramics and special alloys using advanced techniques of analytical electron microscopy TEM/SEM including atomic resolution imaging (HRTEM, HAADF STEM), elemental mapping at atomic resolution (HRSTEM EELS), electron tomography, structural mapping (SEM-EBSD, precession electron diffraction).

Multifrequency and multiresonance EPR investigation of the paramagnetic point defects, either intrinsic or induced by impurities or radiations in insulators and wide-bandgap semiconductors.

Investigation of the physical chemical mechanisms at the bottom of the detection process in nanostructured materials for gas sensing applications.

Interdisciplinary researches on cellular and non-cellular in vitro interactions and biomedical applications of inorganic nanomaterials and hybrid nanostructures

Main research infrastructure

Among the important research equipment we mention: aberration-corrected analytical transmission electron microscope (HRTEM/HRSTEM) provided with probe Cs corrector of the spherical aberration and EDS and EELS microanalytical facilities, allowing sub-Ångström spatial resolution and atomic elemental mapping; high-resolution analytical electron microscope for electron tomography and in-situ heating/cooling experiments; SEM-FIB dual analytical system used for morphostructural and microanalytical investigations (SEM, EDS, EBSD) as well as for the advanced materials processing at micro and nanometric scale by means of a Ga^+ ion beam and nanomanipulators; specialized equipment for TEM/SEM specimens preparation by mechanical thinning and polishing, ion milling, electropolishing; continuous wave (cw) X-band (9.8 GHz) EPR spectrometer with variable temperature (VT) accessories in the range 80 to 500 K; cw Q-band (34 GHz) EPR spectrometer with ENDOR (Electron-Nuclear Double Resonance) and VT: 5 to 300 K accessories; pulse X-band (9.7 GHz) EPR spectrometer equipped with pulse ENDOR, pulse ELDOR (Electron-Electron Double Resonance) and VT: 5 to 300 K accessories; automatic liquid He plant completed with a helium recovery system; gas mixing station and associated electrical measurements equipment for materials testing under controlled atmosphere; specialized equipment for hydrothermal and co-precipitation chemical synthesis.

a. Bruker EPR spectrometer in X band (9.7 GHz) in pulsed regime with ENDOR accessories; b. Bruker EPR spectrometer in CW Q-band with ENDOR accessory;

c. Setup for electrical measurements under controlled atmosphere gas mixing station.
d. JEM 2100 high-resolution analytical transmission electron microscope;
e. Tescan Lyra III analytical SEM-FIB dual system;
The HRTEM and EPR spectroscopy facilities are included in the Central-European network of research infrastructures CERIC (http://www.c-eric.eu/) since its creation in 2014. NIMP-LASDAM is the Romanian representing entity and partner facility in CERIC along with advanced laboratories from research institutions and universities in Austria, Croatia, Czech Republic, Hungary, Italy, Poland and Slovenia.

Services

Apart from the scientific research activities developed within national and European research projects, LASDAM offers a wide range of R&D services contracts for the private and public sectors:

i.High-resolution FEG-SEM morphological characterization of advanced materials, from nanopowders and nanowires/nanotubes to bulk ceramic or metallic materials;

ii. Microstructural characterization of nanostructured materials (powders, nanowires), thin films, ceramics, alloys by TEM/HRTEM and SEM;

iii. Chemical elemental composition measurements by EDS;

iv. Large area and/or local elemental mapping by SEM-EDS and STEM-EDS;

v. Multifrequency EPR characterization of bulk and nanostructured insulating and semiconductor materials.

Determination of the nature, concentration, localization, formation mechanism and stability of the paramagnetic centers (intrinsic defects, impurities, radiation defects, radicals etc.) present in the materials.

Investigation of chemical transformations, structural or magnetic transitions.

Detection and characterization of radicals in materials with biochemical applications using EPR spin-trapping.

vi. Controlled simulation of toxic and explosive gas environments (CO, CH_4, NO_2, H_2S, NH_3, SO_2) for testing and calibration of gas sensors; temperature-voltage calibration for the optimization of power consumption for substrates and gas sensors.

As partners in the CERIC consortium, we perform specific TEM and EPR investigations on projects submitted by external users worldwide. The technical and scientific peer review evaluation system guarantees a competitive free access to nearly 50 multi-probe available techniques. Six teams of international external users are hosted by LASDAM in average every year, which represents a significant contribution to the increase of international visibility and scientific prestige of NIMP.

Results

Researches developed within LASDAM contributed to the publication of 33 ISI scientific papers, a patent application as well as 21 participations in scientific conferences during 2019. Among the significant results we mention those concerning the description of the complex physical-chemical mechanisms of the detection process in the case of chemo-resistive gas sensors based on metallic oxide semiconductors obtained in the frame of PN-III-P4-ID-PCE-2016-0529 project developed within the laboratory. Through a complex approach starting from the synthesis of the mesoporous material based on SnO_2 doped with Zn/In and loaded with Pd/Fe nanoparticles, followed by in-depth microstructural and functional characterization, we have correlated the nanoscale and atomic structural properties, evidenced by advanced techniques of electron microscopy (TEM/HRTEM, FEG-SEM, EELS, EDS, electron tomography), electron paramagnetic spectroscopy and X-ray diffraction, with the selective sensitivity to toxic gases (NO_2, CO, NH_3) determined by electrical measurements in controlled atmosphere.

Also, through correlated EPR, microstructural and optical studies within the PN-III-P4-ID-PCE-2016-0079 project developed within the laboratory, we have determined the local atomic structure and the electronic properties of the point defects, intrinsic or associated to impurities, in crystalline amber and dark cBN, prepared by high-temperature and high-pressure synthesis. We have evidenced modifications in the aggregation of the impurities and of the paramagnetic defects in cBN by thermochemical treatments and/or irradiation.

FUNDAMENTAL PROPERTIES OF MATERIALS

SELECTED RESULTS

Back-action effects in cavity-coupled mesoscopic conductors

V. Moldoveanu, I. V. Dinu

Quantum emitters coupled to photon modes and to particle reservoirs are nowadays routinely designed in order to study the entangled dynamics generated by the light-matter interaction [1,2].

The present theoretical study [3] is concerned with the time-dependent transport properties of a quantum hybrid system composed of a pair of distant nanosystems ($S_a$and S_b) embedded in a single-mode quantum cavity. Each subsystem is connected to source and drain particle reservoirs and the electron-photon coupling is described by the Tavis-Cummings Hamiltonian. The chemical potentials of the four leads are denoted by $\mu_{l,a}$ and $\mu_{l,b}$, l=L,R. We considered that in each subsystem the electronic tunneling involves only the lowest two single-particle energies ε_{is}(i=1,2).

In this regime, the photon-mediated interaction is only active if each subsystem accommodates at least one electron. In order to discuss the numerical results it is useful to introduce the mean occupation numbers $q_{i,s}$ of the two levels of each subsystem. If the two subsystems are identical, the resonance frequency is set to $\hbar\omega=\varepsilon_{2s}-\varepsilon_{1s}$. The first transport regime we analyzed emphasizes of the switching between the Jaynes-Cummings (JC) and the Tavis-Cummings (TC) dynamics. More precisely, the chemical potential μ_{Ra} is chosen such that ε_{2a} lays within the bias `window' $\mu_{La}-\mu_{Ra}$ while $\varepsilon_{1a}<\mu_{Ra}$ (see the inset of (**Fig. 1(a)**). On the other hand μ_{Rb} is fixed such that both single-particle levels of subsystem S_b are allowed to participate in transport.

We first calculated the current J_{La} which enters subsystem S_a if S_b is not connected to particle reservoirs and does not contain electrons. In the initial state denoted by $|00,0\rangle$, the photons emitted by S_a cannot be absorbed by S_b and the system dynamics are described by the JCHamiltonian.

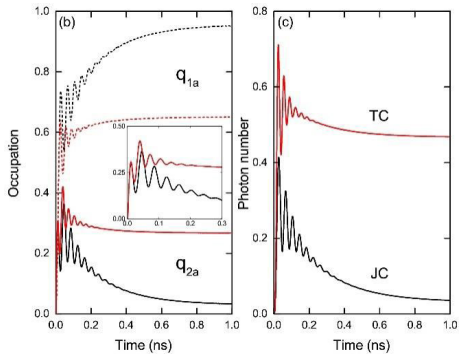

Fig. 1. **a**) *The transient currents associated to the JC and TC configurations. Those dashed lines show the same currents calculated in the absence of the electron-photon coupling.*

Inset: the optical and tunneling processes for the dinamics. b) The occupation of the optically active levels in the subsystem S_a in the JC (dashed line) and TC (solid line) regimes. Inset: q_{2a} in the transient regime. c) The mean photon number in the JC and TC regimes. Other parameters: μ_{La}=μ_{Lb}=45 meV, μ_{Ra}=41.5 meV, μ_{Rb}=35 meV, g_0=53 μeV, loss parameter κ=0.

The 2nd numerical simulation starts from the same initial state, but now the two subsystems are *simultaneously* coupled to the four particle reservoirs such that the Tavis-Cummings states can also participate to transport. In (**Fig. 1(a)**) we present the transient currents for the JC and TC configurations.

In the absence of transport through subsystem S_b the open subsystem S_a evolves to the Coulomb blockade regime such that in the steady-state regime J_{La}=0 and $q_{1a}\approx1$. This feature is confirmed by the evolution of the charge occupation of the levels q_{1a} and q_{2a} which is shown in (**Fig. 1(b)**). The optical Rabi oscillations are visible in the transient regime but dissappear in the stationary-state because the coupling to the particle reservoirs acts as a dissipation source.

The period of the JC Rabi oscillation is T_0=39ps and corresponds to the vacuum Rabi frequency Ω_0. We recall that in general the Rabi frequency associated to a fixed number of photons N is calculated as $\Omega_N=2g_0\sqrt{N+1}$. It also lets us notice that in the stationary state the mean number of photons vanishes.

The TC regime shows significant differences. From (**Fig. 1(a)**) one observes that in the stationary state the current J_{La} is finite and thus proves the activation of the tunneling processes form the excited level ε_{2a} to the reservoir R_a. This 'lifting' of the Coulomb blockade at the level of subsystem S_a is due to the photon exchange with the other subsystem. The mechanism is suggested in inset of (**Fig. 1(a)**): i) The subsystem S_b generates photons even in the stationary state via relaxation processes $\varepsilon_{2b}\rightarrow\varepsilon_{1b}$; ii) the emitted photons excite electrons from the level ε_{1a} to excited level which contributes to the non-vanishing steady-state current in S_a. This scenario is also confirmed by the results shown in (**Fig. 1(b)**), i.e. in the stationary state the energy level $\varepsilon 1a$ is not completely filled anymore.

One also notices that the TC and JC regimes exhibit different periods of the Rabi oscillations. Indeed, the Rabi oscillations corresponding to the N-photon Tavis-Cummings 'dressed' states have the periods $\hat{\Omega}_N=2g_0\sqrt{4N-2}$ and $\hat{\Omega}_N/2$.

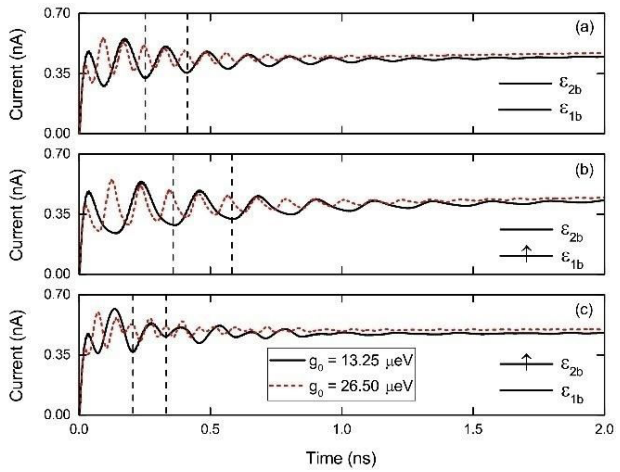

Fig. 2. a) *The transient Rabi oscillations of the output current J_{Ra} for different intial states of the neighbour subsystem indicated in the insets of each* ***Figure****. The vertical dashed line marks the Rabi oscillation period. Other parameters: $\mu_{La}=\mu_{Lb}=45$ meV, $\mu_{Ra}=41.5$ meV, $\mu_{Rb}=35$ meV, $g_0=53$ μeV, loss parameter $\kappa=0$.*

In order to capture transient effects of the photon-mediated interaction we considered a setup in which subsystem S_b is still closed but is initialized in different electronic states (see the inset in (**Fig. 2)**) before coupling the neighbour subsystem to the leads.

As (**Fig. 2**)clearly shows the three transient currents J_{Ra} display different periods of the Rabi oscillations. These periods can be calculated/ estimated by taking into account the dynamics and the structure of the 'dressed' TC and JC states. This feature proves that the photon-induced correlations can be used to probe the state of a closed system by looking at the transient current passing through the neighbour subsystem.

References

[1] G.-W Deng et al. Nano Lett. 15, 6620 (2015).
[2] Y.-Y. Liu et al. Phys. Rev. Applied 9, 014030 (2018).
[3] V. Moldoveanu, I. V. Dinu, A. Manolescu, V. Gudmundsson, Phys. Rev. B 100, 125416 (2019).

Spontaneous symmetry breaking in the laser transition

P. Gartner

The lasers were recognized quite early oa as examples of systems undergoing a phase transition in conditions of *nonequilibrium*. The lasing regime plays the role of the 'ordered' phase, separated from the 'normal' one by a critical point, the laser threshold. The latter is usually identified by a jump in the population of the resonant cavity mode as a function of pumping. In a log-log plot, this jump in the input-output curve is given by $\ln\beta$ where the β-factor is the fraction of photons spontaneously emitted into the lasing mode.

The advent of nanolasers, with few emitters and well-confined photon modes, allowed for β-factors close to unity, erasing the intensity jump in the so-called 'thresholdless' lasers. Consequently, alternative lasing criteria have been proposed, not always agreeing with each other. Some are still based on the photon number n, by requiring $n>1$. Also, coherence tests, probing the Poissonian photon statistics are usually applied, the most frequently invoked being the requirement for the second order auto-correlation function at zero delay, $g^{(2)}(0)$, to be close to unity. Other criteria have been considered as well, and the issue is still debated *("What is Laser Threshold ?"*[1]).

Therefore it is surprising that a common feature of *equilibrium* phase transitions, namely the spontaneous symmetry breaking, was largely ignored. The instability against symmetry-reducing perturbation is a characteristic of the ordered phase, like the spontaneous magnetization in ferromagnetism. In this paper [2] we address the problem of an analog behaviour in the lasing regime. The task is to identify a symmetry of the problem, and to show that it is spontaneously broken if and only if the system is in the lasing regime.

As illustration, we consider the case of a single, two-level emitter interacting resonantly with a cavity mode. In the rotating frame, the Hamiltonian reads $H=gb^{\dagger}\sigma+g^{*}b\sigma^{\dagger}$. Here $b^{\dagger},b$ are the operators of the photon mode, $\sigma^{\dagger},\sigma$ are the pseudo-spin raising and lowering operators for the two-level system, and g is the Jaynes-Cummings (JC) coupling constant. The emitter is a quantum dot exciton and the symmetry is the invariance with respect to an arbitrary common phase factor assigned to the photon $b\rightarrow be^{i\varphi}$ and exciton operator $\sigma\rightarrow\sigma e^{i\varphi}$ ($U(1)$ invariance).

The equation of motion for an arbitrary operator A consists of a coherent, von Neuman part, supplemented by incoherent Lindblad terms, describing dissipative processes resulting from the interaction with the environment. Three such processes are considered: the excitonic spontaneous recombination, the cavity losses and the pumping of the excitonic state, simulated as an up-scattering process. The corresponding rates are denoted by γ, κ and P, respectively.

Obviously, the problem as stated in the equations above is $U(1)$- symmetric. The symmetry-breaking seed is represented by adding to the Hamiltonian a term driven by a coherent excitation field E, coupled only to the excitonic degree of freedom $E^{*}\sigma+E\sigma^{\dagger}$. It breaks the $U(1)$ phase symmetry, and generates *anomalous* averages, like $<b>$ and $<\sigma>$ i.e. expectation values that are strictly zero in the symmetric case. The 'spontaneous' nature of the symmetry breaking is defined as the persistence of the anomalous averages in the limit of zero perturbation $E\rightarrow 0$, as in the case of nonzero magnetization in magnetic systems for vanishing external magnetic field.

In order to show that the anomalous averages survive in exactly the same parameter domain which define the lasing regime one has to clearly identify the latter. In a previous paper [3] we have shown that a sharp phase transition, with a well-defined threshold point is obtained by scaling down to zero simultaneously both the cavity losses κ and the JC coupling g, so that the ratio g^2/κ remains finite. This is the nonequilibrium counterpart of the thermodynamic limit, an essential ingredient in equilibrium theories.

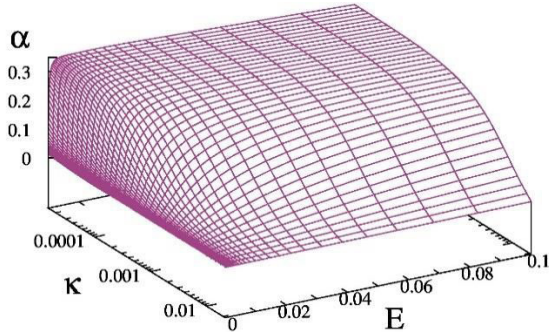

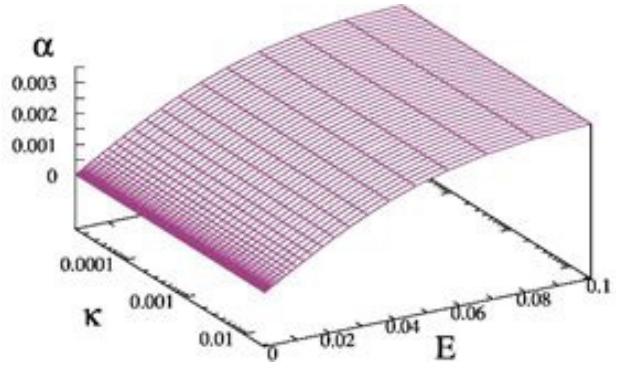

Fig 1. .*The anomalous average α as function of the symmetry-breaking seed E, for different values of κ, in lasing (upper panel) and in the normal regime (lower panel).*

The order of limits is crucial, the scaling limit should be performed *before* taking $E \to 0$. We show that in this case, the survival of the anomalous averages takes place in the lasing regime, and only there.

Obviously, such statements require a proof by analytic methods, and this is provided in our paper [2]. Nevertheless, a numerical illustration explains intuitively the increased sensitivity to symmetry-breaking when approaching the limit point. In (**Fig.1**) the anomalous average $\alpha \sim \langle b \rangle$ is plotted versus κ and the symmetry-breaking seed E. With g^2 kept proportional to κ, the scaling limit is read on the plot as $\kappa \to 0$. The upper panel corresponds to lasing conditions and one sees that by taking first the $E \to 0$ limit, the anomalous average vanishes for any given $\kappa > 0$. Yet, one can read from the plot that the convergence of α to zero is systematically delayed by decreasing κ.

This is suggestive for the analytic result that taking first $\kappa = 0$ the anomalous average persists when $E \to 0$. On the contrary, in the lower panel the parameters do not meet the lasing condition and one sees that the decrease of α with E is completely insensitive to the κ values. Also note the absolute values, which in this case, are two orders of magnitude lower.

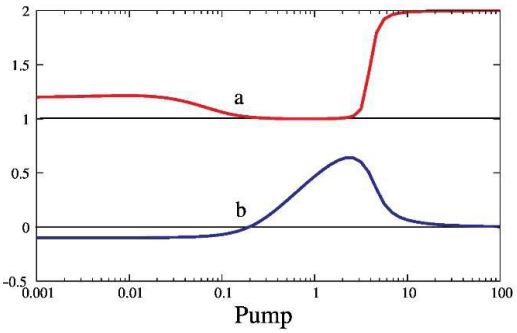

Fig. 2. *(a) $g^{(2)}(0)$ and (b) α as functions of pumping.*

Also, from a practical point of view, we compared the symmetry breaking as the lasing criterion with the condition of coherence $g^{(2)}(0)=1$, commonly used in the literature. One can see in (**Fig.2**) that α shows a positive bump precisely in the pumping interval in which the photon autocorrelation function at zero time delay, $g^{(2)}(0)$, is close to unity.

It is important to stress that the criterion using the anomalous averages is both necessary and sufficient, while $g^{(2)}(0)=1$ is necessary but not sufficient for proving coherence.

Also, computationally our criterion is cheaper, being available even at the mean-field level of the theory.

References

[1] C. Ning, IEEE J. Sel. Top. Quantum Electron. 19, 1503604 (2013).
[2] P. Gartner, Phys. Rev. B 99, 115313 (2019).
[3] P. Gartner, Phys. Rev. A 84, 053804 (2011).

Berry-phase polarization calculation for ABO_3 ferroelectrics

L. D. Filip, N. Plugaru and L. Pintilie

Ferroelectric polarization is an intrinsic property most commonly observed in a sub-class of materials know as perovskites. Applications taking advantage of this property vary from random access memories to actuators and many more. Unfortunately, the largest values for polarization are obtained in lead containing materials such as $Pb(Zr,Ti)O_3$ (PZT) and it raises pollution issues due to Pb toxicity. Searching for a replacement, the most straightforward method is through materials screening using advanced computational methods and high-throughout calculations.

Obtaining the ferroelectric polarization using computational methods is not a straightforward process. The most precise method implemented in most numerical codes is the Berry phase method which is the foundation of the so called modern theory of polarization [1,2].

Using this approach, the ferroelectric polarization is not obtained as an absolute quantity, but it is defined as the following difference: ferro ref $\Delta P = P_{ferro} - P_{ref}$, where ferro P is the polarized ferroelectric state and ref P_{ferro} is a reference non-polarized state (see **Fig. 1**).

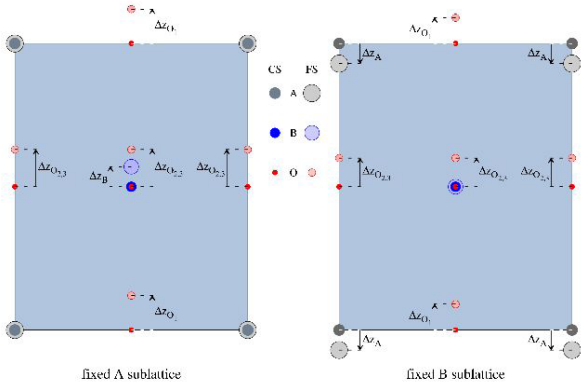

Fig. 1. *Ferroelectric (FS) and non-polarized state (CS) for a generic ABO_3 perovskite.*

To complicate matters further, in the framework of the modern polarization theory, this quantity ΔP is not unique, but a multi-valued function, such that all values $\Delta P + NP_q$ are correct polarization values, where $n \in Z$. P_q is a polarization quantum that is defined as:

(1)
$$P_q = \frac{e\boldsymbol{R}}{\Omega}$$

where R is any lattice vector and Ω is the unitcell volume.

This new definition of polarization obviously creates a problem since experimentally, only one value is obtained and not an entire family of values.

This apparent problem arises from the fact that both polarizations entering the new definition of ferroelectric polarization are in fact multivalued. In order to obtain an absolute value for the ferroelectric polarization, one must ensure that the calculated values for the ferroelectric and reference state belong to the same family of polarization values, or polarization branch as it is normally called.

Here lies the problem of the current implementations of the Berry phase method for calculating the ferroelectric polarization. One cannot control the polarization branch for the ferroelectric and reference states. This means that a number of intermediary states must be studied in order to discern each branch and perform the necessary corrections in order to obtain the correct polarization value.

Our study was focused on obtaining a method for correctly calculating the ferroelectric polarization for perovskite materials using the smallest number of steps [Ref. Filip]. It was shown that in order to achieve a certainty level, a number of three states must be included in the calculation. More to the point, the proposed strategy can be applied in the same way to any ABO_3 material.

The idea behind the proposed strategy is as follows: starting from the reference state (RS) the polarization, $P_{RS} = P^0_{RS} + K P_q$, can be obtained as a multi-valued function, with $k \in Z$ and P^0_{RS} is the value obtained from the numerica computation package (Quantum Espresso, VASP etc.).

The system is then distorted by an infinitesimal amount toward the final ferroelectric state and the polarization is calculated in the new state.

The new value of the polarization, $P_{inf}=P^0_{inf}+\iota P_q$ is again a multivalued function, where $\iota \in Z$ and P^0_{inf} is the calculated polarization. Generally, $k \neq l$, but one can now impose that the *calculated* value P^0_{RS} is the *reference* value. This allows one to find the correction for P_{inf} value in order to bring it to the same branch as P^0_{RS} by finding n such that:

$$\left|\frac{P^0_{inf}+nP_q-P^0_{RS}}{d\lambda}\right|=\min, \quad (2)$$

where, dλ is the amount of the system distortion [3].

By establishing that the two infinitesimally close polarization values belong to the same branch, it is possible to approximate the rest of the polarization values on the branch using a linear fit. At maximum distortion, the system is in the ferroelectric state and the third calculated value is obtained. Comparing the calculated value to the one obtained from the linear fit, one can accurately find the necessary correction to bring the calculated polarization in the ferroelectricstate to the same branch as P^0_{RS} by adding or subtracting an integer number of P_q. This procedure was summarized in **Fig. 2**, where the PZT polarization was obtained.

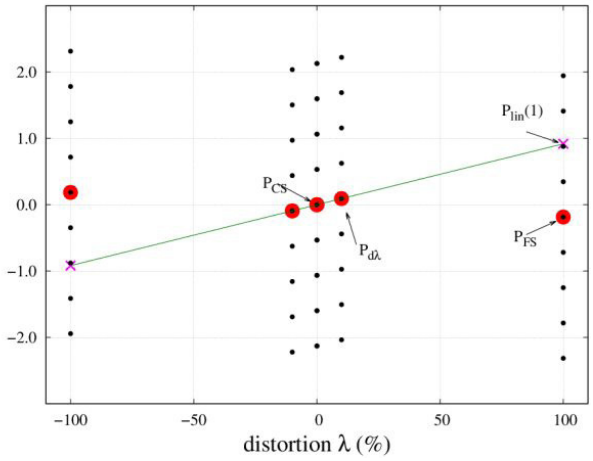

Fig. 2. *Summary of the strategy to obtain the ferroelectric polarization using the Berry phase method for the case of PZT.*

The advantage of the proposed method is that it can be included in automated screening methods for finding new ferroelectric materials.

Acknowledgement

The authors would like to acknowledge the funding by the Romanian MEN-UEFISCDI through the Young Research Team Grant PNII-RU-TE- 2012-3-0320 (Contract No. 11). And the financial support from the NIMP Core Program nr. PN18-110101 and the PCCF project nr. PN-III-P4-IDPCCF- 2016-0047 funded by the Ministry of Research and Innovation though UEFISCDI executive unit. 6.

References

[1]. Resta R., Posternak M. and Baldereschi A. Phys. Rev. Lett. 70 1010–3. (1993)

[2.] Rabe, K. M., Charles H. Ahn, and Jean-Marc Triscone. Physics of Ferroelectrics: A Modern Perspective. Topics in Applied Physics, 105. Berlin: Springer, (2007).

[3.] Filip, L. D., N. Plugaru, and L. Pintilie, Modelling and Simulation in Materials Science and Engineering, 27, 045008 (2019).

Ferroelectric – dependent band alignment at metal/$BaTiO_3$ interfaces

Dana G. Popescu, Marius A. Husanu

The central component in the emerging field of ferro-functional materials is a ferroelectric (FE) material, which, in contact with a metal electrode is driven in one of its distinct stable states by applying a voltage pulse to the metallic electrode. Understanding what the mechanisms which influence the electronic properties of the metal/FE interface are, allows to choose the most convenient materials and fine tune the production steps for the desired functionality. Particularly, the height of the Schottky barrier measures the „effort" paid by an electron or hole to travel between the metal and the FE and is directly involved in shaping the functionality of the interface. Depending on some material parameters, notably the work function (Wf) and the FE state, the contact can have rectifying or ohmic properties. The former find application in FE diodes, the latter are relevant when easy flow of charge along the junction is desired.

Two recent experiments [1,2] reveal the mechanisms which control the different alignment of FE $BaTiO_3$ (BTO) electronic bands at that of the metallic contacts. By gradually growing Au and Cu, with atomic layer precision on BTO prepared in two distinct states – with the FE polarization pointing either away from the surface (P^+) or towards the bulk (P^-), we identify the signature and isolate the contribution of the charge carriers within BTO at stabilizing the well defined orientation of the FE polarization.

At the bare BTO surface and in the first metal deposition stages, most mobile charges available within the FE material are involved in screening the depolarizing field and stabilizing the particular orientation of the FE polarization thus defining the intrinsic compensation mechanism.

During the gradual growth of (Au, Cu) on BTO, we identify that a crossover from intrinsic to extrinsic compensation, which involves the electrons in the metallic contacts, occurs at a thickness of the metallic overlayer of ~ 2.5 nm. The intrinsic charges identified in the XPS experiments are the electrons released upon the creation of oxygen vacancies (VOs) in BTO.

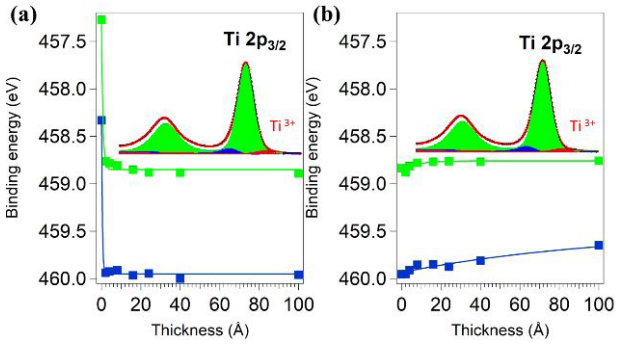

Fig. 1. *Variation of Ti $2p_{3/2}$ binding energy as a function of top metal thickness, Au (a) and Cu (b). In inset is a generic Ti 2p XPS spectra simulated with three Voigt lines.*

This was clearly indicated from the analysis of the Ti *2p* core levels obtained in our XPS measurements (**Fig. 1**). Firstly, the experimentally derived stoichiometry, with the O/Ti ratio deviating from the ideal value of 3 suggests the oxygen defficient nature of BTO. Additionally, the third component of the spectra, at lower binding energies (BEs) which is compatible with Ti^{3+} chemical state explains the origin of the understoichimetric oxygen concentration in the creation of OVs.

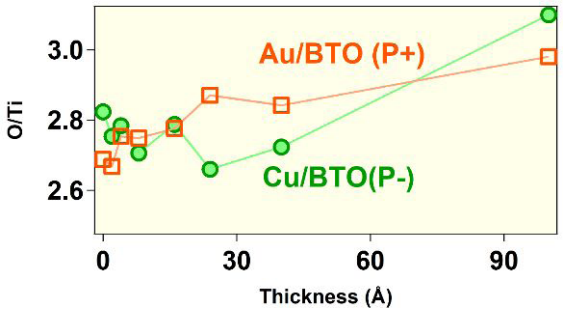

Fig. 2. *Variation of the O/Ti atomic ratio deduced from the XPS stoichiometry.*

In the case of BTO, which is known to easily form oxygen vacancies with the consequent *n* - doping of the material, we find that the P^+ or P^- FE states involve a particular distribution of the OVs. The OVs density profile and its variation upon gradual growth of the top metal was inferred from the variations of the O/Ti atomic ratios (**Fig. 2**). Notably, the variation of the O/Ti follows well the Ti^{3+}/Ti^{4+} ratio within the probed thickness, further indicating that for the Au/BTO(P^+) system, the extrinsic screening due to Au top contact gradually replaces the intrinsic screening involving the free electrons in BTO. This corresponds to a variation of the OVs density in the probed thickness of the film as in (**Fig. 3c**).

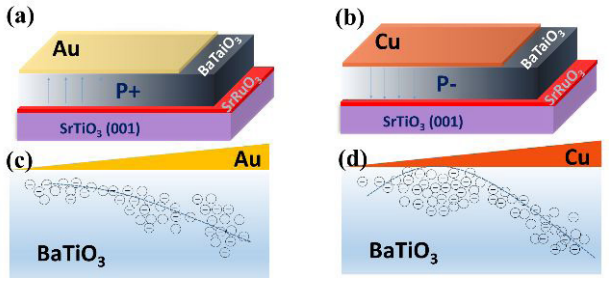

Fig. 3. *Mechanisms of compensation of a well defined out-of-plane FE polarization involving oxygen vacancies.*

Cu/BTO(P^-) system on the other hand is featured in the early Cu deposition stage by ever increasing OVs close to the interface (**Fig. 2**) and stronger deviations from the ideal O:Ti stoichiometry.

However, from a critical thickness of Cu overlayer of ~2.5 nm, when the top layer becomes continuous, the extrinsic screening due to available electrons in Cu is effective in compensating the FE state. This corresponds to a scenario like in (**Fig. 3d**), with the OVs diffusing towards the bulk of BTO, which at the interface recovers then the ideal stoichiometry.

The complex dynamics of FE compensation by free charges in BTO is in direct connection with the band bending at the surface of BTO and the resulting interface band alignement. The fact that in both cases the electrons are involved in compensating both P^+ and P^- FE states, indicates that the interplay between work function and ferroelectric-induced band bending should operate differently for the two systems. Indeed, from the BEs variation of Ti *2p* and Ba *3d* core levels, upon gradual deposition of Au and Cu on BTO, rigidly following the shifts of the valence band one can formulate the picture of interface band alignment in (**Fig. 4**).

Differently from the metal/semiconductor junction, where the Schottky barrier height (SBH) is defined by the Wf difference only, we prove that at our metal/FE contact, the polarization state of BTO either decreases [1] or increases [2] the value of the SBH expected from the values of the Wf differences. This is due to the additional FE-induced band bending, which, in the case of a P^- states translates in „upwards" bending of the electronic bands while for P^+ polarization, it translates in downwards band bending. Such effects are detected in XPS measurements by the shifts of the BEs towards lower, respectively higher values.

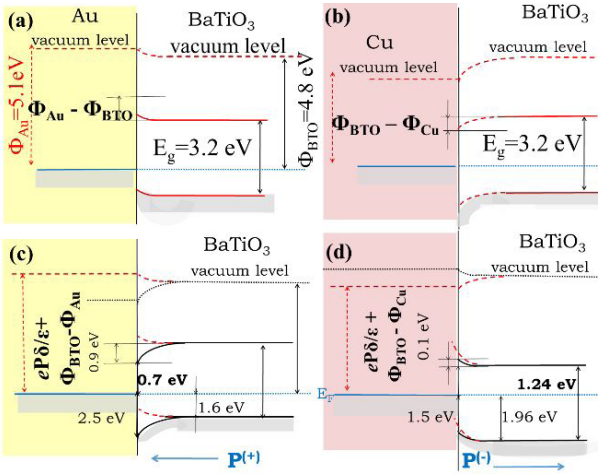

Fig 4. *Band alignment mechanism derived from the BE variation upon gradual growth of Au (a,c) and Cu (b,d).*

In this way, by comparing the scenario of a band alignment based on the Wf difference, one should have a band alignment mechanism as in (**Fig 4a**) for Au/BTO(P^+) system and as in (**Fig. 4b**) for Cu/BTO(P^-). However, experimentally, the correction accounting for the polarization state of BTO is in such a way that at Au/BTO(P^+) interface the leading term is the ferroelectric state, which reverses the expected band bending (**Fig. 4**c), while the Cu/BTO(P^-) system is featured by synergic effects of FE-assisted and Wf- controlled band bending.

These results are useful in understanding the behavior of FE polarization in artificial heterostructures and, by clarifying practical aspects involved in the fabrication of ferro -functional devices shed light on the complex metal/ferroelectric interface formation.

References

[1] D. G. Popescu, M. A. Husanu, C. Chirila, L. Pintilie, C. M. Teodorescu, Impact on Ferroelectricity and Band Alignment of Gradually Grown Au on BaTiO3, Phys. Stat. Solidi – RRL 13 1900077 (2019)

[2] D. G. Popescu, M. A. Husanu, C. Chirila, L. Pintilie, C. M. Teodorescu, The interplay of work function and polarization state at the Schottky barriers height for Cu/BaTiO3 interface, Appl. Surf. Sci. 502 144101 (2020)

Conductance Model for Single-Crystalline/Compact Metal Oxide Gas-Sensing Layers in the Nondegenerate Limit: Example of Epitaxial SnO_2 (101)

C.E. Simion and A. Stănoiu,
in cooperation with
F. Schipani[1], A. Papadogianni[2], M. Budde[2], A. Oprea[1], U. Weimar[1], O. Bierwagen[2], N. Bârsan[1]
1Institute of Physical and Theoretical Chemistry, University of Tuebingen, Germany
2Paul-Drude-Institut für Feskörperelektronik, Leibniz-Institut im Forschungsverbund Berlin, Germany

In this report, a detailed analytical model of transduction function for *n* and *p* type single-crystalline/ compact metal oxide gas sensors (MOS) was developed, which relates the conductance of the sample with changes in the surface potential [1]. The model is valid in the region where Boltzmann approximation still holds [2]. Thus, the total conductance of a compact layer of which surface is exposed to the surrounding atmosphere can be written as:

$G_{total} = G_s + G_b$ (1)

where, G_s is the surface conductance and G_b represents the bulk conductance.

Considering the geometrical parameters of the sample depicted in (**Fig. 1)**, the equation (1) becomes:

$$G_{total} = \tilde{\sigma_s}\frac{z_0 W}{L} + \sigma_b\frac{(D-z_0)W}{L} \qquad (2)$$

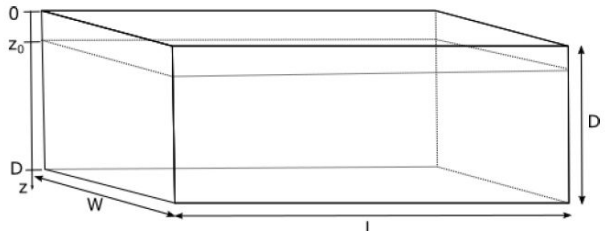

Fig. 1 *Representation of a compact sensitive layer and its geometrical characteristics.*

In the case of an n-type MOS where the surface effects do not affect the full layer, one can write the surface and bulk conductivity as: $\tilde{\sigma}_s = e\mu\tilde{n}_s$ and $\sigma b = e\mu n_b$. In this respect, the equation (2) can be written as follows:

$$G_{total} = \frac{e\mu\tilde{n_s}z_0 W}{L} + \frac{e\mu n_b(D-z_0)W}{L}$$
$$= \frac{e\mu W}{L}[\tilde{n_s}z_0 + n_b(D-z_0)]$$
$$= \frac{e\mu w}{L}[z_0(\tilde{n_s} - n_b) + n_b D]$$

Considering that our model obeys the Boltzmann statistics in the whole layer, one obtains the dependence of the overall conductance on the surface band bending eVs.

$$G_{total} = G_b[1 \pm \sqrt{2}\frac{L_D}{D} * * \left[\exp\left(-\frac{eVs}{k_B T}\right) + \frac{eVs}{k_B T} - 1\right]^{\frac{1}{2}}] \qquad (4)$$

Fig. 2. *Shows the dependence of the normalized conductance of the compact layer, depending on the variation of the surface potential in relation to the thermal energy for different values of the Debye length (L_D).*

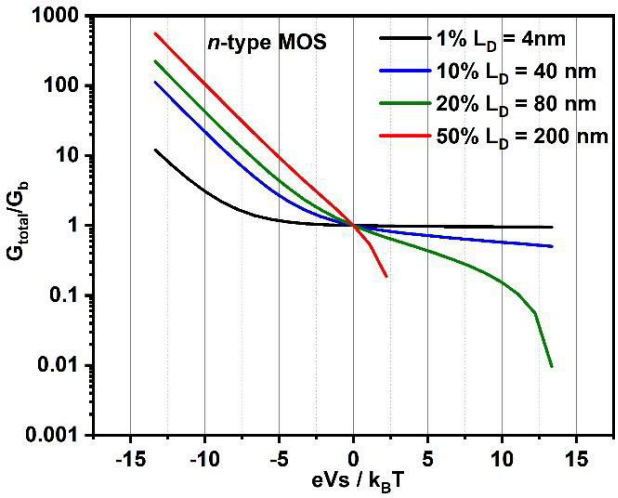

Fig. 2. *Normalized conduction changes as a function of surface band bending for different Debye lengths.*

The positive values of the $\frac{eVs}{k_B T}$ ratio are associated with the occurrence of a depletion layer, whereas the negative values with the appearance of a charge accumulation layer at the surface.

In the case of a *p*-type MOS where the surface effects do not affect the full layer, one can write the expression of the total conductance as:

$G_{total} = G_s + G_b \sim \tilde{p}_s z_0 + p_b(D - z_0)$ (5)

where the term $\tilde{p}_s z_0$ represents the surface contribution and the term $p_b(D-z_0)$ represents the bulk contribution.

Following the same mathematical approach as in the case of *n*-type MOS, one can obtain:

$$G_{total} = G_b[1 \pm \sqrt{2}\frac{L_D}{D} * \\ * \left[\exp\left(\frac{eVs}{k_BT}\right) - \frac{eVs}{k_BT} - 1\right]^{\frac{1}{2}}]$$

Figure 3. shows the dependence of the normalized conductance of the compact layer, depending on the variation of the surface potential in relation to the thermal energy for different values of the Debye length (L_D).

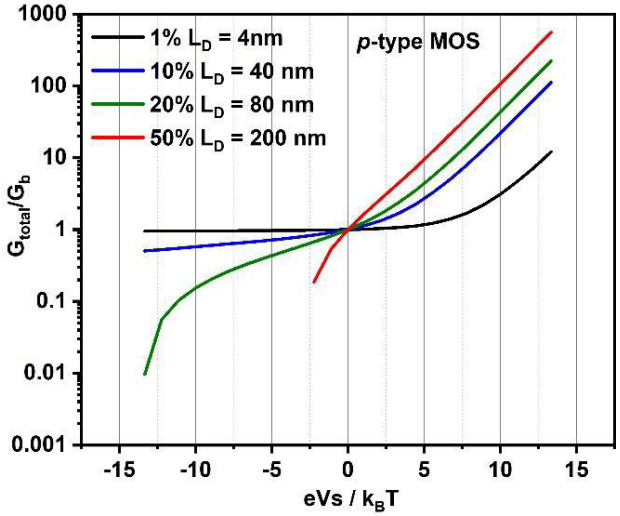

Fig. 3 *Normalized conduction changes as a function of surface band bending for different Debye lengths.*

The negative values of the $\frac{eVs}{k_BT}$ ratio are associated with the occurrence of a depletion layer, whereas the positive values with the appearance of a charge accumulation layer at the surface.

The present study demonstrates that the translation of surface interactions takes place differently depending on the nature of the semiconductor character as well as on the intrinsic (Debye length-L_D) and geometric (film D thickness) properties.

In the case of an *n* MOS, the charge accumulation layer induces an exponential dependence of the normalized conductance, for small values of surface potential (Vs) and large Debye lengths, whereas in the case of a surface layer, only values over 10% of the Debye length produce major changes in the normalized conductance.

In the case of a *p* MOS, the variations of the normalized conductance follow the same profile, but the accumulation layer appears for positive values of the $\frac{eVs}{k_BT}$ ratio, whilst the depletion layer for negative values of the same ratio.

In order to validate the theoretical approach, electrical resistance and work function measurements have been performed onto epitaxial SnO_2 thin film (**see Fig. 4**).

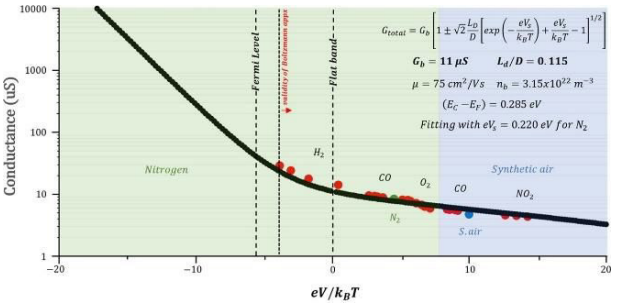

Fig. 4. *Experimental results of conductance versus relative band bending changes for SnO_2 sensing layer.*

The relation (4) was used to accomplish the fitting procedure, when the sensor was operated at 300°C and exposed to different concentrations of H_2 (in Nitrogen atmosphere), CO (in Nitrogen and Dry synthetic air atmosphere), O_2 and NO_2.

References

[1] C.E. Simion, F. Schipani, A. Papadogianni, A. Stanoiu, M. Budde, A. Oprea, U. Weimar, O. Bierwagen, N. Barsan, ACS Sens. 4 (2019) 2420-2428

[2] N. Barsan, U. Weimar, J. Electrocer. 7 (2001) 143-167.

Adsorption of 1,4-phenylene diisothiocyanate onto the graphene oxide sheets functionalized with polydiphenylamine in doped state

M. Baibarac, M. Daescu

in collaboration with
S. Fejer
Pro-Vitam Ltd., Sfantu Gheorghe, Romania

Using graphene oxide (GO) sheets and GO yers modified with polydiphenylamine (PDPA), the adsorption of 1,4-phenylene diisothiocyanate (PDITC) on the two platforms were studied by Raman scattering and photoluminescence [1].

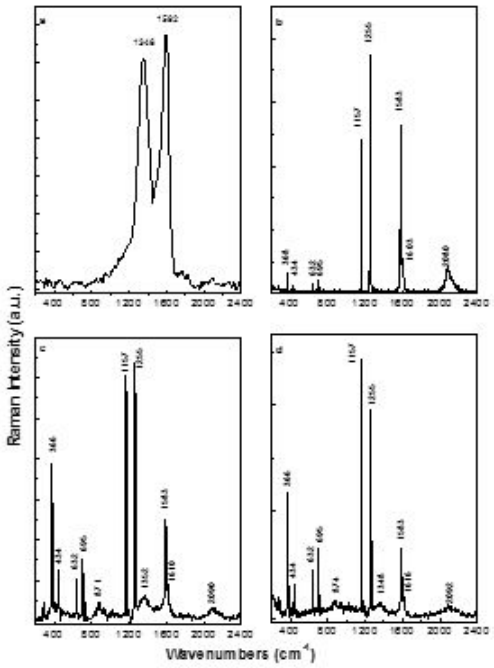

Fig. 1. *Raman spectra of GO sheets (a), PDITC (b) and platelets of PDITC with 1 wt.% GO (c) and 2 wt.% GO (d).[1]*

According to the changes reported in the Raman spectra of PDITC and the GO sheets (**Fig. 1**), i.e. i) the enhancement of the PDITC Raman lines situated in the 400-800 and 1000-1300 cm^{-1} spectral ranges, ii) the change in the ratio between the intensities of the Raman lines at 1585 and 1602 cm^{-1} accompanied by an up-shift in the case of the second line and iii) the shift of the PDTIC emission band from 502 to 491 nm, two compounds were identified to result.

One corresponding to the PDITC intercalated GO layers, exhibiting o-thiocarbamates groups, and a second one with the GO sheets modified with PDITC when the molecular structures both the o othiocarbamate functional groups and an isothiocyanate terminated surface are resulted.[1]

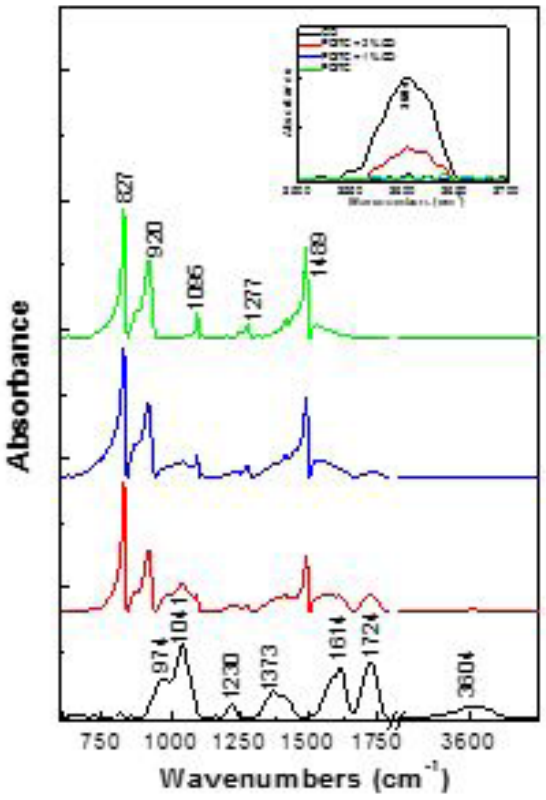

Fig. 2. *IR spectra of GO sheets (black curve), PDITC (green curve) as well as platelets of PDITC with 1 wt.% GO (blue curve) and 2 wt.% GO (red curve)[1]*

Additional information are shown in **Fig. 2**, which highlights that the PDITC interaction with the GO sheets leads to the changes of the IR spectra of the two constituents as follows: i) a diminution of the ratio between the absorbance of the two IR bands of PDITC at 1489 and 827 cm^{-1} from 0.71 to 0.43 and ii) an enhancement of the ratio between the absorbance of the IR bands of the GO sheets at 1724 and 3604 cm^{-1}, from 5.4 to 9.84 and 23 simultaneously with the decrease in the absorbance of the IR band at 3604 cm^{-1}.

Based on the absorbance diminution of the IR band at 1489 cm^{-1}, a smaller weight of the –C=N- benzene ring vibrational mode was reported.

The DPA electrochemical polymerization in the solution of 10-^{3}M $H_3PMo_{12}O_{40}$ and 1M HCl in DMF: H_2O, when screen-printed carbon electrodes (SPCE) modified with GO were used as working electrodes, leads to the GO layers covalent functionalized with PDPA in doped state.[1] In order to support this sentence, **Fig. 3** highlights: i) an intensity increase of the Raman lines at 885 and 1000 cm^{-1}, the former belonging to the MoO_3 vibrational mode [2]; ii) the shift of the Raman line from 833 to 815 cm^{-1} simultaneous with the change of the ratio between the intensities of the Raman lines at 1602-1609 and 1200-1204 cm^{-1} from 3.2 to 2.3; and iii) the gradual diminution of the GO D band intensity and the appearance of the Raman lines at 1283, 1329 and 1372 cm^{-1}.[1] Chemical mechanism of the reaction of PDPA doped with the $H_3PMo_{12}O_{40}$ heteropolyanions with the GO sheets is shown in **Fig. 4. [1]**

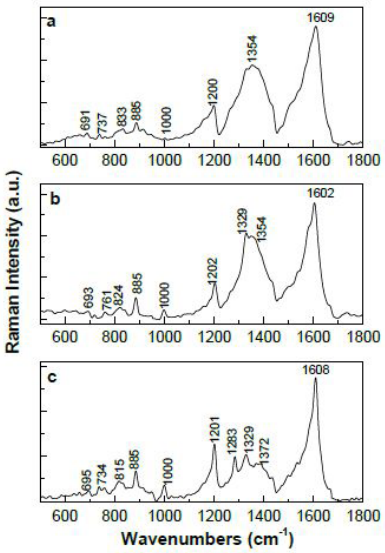

Fig. 3. *Raman spectra of the GO sheets electrofunctionalized with PDPA, when SPCE was immersed into the solution 10-^{3}M $H_3PMo_{12}O_{40}$ and 1M HCl in DMF : H_2O and various DPA concentrations, i.e.10-^{3} (a), 5 10-^{3} (b) and 10-^{2} M (c).[1]*

The PDITC adsorption onto the GO layers covalent functionalized with PDPA in doped state involves the appearance of the thiourea groups simultaneously with those of the type o thiocarbamate, according to **Fig. 5. [1]**

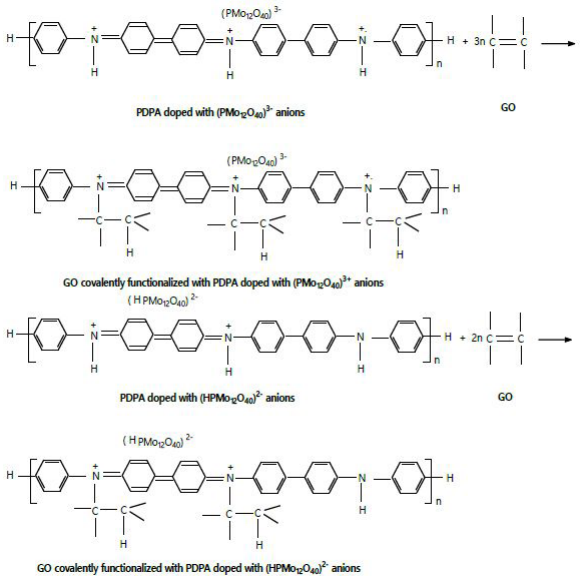

Fig. 4. *Reaction of PDPA doped with the $H_3PMo_{12}O_{40}$ heteropolyanions with the GO sheets [1]*

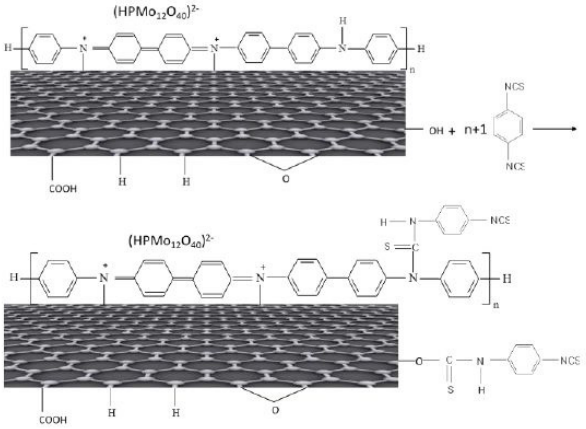

Fig. 5. *The reaction of PDITC with the doped PDPA functionalized GO layers [1]*

References

[1] M. Baibarac, et al., Sci. Rep. 9 (2019), 14278.
[2] J.M. Tatibouet et al., J. Catal. 169 (1997), 22–32.

Evaluation of the static background dielectric constant in epitaxial ferroelectric thin films of PZT

A.G Boni, C. Chirila, L. Hrib, R. Negrea, L. D. Filip, I. Pintilie and L. Pintilie

Ferroelectrics are materials of interest for fundamental research but also for many applications. However, many related aspects remain under debate or controversy. The magnitude of the dielectric constant can be found in the specialized literature to vary with orders of magnitude even for the same material and as such it warrants a careful analysis approach.

The present study refers to the evaluation of the static background dielectric constant related to the linear dielectric response for any material. For this analysis, three PZT epitaxial thin films with different thicknesses were used together with various capacitance measuring methods [1].

In **Fig. 1a)**, the working principle of two capacitance measuring methods is schematically presented for the case of a ferroelectric capacitor. The dynamic mode is based on applying a staircase type voltage train - the voltage is increased in small steps, for each step a value of the capacitance is recorded after a delay time necessary for the stabilization of the system. The new proposed method is referred to as the static mode, based on applying short voltage pulses and recording the capacitance at 0V d.c. after each pulse. The results of capacitance measurements using both methods are presented in **Fig. 1 b)**. It can be seen that both loops present the well-known butterfly-like shape, but the major differences are related to the totally reversed polarization states. For the dynamic mode, the capacitance has a dependence on applying voltage intensity similar to a depleted semiconductor, while in the static mode, the capacitance is constant as long as there is no contribution from polarization switching.

In **Fig. 2 a)** are presented the results of static capacitance measurements for different ferroelectric layer thicknesses. For 20 nm and 50 nm thickness, it can be seen that the values of the capacitance are different when polarization is oriented upward or downward.

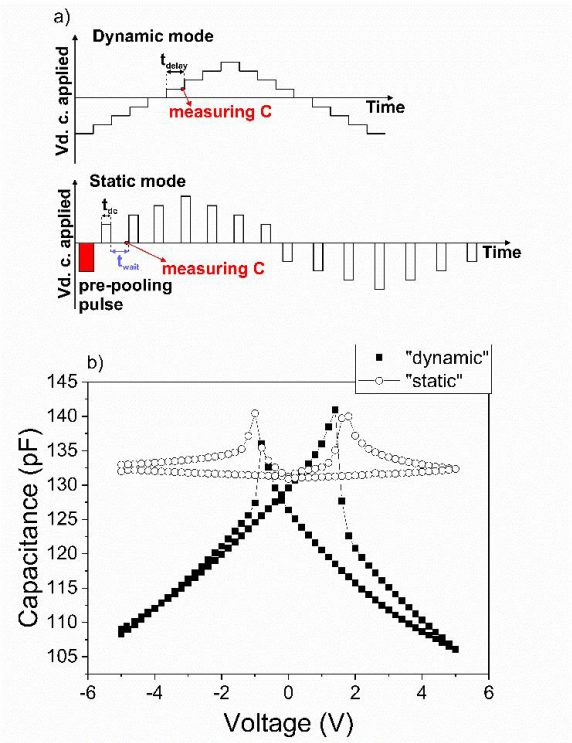

Fig. 1. a) *The schematic representations of the capacitance measurements modes; b) the capacitance measurement loops using the two different modes, on a 150 nm PZT thin film.*

This is attributed to internal fields contributions. For thick enough films this contribution diminishes. As the results from **Fig. 2b)** suggest, after setting the polarization in one or the other direction, there is no back-switching contribution when the voltage returns to zero-rectangular shape of the hysteresis. Thus, we can assume that the polarization contribution to the evaluation of the background dielectric constant is reduced.

In **Fig. 3** the dielectric constants evaluated for all samples are presented for different conditions: static mode at 0V, dynamic mode in 0V, dynamic mode at V_{max}, and for Reyleigh method.

The most important observations from these results are: all methods give similar results for the dielectric constant for the thinnest samples and all thickness dependences are linear with a very good fitting confidence [1]. Considering that the same empirical thickness dependence for ultra-thin epitaxial layers, the values of the background dielectric constant could be as low as 14-15 for a 1.2 nm PZT thin film and even lower for a mono-domain, defect free layer. Thus, the large values of the dielectric constants reported for ferroelectric materials are mostly due to extrinsic contributions such as structural defects, domains and domain walls.

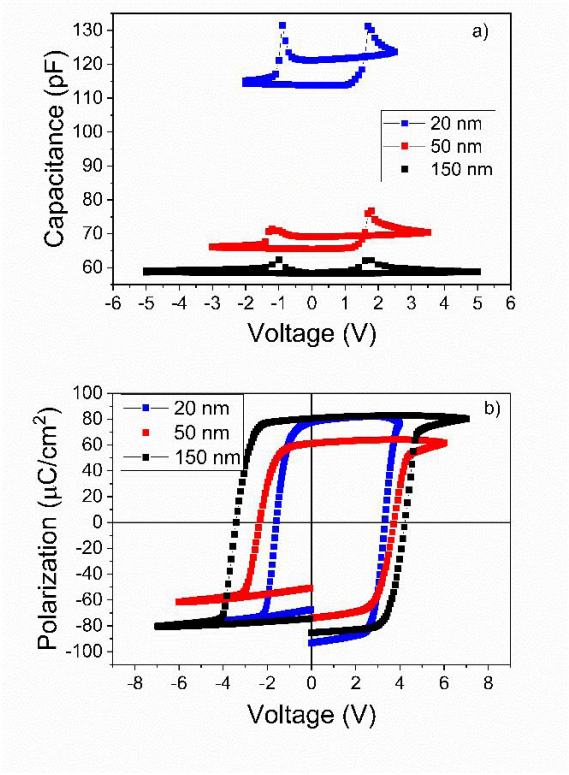

Fig. 2. a) *The capacitance measurements using static mode, for different thickness of the PZT layer. b) The polarization hysteresis loops for different thickness of the PZT layer.*

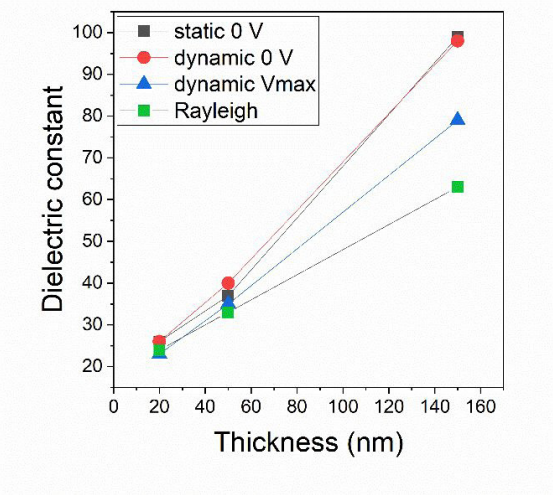

Fig. 3. *The evaluated dielectric constants for different thickness of PZT layer and for different conditions of measurement of the capacitance.*

The work was carried out in the frame of the CEPROFER/PN-III-P4-ID-PCCF-2016-0047,Core Program of NIMP and 12PFE/2018.

References

[1] A.G. Boni et all., Scientific Reports 9, 14698 (2019)

Tailoring the Dopant Distribution in ZnO:Mn Nanocrystals

D. Ghica*, I. D. Vlaicu*, M. Stefan*, V. A. Maraloiu, A. C. Joita, C. Ghica

The synthesis of semiconductor nanocrystals with controlled doping is highly challenging, as a significant part of the doping ions are often found segregated at nanocrystals surface, even forming secondary phases, rather than incorporated in the core [1-3].

The present work [4] is focused on the assessment and control of the dopant distribution in nanocrystalline ZnO doped with a low concentration (0.1 at%) of Mn^{2+} ions (nano-ZnO:Mn) prepared by co-precipitation from nitrate precursors followed by mild thermal treatments (annealing for 10 min. at temperatures up to 250 ^{0}C). An important part of this approach concerns the control of the amount and chemical composition of the secondary intermediate phases, expected to contain a non-negligible concentration of dopant Mn^{2+} ions, by minor adjustments of the synthesis route. The samples were investigated by electron paramagnetic resonance (EPR) and Fourier transform infrared (FTIR) spectroscopies combined with microstructural investigations. The dynamics of the dopant distribution under mild isochronal thermal treatments were monitored by EPR.

By varying one synthesis parameter from one sample to another we obtained two nano-ZnO:Mn samples (ZOM1 and ZOM2) with different dopant distributions and minority phases and a polycrystalline Mn-doped zinc hydroxynitrate sample (ZHNMn) - **Figs. 1 - 4.** The minority phases from the two nano-ZnO:Mn samples (below the detection limit of XRD, see **Fig. 1**) were identified by EPR and FTIR as residues of precursor nitrate compounds in the ZOM1 sample and ZHN in the ZOM2 sample.

In the as-prepared ZHNMn sample the Mn^{2+} ions were substitutionally localized in the two types of Zn^{2+} sites (paramagnetic centres Mn^{2+}(I) and Mn^{2+}(II) in **Fig. 5a**). The isochronal annealing treatment up to 200^{0}C leads to the complete transformation of the ZHNMn sample into nanocrystalline ZnO, with all Mn^{2+} ions uniformly distributed in the core of the ZnO nanocrystals (Mn^{2+}(c) centres in **Fig. 5a**).

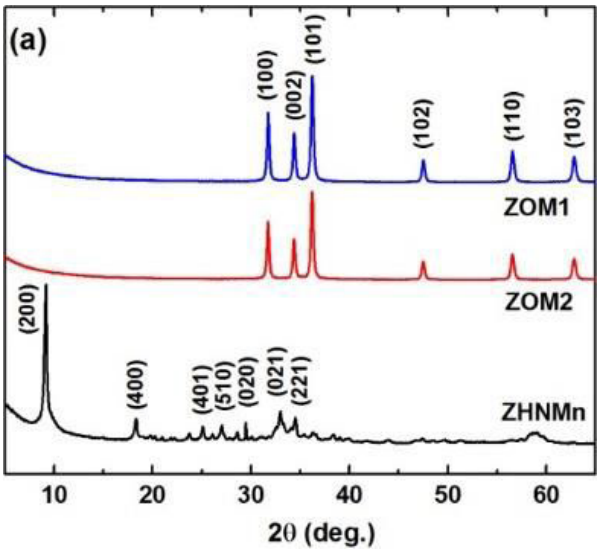

Fig. 1. *XRD patterns of the ZOM1, ZOM2 and ZHNMn samples indexed according to the ZnO and $Zn_5(OH)_8(NO_3)_2{\cdot}2H_2O$ structures, respectively. Only the main peaks are indicated for the ZHNMn sample.*

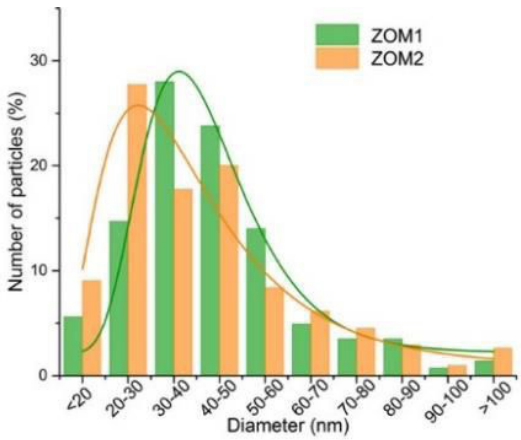

Fig. 2. *Nanocrystals size distributions from TEM images of the ZOM1 and ZOM2 samples and their fit with the log-normal function (thin lines).*

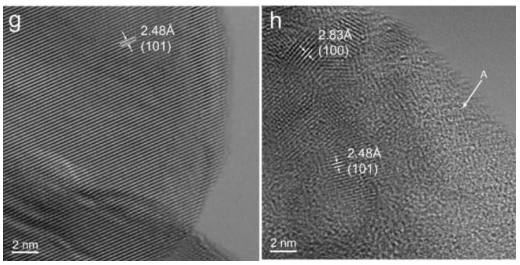

Fig. 3. *HRTEM images showing different crystallization degrees of the superficial layers of the nanoparticles in the ZOM1 (a) and ZOM2 (b) samples (A – amorphous layer).*

A very different situation was encountered for the as-prepared ZOM2 sample: only 21% of the Mn^{2+} ions were incorporated in ZnO, while 79% of them (Mn^{2+}(y) centres in **Fig. 4b**) were localized in the minority ZHN phase, present as a thin amorphous layer around the ZnO nanocrystals (see **Fig. 3b**). This is quite an interesting result, showing the possibility to functionalize the ZnO nanocrystals with ZHN, a layered material with various applications.

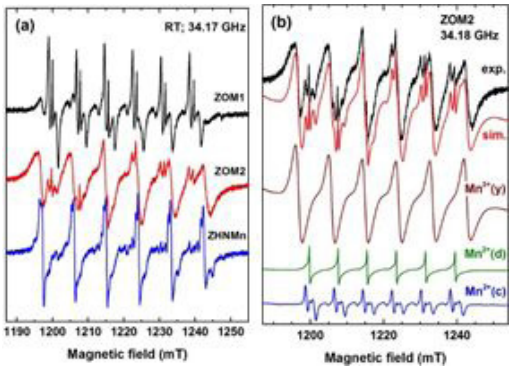

Fig. 4. (a) *EPR spectra of the as-prepared samples measured at RT. (b) Experimental (exp.) and simulated (sim.) EPR spectra of the ZOM2 sample. The component spectra of the indicated centres are presented below with their relative intensities.*

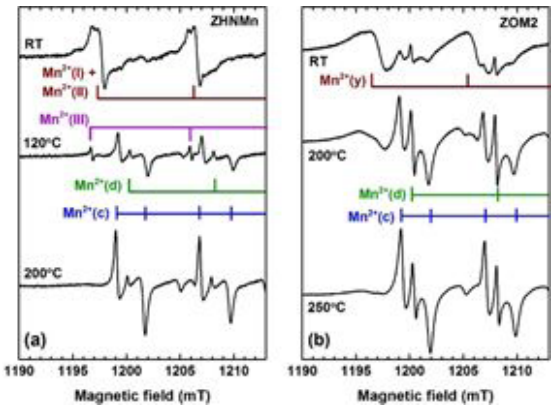

Fig. 5. *Detailed view of selected EPR spectra of the Mn^{2+} ions in the ZHNMn and ZOM2 samples, as-prepared (RT) and isochronally annealed at the indicated temperatures.*

For all spectra only the first two hyperfine transitions at low-field are displayed.

The annealing process up to 250 ^{0}C leads to the decomposition of three quarters of ZHN directly into ZnO, with part of it adding as crystalline layers on the initial nanocrystals and the rest remaining as disordered ZnO. After the last annealing step, the ZnO nanocrystals contained 58% of the Mn^{2+} ions, 17% uniformly distributed in the core and 41% in the outer layers (Mn^{2+}(c) and Mn^{2+}(d) centres in **Fig. 5**).

The distribution pattern of the Mn^{2+} ions in the annealed ZOM1 sample is an intermediate case, with a smaller difference between the core and surface concentrations than in the annealed ZOM2 sample.

Our results [4] demonstrate a strategy to tailor the dopant distribution in colloidal ZnO nanocrystals by small adjustments of the preparation algorithm by a simple and cost-effective method. Thus, the most appropriate route to obtain a uniform dopant distribution in the ZnO nanocrystals volume seems to be the thermal decomposition of a doped precursor, while a non-uniform distribution with dopant-rich layers at the nanocrystals surface can be obtained from the thermal decomposition of minority phases. ZnO nanocrystals covered by a dopant-rich shell are of interest for surface sensitive applications like catalysis or gas-sensing, while uniformly doped ZnO:Mn nanocrystals are suitable for applications in nanoelectronics, optoelectronics or spintronics.

Funding from the Core Program project number PN18-110201 and UEFISCDI grants PN-II-RU-TE-2014-4-0939, PN-III-P4-ID-PCE-2016-0529 and PN-III-P1-1.2-PCCDI-2017-0062.

References

[1] D. Ghica, M. Stefan, C. Ghica, G.E. Stan. Evaluation of the Paramagnetic Impurities Segregation at Grain Boundaries in Nanostructured ZnO Films. ACS Appl. Mater. Interfaces 6, 14231 (2014).

[2] M. Stefan, I.D. Vlaicu, L.C. Nistor, D. Ghica, S.V. Nistor. Origin and chemical composition of the amorphous material from the intergrain pores of self-assembled cubic ZnS:Mn nanocrystals. Appl. Surf. Sci. 426, 342 (2017).

[3] M. Stefan, D. Ghica, S.V. Nistor, V.A. Maraloiu, R. Plugaru. Mn^{2+} ions distribution in doped sol-gel deposited ZnO films. Appl. Surf. Sci. 396, 1880 (2017).

[4] D. Ghica, I.D. Vlaicu, M. Stefan, V.A. Maraloiu, A.C. Joita, C. Ghica. Tailoring the Dopant Distribution in ZnO:Mn nanocrystals. Sci. Rep. 9, 6894 (2019).

Complex exchange coupling mechanisms in SRO/BFO/Fe heterostructures

S.G. Greculeasa, G. Schinteie, L.M. Hrib, V. Stancu, I. Pasuk, A. Kuncser, V. Kuncser

The unidirectional anisotropy in bidimensional heterostructures is of high interest for a considerable number of technological applications, such as magnetic recording media, spin valves for spintronics, domain stabilizers in reading heads, magnetoresistive random-access memories (MRAM) etc. Multilayers formed by interfacing an antiferromagnetic-like BFO film with a ferromagnetic film might undergo unidirectional/ exchange bias effects in specific conditions. In order to give more insight into the interfacial FM-BFO exchange coupling phenomena, structural, morphologic and magnetic investigations over a wide temperature range were reported for the SRO/BFO/Fe layered system [1].

The BFO/Fe heterostructures were prepared by PLD and sputtering, respectively, on the STO(0 0 1) substrate with a 20 nm SRO buffer layer. Two sets of samples were considered: with Fe film thickness of 16 nm (A) and 8 nm (B), respectively. An annealing treatment in external magnetic field was applied (B_t).

The formation of the BFO single phase and the c axis orientation of the SRO and BFO pseudocubic structures are evidenced in XRD. The Pendellösung fringes accompanying the SRO Bragg peaks, demonstrate the nearly perfect atomic structure and smoothness of the interfaces of the SRO film and are indirect evidence of the epitaxial growth of SRO. Both SRO and BFO structures have the same in-plane lattice parameter as the substrate, thus they are fully strained. Grains of roughly 150 nm in diameter, with an average RMS roughness of 4 nm and peaks and valleys like morphology with bottom-up differences of up to 20 nm are evidenced on top of the continuous BFO film in the atomic force microscopy results.

In the case of the as-prepared sample, the STEM-DF micrographs (DF-dark filed) give evidence for epitaxial STO/SRO/BFO structure with a polycrystalline Fe film on top. The overall layer sequence was also confirmed by the elemental composition of the layers obtained via the sectional X-ray Energy Dispersion technique. Accordingly, all the interfaces of this structure are relatively smooth. On the other hand, no smooth interfaces of the BFO layer, mainly at the BFO/Fe side of the structure were evidenced after the annealing treatment. A buried Fe/BFO interface can be mentioned, pointing to clustered Fe penetrating also in the top layer of the BFO film, which in turn is no more epitaxial.

However, the corresponding Selected Area Electron Diffraction (SAED) pattern indicates still well formed epitaxial STO and SRO phases.

The conversion electron Mössbauer (CEM) spectrum reveals the presence of three magnetic sextet contributions. The main sextet (84%) is assigned to the bcc Fe phase. The second sextet (6%), is related to a distorted/amorphous-like Fe contribution at the interface with the BFO film. A small magnetic contribution (4%) is due to the BFO phase. In addition, a paramagnetic doublet (6%) is also evidenced, being assigned to paramagnetic Fe atoms diffusing into the oxidic structure from the bcc Fe side of the interface.

The temperature dependence of the magnetic moment indicates that the selected temperature interval is far from the transition temperature of Fe and only the transition of the SRO phase is evidenced. The magnetization at high temperatures is due only to the Fe film and it increases abruptly by 2.4% at temperatures lower than 160 K, because of the magnetic contribution of the SRO film. T_C of the SRO phase was determined as 142 K.

The hysteresis curves of sample A reveal two magnetic contributions: the main ferromagnetic phase is attributed to the Fe film, showing a loop shift towards left at low temperatures, thus indicating the presence of exchange bias. A secondary magnetic contribution of only 15(5) % roughly, with different anisotropy and switching mechanisms, can be related to the SRO film. The thickness of the Fe film was estimated as 14 ± 2 nm, similar to the thickness obtained in the TEM measurements, by considering the saturation magnetization at low temperature and the secondary contribution of the SRO film (the contribution of the BFO film is assumed as negligible), with a thickness of 20 nm. The coercive field (H_C) of the main soft phase is found in the range from 300 Oe (at 10 K) to 50 Oe (at room temperature). The exchange bias field (H_{EB}) presents a nonmonotonic dependence with temperature. The already negligible H_{EB} above 50 K suggest a blocking temperature for H_{EB} ~50 K. In the case of sample B, the two magnetic components are more pronounced than in the case of sample A, due to the much thinner soft amorphous-like Fe film. Both contributions to the hysteresis are shifted, indicating the presence of unidirectional exchange coupling for each ferromagnetic component interfaced with the BFO film (Fe layer and SRO layer).

The hysteresis loops at low temperatures for the two involved ferromagnetic films have roughly equal contributions in magnetization. Therefore, from the overall value of the saturation magnetization, half was assigned to the top amorphous/ defect Fe film. Accordingly, the thickness of the Fe film was estimated at 7 ± 2 nm, similar to that resulting from the electron microscopy data. The H_C values of sample B are similar to those of sample A at low temperatures and are a few times lower at room temperature, supporting a faster decrease of the interfacial coupling with the temperature in sample B. At low temperatures, the hysteretic component assigned to the SRO layer presents slightly higher H_C values, relative to the component assigned to the Fe film. Similar to the case of sample A, the decreasing rate of H_C is considerably higher at low temperature relative to the high temperature regime. The field cooling protocol seems to have a slight impact on H_C, especially at lower temperatures. The H_{EB} field assigned to the Fe film at the lower temperature of 5 K is more pronounced relative to sample A (e.g. 67(10) Oe as compared to 47(5) Oe) after cooling in 0.6 kOe, as expected for a thinner film. A negative H_{EB} of 37(5) Oe was also evidenced at 5 K for the SRO film. A much lower blocking temperature for both H_{EB} (e.g. ~ 10 K) has to be mentioned for sample B. After annealing, the two magnetic phases evidenced in the hysteresis curves of the as deposited sample B, are no longer distinctly observed (**Fig. 1a**).

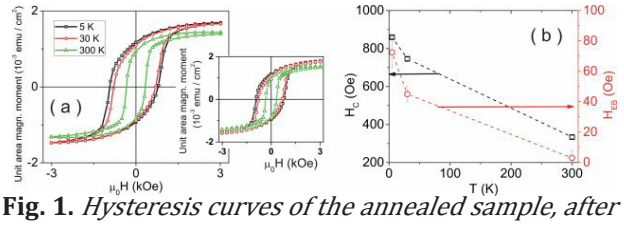

Fig. 1. *Hysteresis curves of the annealed sample, after the extraction of the linear component (a). The inset of (a) shows the corresponding raw hysteresis curves. Temperature dependence of the coercitivity (H_C) and of the exchange bias field (H_{EB}) (b).*

Due to the increase of the overall saturation magnetization of the annealed sample, it might be supposed that the annealing treatment affects the structure of the antiferromagnetic BFO film, which becomes partially uncompensated especially at the two interfaces with the ferromagnetic layers.

A magnetostatic (orange-peel) type of coupling could appear between the two ferromagnetic layers, as specific to rough interfaces with sinusoidal like morphologies of the BFO spacer layer [2]. Accordingly, an additional long range magnetic coupling could appear directly between the two ferromagnetic layers, supporting their simultaneous reversal, however, also under the competing interfacial interactions (with uniaxial and unidirectional components). Enhanced H_C values are evidenced (approximately 3 times higher at low temperatures and 20 times higher at room temperature; **Fig. 1b**). Also the H_{EB} at low temperatures are more pronounced after the magnetic field annealing treatment (**Fig. 1.b**): 73(10) Oe at 5 K and 45(5) Oe at 30 K. After the annealing treatment, the interfacial Fe clusters (extending in part inside the BFO layer) are increasing the specific area of the interface with the BFO phase, inducing an increase of the exchange bias coupling. To note also the much higher blocking temperature of the exchange bias in this system relative to the as prepared counterpart.

Authors acknowledge PN-III-P1-1.2-PCCDI -2017-0871 and the Core Program PN18-11.

References

[1] S.G. Greculeasa, G. Schinteie, L.M. Hrib, V. Stancu, I. Pasuk, A. Kuncser, V. Kuncser, J Alloy Compound 773 (2019) 338-345.

[2] J.F. Bobo, et a, J. Phys. Condens.w Matter 16 (2004) S471.

Dimensionality and functionality in transition metal interface oxides

M. A. Husanu
in collaboration with:
A. Arab, W. Yang, R. Chandrasena, E. J. Moon, A. Grey, Temple Univ., Dept. Phys, Philadelphia, PA 19122 USA
X. Liu, J. Chakalian, Dept. Phys. & Astr., Rutgers Univ., Piscataway, New Jersey 08854 USA
O. Köksal, R. Pentcheva, Dept. Phys., Duisburg-Essen, Duisburg 47057, Germany
S. Middey, S. Kumar, Department of Physics, Indian Inst. Sci., Bengaluru 560 012, India
V.N. Strocov, Swiss Light Source, Paul Scherrer Institute, Villigen, Switzerland
Z. Yang, L. Gu, Beijing Natl. Lab. Cond. Mat. Phys. and Inst. Phys., Chin. Acad. Sci., Beijing 100190, People's Rep. of China
T.-L. Lee, Diamond Light Source Ltd., Didcot, Oxfordshire OX11 0DE, United Kingdom
J. Minár, New Technologies-Research Ctr, Univ. of West Bohemia, CZ-30614 Pilsen, Czech Republic
R. M. S. dos Reis, J. Ciston, Nat;. Ctr. Electron Microscopy, Lawrence Berkeley Natl Lab., Berkeley, California 94720, USA
M. Gu, J. M. Rondinelli, Dept. Mat. Sci. Eng., Northwestern Univ., Evanston, Illinois 60208, USA
E. M. Gullikson, Advanced Light Source, Lawrence Berkeley National Laboratory, Berkeley, California 94720, USA

A general strategy to enhance or even to create new functionality in a wide range of compounds is by exploiting the interface effects close to the contact region of two dissimilar materials. Oxide physics greatly benefits from this approach by, for example, emerging two dimensional conduction channel in the form of an electron gas (2DEG) at the interface of two band insulators $LaAlO_3$ - LAO and $SrTiO_3$ - STO [1] or by selectively tuning the magnetic response of two dimensional $NdNiO_3$ (111) layer sandwiched between 4 unit cells of LAO [2].

The key question is how to extract the electronic properties of the interface and separate its contribution from that of the bulk. On the one hand, electric and magnetic measurements give the direct measure of device functionality. However, by probing the overall response of the system, they fail to exclusively disentangle the interface contribution from that of the bulk, whereas electron microscopy, by solving with unprecedented resolution most in-depth details of the interface crystalline structure, rarely connects straightforwardly with the interface functionality. In this context, in a series of photoemission experiments conducted with synchrotron radiation in the soft X-ray (SX) range [1-3], the dispersion of the electronic bands as a function of electron momentum $E(k)$ have been derived for the LAO/STO [1], LAO/NNO [2] and $LaSrMnO_3$ / $EuSrMnO_3$ (ESMO/LSMO) [3] interfaces.

The angle resolved photoemission (ARPES) technique performed with SX radiation enhances the probing depth and may selectively enhance the interface contribution through resonant excitation at X-ray absorption edges. In [1] it has been shown how the conductivity and the electronic phase separation (EPS) of the interface can be modified by tuning the concentration of oxygen vacancies, which defines a mixed dimensionality 2D and 3D character of the mobile electron systems (MES).

The experiment used resonant photoemission at the Ti $2p$ edge to follow the evolution of the interfacial electronic structure as a function of oxygen vacancies (OVs) concentration gradually developing under x-ray irradiation (**Fig. 1a-c**). The OVs generated by x-ray build up a dichotomic electron system where weakly correlated and nonmagnetic delocalized MES electrons coexist with strongly correlated and magnetic localized in-gap state electrons. The observed irradiation dynamics of the oxygen defficient LAO/STO electronic structure identifies the EPS as accumulation of the MES electrons in quasi-3D conducting puddles (**Fig. 1d**) with fixed electronic structure, which are embedded in the insulating phase.

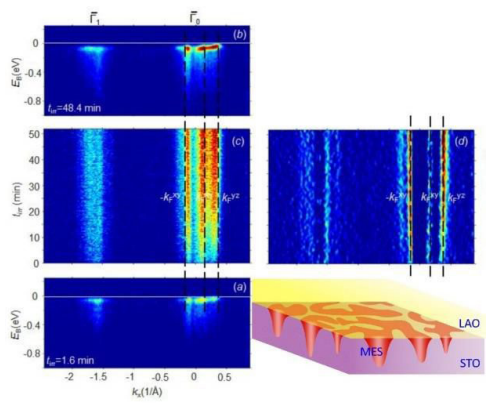

Fig. 1. *ARPES images of E(k) at small and large t_{ir}, respectively (a,b); (c,d) Fermi intensity I_F and its negative gradient $-dI_F/d|k|$, respectively, as a function of t_{ir}. k_F of the d_{xy} - and d_{yz} - bands determined from the $-dI_F/d|k|$ maxima are marked through with red dashed lines and schematic representation of quasi-3D conducting puddles of MES in OD-LAO/STO.*

Secondly, we show how by engineering the growth of oxide heterostructures in a well defined sequence, we control the magnetism of NNO. More exactly, two unit cell NNO were sandwiched between 4 unit cells of LAO grown on (111) oriented $NdGaO_3$ substrate. The graphene-like NNO (**Fig. 2 a,b**) has its electronic structure explicitly obtained in our SX-ARPES experiments (**Fig. 2 c,d**) perfectly compatible with the calculated antiferro-orbital arrangement in a 1×1 unit cell.

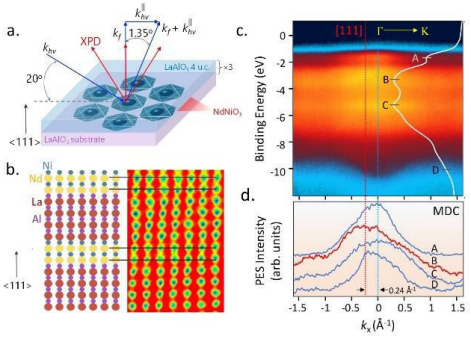

Fig. 2. *Schematic diagram of the SX-ARPES experimental geometry with all relevant momentum vectors shown and labeled (a) and the structure of the NNO(111) deduced from HRTEM (b). SX-APRES spectrum of the valence-band dispersion measured along the K′–Γ-K high-symmetry direction (c) and momentum distribution MDC curves recorded at the binding energies of the A-D features in (c).*

Thirdly, we show how to selectively access the electronic structure of a ESMO/LSMO multilayer by tuning the angle between the sample and the incoming X-ray beam at the Bragg condition (**Fig. 3a**), so that to selectively enhance and separate the signature of the top-most layer from that of the buried ones (**Fig. 3b**). This approach defines the standing waves (SW) X-ray photoelectron spectroscopy (XPS) technique [3]. The depth-dependent SW-XPS of the valence bands, strongly suggests the emergence of a surface-reconstructed (relaxed) ESMO layer, characterized by the presence of sites with tetrahedral oxygen coordination. The white-to-blue color scale in **Fig. 3**c represents the simulated intensity of the X-ray SW E-field (E^2) inside the superlattice as a function of depth and grazing incidence angle. The line-cuts and the corresponding E-field intensity plots on the right side show that at the grazing incidence angles of 18.7°, 19.2° and 19.8° too, preferentially highlights the top, middle and bottom unit-cells of ESMO, respectively

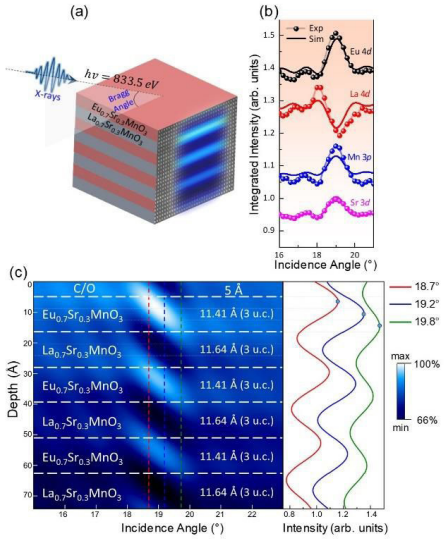

Fig. 3. *Schematic diagram of the sample and the experimental geometry, showing the soft x-ray beam, incident at the grazing angle corresponding to the first-order Bragg condition, and the resultant x-ray SW within the superlattice. (b) The best fits between the experimental and calculated SW rocking curves (RCs) for the Eu 4d, La 4d, Mn 3p, and Sr 3d core levels. (c) The resultant model of the superlattice, which self-consistently describes the shapes and amplitudes of the RCs for every constituent element in the structure.*

These results demonstrate both the power and necessity of depth-resolved x-ray techniques (such as SW-XPS) that are capable of probing buried layers and interfaces and thus go beyond conventional surface-specific or depth-averaging electronic-structure studies.

References

[1] V. Strocov et al. Electronic phase separation at LaAlO3/SrTiO3 interfaces tunable by oxygen deficiency, Phys. Rev. Mater. 3 106001 (2019).

[2] A. Arab et al, Electronic Structure of a Graphene-like Artificial Crystal of $NdNiO_3$, Nano Lett.19, 8311 (2019).

[3] W. Yang et al. Probing single-unit-cell resolved electronic structure modulations in oxide superlattices with standing-wave photoemission, Phys. Rev. B 100, 125119 (2019).

MATERIALS PREPARATION AND CHARACTERIZATION

SELECTED RESULTS

The influence of pH and UV light on the folic acid photodegradation

M. Baibarac, I. Smaranda, A. Nila
in collaboration with
C. Serbschi
Bioelectronic SRL, Ploiesti, Romania

New experimental evidences regarding the folic acid (FA) photodegradation into two products (pterine-6-carboxylic acid and p-amino-benzoyl-L-glutamic acid) (**Fig. 1**) were reported through UV-VIS absorbtion spectroscopy, photoluminescence excitation (PLE) spectra and IR spectroscopy studies [1].

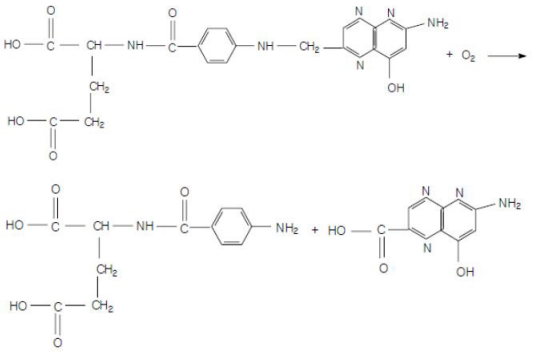

Fig. 1. *The photodegradation reaction of FA in aerobic conditions[1]*

The absorption spectra of FA in phosphate buffer (PB) solution having different pH values (7, 6.4 and 5.4) highlight two absorption bands in the spectral range of 200-300 (1st band) and 300-400 nm (2nd band) assigned to the π-π* and n-π* electronic transitions of pterine and p-aminobenzoyl acid, respectively (**Fig. 2**). Additionaly, as increasing the UV irradiation time, the intensity of the 1st band gradually decreases, while the 2nd band increases in intensity [1]. This behavior determines the appearance of the isosbestic point for all the three pH solutions indicating the formation of new chemical compounds as a consequence of the photochemical reaction of FA in aerobic conditions. The mechanism of FA photodegradation was proposed by Akhtar *et al.* [2], who indicated that two photodegradation products (pterine-6-carboxylic acid and p-aminobenzoyl- L-glutamic acid) are formed.

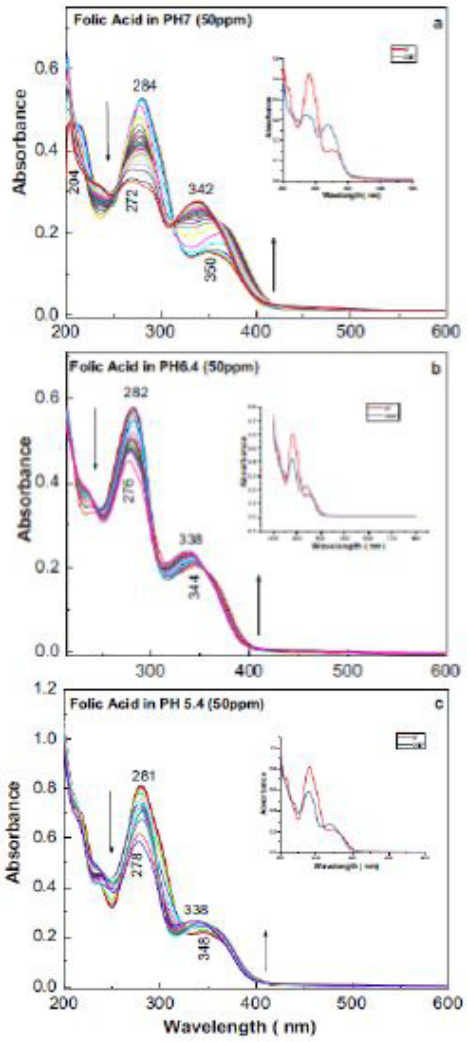

Fig. 2. *UV-VIS absorption spectra of FA in PB having the pH equal with (a) 7, (b) 6.4 and (c) 5.4[1]*

Further information regarding the photochemical reaction of FA is given by PLE spectra, which reveal a gradual increase of intensities after 317 min. of continuous irradiation (**Fig. 3**), the most significant variation being observed for the solution with pH=5.4. The explanation is based on the photolytic reactions (acid-base interaction) of the two photodegradation products, when their - NH_2 groups react completely with the acid solution to form the ammonium salt. These results indicate that FA samples for medical analyses must be handled in the absence of UV light.[1]

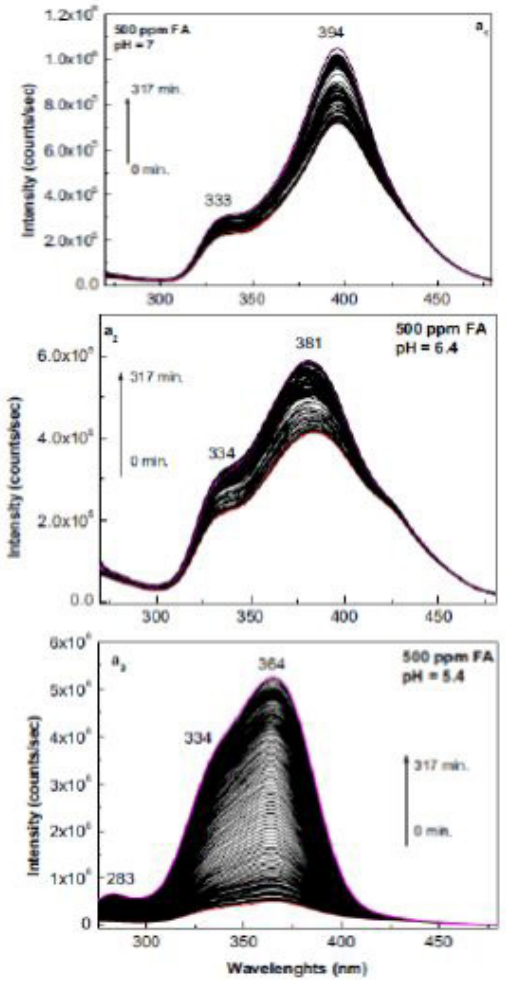

Fig. 3. *PLE spectra (λ_{em}=500 nm) of FA in PB having the pH equal with (a) 7, (b) 6.4 and (c) 5.4[1]*

Additional data concerning the reaction products of FA is given by IR spectroscopy. **Fig. 4** shows the IR spectra of FA in the powder state and thin film deposited onto a rough Au support.

The IR absorption bands of FA in a powder state were assigned to the three moieties of FA, namely, pterine, p-amino-benzoyl amide and glutamic acid. For the case of thin film of FA, significant changes are revealed in the IR spectrum such as changing the ratio between some IR bands (600- 800 and 800-1800 cm^{-1}) to higher values or disappearance of the IR band located at 1338 cm^{-1}, all of these being valid when FA was deposited as a thin film. These variations suggest a preferential orientation of the pterine, pamino-benzoyl amide and glutamic acid entities of FA onto the rough Au support (**Fig. 5**).[1] Regarding the black and red curves in **Fig. 4,** the UV light induces: (a) an increase in absorbance of the IR bands intensities at 948, 1070, 1331 and 1197 cm^{-1} indicating the increase in the mass of the amine and carboxyl groups in the analysed sample, which was a consequence of the photodegradation reaction of FA; (b) the appearance of IR bands at 948 and 1331 cm^{-1} attributed to the C-C bending vibrational modes in alkyl and benzene ring and C=O stretching in COOH groups and C-H in the benzene ring and NH in amine group of p-amino-benzoyl-L-glutamic acid.[1]

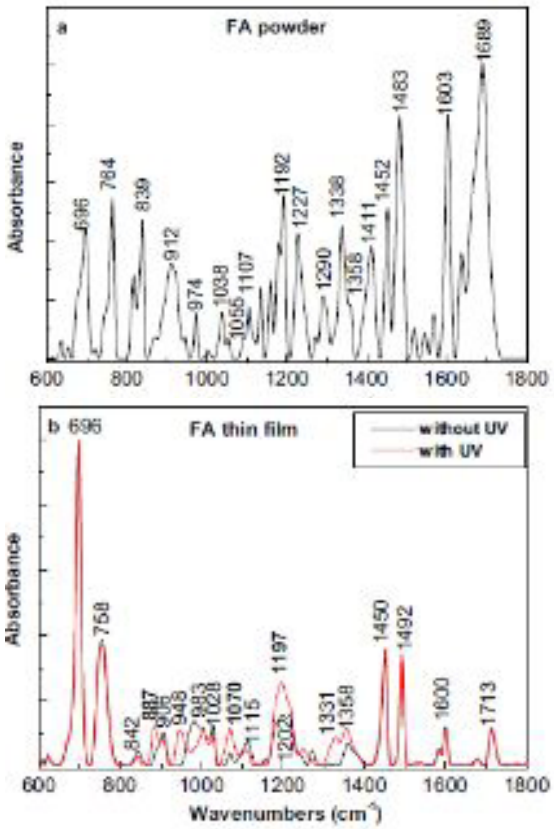

Fig. 4. *IR spectra of FA in the powder state (a) and as thin film deposed on Au support (b).[1]*

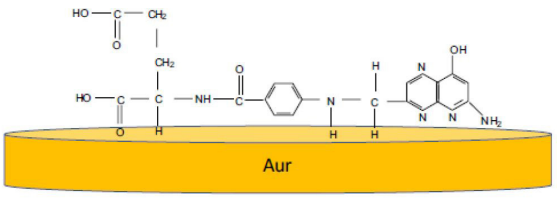

Fig. 5. *Adsorption of FA on the Au support[1]*

References

[1] M. Baibarac, et al., Sci. Rep. 9 (2019), 14278.
[2] M. J.Akhtar et al., J. Pharm. Biomed. Anal. 31(2003), 579–588.

Ferroelectric heterostructures for memcomputing applications

A.G Boni, L. D. Filip, C. Chirila, A. Iuga, I. Pasuk, L. Hrib, L. Trupina, I. Pintilie and L. Pintilie

The present and future global computational and storage needs are ever-increasing with a high demand for faster computing speed and higher information storage density. This brings the regular technology closer to its limitations of size reduction and fabrication costs. New computing paradigms have been proposed for overcoming some computing obstacles, many of them being inspired by the human-brain working principles: e.g.memcomputing or neuromorphic computing.

In the present study we theoretically and experimentally prove that simple ferroelectric (FE) multi-layered capacitor structures could be used as a memcapacitor unit cell but also presents basic properties as analogue capacitive spectrum for a neuromorphic circuit.

In **Fig**. **1a**) the architecture of the multilayered heterostructure is presented (two thin FE layers separated by an insulator interlayer). In **Fig**. **1b**) is represented the free-energy of the structure obtained using a Landau-Ginzburg-Devonshire model. The free energy presents 4 minima attributed to the different relative orientation of the polarization in the FE constituent layers. By changing the applied voltage, the system could pass through all these minima and all these states are stable and could be separately accessed by different voltage pulses. Considering that this structure could be approximated by three capacitors connected in series, the equivalent dielectric constant of the structure has a strong dependence on the dielectric constants and polarization of the layers, thus resulting a difference between the capacitance of the system when the FE polarization is totally reversed in both layers or when it has different orientation in the FE layers.

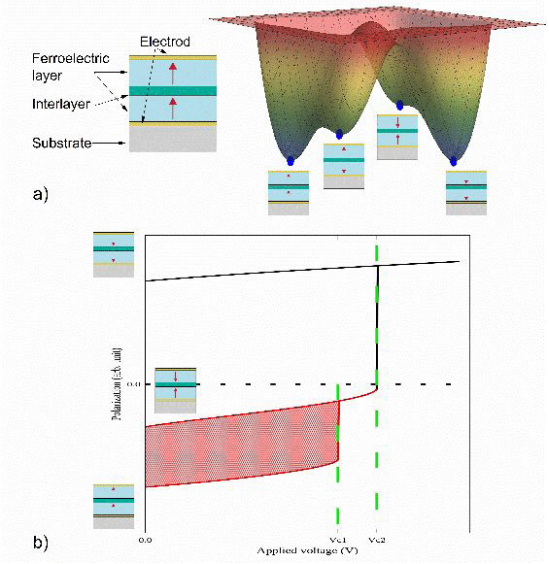

Fig. **1a**) *The architecture of a FE-I-FE structure; b) the free-energy landscape, c) the switching between different polarization states.*

For experimentally testing this hypothesis, two heterostructures have been deposited: Pb(Zr,Ti)O_3-$SrTiO_3$-Pb(Zr,Ti)O_3 and Pb(Zr,Ti)O_3-$BaTiO_3$-Pb(Zr,Ti)O_3 [1].

Both structures present a sequential polarization switching, with four distinct and stable polarization states. Thus after setting each polarization state, the capacitance of the structure has been measured as a function of frequency and the results are presented in **Fig**. **2** for the structure with BTO-interlayer. It can be easily observed that the system presents a low capacitive state (LCS) when it has both ferroelectric layers polarized in the same direction, while the system presents a high capacitive state when the polarization of the FE constituent layers has opposite directions. The relative differences between the capacitive states has a strong dependence on frequency and on the a.c. voltage of the measurement signal.

These results can be seen as the possibility to construct a non-volatile FE memory with non-destructive reading using a simple capacitor architecture.

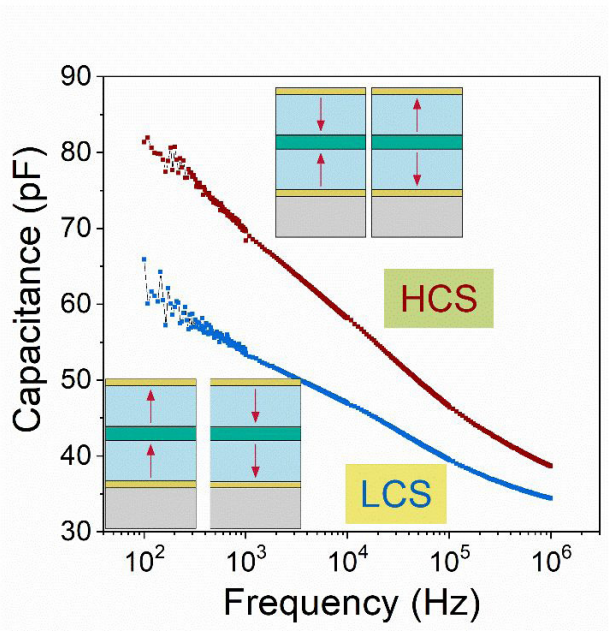

Fig. 2. *The capacitance-frequency characteristics for the two capacitive states.*

There is a complex scheme of the possibilities of switching between the four distinct polarization states which have associated two different capacitive states as it is presented in [1]. Thus it could be used to performed logic Boolean operations such as OR/NOR or AND/NAND [1]. For example, the algorithm of computing a OR/NOR operation using a ferroelectric tri-layer structure is schematically represented in **Fig. 3**. By applying a large negative voltage pulse, the system is set in the initial state having associated a LCS. If logic 0 is defined as a low, positive voltage pulse and logic 1 is defined as high positive voltage pulse, it can be seen that only two consecutive 0 inputs leave the system in a HCS, while the other 3 combinations set the system in a LCS. Depending how these capacitive states are defining as 0 or 1 output, this computation could be the result of OR or NOR logic operation. In similar ways AND and NAND operations could also be defined.

Moreover, cascade computation could be performed on only one capacitor cell. The final results could be stored on the unit and then could be non-destructively read.

These results proved that these structures could be used to compute and store the information thus representing a memcapacitor unit based on a ferroelectric capacitor structure.

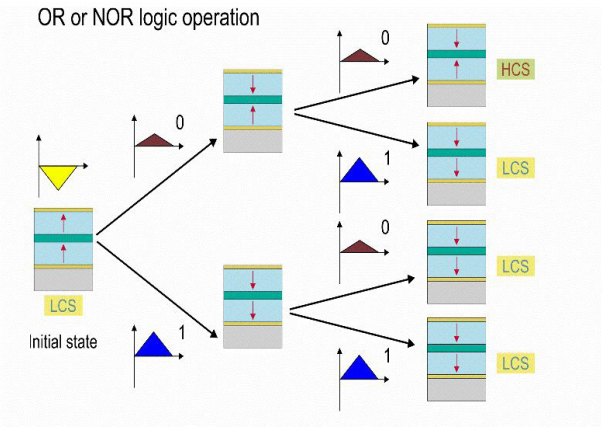

Fig. 3. *The schematic representation of OR/NOR Boolean Logic operation.*

Furthermore, in the paper [1] it is shown that these systems could present quasi-stable in time partially switch polarization in the FE layers which presents a continuous spectrum of capacitive values between HCS and LCS. These results could be used for development of a non-volatile analogue capacitive memory for constructing neuromorphic circuits.

The work was carried out in the frame of the Nucleus Program No. PN18-110101 and PN-III-P4-ID-PCCF-2016-0047.

References

[1] A.G. Boni et all., Physical Review Applied 12, 024053 (2019).

XPS, a valuable tool in supporting investigations related to graphene based catalysts

Ioana Cristina Bucur
in collaboration with
A. Primo[1], J. He[1], H.Garcia[1], P. Conception[1], A. Simion[2], S.M. Coman[2], B. Jurca[2], B. Cojocaru[2], V.I. Parvulescu[2], N. Candu[2], I.Man[3]
1Instituto Universitario de Tecnología Química, Consejo Superior de Investigaciones Científicas-Universitat Politécnica de Valencia, Universitat Politecnica de Valencia, Spain.
2Department of Organic Chemistry, Biochemistry and Catalysis, Faculty of Chemistry, University of Bucharest, Bucharest, Romania
3Center of Organic Chemistry "C.D. Nenitescu" of Romanian Academy, Spl. Independentei 202B, Sector 6, Bucharest, Romania

One of the top priorities in current research in catalysis is to develop renewable catalysts alternative to those based on metals. Graphene is relevant in catalysis, due to large specific surface area, accessibility of active sites, high adsorption capacity, and the possibility to engineer active sites on the sheet either by varying the density of defects or by doping with different heteroatoms (B, N, O, P and S).

Three common bonding configurations are normally obtained when doping nitrogen into the graphene: pyridinic N, pyrrolic N, and quaternary (or graphitic) N. It is expected that the presence of pyridinic and pyrrolic heterocycles inside the graphenic structure should change the basic properties of graphene, nitrogen serving as an electron donor site.

First study reported N-doped, defective graphene [(N)G] obtained by pyrolysis of chitosan at 900°C under Ar that exhibits catalytic activity for the Sabatier hydrogenation of CO_2 to CH_4 at temperatures about 500°C with estimated turnover frequencies and activation energy values of 73.17 s^{-1} and 24.3 kcal×mol^{-1}, respectively [1]. B- and P-doped graphenes (B-dG and P-dG, respectively) were obtained by submitting to pyrolysis the corresponding borate and phosphate esters of alginic acid. XPS investigation performed on this sample, showed the C1s peak that can be deconvoluted as graphenic carbon in a percentage of 80% or above, while for B1s the two components have binding energies indicating BCCC and BCOO environment. The P2p peak exhibits two different families that correspond to PCCC and PCOO.

In the case of N doping, four different populations of N atoms similar to pyridinic, pyrrolic, graphitic and N-oxide types of N atoms were determined.

XPS data highlighted that the enhanced catalytic activity reported compared to other related doped defective graphene derives from the presence of pyridinic N atoms that adsorbs CO_2 forming carbamate-type adsorbates.

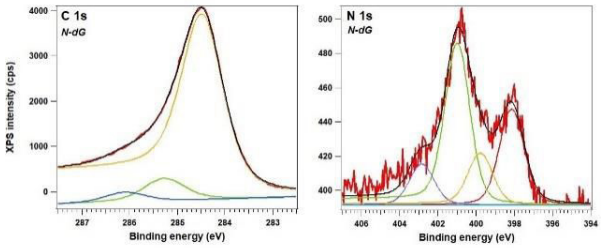

Fig. 1. *Presents selected Raman spectra, a representative transmission electron microscopy (TEM) image and XPS peaks to illustrate the data of the most active N-dG sample under study [1].*

A previous study [2] concerned also the pyrolysis at 900 ^{0}C of chitosan that yielded (N)G containing about 3.7% of residual N atoms, distributed as pyridinic, pyrrolic and graphitic N atoms. It was evidenced that (N)G acts as basic catalyst affording the active sites required by the Michael or Henry additions. XPS confirmed the doping of graphene with N and the presence of residual O atoms. Deconvolutions of the C1s spectra yielded the presence of graphitic sp^2 C atoms, as well as sp^2 C atoms bonded with N and O. (N)G as catalyst shows an intermediate behavior between that of pyridine and pyrrole, in agreement with the XPS measurements that shows that (N)G contains simultaneously pyridinic and pyrrolic N atoms in similar proportion as can be observed from **Fig. 2** .

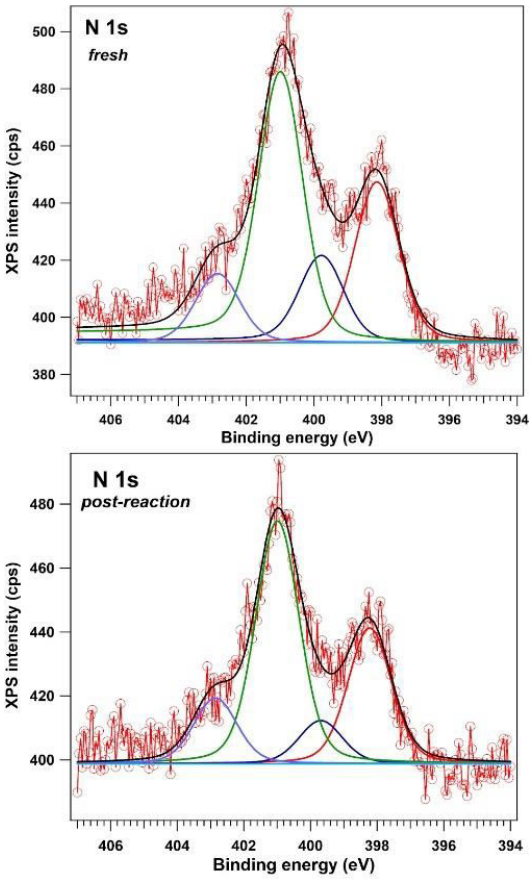

Fig. 2. *XPS Spectra of the investigated (N)G catalyst in fresh and post-reaction state .*

The use of molybdenum disulfide supported on graphene for electrocatalytic hydrogen evolution has been considered a major development in this area, since this composite material can exhibit catalytic performance close to that of Pt nanoparticles due to the combination of the electrical conductivity of graphenes and the catalytic activity of MoS_2.

In this study [3], the catalytic activity of MoS_2/G for CO_2 methanation is reported, comparing the performance of MoS_2/G with MoO_3/G. XPS characterization of the samples before and after using the materials as catalysts for CO_2 hydrogenation showed no difference in the case of MoO_3/G, in agreement with the notable stability of these samples. In the case of MoS_2/G, some changes in the Mo 3d peak were observed in the MoS_2/G sample submitted to exhaustive use as catalyst in the CO_2 hydrogenation that are compatible with the formation of some Mo(VI) component in about 20%. **Fig. 3** presents the XPS Mo 3d and O 1s peaks of the MoS_2/G sample fresh and after its use as CO_2 hydrogenation catalyst, where the remarkable changes in the shape and distribution of the O 1s peak can be seen, as well as the appearance in Mo 3d of a component attributable to oxidized Mo(VI). Therefore, the catalytic activity of MoS_2/G with that of MoO_3/G shows that the latter is less efficient, but more selective for CO_2 methanation.

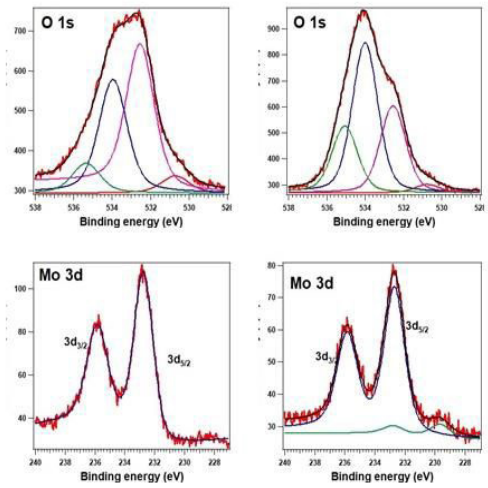

Fig. 3. *Deconvolutions of XPS O 1s and Mo 3d peaks of the MoS_2/G catalyst fresh (left) and after being exhaustively used as CO_2 hydrogenation catalysts* (right).

In conclusion, XPS provided in a non-destructive way, information about the top-most atomic layers of these graphene based materials, related to the chemistry and binding energies associated to different chemical bonds and surface composition and its findings corroborated with other methods are important for sample characterization.

References

[1] B. Jurca et al., ChemCatChem 11, 985-990 (2019).
[2] N. Candu et al, J.Catalysis 376, 238-247 (2019).
[3] A. Primo et al, Appl. Catal. B: Environmental, 245, 351-359 (2019).

Carbon-based sprayed electrodes for pyroelectric applications

C. Chirila, M. Botea, A. Iuga, A. G. Tomulescu, L. Balescu, A. C. Galca, A. G. Boni, L. Leonat, I. Pintilie, L. Pintilie

In the field of pyroelectrics applications, the electrodes play a major role, they have to possess a good electrical conductivity, fast electron mobility and good absorption of IR radiation. A large variety of carbon based materials have been investigated for use as electrodes on pyroelectric materials, especially due to their absorption capabilities given by their black colour.

Various techniques have been tested in order to obtain and design carbon-based structures as electrodes. Large efforts have been made to integrate 2D (graphene) materials through various electrospinning, chemical-vapour deposition, self-assembling, wet spinning, or template-assisted methods in macroscopic structures.

All these methods have led to improved performance of the devices, but they are time consuming, expensive and their integration at a large scale is still difficult.

Our results are based on obtaining through a new method, carbon- based sprayed electrodes (CBSE), as top contacts on the surface a PZT/SRO/STO/Si structure and testing their performances on pyroelectric properties. Spray deposition consists in the pulverization of a carbon based material, using a carrier gas, through a spray nozzle onto a preheated substrate to evaporate the solvent. In order to obtain a dispersion of 1:10 (volume ratio) commercial carbon paste was dispersed in acetone, using an ultrasonic bath for 15 minutes. A schematic representation of the deposition process is presented on **Fig.1.** The thickness and morphological properties of the CBSE electrodes were tested by SEM, see **Fig. 1**. X-ray diffraction performed after CBSE deposition on PZT/SRO/STO/Si structure confirm the existence of highly crystalline form of graphite, see **Fig. 2**. The peaks at 26.57° and 54.66^0 2θ correspond to the (002) and (004) reflection in hexagonal graphite with a measured interplanar spacing of 0.335 nm and 1.67 nm respectively.

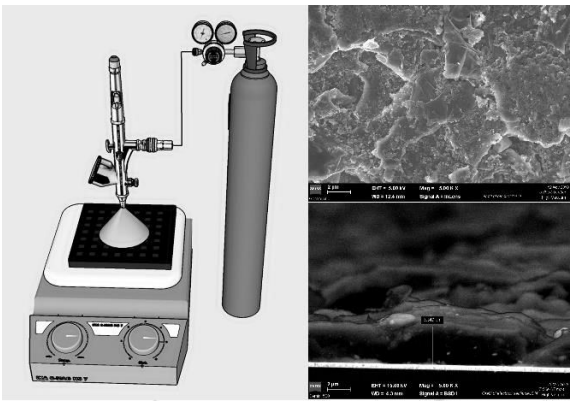

Fig. 1. *Schematic representation of CBSE deposition process, and their morphologic properties.*

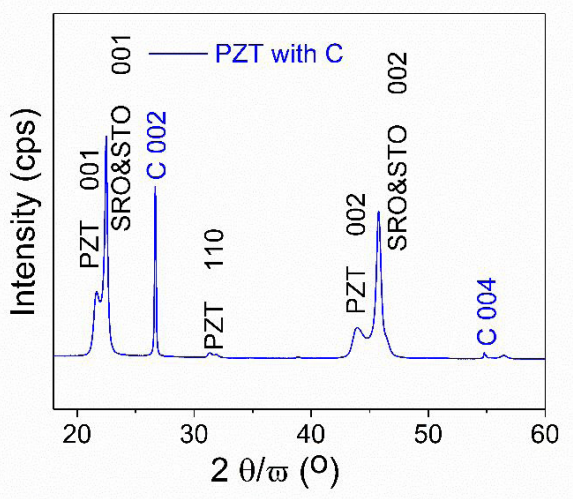

Fig. 2. *XRD peaks associated to the deposited PZT, SRO, STO and carbon layers.*

The electrical properties of the CBSE were analyzed at room temperature through current-voltage (I-V) and impedance spectroscopy measurements. The linear dependence of the current as a function of voltage supports a resistive like behavior, and from the slope of this linear dependence a value of 247 ohms was estimated for the sheet resistance of CBSE. The impedance presents an approximatively constant value of 250 ohms for the frequency range between 100 Hz to 1 MHz. According to the electrical response, **Fig. 3**, we can consider that CBSE may be successfully used as electrode to build capacitor-like structures for pyroelectric applications.

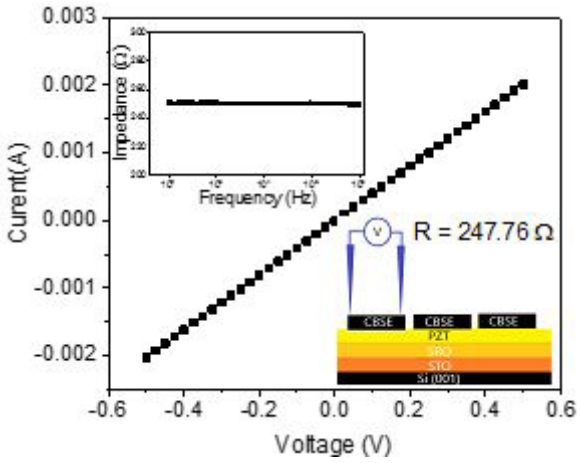

Fig. 3. *Electrical properties of CBSE electrodes.*

The pyroelectric properties of the PZT/SRO/STO/Si structure with CBSE electrodes have been evaluated in comparison with SRO/Au electrodes in order to verify the CBSE electrodes performances for pyroelectric applications.

The pyroelectric measurements were performed with modulated light from an IR source (a laser diode of 30mWat 800 nm). The beam was modulated electronically using a signal generator.

The pyroelectric signal was collected in the voltage mode, using a J-FET type impedance converter and recorded with a lock-in amplifier. In **Fig .4** the dependencies of the pyroelectric signal on the reverse of the modulation frequency for the two type of top electrodes are presented. The pyroelectric signal recorded on CBSE is 2.5 times higher than for SRO / Au, at low frequencies. As the modulation frequency of the IR beam increases, the response of the CBSE structure decreases faster, approaching the values obtained in the case of the SRO/Au electrode [1,2].

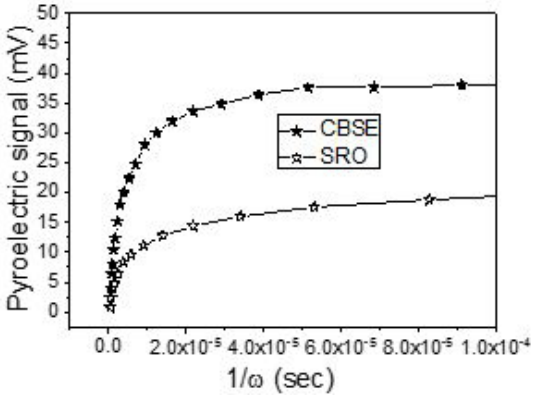

Fig. 4. *The pyroelectric signal as a function of the reverse of the modulation frequency recorded for two different top electrodes.*

The pyroelectric coefficients were extracted from figures of merit and their values are $9.73 \cdot 10^{-4}$ C/m^{2}K for CBSE electrodes and $3.36 \cdot 10^{-4}$ C/m^{2}K for SRO/Au respectively. The enhancement in the pyroelectric response for CBSE is attributed to a more efficient collection of the charge generated by pyroelectric effect and to a more efficient absorbtion of the IR radiation due to larger emissivity (close to 1, compared with 0.37 for SRO/Au).

This new deposition process is also compatible with industrial manufacturing of certain devices such as pyroelectric detectors, energy harvesters, as well as solar cells.

The work was carried out in the frame of the Core Program PN18-110101 and the IFA-CEA (Contract No. C503/2016).

References

[1] Chirila C, Botea M, Iuga A, Tomulescu AG, Balescu L, Galca AC, et al. (2019) PLoS ONE 14(8): e0221108.
[2] M. Botea, A. Iuga, and L. Pintilie, Appl. Phys. Lett., vol. 103, 2013, doi: 10.1063/1.4838035.

Orthorhombic HfO_2 with Ge nanoparticles in nonvolatile memories for radiation detection

C. Palade, A. Slav, A.-M. Lepădatu, I. Stăvărache, I. Dăscalescu, V. A. Mărăloiu, C. C. Negrilă, C. Logofătu, T. Stoica, V. S. Teodorescu, M. L. Ciurea, S. Lazanu

The system of Ge nanoparticles (NPs) embedded in HfO_2 combines the advantages of Ge NPs (high exciton radius, low thermal budget of formation) with those of high-*k* H*f*O_2, and more than that, with the recently discovered ferroelectric properties of the non-centrosymmetric orthorhombic phase of H*f*O_2. Applications of this system cover mainly nonvolatile memories and photodetectors.

Floating gate (FG) MOS capacitors with the structure *control* H*f*O_2/FG of Ge NPs in H*f*O_2/ *tunnel* H*f*O_2/Si *substrate* were obtained by sequential deposition of the layers on p-Si wafers using magnetron sputtering followed by rapid thermal annealing in N_2 atmosphere at 620^0C, and finally by depositing Al contacts on top and backside of the sample, to be used as dosimeters [1].

HRTEM, HAADF-STEM and XPS were employed for characterizing the trilayer structures. The response of the capacitors to α particle irradiation was tested using a ^{241}Am source by measuring electrical characteristics before and after irradiation.

The trilayer morphology was revealed by HRTEM measurements (**Fig**. **1**). The control H*f*O_2 layer is composed from two regions with different contrast, the darkest one being adjacent to the intermediate layer/FG (H*f*O_2+Ge).

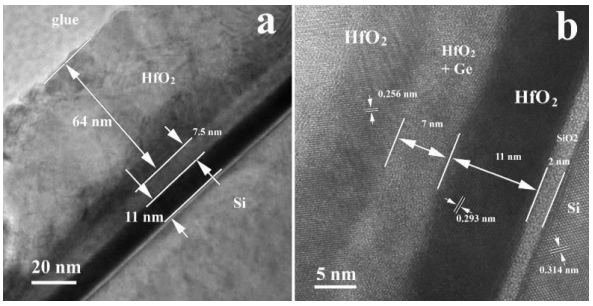

Fig. **1**. *XTEM images of the trilayer structure at different magnifications: (a) image of the cross-section of all the structure; (b) detail of the intermediate layer*

In and adjacent to the intermediate layer, HfO2 is in orthorhombic/tetragonal phase. The measurement of the lattice fringe distance of 0.294±0.003 nm cannot discriminate between the 0.294 nm (211) plane or (111) plane, both of the orthorhombic phase, and the similar lattice fringes of 0.297 nm of the tetragonal H*f*O_2 structure. Toward the free surface of the trilayer, the control H*f*O_2 lattice relaxes to monoclinic phase.

The intermediate layer (**Fig**. **2**) contains also small (2–3 nm) spheroidal amorphous Ge NPs (evidenced by white elliptic borders) organized in two rows, located near the interfaces of the intermediate layer with the H*f*O_2 tunnel and control layers.

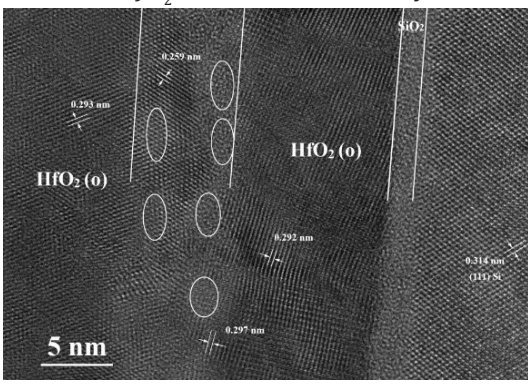

Fig. **2**. *HRTEM image of the intermediate layer (zone II) and adjacent areas. Zone I - control HfO_2, mostly monoclinic with nanocrystals of orthorhombic (or tetragonal) HfO_2 near the FG. Zone III – tunnel, mostly orthorhombic (or tetragonal) phase.*

XPS analysis revealed that Ge is mainly in the metallic state, the oxidized Ge being about 20% of total Ge. The metallic Ge is located in the two rows of Ge NPs observed in HRTEM and STEM-HAADF images. These Ge NPs are the charge storage centers inside the floating gate.

On the other hand, it is known that orthorhombic non-centrosymmetric H*f*O_2 has ferroelectric properties and can contribute to the memory effect. The charging and storage capabilities of the structure were investigated by capacitance voltage (*C-V*) and capacitance time measurements. Counter clockwise hysteresis loops in *C-V* curves are obtained, with memory windows of 3.2 and 6.1 V for charging times at both accumulation and inversion regimes of 30 and 600 s respectively.

The working of the memory capacitor can be influenced by the charging-discharging of traps

located at the substrate interface or distributed in HfO_2, which contribution has been analyzed by frequency dependence measurements and the modelling of the experimental curves of measured capacitance and resistance versus bias voltage.

By using the method of Nicollian and Brews, the frequency dependence of the series resistance (R_s) was extracted, then the frequency dependence of the parallel capacitance (C_p) and conductance (G_p) were also modelled – **Fig. 3**. The G_p peaks are close to corresponding values of V_{FB} obtained from the two hysteresis branches of the *C-V* curves. The shift of the position of the two peaks in **Fig. 3d** is due to the contribution of traps to the charge storage. This shift is explained by a broad distribution in carrier capture rates of traps.

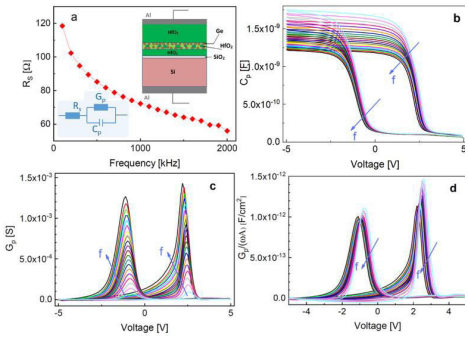

Fig. 3. (a) *Frequency dependence of R_s; insets: top right-sketch of the trilayer capacitor and bottom left-equivalent circuit of the trilayer; (b) bias dependence of C_p for f=100 kHz÷2 MHz in steps of 100 kHz; (c) bias dependence of G_p; (d) voltage dependence of G_p normalized to electrode area and frequency*

For the use of the trilayer as dosimeter, the effect of α particle irradiation on memory state after charging was investigated. The passage of α particles in the sample was simulated using the Monte Carlo code SRIM and the results are presented in **Fig. 4**. The energy of the α particle at the free surface of the trilayer is 3.80 MeV. The resulted range is 16.40±0.19 μm, i.e. α particles are stopped deep inside the Si substrate. This means that the memory state is mainly changed by the ionizing effect of the radiation flux passing through the active region of the memory structure. The flatband voltage was monitored during exposure to α particles, and the time dependence of ΔV_{FB} is translated into dose dependence in **Fig. 5.**

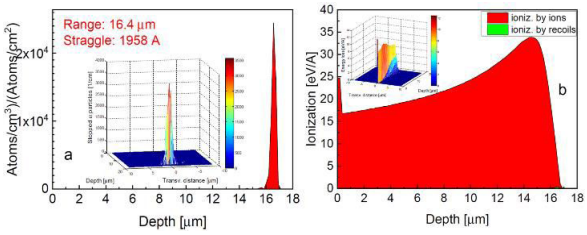

Fig. 4. *SRIM simulation of α particles penetration in the FGMOS capacitor: (a) distribution of stopped ions; (b) depth distribution of the energy lost by ionization; inset: spatial distribution in the depth radius plane.*

Prior to exposure to radiation, the FG was charged with electrons at +5V for 30 s, and ΔV_{FB}=1V - top left inset in **Fig. 5,** in which the *C-V* curves of initial and after positive voltage charging memory states are shown. One can see that ΔV_{FB} varies linearly with the dose up to 50 Gy with a saturation trend at higher doses, resulting a sensitivity of our dosimeter of ≈ 0.8 mV/Gy. Sequential relaxation-charging-irradiation experiments have shown that repeated operation of the dosimeter without any annealing step for removal of the radiation induced defects results in a decrease of the sensitivity. The bottom right inset in **Fig. 5** presents the dose dependence of ΔV_{FB} in 4 irradiations performed one after the other, at which the sensitivity is sequentially reduced up to 0.4 mV/Gy.

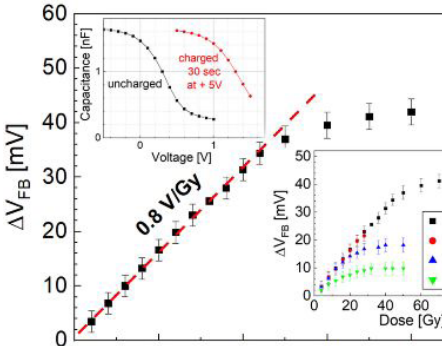

Fig. 5. *ΔV_{FB} after charging with electrons versus absorbed dose of α particles. Insets: top left-effect of FG charging on C-V characteristic; bottom right-effect of successive irradiations on the sensitivity of the dosimeter.*

Consequently, the *control* HfO_2/FG of Ge NPs in HfO_2 / *tunnel* HfO_2 /Si *substrate* structure presents enhanced memory performance due to the contribution of both Ge NPs and ferroelectric HO_2 matrix and has a high sensitivity of 0.8 mV/Gy to α article irradiation, being proper for dosimeter applications.

References

[1] C Palade, A Slav, AM Lepadatu, I Stavarache, I Dascalescu, AV Maraloiu, C Negrila, C Logofatu, T Stoica, V S Teodorescu, M L Ciurea and S Lazanu, Nanotechnology 30, 445501 (2019).

Ge nanoparticles in SiO_2 for high performance Vis-NIR photodetectors

Ionel Stăvărache, Valentin Șerban Teodorescu, Constantin Logofătu,
Magdalena Lidia Ciurea
in cooperation with
Petronela Prepeliță
National Institute for Laser, Plasma and Radiation Physics, Romania

Ge nanoparticles (NPs) in oxides are the most promising candidate for many structures / devices. The films of Ge-NPs embedded in oxides are photosensitive as photogenerated holes (in Ge-NPs) are trapped in defects. We prepared ITO/ Ge-NPs:SiO_2 active layer/ native SiO_2/ n-Si/ Al structure. Ge-NPs formation in SiO_2 (Ge:SiO_2, 25%:75 vol%) layer during deposition on 300, 400 and 500°C Si substrate that are lower than that corresponding to Ge-NPs formation by post-deposition annealing. The $GeSiO_2$ layer was co-deposited by magnetron sputtering from SiO_2 and Ge targets. The area of ITO electrodes is 3 × 3 mm2. We aim to get photosensitive structures in near infrared (NIR) by lowering the formation temperature of Ge-NPs, so avoiding Ge fast diffusion and precise control of NPs size. These issues are common for post-deposition annealing at high temperatures. The films are studied by x-ray Photoelectron Spectroscopy (XPS), Cross Section TEM (XTEM) and, measurements of current density-voltage (J–V) and photocurrent spectra.

Fig.1 shows XTEM images of films deposited on Si substrates at 300°C (a), 400°C (b) and 500°C (c). The films thicknesses decrease with temperature increase and are due only to the substrate temperatures, the rest of the parameters (pressure, power, time) were kept constant. Ge layer appears near the Si interface for films deposited at 400^{0}C and 500°C and only a small agglomeration for films deposited at 300°C. The atomic Ge/Si ratio in the film deposited at 300°C is 0.33 (EDX-**Fig**. **2a**). Selected area electron diffraction (SAED) also shows that GeSiO film is amorphous (**Fig**. **2b**). For 500°C films, only few Ge-NPs in SiO_2 matrix are crystallized (**Fig**. **2c** inset), but the majority remain amorphous. The lattice fringes of 0.326 nm belong to (111) Ge planes. The average size of crystallized Ge-NPs is 3.8 ± 0.7 nm. The amorphous Ge-NPs size appears to be bigger (5–6 nm) as their interface with matrix is not precise.

The atomic concentration depth profile results (**Fig**. **3**) from XPS spectra on the film thickness, for (a) 300°C and (b) 500°C films after Ar^+ etching. The curves evidence the concentrations as a function of the film depth for metallic, oxidized Ge, total Ge, O and Si concentration. In the films deposited at 300°C, total Ge content of 12–14% is in agreement with EDX data (see below). The sample at 500°C is different, so almost the whole amount of Ge is oxidized and the content of oxidized Ge decreases from the film/Si interface to the film free surface. This suggests that a part of Ge is lost during film deposition at higher temperature by GeO formation. **Fig**. **4** shows *J–V* curves in dark and under illumination (sandwich configuration), at RT, on SiO_2 films with embedded Ge-NPs deposited at 300, 400 and 500°C and without Ge-NPs (500°C substrate).

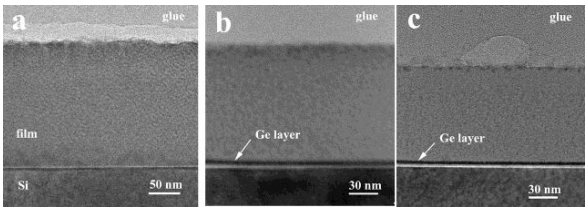

Fig. **1**. *XTEM images of the films deposited at 300 °C (a), 400 °C (b) and 500 °C (c).*

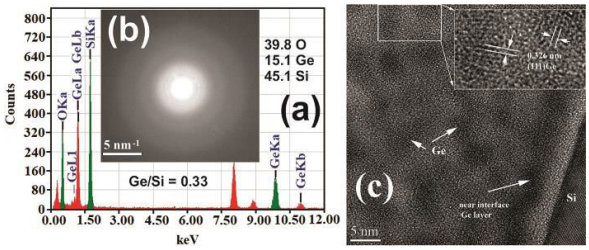

Fig. **2**. *(a) EDX spectrum of the GeSiO film at 300 °C; (b) SAED on the film deposited at 300 °C; (c) HRTEM image of film deposited at 500°C; few Ge-NPs are crystallized, but the majority remain amorphous (inset).*

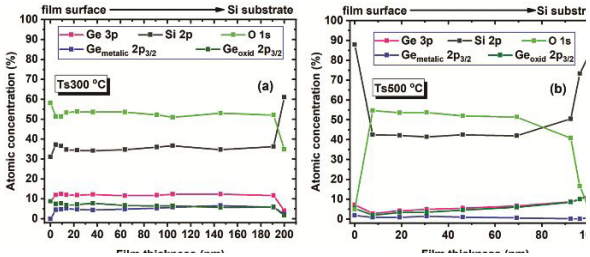

Fig. 3. *Atomic concentration versus film thickness, for (a) 300 °C and (b) 500 °C for O1s, Ge3p and Si2p lines. Ge and Si chemical states result from Ge2p3/2 and Si 2p XPS spectra.*

All *J–V* curves show a low rectifying behavior, while for 500 °C shows a good diode behavior (**Fig. 4c**) due to the Ge-NPs:SiO_2 film/Si interface. Under illumination, the reverse photocurrents (300 and 400°C) are higher with at least one order of magnitude compared with dark currents. The SiO_2 layer without Ge-NPs embedded in is not photosensitive (**Fig. 4d**).

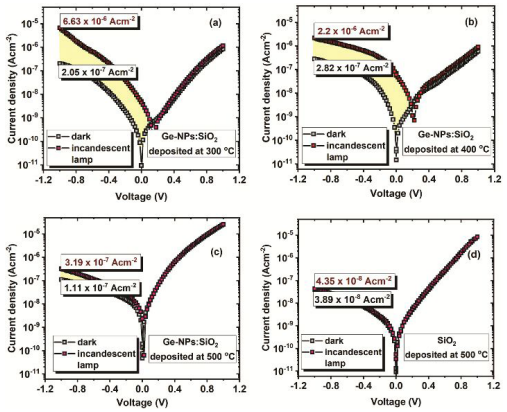

Fig. 4. *J–V curves taken at RT, in dark and under illumination with an incandescent lamp, on a Al/Si-n/Ge-NPs:SiO_2/ITO structure annealed at: 300°C (a), 400 °C (b) and 500 °C (c). Similar structure without Ge incorporated into the SiO_2 layer deposited at 500 °C (d);*

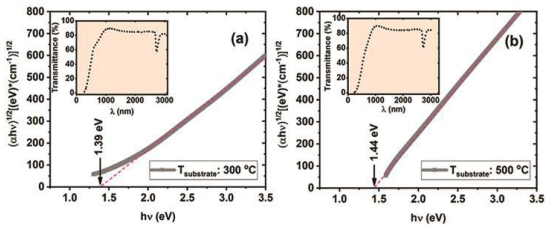

Fig. 5. *Absorption coefficient: Tauc plot (solid lines) and linear fits (dash lines) for Ge-NPs:SiO_2 deposited at 300 °C (a) and 500 °C (b). Insets: corresponding transmittance for 300 and 500 °C deposition temperature*

The optical properties of the films deposited on quartz at 300°C and 500°C are shown in **Fig. 5a,b**. The optical bandgaps are E_g=1.39 eV for 300 °C and E_g=1.44 eV for 500°C. The higher E_g can be explained by the lower Ge content and higher oxidation level in respect to that for 300°C deposited samples. **Fig 6 a,b** shows the photocurrent spectra on films at 300 and 500°C that are deconvoluted by 5 maxima having a broadband of sensitivity of 400- 1325 nm. The cutoff wavelengths (**Fig. 6,** inset) are 1325 and 1267 nm for films at 300 and 500 °C, respectively. The peak at 1100 nm is due to Si substrate. That at 1200 nm is attributed to Ge rich layer at the interface with Si substrate. The maxima below 1100 nm can be attributed to photo-effects in Ge-NPs:SiO_2 films (Ge related defects acting as traps).

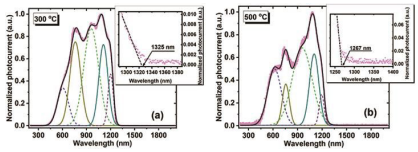

Fig. 6. *Photocurrent spectra obtained on films deposited at 300 and 500 °C substrate temperature. The insets present the cutoff wavelengths in detail.*

The responsivity (**Fig. 7a** left axe) calculated considering the incident optical power (**Fig. 7a** right axe) has values of 2.42 AW^{-1} for 300 °C and 0.69 AW^{-1} for 500 °C films. With the temperature increase from 300 to 500 °C, the responsivity decreases about 4 times, due to both Ge loss and oxidation.

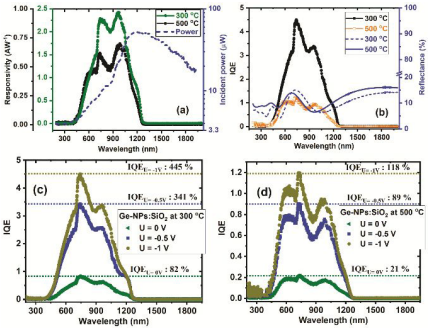

Fig. 7. *Ge-NPs:SiO_2 films deposited at 300 and 500 °C: (a) spectral responsivity (left axes) and incident power (right axes); (b) IQE (left axes) and reflectance (right axes); (c) and (d) spectral IQE at different external applied voltages.*

Internal quantum efficiency (IQE) (**Fig. 7b** left axes) were calculated by using the reflectance spectra obtained on Ge-NPs:SiO_2 films deposited at 300 and 500 °C (**Fig. 7b** right axes). The maximum IQE value is 445% for 300 °C and about 118% for 500°C explained by considering trapping of the photogenerated holes on Ge related defects/traps. For supporting the IQE values higher than 100%, in **Fig. 7c,d** are presented the IQE spectra obtained for different external applied voltage 0, −0.5 and −1 V.

We can conclude that the temperature necessary for formation of photosensitive / active layer of Ge NPs embedded in SiO_2 is the key for enhancing the photosensitivity in NIR.

Reference

[1] I. Stavarache, V. S. Teodorescu, P. Prepelita, C. Logofatu, M. L. Ciurea, Scientific Reports 9:10286, 1-8 (2019).

High Sn concentration GeSn nanocrystals for photodetection extended to 2.5 μm

Adrian Slav, Cătălin Palade, Constantin Logofătu, Ioana Dăscalescu, Ana-Maria Lepădatu, Ionel Stăvărache, Sorina Lazanu, Valentin Serban Teodorescu, Magdalena Lidia Ciurea, Toma Stoica
in collaboration with
Mariana Braic, National Institute for Optoelectronics;
Dan Bucă - Peter Grünberg Institut (PGI 9) and JARA Fundamentals of Future Information Technologies, Forschungszentrum Jülich, Germany;
Florin Comănescu - National Institute for Research and Development in Microtechnologies;
Sorina Iftimie, Stefan Antohe - Faculty of Physics, University of Bucharest

The research for new materials for light emitting and detection in the 1.5 – 3 μm wavelength range (shortwave infrared – SWIR) is motivated by applications in sensing, process monitoring, or machine vision systems. As the SWIR window 1.7 – 3 μm cannot be covered by III-V materials (InGaAs), novel materials, as well as simple and cost-effective production technologies are studied, such as GeSn.

Recent progress in epitaxy of GeSn alloys has led to the proof of fundamental direct bandgap in GeSn alloys for Sn contents above 8%. The difficulty is that the GeSn alloy is thermodynamically unstable for more than 1% Sn, favoring Sn segregation. Crystalline GeSn has the advantage of increased radiative recombination probability and, additionally, bandgap tuning by composition, nanocrystal (NC) size and strain variation. By embedding GeSn NCs in a dielectric matrix, surface passivation of NCs is achieved, and thus the decrease of recombination centers induced by grain boundaries.

Layers of $GeSnSiO_2$ were deposited by magneton cosputtering of Ge, Sn, and SiO_2 on p-type c-Si wafer. The nanocrystallization was obtained *ex situ* by rapid thermal annealing (RTA) at T_{RTA} as well as *in situ* (dynamic annealing) by increasing the substrate temperature during deposition (T_{sub}).

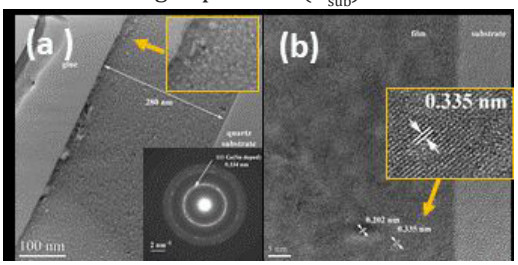

Fig. 1. *HRTEM images of a $GeSnSiO_2$ layer $[(Ge_{1-x}Sn_x)_{1-y}(SiO_2)_y$ with x and y values both of about 9%] after RTA at 400 °C: (a) low magnification TEM image with SAED pattern in the inset. (b) HRTEM image at bottom part of the film.*

The nanocrystallization of $GeSnSiO_2$ films was investigated by electron microscopy, XRD and Raman scattering, and we found that GeSn NCs formation by *ex situ* annealing occurs in a limited temperature range: it starts at 350°C and is degraded at 450 °C with the segregation of β-Sn. Sn concentration in GeSn NCs increases compared with the mean value in the as-deposited sample and decreases later on when Sn segregation occurs.

TEM investigations of the $(Ge_{1-x}Sn_x)_{1-y}(SiO_2)_y$ layer deposited at RT, with x = y of about 9%, after RTA at 400 °C, put in evidence a homogeneous size and distribution of the GeSn NCs and low-density amorphous material in the bulk, while at the sample surface there is an inhomogeneous region of about 20 nm, indicating large Sn diffusion – **Fig. 1.** Strong composition nonuniformity, with large spatial density fluctuations is found for $T_{RTA} = 450\ ^0C$ for which in the bulk of the film Sn content of the NCs is only 2 at. %, while in the surface region it increases to 8 % (SAED pattern) [1]. The missing Sn is found at the surface, as β-Sn (XRD spectra, **Fig. 2**). At moderate $T_{RTA} = 350\ ^0C$ the $GeSnSiO_2$ layer with $xSn = ySiO_2 = 9\%$ shows only a very broad diffraction peak, typical for the amorphous phase; the increase of T_{RTA} at 400 ^0C conduces to clearly defined diffraction peaks, and also to an increase of Sn concentration in NCs up to 15 ± 1.1 at. %, in respect to 9 at. % in the whole layer (from SEM-EDX). Increasing the annealing temperature to 450 °C leads to improved crystallinity and also to decreased Sn content in NCs to about 8 ± 0.45 at. %, the rest of the Sn being segregated – **Fig 2a.** These results are in good agreement with those obtained from Raman measurements (**Fig. 2b**). XPS analysis (**Fig. 3**) evidenced that Ge is 50−60% oxidized at the surface for both as deposited and 400 ^0C RTA samples, while Sn shows surface oxidation only after annealing. In the "bulk" (after etching of top 50 nm), both Ge and Sn are essentially not oxidized.

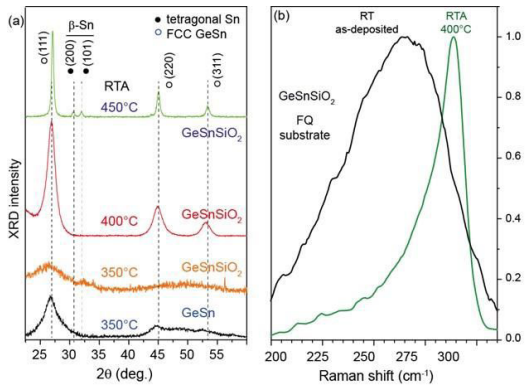

Fig. 2. *(a) Diffractograms of deposited layers after T_{RTA} = 350, 400 and 450 °C in comparison with GeSn sputtered sample annealed at 350 °C; (b) Raman spectra for amorphous and annealed samples deposited at RT.*

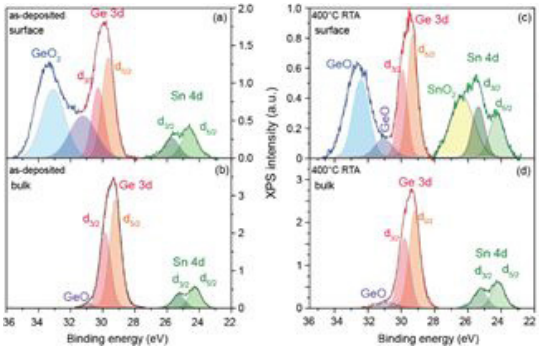

Fig. 3. *XPS spectra and their deconvolution curves measured on $(Ge_{1-x}Sn_x)_{1-y}(SiO_2)y$ with x = y = 9%. (a, b) as-deposited sample; (c, d) after RTA at 400 °C; (a, c) from layer surface; (b, d) after etching top 50 nm.*

The formation GeSn NCs was investigated for samples with different fabrication and processing parameters. We found that the increase of T_{RTA} and T_{sub} have similar effects on nanocrystallization and β-Sn segregation. By annealing, Ge and Sn segregate to form GeSn NCs embedded in the rest of the $GeSnSiO_2$ of less GeSn content. The SiO_2 around GeSn NCs has the role of surface passivation, but it must not electrically isolate the NCs for high photoconduction. The segregation of Ge and Sn is accompanied by their diffusion and oxidation at the film surface during exposure to air.

Because Sn seems to be faster segregated than Ge, the GeSn particles have a higher Sn concentration in the first stage of this process, such as this effect enhances the crystallization. Annealing at higher temperatures results in phase separation of Sn from GeSn crystals due to low miscibility of Ge and Sn. Consequently, the crystallization is increased but GeSn NCs have lower Sn concentration.

Photocurrent measurements were performed on ITO/GeSn NCs in SiO_2/p-Si substrate/Al heterostructure diodes. The spectral photocurrent was measured in photovoltaic regime at zero voltage bias, using chopped monochromatic light. The spectral dependence of the quantum efficiency at 100 K is represented in **Fig. 4** for two samples. For comparison, direct and indirect bandgaps of Ge are indicated by vertical short lines. The largest SWIR extension of the sensitivity up to 2.4 μm was obtained in the sample S5 with $T_{sub} = 200^0$C, and $T_{RTA} = 400^0$C (red line in **Fig. 4**), which does not show β-Sn segregation. In sample S8 with $T_{sub} = 340^0$C and without post-annealing (in blue), the photocurrent is detected up 2.2 μm. Thus, different nanocrystallization parameters can induce differences in film uniformity and NCs size distribution, explaining the variation in spectral responses of S5 and S8 layers.

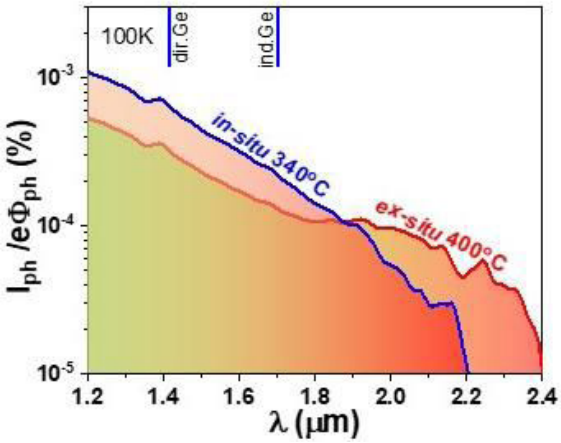

Fig. 4. *Spectral dependence of the quantum efficiency of the photovoltaic current.*

We can conclude that SWIR photosensitivity of the heterojunction of GeSn NCs embedded in SiO2 with Si substrate is well correlated with the fabrication conditions and nanocrystallization particularities. The SWIR extension of the sensitivity up to 2.4 μm was found in a $(Ge_{1-x}Sn_x)y(SiO_2)_{1-y}$ (x ≈ 18% Sn and y ≈ 15% SiO_2) layer deposited at 200 °C that formed GeSn NCs of about 15% Sn after RTA at 400°C.

Reference

[1] A. Slav, C. Palade, C. Logofatu, I. Dascalescu, A.M. Lepadatu, I. Stavarache, F. Comanescu, S. Iftimie, S. Antohe, S. Lazanu, V.S. Teodorescu, D. Buca, M.L. Ciurea, M. Braic, T. Stoica, ACS Appl. Nano Mater. 2, 3626 (2019).

Water stable core-shell ZnO-Cu_xO nanowire arrays for photocatalysis applications

A. Costas, C. Florica, N. Preda, M. Beregoi, A. Kunser, N. Apostol, C. Popa, G. Socol, V. Diculescu, I. Enculescu

Core-shell nanowires represent an interesting path for obtaining new optoelectronic devices [1]. Zinc oxide is a n-type wide band semiconductor (3.3 eV) while copper oxide is a p-type narrow band semiconductor (1.74 eV), these two metal oxides forming a p-n staggered gap radial heterojunction. The use of copper oxide as shell has 2 major advantages: to harvest a higher range of solar energy for pollutants removal and to overcome the zinc oxide nanowires dissolution in water based solutions. Water stable photocatalysts were prepared in two simple steps: ZnO nanowire arrays prepared by thermal oxidation in air were covered with a Cu_xO thin film by magnetron sputtering. **Fig. 1** reveals the FESEM and TEM images of the ZnO-Cu_xO core-shell nanowire arrays.

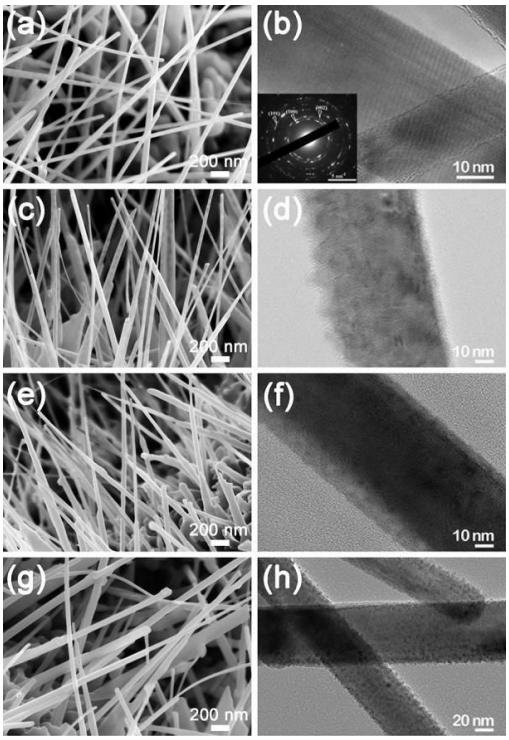

Fig. 1. *FESEM (left side) and TEM images (right side) of the obtained (a, b) ZnO nanowires, (c, d) ZnO–Cu_xO_1, (e, f) ZnO–Cu_xO_2 and (g, h) ZnO– Cu_xO_3 core-shell nanowires. Inset: SAED pattern proving the ZnO wurtzite phase*

Fig. 1 evidences that the ZnO nanowires have diameters of about 30 nm and the ZnO-Cu_xO nanowires have a Cu_xO shell thickness of about 5 nm for ZnO-Cu_xO_1, 10 nm for ZnO-Cu_xO_2 and 15 nm for ZnO-Cu_xO_3.

Fig. 2 shows a TEM image and the EDX elemental map of the ZnO–Cu_xO_3 core-shell nanowires. Thus, demonstrating the radial heterojunction between ZnO and Cu_xO in the core-shell nanowire by evidencing the spatial distribution of all constituting elements having Zn K-edge signals emitted from the core area, Cu K-edge signals emitted at the edges and O K-edge signals uniformly distributed along the nanowire.

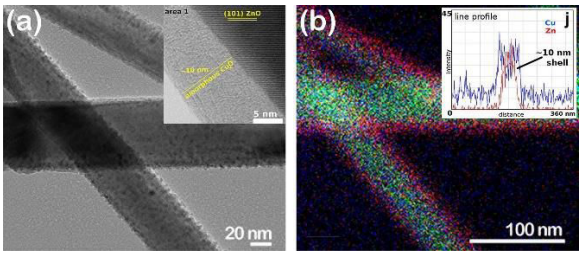

Fig. 2. *(a) TEM image and (b) EDX elemental map of ZnO–Cu_xO_3 core-shell nanowires. Inset: EDS line profile analysis by STEM.*

Fig. 3 (**a-up, c and e**) exhibits the XRD pattern, reflectance and photoluminescence spectra of the pristine ZnO nanowires, revealing a hexagonal wurtzite crystalline structure, an energy band gap around 3.3 eV and two emission bands, typical for ZnO. The XPS analysis (**Fig. 3** (**b, d and f**)) evidenced the ZnO core of the core-shell nanowires and the Cu_xO shell oxidation state, being a mixture between Cu2O and CuO with a ratio of 3:1 for ZnO–Cu_xO_1 and 1:1 for ZnO–Cu_xO_2 and ZnO–Cu_xO_3. Consequently, the XPS investigations proved the formation of a radial heterojunction between ZnO and Cu_xO in the core-shell nanowire. The XRD pattern (**Fig 3** (**a-down**)) and the Kubelka-Munk representation (Inset) of a Cu_xO layer deposited on Si/SiO_2 substrate revealed the amorphous nature of the Cu_xO film and a band gap of 1.74 eV.

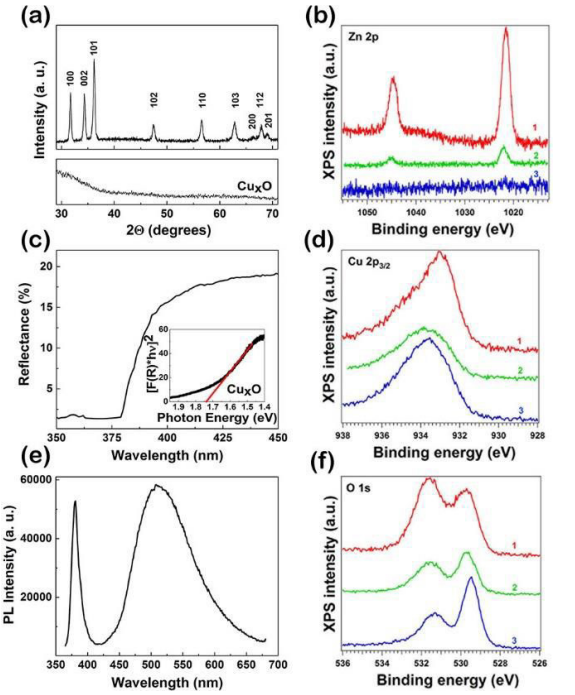

Fig. 3. *(a)-up XRD pattern, (c) reflectance and (d) photoluminescence spectra of the pristine ZnO nanowires and the XPS spectra of the (b) Zn 2p levels, (d) Cu 2p3/2 levels and (f) O 1s levels for the ZnO-Cu$_x$O core-shell nanowires; (a)-down XRD and (b-inset) Kubelka-Munk representation of the Cu$_x$O layer grown in the same conditions as ZnO-Cu$_x$O_3 sample.*

The EIS investigations (**Fig. 4** (**a**)) proved that all the samples have 3 main regions and are suitable for charge transfer processes. The first region (100 kHz - 100 Hz corresponds to the electron transfer and diffusion process, the second region (100 Hz - 0.25 Hz) has a semi-circular part due to pure electron transfer and the third region (below 0.25 Hz) being an inverse loop due to an inductive component. Also the spectra are fitted with an equivalent electrical circuit (**Fig. 4** (a Inset)). The kinetic curves for photocatalytic degradation of MB, under UV irradiation show that the degradation of MB by ZnO occurs with 54% efficiency, for Cu$_x$O thin film with 4% efficiency and for ZnO-Cu$_x$O_1, ZnO-Cu$_x$O_2 and respectively ZnO-Cu$_x$O_3 with 35%, 47% and 57% efficiencies. The FESEM images of the ZnO (**Fig. 4** (c)) and ZnO-Cu$_x$O_3 nanowires (**Fig. 4** (d)) confirm the dissolution of ZnO nanowires and the stability of the ZnO-Cu$_x$O_3 nanowires in water based solutions under UV-light irradiation. The MB photocatalysis degradation mechanism under UV irradiation for ZnO and ZnO-Cu$_x$O_3 nanowires (Insets c and d) takes into account the ZnO dissolution in aqueous based solutions and the formation of a staggered gap heterojunction between ZnO and Cu$_x$O, increasing the photogenerated charges separation at the interface.

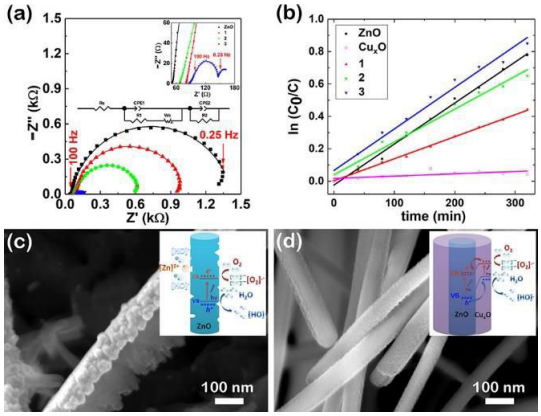

Fig. 4. *(a) Nyquist representation of the EIS and (b) kinetic curves for photocatalytic degradation of MB, under UV irradiation for ZnO nanowires, ZnO-Cu$_x$O_1, ZnO-Cu$_x$O_2, ZnO-Cu$_x$O_3 nanowire arrays and Cu$_x$O film. FESEM images of the (c) ZnO and (d) ZnO-Cu$_x$O_3 nanowire arrays after the photocatalysis experiment. Insets: (a) equivalent electrical circuit fitting the spectra (c, d) the MB photocatalysis degradation mechanism under UV irradiation.*

ZnO–Cu$_x$O core-shell nanowires represent promising water stable photocatalysts. For an optimum thickness of the Cu$_x$O shell, the ZnO-Cu$_x$O nanowires are protected against dissolution in water based solutions enhancing in the same time their photocatalytic properties under UV irradiation due to the formation of a radial heterojunction between the 2 metal oxides.

Funding from Core Program, contract No. PN18-11; PN-III-P2-2.1-PED-2016-1249; IDEI 124/2017, 12PFE/2018; NANOBIOSURF-SMIS 103528.

Reference

[1] C. Florica, A. Costas, N. Preda, M. Beregoi A. Kuncser, N. Apostol, C. Popa, G. Socol, V. Diculescu, I. Enculescu, "Core-shell nanowire arrays based on ZnO and Cu$_x$O for water stable photocatalysts", Scientific Reports 9, 17268 (2019).

$(Ba,Sr)TiO_3$ solid solutions sintered from sol-gel derived powders: An insight into the composition and temperature dependent dielectric behavior

Roxana Elena Patru, Constantin Paul Ganea, Catalina-Andreea Stanciu, Vasile-Adrian Surdu, Roxana Trusca, Adelina-Carmen Ianculescu, Ioana Pintilie, Lucian Pintilie

Of all ferroelectric oxides, barium titanate (BT) is one of the most common and studied materials alongside its solid solutions. The composition dependent, non-linear and hysteretic dielectric properties allow BT-based materials to bring multi-functionality suitable for a large number of microelectronics applications.

In the present study, several barium strontium titanate ($Ba_{1-x}Sr_xTiO_3$) compositions having the ferroelectric-paraelectric phase transition located near the room temperature were investigated via broadband impedance spectroscopy [1]. Our results based on the complex analysis on the low field dielectric properties meant to elucidate the critical role played by temperature in the ferroelectric state or close to the Curie point.

The Curie point of the investigated compositions was tailored by Sr addition [2], so that $Ba_{1-x}Sr_xTiO_3$ with $x = 0.4$ and $x = 0.375$ exhibit a paraelectric behavior at RT, $x = 0.35$ is facing the ferroelectric to paraelectric phase transition at RT, $x = 0.325$ and $x = 0.3$ are in the ferroelectric state at RT.

The dielectric properties of BST specimens were registered by an Alpha-A Novocontrol low frequency impedance-meter system in the frequency range of 10^2Hz-10^6Hz. Data were recorded following a protocol for heating and cooling with a rate of 0.6°C*min^{-1} in the temperature range of -50^{0}C-100^{0}C. XRD and FESEM tested the purity phase for dense and uniform microstructures. **Fig. 1** illustrates a schematic representation of the influence of Sr concentration on the Curie point in the case of the proposed compositions.

The average grain size and thermal hysteresis evolves with Sr addition following a downward trend. BST ceramics present relative density values ranged between 87 – 92% and grain sizes decrease from 15.6 μm in BST30 down to 2.1 μm in BST40.

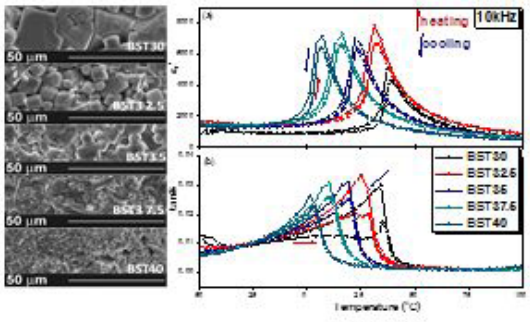

Fig. 1. *Microstructural characterization of BST ceramics and the temperature dependence of the dielectric constant (a) and losses (b) represented for a ixed frequency of 10kHz*

All the specimens fully satisfy the classical Curie- Weiss law in the paraelectric state. The diffuseness degree and the peak broadening were determined by using a modified Curie– Weiss law based on the data measured during the different thermal cycles as a function of frequency in accordance with the Sr content.

The frequency dependence of the dielectric constant disclose particular information about the electrical polarization mechanisms and dielectric relaxations inside the BST ceramic specimens.

The ferroelectric domains below the Curie point and the polar fluctuations near the Curie point caused by atoms, both stand out through dielectric anomalies in the frequency dependence of the complex dielectric constant.

Fig. 2 shows the frequency dependence of the complex dielectric constant at room temperature. Values of the dielectric constant in **Fig. 2** (a) are specific to compositions in different phases ($x = 0.375$ and 0.4 in the cubic paraelectric, $x=0.3$ in the ferroelectric state, $x=0.325$ and 0.35 in the transition proximity) at room temperature with enhanced dielectric relaxations in the whole frequency range (b).

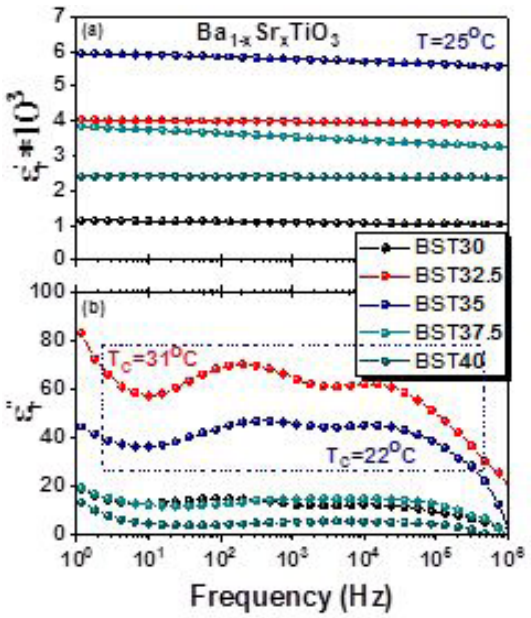

Fig. 2. *The real part (a) and the imaginary part (b) of the complex dielectric constant at room temperature, as a function of frequency*

Withal, the enhancement of the loss factor in low frequency range (**Fig. 2.** (b)) is origin of the dc conduction and reflects accumulation of spatial charges with increased mobility in the grain boundary regions process. In grains, the ferroelectric domains alignment evolves with temperature below the Curie point, after which they completely disappear.

At the boundaries and interfaces, the accumulated spatial charges are released when temperature increases highlighting thermally activated processes (07- 0.77eV). The cumulative complex contributions coming from different sources were divided by performing impedance spectroscopy analysis and by fitting the experimental data to a specific equivalent circuit including two parallel R–C circuits connected in series. Oxygen vacancies in $SrTiO_3$ donate excess of electrons, and the Ti sites trap them at low temperatures. With temperature increase, they become mobile and produce effects through a strongly increasing of conductivity in the high frequency region.

The interaction degree between mobile ions and the media was calculated by using the Jonscher power law on the frequency dependence of the electrical conductivity. Both the computing parameters and the circuit elements exhibit a strong temperature dependence in the transition region that can lead to further clarifications on the fundamental phenomenon responsible for conduction and relaxation processes in this type of ceramics. **Fig. 3** shows the Bode plots fitted using the equivalent circuit composed by series of R-C ele

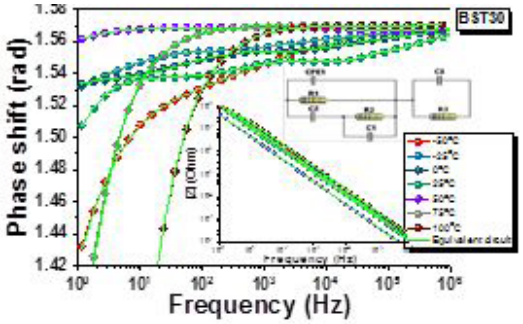

Fig. 3. *Phase shift and complex impedance as a function of frequency verified by the proposed equivalent circuit Sr addition is a powerful way to fine-tune the multifunctional properties of BT ceramics. The change in the transition temperature comes together with a more dispersive nature of the dielectric properties when Sr concentration increases.*

The work was carried out in the frame of the PCCF 16/2018 and PN–III–P4-ID-PCE-2016-0072 grants and of the PN19-03 Core Program of NIMP.

References

[1] R. E. Patru, et al. (2020) Ceram. Int. vol. 46 (2020) pp. 4180-4190 doi:10.1016/j.ceramint.2019.10.136
[2] A. Ianculescu, et al., Ceram. Int., 42 (2016), pp. 10338-10348, 10.1016/j.ceramint.2016.03.152

Synthesis, Characterization, and Antimicrobial Activity of Zinc-Doped Hydroxyapatite and Magnesium-Doped Hydroxyapatite Suspensions

D. Predoi, S. L. Iconaru, G.E. Stan
in collaboration with
M.V. Predoi (University Politehnica Bucharest, Romania)
N. Buton (HORIBA Jobin Yvon S.A.S., Longjumeau, France)
M. Motelica-Heino(ISTO, UMR 7327 CNRS Université d'Orléans)
R. Guegan (Faculty of Science and Engineering, Global Center for Science and Engineering, Waseda)

In the last years, due to an alarming increase in bone-related conditions, the need for regenerative or replacement tissues has become of interest at a global scale. This has driven both the scientific and industrial communities to extend their efforts on developing successful and cost-effective materials that could replace damaged tissue, organs and also improve their functions. Hydroxyapatite, was greatly studied for bone regeneration applications due to its similarity to the human hard tissue. In order to improve HAp properties, researchers have turned their attention towards the effects induced by single ionic substitutions in the HAp lattice[1,2]. In this context, our work aims to provide insight on the physico-chemical and biological properties as well as the stability of suspensions of zinc and magnesium doped hydroxyapatite nanoparticles synthesized by an adapted chemical co-precipitation method. The XRD results of the zinc doped hydroxyapatite doped with various zinc $x_{Zn} = 0$; $x_{Zn} = 0.07$, and $x_{Zn} = 0.2$, (HAp, 7ZnHAp and 20ZnHAp) and magnesium doped hydroxyapatite with x_{Mg}=0.1 (10MgHAp) samples are depicted in **Fig .1** (left, right) [1,2].

The results of the XRD patterns of ZnHAp samples (**Fig.1** left) highlighted that between the experimental data and the calculated data, a good similarity was observed. Following the use of the Rietveld refining method for the XRD analysis of the obtained samples, a single phase corresponding to the hexagonal hydroxyapatite was revealed. The calculated lattice parameters of HAp, 7ZnHAp, and 20ZnHAp samples are in good accord with the standard data of a = b = 9.418 Å, c = 6.884 Å. The average crystallite sizes decreased with the increase of zinc concentration from 23.18 ± 0.3 nm for HAp sample to 19.38 ± 0.5 nm and 9.96 ± 0.8 nm for 7ZnHAp and 20ZnHAp sample, respectively. For the analysed samples, an increase in the network parameter "a" was observed with increasing zinc concentration in the sample, while for parameter "c" a decrease was observed [1].

Furthermore, all the diffraction maxima recorded in the case of the 10MgHAp sample are associated to a hexagonal hydroxyapatite phase (ICDD-PDF4: 00-009-0432), namely to the 002, 210, 211, 112, 300, 310, 222, 213, 004, and 304 crystal plane reflections. There was no evidence (at the sensitivity limit of the machine) of residual phases or segregated compounds [2].

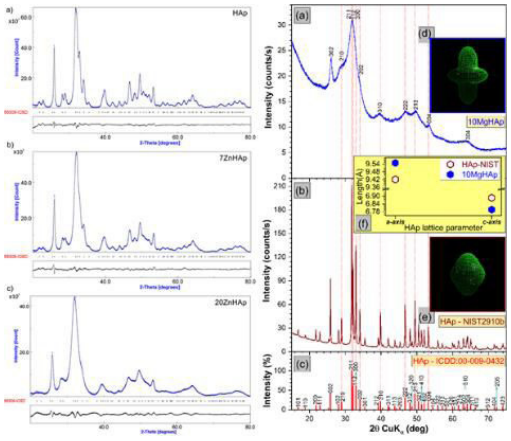

Fig. 1. *Rietveld refinement fit of powder XRD data of hydroxyapatite (HAp) (a), 7ZnHAp (b), and 20ZnHAp (c). (left) [1]; The comparative XRD patterns of the (a) 10MgHAp and (b) NIST SRM2910-b samples with respect to the (c) ICDD-PDF4: 00-009-0432 reference file of hexagonal hydroxyapatite. (right) [2].*

Additional information about the ZnHAp ($x_{Zn} = 0$, $x_{Zn} = 0.07$, and $x_{Zn} = 0.2$) particle suspensions, was obtained through ultrasound measurements. The results are presented in **Fig. 2** [1]. The ultrasonic signals have been recorded every 5 s, and 5 to 7 echoes were recorded. The results have shown that the signals were identical since during the 40 s, the fluid properties remained unchanged (**Fig. 2**) [1].

The results revealed that the stability parameter has decreased from 0.00000 ± 1e1E-6 in reference fluid to 0.00066 s^{-1} in sample HAp. Moderate stability was observed in sample 7ZnHAp when the stability parameter was equal to 0.00021 $s^{-1.}$ A very stable parameter of only 0.00007 s^{-1} was determined for sample 20ZnHAp.

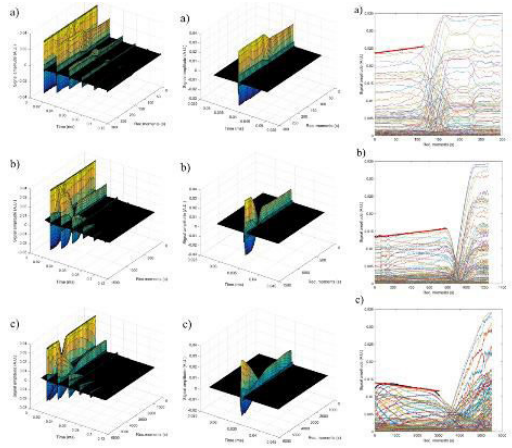

Fig. 2. *Signals recorded for (HAp) (a), 7ZnHAp (b), and 20ZnHAp (c). (left).The same 2nd echo of hydroxyapatite (HAp) (a), 7ZnHAp (b), and 20ZnHAp (c) samples selected for investigation. (middle) Evolution in time of the amplitudes of the selected echo, for the samples hydroxyapatite (HAp) (a), 7ZnHAp (b), and 20ZnHAp (c) (right) [1].*

The stability assessment of 10MgHAp suspensions by ultrasound measurements was also performed and the results are depicted in **Fig. 3 [2].**

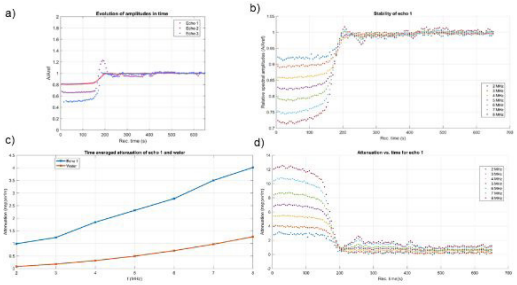

Fig. 3. *Relative amplitudes evolution vs. the recording moments (a). Spectral amplitudes relative variation vs. time, for the first echo (b). Attenuation vs. time for the spectral components of Echo 1(c). Attenuation vs. frequency for the first transmitted echo of the suspension (blue) and the reference fluid (red) (d). [2].*

The results have revealed that the attenuation is considerably higher (1–4 nepper/m) for the sample compared to 0.3–1.3 nepper/m for the reference fluid and that during the asymptotic sedimentation period (after 200 s in this case), the attenuation coefficients tend towards stable values, which correspond to those in the reference fluid.

In addition, the antibacterial activity of the ZnHAp and MgHAp samples were investigated using reference bacterial strains. The results of the antibacterial assays are presented in **Fig. 4** [1,2].

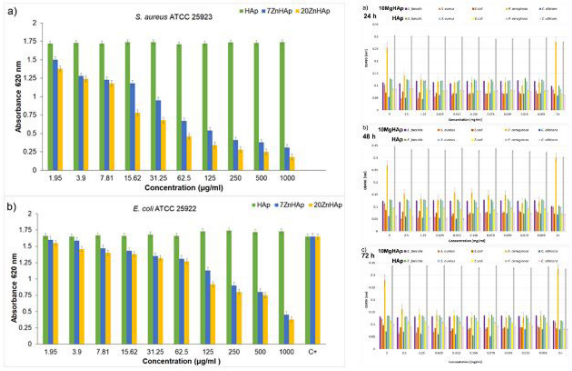

Fig. 4. *S. aureus ATCC 25923 (a) and E. coli ATCC 25922 (b) in the presence of ZnHAp with x_{Zn} = 0, x_{Zn} = 0.07 or x_{Zn} = 0.2 (left) [1]. The dynamics of the antimicrobial activity of 10MgHAp and HAp against E. faecalis ATCC 29212, S. aureus ATCC 25923, E. coli ATCC 25922, P. aeruginosa ATCC 27853, and C. albicans ATCC 90029 microbial cells after (a) 24 h, (b) 48 h, and (c) 72 h of incubation (right) [2].*

The antibacterial assays have shown that the antibacterial properties of of ZnHAp solutions were influenced by the zinc content. Moreover, the results revealed that S. aureus ATCC 25923 was more sensitive than E. coli ATCC 25922 to ZnHAp solutions compared to the control. Furthermore, the 10MgHAp suspensions demonstrated antimicrobial efficacy against P. *aeruginosa*, S. *aureus*, and C. *albicans* microbial strains [1,2].

These results bring new contributions on the stability and biological properties of HAp, ZnHAp and MgHAp materials that could be successfully used in biomedical applications.

The authors acknowledge the Romanian Ministry of Research and Innovation through the following projects: PN-III-P1-1.2-PCCDI-2017-0629, Contract No. 43PCCDI/2018, PCCDI–UEFISCDI, project number PN-III-P1-1.2-PCCDI-2017-0062/contract no. 58/component project no. 2), Core Program funded by Romanian Ministry of Research and Innovation (21N/2019).

References

[1]. Predoi, D.; Iconaru, S.L.; Predoi, M.V.; Motelica-Heino, M.; Guegan, R.; Buton, N. Nanomaterials 2019, 9, 515.

[2]. Predoi, D.; Iconaru, S.L.; Predoi, M.V.; Stan, G.E.; Buton, N. Nanomaterials 2019, 9, 1295.

Nanoclustered Pd decorated nanocrystalline Zn doped SnO_2 for ppb NO_2 detection at low temperature

A. Stanoiu, C. Chica, C.E. Simion, A.C. Kuncser, A.M. Vlaicu, M. Stefan,
D. Ghica, O.G. Florea, I.F. Mercioniu,
in cooperation with
S. Somacescu[1]
1"Ilie Murgulescu" Institute of Physical Chemistry, Romanian Academy, Bucharest, Romania

In this report, nanoclustered multi-valence Pd (2mol.%) was used to decorate Zn doped SnO_2 (10mol.% Zn) in such a way to improve its sensing performances. Zn doped SnO_2 built from nanoparticles was prepared by a hydrothermal method using a non-ionic surfactant - Brij52 and Tripropylamine (TPA) as co-templates. The coexistence of a mixture of valence states (Pd^0, Pd^{2+} and Pd^{4+}) was highlighted on the surface of the screen printed in thick layers: SnO_2, SnO_2_10Zn and Pd/SnO_2_10Zn. Several aspects have been followed regarding the Zn and Pd dispersion into the SnO_2 matrix: the large scale and low scale morphology (SEM and TEM/HRTEM) in relation with the synthesis route, the obtained crystallographic phases (XRD, SAED) and the way in which the Zn^{2+} ions are inserted into the SnO_2 structure (XRD, XPS, EPR), the spatial distribution of the added chemical elements, Zn and Pd (SEM, STEM, EDS). The samples show similar morphological features (**Fig. 1a**). The electron diffraction patterns from different selected clusters of nanoparticles may contain additional diffraction spots along with the SnO_2 rings, indicating the presence of a second minor crystallographic phase.

Such a diffraction pattern is presented in **Fig. 1b** where the additional diffraction spots have been identified and assigned to a cubic substoichiometric palladium oxide, $Pd_{3.5}O_4$, space group Pm-3n (ICDD file 04-005-4750). The presence of Pd and Zn has been confirmed by EDS measurements where the quantitative analysis indicates an average ZnO concentration of 7.4 mol%, while Pd shows an uneven distribution, with local concentration values varying between 1-5 mol% (taking Pd as PdO in the quantification of the EDS spectra). This uneven distribution is confirmed by the chemical mapping of Pd, obtained by STEM-EDS (**Fig. 1** c-f), which indeed reveals the clustering of Pd-rich nanoparticles in bunches of several tens of nanometers, decorating the nanoporous Zn-doped SnO_2 powder [1].

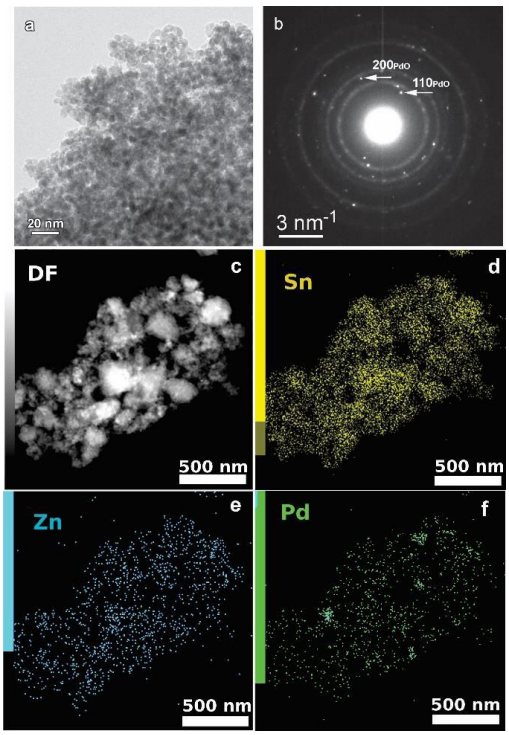

Fig. 1. *(a) Low magnification TEM image of the Pd/SnO_2_10Zn sample showing nanograins in the range of 5 nm size; (b) SAED pattern showing the substoichimoetric oxide of palladium; (c)-(f) STEM-DF image and the corresponding elemental maps for Sn, Zn and Pd for a typical cluster of nanograins showing the uniform distribution of Zn and clustering tendency for Pd.*

As a first sensing investigation step, the sensors were subject to sensitivity screening for 3 ppm (detection limit), over a wide range of operating temperatures (100-300°C), under 50%RH background conditions (infield conditions). Sensor response was evaluated as the ratio of resistance: $S=R_{NO2}/R_{Air}$ [2]. As can be seen in **Fig. 2** the sensing responses exhibit a maximum at different temperatures except the case of pure SnO_2 based gas sensor, suggesting that doping of SnO_2 with Pd and Zn, represents an effective way to improve

the NO_2-sensing performances, at low operating temperatures.

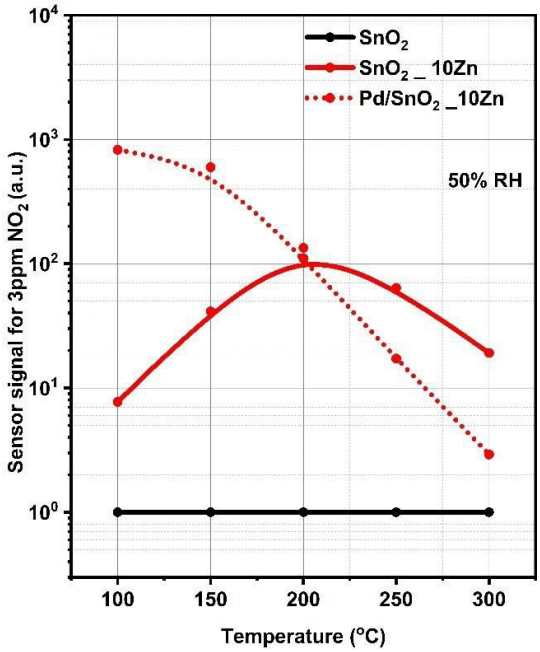

Fig. 2. *NO_2 sensor signal screening over a wide range of operating temperatures*

Since the maximum sensor signal was attained at 100°C, we pursue the evaluation of the sensor signal dependence with respect to the NO_2 concentrations (**Fig. 3**), highlighting that the interaction mechanism strongly depends on the intrinsic properties of the investigated sensors. In this respect, the possible surface interaction mechanisms are:

$$NO_2 + M_{lattice} + e^- \rightarrow M_{lattice} - NO^-_2 \quad (1)$$

which represent the direct ionosorption of NO_2 on the sensitive surface and:

$$NO_2 + V^o_o + e^- \rightarrow O^-_o + NO \quad (2)$$

as dissociative adsorption of NO_2 onto surface leading to the healing of a free oxygen vacancy and presence of NO as secondary product in the downstream gas [3].

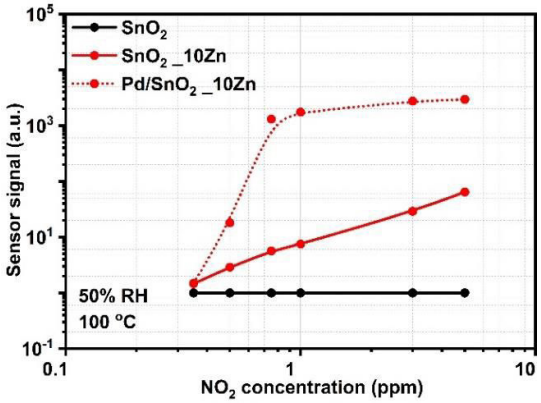

Fig. 3. *Log-log plot of the sensor signals over a wide range of NO_2 concentration*

To complete the gas sensing investigation, cross-sensitivity effects have been analysed for the most sensitive material (**Fig. 4**).

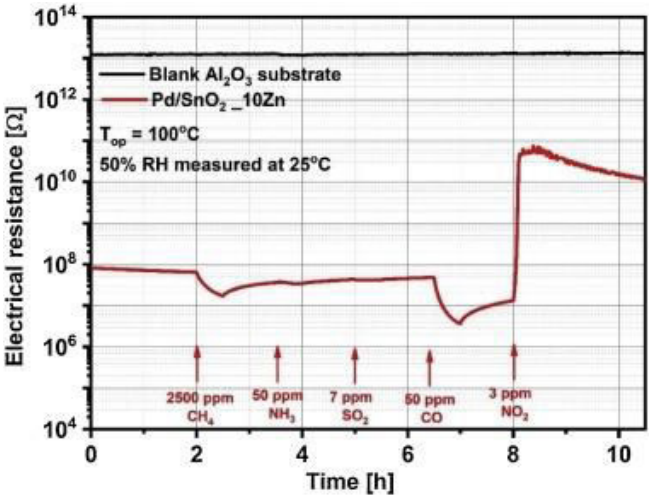

Fig. 4. *Selective sensitivity analysis of Pd/SnO_2_10Zn sensitive material.*

Through this study we could harvest the specific role of the loadings towards selective detection of low NO_2 concentrations, at low operating temperature, for infield conditions.

References

[1] S. Somacescu, C. Ghica, C.E. Simion, A.C. Kuncser, A.M. Vlaicu, M. Stefan, D. Ghica, O.G. Florea, I.F. Mercioniu, A. Stanoiu, Sens. Actuators B: Chem. 294 (2019) 148-156.

[2] B. Kamp, R. Merkle, J. Maier, Sens. Actuators B: Chem. 77 (2001) 534-542.

[3] M. Breedon, M.J. S. Spencer, I. Yarovsky, J. Phys. Chem. C, 114 (2010) 16603-16610.

Comparative method preparation study for Mn and Ce modified Alumina Oxides

Ștefan Neațu, Mihaela M. Trandafir, Adelina Stănoiu, Ovidiu G. Florea, Cristian E. Simion, Lucia N. Leonat, Mihaela Florea, Florentina Neațu
in collaboration with
Cornel Cobianu, Marin Gheorghe
NANOM-MEMS SRL, G. Cosbuc 9, 505400 Rasnov, Romania

Complete oxidation of carbon-based fossil fuel in industrial chemistry and the automotive industry based on internal combustion engines is nowadays one of the biggest scientific challenges.

In these aspects, the purpose of this work was to perform extended research on the catalytic performances of CeO_2–MnO_x composite deposited/incorporated within a lanthanum-modified alumina matrix for CH_4 combustion as function of three syntheses methods, such as: co-precipitation, incipient impregnation and citrate-based sol-gel. Thus, for the incipient impregnation method a commercially available 4 wt.% La_2O_3–Al_2O_3 support from Puralox was used, while for the rest of the syntheses, the precursors of all components were mixed and precipitated simultaneously. In this way, the role of bulk versus surface modification of La-doped Al_2O_3 with Mn and Ce on catalytic activity was investigated.

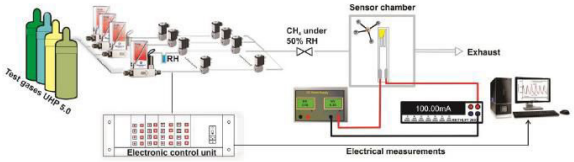

Fig. 1. *The setup for catalytic evaluation*

To evaluate the catalytic properties of the above catalysts, a self-heated catalytic micro-converter was devised. This device consists of an alumina strand above which a resistive platinum meander was deposited by thick film technology. Further, above this future heater, our catalysts were deposited. This way, we were able to mimic the catalytic combustion process of methane in a real catalytic converter. By monitoring the voltage and current through the platinum heater in the absence or presence of methane, the thermal effects of catalytic combustion were indicated in the electric current variation (**Fig. 1**). Thus, we were able to evaluate and discriminate between different synthetized catalysts.

As expected, the catalytic properties were affected by the adopted preparation techniques. Geometry and redox state of the metal cations are among the several factors that might alter the strength of the oxygen chemical bondings near the catalytic sites, thus affecting their activity.

The three preparation methods adopted in this study allowed us to investigate the effect of accessible active centre distribution on the surface of the support or intimately mixing of the catalyst at the bulk level with the support. For instance, in the case of co-precipitation (7Ce3Mn/10LaAl_pp) and citrate-based sol-gel (7Ce3Mn/10LaAl_cit) methods, the precursors of the support were mixed with the precursors of the active species and therefore a bulk mixing between the active species and the support was obtained. In the meantime, to obtain the impregnated catalyst (7Ce3Mn/10LaAl_imp) the active species were deposited only on the surface of the commercial support (Puralox) with the scope to obtain the well dispersed active species on the surface. This material preserves a high surface area (118 m^2/g) with respect to initial value of the support (150 m^2/g), as shown by our BET analysis.

In order to compare the behavior of a bulk versus surface modification of alumina with Mn and Ce based oxides, a higher consideration was given to the interaction between Mn and Ce oxides and support. Thus, for the impregnated sample, the XRD pattern indicates the presence of a mixed phase of Ce_2MnO_6 on the surface. Such a mixed phase may contribute locally to increased defects and further distortions of the atomic architecture of the catalytic sites and thus may further increase the catalytic activity of this type of supported catalyst.[1]

On the other hand, the H_2-TPR and XPS data clearly demonstrate the interaction of Mn and Ce oxides with alumina, on the surface or in bulk. In particular, H_2-TPR analyses evidenced the presence of the same type of reducible species for all prepared materials (**Fig. 2**).

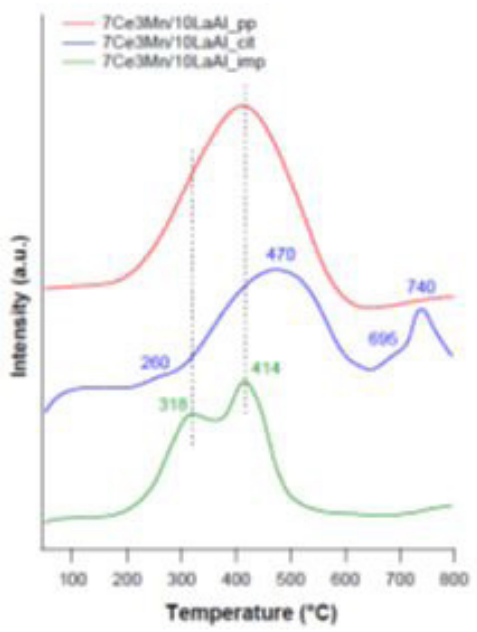

Fig. 2. *H_2-TPR profiles of the samples*

However, taking into account the shift in the reduction temperature and the lowest onset, it can be inferred that impregnated sample can be more active than the bulk ones, due to the higher mobility of the oxygen species and lower interaction of Mn and Ce oxides with the support. Moreover, the presence of more reducible sites on the impregnated sample surface facilitate the adsorption and activation of CH_4 during the catalytic reaction and thus enhance its catalytic activity. This behavior is in agreement with the theoretical predictions obtained by density functional theory, which showed a direct correlation between reaction energy for catalytic methane oxidation and surface reducibility of doped CeO_2. From XPS data, the higher ratio between O bonded to Mn and Ce and the O bonded to Al for the impregnated sample indicates that the oxygen species related to Mn and Ce are more active for CH_4 combustion and have moderate interaction (derived from H_2-TPR data) with the support during the reaction. Thus, surface deposition of CeO_2–MnO_x is much more desirable than the bulk one.

The presence of reducible Ce^{4+} and Mn^{4+} at the surface of the impregnated sample is an indication of the Mars Van Krevelen mechanism.

In such mechanism, the oxidation of CH_4 takes place using the weakest bonded oxygen from the lattice, in this particular case bonded to manganese and cerium cations, followed by the reduction of Ce^{4+} and Mn^{4+} to Ce^{3+} and Mn^{3+}, respectively. Furthermore, the oxygen from the gaseous phase reoxidize the surface and assure another catalytic cycle.

In agreement with the above catalytic properties, the highest conversion rate was attained by the self-heated catalytic micro-converter covered with the impregnated catalyst. An additional explanation for this increased catalytic activity might be related to the increased diffusion of both oxygen and CH_4 toward catalytic sites due to higher pore sizes found for this impregnated catalyst.

In conclusion, by means of an extensive material characterization, it was shown that surface modification of a commercial 4 wt. % La_2O_3–Al_2O_3 support with more accessible CeO_2–MnO_x catalyst may be a promising direction for pushing further the research on complete oxidation of methane at lower temperatures, a major challenge for today's research.

Reference

[1] S. Neaţu, M. M. Trandafir, A. Stanoiu, O. G. Florea, C. E. Simion, L. N. Leonat, C. Cobianu, M. Gheorghe, M. Florea, F. Neaţu, Materials 12, 1771 (2019).

The influence of the nanocrystals size and surface on the Yb/Er doped LaF_3 luminescence properties

C.E. Secu, E. Matei, C. Negrila and M. Secu

Rare-earth doped nanomaterials showing efficient up-conversion (UC) luminescence (i.e. near-infrared (NIR) conversion into the visible spectral range) have proposed as fluorescent labels for various bioimaging and regenerative medicine ([1] and references therein). Such applications require a functionalization of their surface by anchors, in order to add functional ligands of biomedical interest, and an improvement of their dispersion stability. Moreover, UC efficiency is dramatically influenced by the nanocrystals size effects [2] and different rare earths ions are present at the *surface* and *inside* the nanocrystals, with different environments [3]. Therefore, a proper and deeper knowledge of the nanoparticles sizes and surface related influence on their optical properties is needed [4,5].

For the preparation of Yb(4%), Er(1%) doped LaF_3 nanocrystalline powders we used chemical precipitation technique at room temperature mediated by ethylene glycol acting as both solvent and stabilizer; the resulting powder was annealed in subjected air at different temperatures [4].

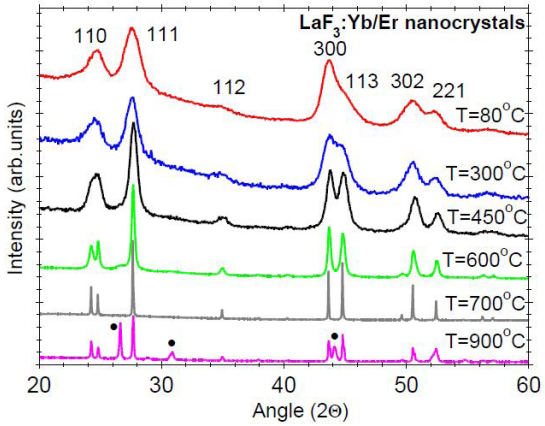

Fig. 1. *Normalized XRD patterns of the LaF_3:Yb/Er nanopowder annealed at indicated temperatures; LaOF phase is shown by dots.*

The XRD pattern (**Fig. 1**) of the dried powder sample showed the characteristic diffraction peaks of the LaF_3 crystalline phase (JCPDS 32-0483); smaller LaOF crystalline phase have been observed after 900 °C annealing.

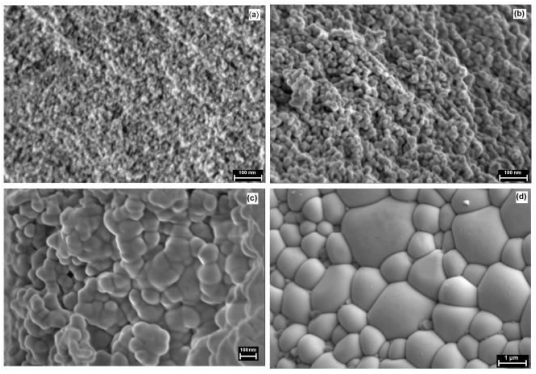

Fig. 2. *SEM images of the LaF_3:Yb/Er as-prepared nanopowder (a) and after 450 °C (b), 600 °C (c), 700 °C (d) annealing*

Electron microscopy (SEM)-**Fig2** measurements have shown a weak increase of nanocrystals up to about 12 nm for low temperatures, described by the Ostwald ripening crystal growth mechanism and an agglomeration processes above 600 °C.

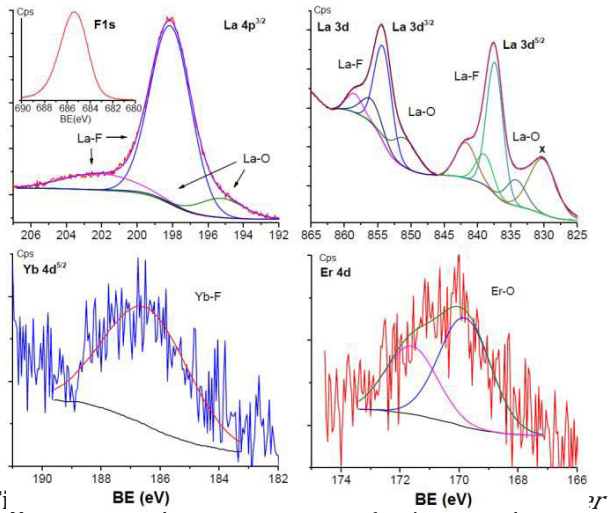

Fi *annealed at 450°C*

X-ray photoelectron spectroscopy (**Fig. 3**) indicated the formation of the LaF_3 nanocrystalline phase: characteristic La ($La3d_{5/2}$, $3d_{5/2}$) peaks and F ($F1_{s1/2}$) peaks at around 837, 851 and 685 eV, respectively. A La and Er oxidized thin layer of about 1 nm at the nanocrystals *surface* was revealed whereas Yb ions are found to be bonded with fluorine ions.

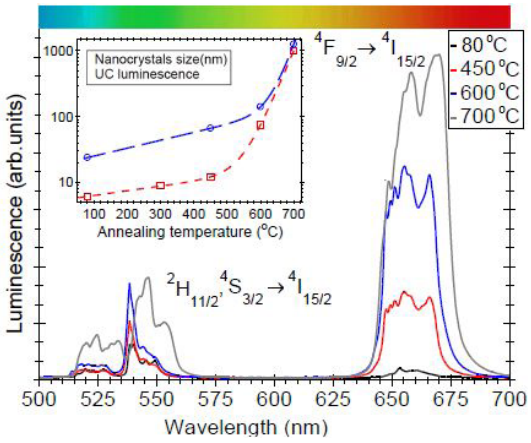

Fig. 4. *UC luminescence spectra recorded on LaF_3:(Yb,Er) powder samples and the nanocrystals size dependence on the annealing temperature (inset).*

Under 980 nm laser light pumping, the annealed samples showed green (($^2H_{11/2}$, $^4S_{3/2}$) → $^4I_{15/2}$) and red ($^4F_{9/2}$ → $^4I_{15/2}$) UC luminescence due to the Er^{3+} ions; it shows a similar dependence as the nanocrystals size, thereby suggesting a close relationship (**Fig. 4-inset**). Subsequent annealing treatments promoted a progressive enhancement of UC luminescence due to the reducing of the quenching effects of the surface and an increase of the fluorine bonded Er-ions fraction (as Yb-Er pairs of ions) involved in the UC luminescence.

The broad shape of the thermoluminescence (TL) curves recorded for smaller nanocrystals (of about 10 nm) were assigned to recombination of trap defects associated with surface states and within the oxidized surface layer. For very small particles, the high ratio of the ions at the surface (with unsaturated coordination) and the loss of such periodicity on the surface due to the lack of atoms that result in structural modifications (required for charge compensation) are mainly responsible for charge carrier trapping.

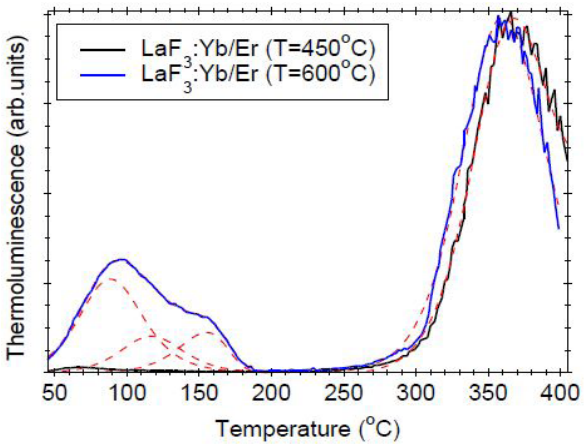

Fig. 5. *Normalized TL curves recorded after X-ray irradiation of LaF_3:Yb/Er nanopowder and deconvolution into single peaks (dotted curves)*

For larger nanocrystals (100-200 nm), the TL curves are complex and composed by several peaks assigned to the recombination of trap defects inside the LaF_3 lattice (at 88 °C, E=0.7 eV activation energy)- **Fig. 5.** They are accompanied by the glow peaks related to the Er and Yb co-dopant ions at 117°C (E=0.8 eV), 155 °C (E=0.8 eV) and 650 °C (E=1.7 eV), respectively. A proper knowledge of the nanosize and surface related effects is crucial for designing new applications and improving the current ones [4,5].

References

[1] X. Qiu, X. Zhu, X. Su, M. Xu, W. Yuan, Q. Liu, M. Xue, Y. Liu, W. Feng, F. Li, Adv. Sci. 6 (2019) 1801834.

[2] X. Xue, S. Uechi, R.N. Tiwari, Z. Duan, M. Liao, M. Yoshimura, T. Suzuki, Y. Ohishi, Opt. Mater. Express 3 (2013).

[3] L.G. Jacobsohn, A. Toncelli, K.B. Sprinkle, C.J. Kucera, J. Ballato, J. Appl. Phys. 111 (2012) 074315.

[4] C.E. Secu. E. Matei, C. Negrila and M Secu J. Alloys Comp. 791 (2019) 1098.

[5] C.E. Secu, Negrila and M Secu J. Phys. D: Appl. Phys. 51 305302 (2018).

Graphitic carbon nitride based photoanodes prepared by spray coating method

Marian Sima[1], Constantin Logofatu[1], Nicoleta Preda[1], Adrian Sima[2], Eugeniu Vasile[3]
1 National Institute of Materials Physics, Bucharest-Magurele ROMANIA
2 National Institute for Lasers, Plasma and Radiation, Bucharest-Magurele, ROMANIA
3 University Politehnica of Bucharest, ROMANIA

Graphitic carbon nitride (g-C_3N_4) is a promising photocatalyst for both hydrogen and oxygen evolution reactions. It has attracted much attention being a metal-free, chemical and thermal stable photocatalyst under light irradiation in aqueous solution. The development of a mild, environmentally friendly deposition method is in great demand to fully exploit g-C_3N_4 in photoelectrochemical (PEC) devices. Our approach to solving this problem was the deposition of g-C_3N_4 nanosheets on different substrates via spray coating method.

Bulk g-C_3N_4 was synthesized by urea pyrolysis in a box furnace. A dispersion of g-C_3N_4 resulted in methanol, 2 mg/ml was prepared by ultrasonication for 5 min followed by an aging process of three days. The dispersion of g-C_3N_4 in methanol was sprayed (**Fig. 1**) on FTO and FTO/TiO_2 substrates heated at 50^{0}C

Fig. 1. *Three different g-C_3N_4 films prepared by spray deposition on FTO substrates. The codes of the prepared and characterized samples are listed in Table 1.*

samples are listed in **Table 1.**

Sample code	Structure description	Deposition time of C_3N_4 films (s)
M1	FTO/C_3N_4	90
M2	FTO/C_3N_4	180
M3	FTO/C_3N_4	270
M4	FTO/C_3N_4	360
M5	Au/C_3N_4	180
M6	FTO/TiO_2	
M7	FTO/TiO_2 + C_3N_4	180

According to the SEM images from **Fig. 2,** the samples consist of small area thin films and aggregates of nanosheets located at micrometer distances from each other on the surface of the substrate. The absorption edge of this few layered g-C_3N_4 (**Fig. 3c**) is about 535 nm, which means a band gap of ~2.32 eV. Compared to band gap value of bulk g-C_3N_4 (~2.7 eV), this band gap value suggests an improved visible light absorption which extends at 535 nm. This change can be attributed to the loss of the long-range order in the crystalline g-C_3N_4 as a result of the disruption of van der Walls and hydrogen bondings and appearance of the nitrogen vacancies as defects during the semiconductor preparation in bulk or film form.

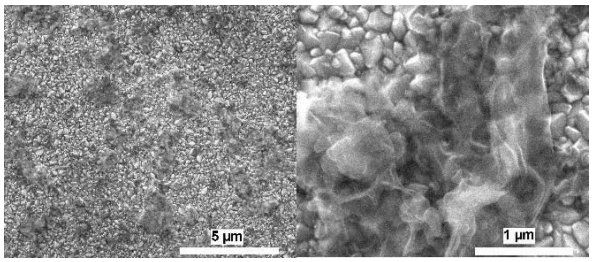

Fig. 2. *SEM images of the sample M3.*

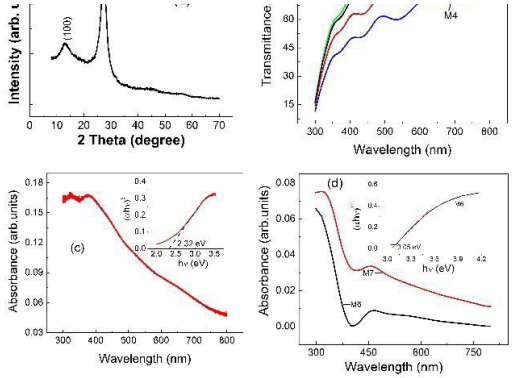

Fig. 3. *a) XRD pattern of bulk C_3N_4; b) Optical transmittance of samples M1, M2, M4 and FTO substrate; c) UV-vis absorption of sample M2; inset-Tauc plot for sample M2; d) UV-vis absorption of samples M6 and M7; inset-Tauc plot for sample M6.*

The UV-vis absorption spectra from **Fig. 3d** show that the absorption edge of the heterostructure TiO_2/g-C_3N_4 (sample M7) was slightly red shifted in comparison with that of the sample M6, absorbing a larger fraction from visible light. The PEC responses of the samples from Table 1 were evaluated by linear sweep voltammetry, impedance spectroscopy (EIS), Mott-Schottky analysis and tests of open circuit voltage decay with time (**Fig.4 and 5 and Tables 2 and 3**).

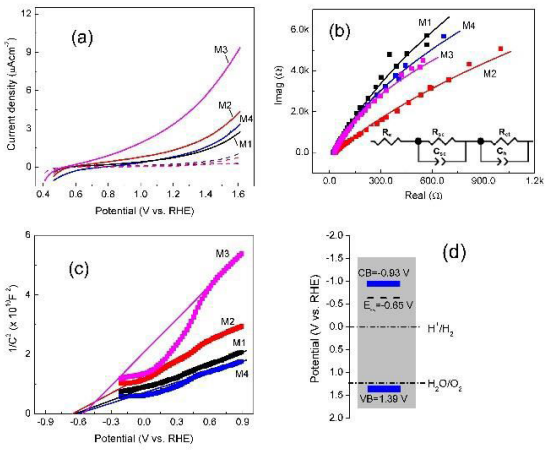

Fig. 4. *(a) J-V characteristics curves obtained under simulated solar illumination, (b) EIS Nyquist plots (inset: equivalent circuit for the simulation of photoelectrochemical mechanism in photoelectrodes) and (c) Mott-Schottky plots of samples M1, M2, M3 and M4 in solution of 0.5 M Na_2SO_4 pH=7; d) energy band diagram for g- C_3N_4 (sample M2).*

Both charge carrier densities, Nd and the flat-band potential (E_{fb}) for the semiconductor/ electrolyte interface were determined using Mott-Schottky equation:

$$\frac{A_S}{C_{sc}^2} = \left(\frac{2}{e_0 \varepsilon \varepsilon_0 N_d}\right)\left((E - E_{fb}) - \frac{kT}{e_0}\right) \qquad (1)$$

where A_S is the surface area of the electrode, Csc is the specific capacitance of space-charge layer (F cm^{-2}), ε is the dielectric constant of carbon nitride (62) or TiO_2 (48), E is the applied potential. Charge carrier densities Nd resulted from the Mott-Schottky plots are of 10^{20} order and the values for the flat-band potential of g- C_3N_4 samples M1, M2, M3 and M4 are close (Table 2).

Sample	Flat-band potential (V vs RHE)	Carrier density, $N_d/10^{20}(cm^{-3})$
M1	-0.63	1.68
M2	-0.65	1.17
M3	-0.55	0.61
M4	-0.61	1.94
M6	-0.28	2
M7	-0.54	2.76

The conduction band (CB) and valence band (VB) positions for g-C_3N_4 film, which influence PEC response of the semiconductor in the water splitting process, were calculated by using the following equations:

$E_{VB} = X\text{-}E_e + 0.5E_g$ (2)

$E_{CB} = E_{VB}\text{-}E_g$, (3)

in which E_{CB} and E_{VB} are the bottom of the conduction band and the top of the valence band, respectively. E_e is the energy of the free electrons on the hydrogen scale (4.5 eV), X is the absolute ctronegativity (4.73 eV), and E_g is the band gap energy (2.32 eV) of g-C_3N_4 resulted from the optical measurements.

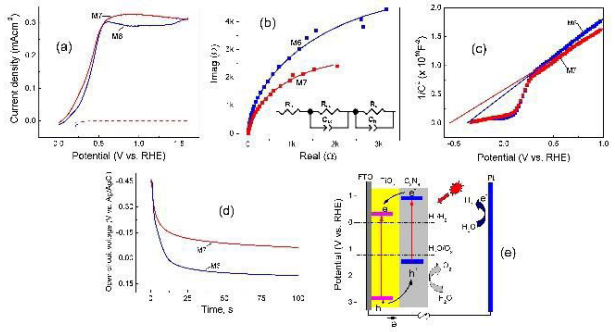

Fig. 5. *(a) J-V characteristics curves obtained under imulated solar illumination, (b) EIS Nyquist plots, (c) Mott-Schottky plots, (d) open circuit voltage decay with time, after stopping the illumination for samples M6 and M7, in solution of 0.5 M Na_2SO_4 pH=7 and (e) schematic diagram for PEC water splitting mechanism of TiO_2/g-C_3N_4 heterojonction (sample M7 used as photoanode).*

Photo anode	R_s (Ωcm²)	C_{sc} (Fcm⁻²)	R_{sc} (Ωcm²)	C_h (Fcm⁻²)	R_{ct} (Ωcm²)
M1	23.6	$3.4x10^{-6}$	2.6	$7.2x10^{-6}$	103910
M2	29.4	$1.6x10^{-7}$	2.6	$5.7x10^{-6}$	66509
M3	26.5	$1.2x10^{-6}$	2.6	$5.2x10^{-6}$	54198
M4	22.2	$4.2x10^{-6}$	2.6	$8.1x10^{-6}$	69884
M6	26.6	$2.4x10^{-6}$	1.5	$7.7x10^{-6}$	9818
M7	24.6	$9.4x10^{-6}$	1	$1.1x10^{-5}$	5396

Table 3. *The parameters of the photoanodes obtained from the EIS analysis.*

Conclusion

g-C_3N_4 and TiO_2/g-C_3N_4 photoanodes were successfully prepared via spray coating method. The repared g-C_3N_4 film showed an enhanced optical absorption of visible light. A significant enhancement of the photocurrent density was obtained with TiO_2/g-C_3N_4 photoanode.

The charge transfer resistance was the determinant parameter in the photoactivity assessment of the photoanodes by edance spectroscopy.

Funding from Core Program, contract no. 21N/08 02 2019.

Reference

[1]M.Sima, E. Vasile, A. Sima, N. Preda, C. Logofatu, Int J Hydrogen Energy 44 (2019) 24430-24440.

Pt and Pd modified Porous Organic Polymers as efficient catalysts for selective hydrogenation

Mihaela Mirela Trandafir[3], Ioana Hristea, Cristian Mihail Teodorescu
in collaboration with:
Lidia Pop[1], Niculina D. Hadade[1], Frank Krumeich[2], Jeroen A. van Bokhoven[2], Ion Grosu[1], Vasile I. Pârvulescu[3]
1. Babes-Bolyai University, Faculty of Chemistry and Chemical Engineering, Department of Chemistry, Cluj-Napoca, 11 Arany Janos str., 400028, Cluj-Napoca, Romania.
2. Institute for Chemical and Bioengineering, ETH Zurich, HCI D 130 Vladimir-PrelogWeg 1, 8093 Zurich, Switzerland, Paul Scherrer Institute, 5323 Villigen, Switzerland.
3. University of Bucharest, Department of Organic Chemistry, Biochemistry and Catalysis, 4-12 Regina Elisabeta Blvd., 030016 Bucharest, Romania.

Chemoselective hydrogenation of organic compounds is an important step in the synthesis of various valuable compounds for both industrial and fine chemical processes [1]. Among others, the selective hydrogenation of the carbonyl compounds to the corresponding alcohols may produce platform molecules for the synthesis of different fine-chemicals [2].

Hydrogenation by molecular hydrogen requires a suitable catalyst able to dissociate the hydrogen and to activate the substrate. Homogenous catalysts used for such reactions contain transition metals and further heterogenization of these catalysts by their deposition onto solid supports, especially as metal nanoparticles (NPs), which provide specific advantages as high turnover frequency (TOF), good selectivity and good recyclability. Supports as porous materials with a high surface area and controlled pore size distribution eliminate drawbacks as NPs agglomeration during the synthesis and allow an increased productivity and shape control selectivity.

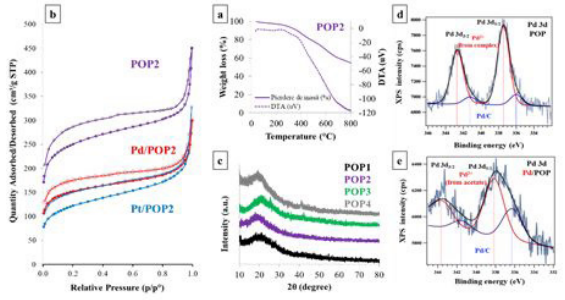

Figure 1. Selected characterization results: (a) TG-DTA curve, (b) N_2 adsorption-desorption isotherms, (c) XRD patterns and (d) Pd 3d level XPS spectra.

Porous organic polymers (POPs) gained a significant interest for catalytic applications, more precisely as adsorbents and catalytic supports, due to their large surface area and good thermal stability. The porous structure is able to stabilize the metal NPs, converting them in highly active and reusable heterogeneous catalysts.

This study was aimed at synthesis and characterization of new POPs using 3,3',6,6'-tetrasubstituted spirobifluorene units. POPs synthesis was realized using either the Sonogashira protocol or acetylenic coupling reactions [3]. The POPs (POP1-4) were used as support for Pd or Pt to produce selective and reusable catalysts for the hydrogenation of several ketones (4-bromobenzophenone (4-BBP) - reported in this study, acetophenone, 1,2-naphtoquinone and 7-nitro-1-tetralone). The new organic polymers are active for the hydrogenation of ketones due to remnant Pd from the homogeneous catalyst used in the Sonogashira synthesis.
The additional noble metal loading was about 0.5 wt.% and the resulted materials were exhaustively characterized.

POPs shown a good thermal stability between 200-400 °C (TG-DTA analysis, see **Fig. 1a**). The adsorption-desorption isotherms of N_2 at -196°C are type IV ones with a H4 hysteresis loop, associated with mesoporous materials enclosing slit-like pores. The deposition of the noble metal onto POP2 did not alter the shape of the adsorption-desorption isotherm (**Fig. 1b**), but a decrease of the surface area was observed with very small changes in the pore size, which confirm that the texture of the polymer could be affected by the deposition-precipitation process and the metal NPs clump into the pores. POP-based materials XRD patterns confirm the amorphous nature of the organic polymers (**Fig. 1c**).

After the deposition of the noble metals, the XRD patterns showed that Pt is deposited in a high

dispersion (no diffraction line), while Pd agglomerated after the reduction in hydrogen (diffraction line at 2θ=41°).

XP spectra of the Pd 3d level, for POP2 and Pd/POP2 (**Fig. 1d, e**), display the typical Pd $3d_{5/2}$ and Pd $3d_{3/2}$ doublets at 337.7 and 342.6 eV, confirming the presence of remnant Pd^{2+} species from the Sonogashira synthesis of the polymers. Further deposition and reduction of Pd led to an increase in the intensity of the peaks from 336.2 and 341.2 eV, associated with the presence of reduced Pd^0 species.

TEM investigation of the POP2 samples reveals that Pd deposition changed the morphology of the POP2 support, while for Pt deposition, the original morphology of POP2 is well preserved. Pd particles have a diameter of about 50–150 nm, while Pt is well dispersed, with a <1nm diameter.

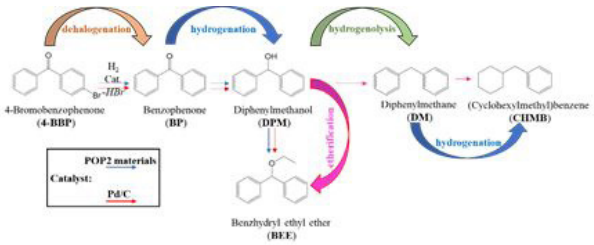

Scheme 1. Reaction pathway proposed for 4-BBP hydrogenation

4-Bromobenzophenone hydrogenation

In the presence of all POP, hydrodehalogenation of 4-BBP occurs and the conversion varied in the order POP4>POP2>POP3~POP1, with high selectivity to benzophenone. POP2 catalyst was the only one able to further hydrogenate benzophenone (BP) to diphenylmethanol (DPM). Consequently, Pd/POP2 and Pt/POP2 were tested for 4-BBP hydrogenation.

The noble metal containing catalyst are very active and selective to BP and the reaction pathway is complex (see Scheme 1). BP is not further hydrogenated to DPM due to a steric hindrance. For comparison, Pd deposited on activated carbon was tested and it was found to be more active - promoting BP hydrogenation to DPM, but with a low selectivity due to a further aromatic ring hydrogenation (Scheme 1).

To sum up, in this study we evidenced the importance of using an adequate catalytic support into the design of highly active and selective catalysts, where noble metal NPs are stabilized due to the texture and to the porous structure of the polymer, affording stable and reusable catalysts.

References

[1] M. Ito, T. Ikariya, Chem. Commun., (2007) 5134-5142.

[2] M. Gopiraman, S.G. Babu, Z. Khatri, K. Wei, M. Endo, R. Karvembu, I.S. Kim, Catal. Sci. & Technol., 3 (2013) 1485-1489.

[3] M.M. Trandafir, L. Pop, N.D. Hadade, I. Hristea, C.M. Teodorescu, F. Krumeich, J.A. van Bokhoven, I. Grosu, V.I. Parvulescu, Chemcatchem, 11 (2019) 538-549.

Additive-driven enhancement of magnetic performances in RE-free permanent magnets

Ovidiu Crisan, Alina Daniela Crisan, Florin Vasiliu, Gabriel Schinteie, Aurel Leca

There is a recent surge of interest for the rare-earth-free permanent magnets and, to this purpose, the best candidates are the systems where the tetragonal hard magnetic $L1_0$ phase is present or can be formed by suitable microstructure processing. Among these systems, of particular interest is the FeMnPt ternary alloy. In addition to be likely to form the L10 phase as its parent binary system (FePt) the ternary FeMnPt exhibit particular magnetic structure due to the influence of the antiferromagnetic (AF) Mn. The Mn addition has been shown to cause a steady reduction of magnetocrystalline anisotropy and saturation magnetization due to the antiparallel alignment of Fe and Mn moments. In the present work [1], we have employed a mixed sputtering technique, based on the use of both elemental and compound target for developing $L1_0$ FeMnPt thin films with specific structural features, which triggers better magnetic performances. The aim is to correlate the Mn induced microstructural and lattice changes with the magnetic properties and to optimize the microstructure for a maximized energy product.

$Fe_{65}Mn_5Pt_{35}$ and $Fe_{50}Mn_{10}Pt_{40}$ films were DC and RF sputtered in Ar atmosphere of 6 x 10^{-3} mbar. Depending on the desired composition, electrical powers between 20 and 50 W in the case of Pt and FeMn or up to 150 W in the case of the Fe target have been applied on the magnetrons. Alternative deposition sequences resulted in film thickness of about 63 nm, as detected from X-ray interferometry measurements. Some of the as-obtained films have been in-situ thermally annealed at 550°C for 1h, inside the sputtering chamber, in high vacuum. Structural characterization has been extensively performed using grazing-incidence X-ray diffraction (GIXRD), high-resolution electron microscopy (HREM) and selected area electron diffraction (SAED). Magnetic characterization has been performed by using magneto-optic Kerr effect (MOKE) magnetometry as well as with a Superconducting Quantum Interference Device (SQUID).

The hysteresis loops have been obtained by SQUID measurements with a magnetic field of up to 3T applied parallel to the sample plane.

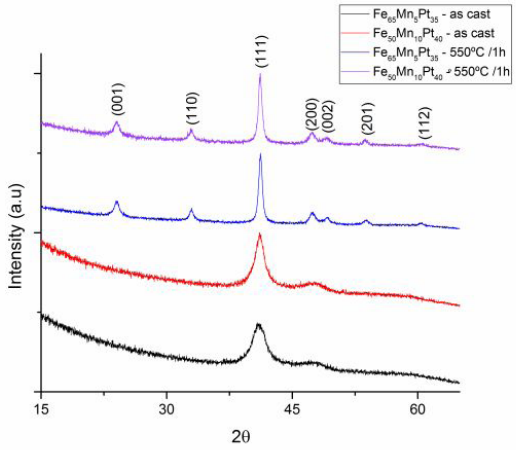

Fig. 1. *X-ray diffractograms of samples $Fe_{65}Mn_5Pt_{35}$ and $Fe_{50}Mn_{10}Pt_{40}$ both as-cast and annealed at 550°C for 1h.*

The X-ray diffraction analysis has been performed with Cu Kα radiation (λ = 0.15402 nm) in grazing incidence geometry. The X-ray diffractograms of both as-cast and annealed samples are displayed in **Fig. 1**. It can be seen that for the as-cast samples, the two diffractograms show rather similar features, with broad peaks of low intensity, identified as the Bragg lines of the (111) and (200) reflections of the face centered cubic (fcc) phase, space group: *Fm3m*.

As expected, XRD profiles of the annealed samples are different. Both the annealed samples diffractograms show additional Bragg peaks, such as the superlattice peaks (001) and (110) belonging to the tetragonal $L1_0$ ternary FeMnPt phase, space group: *P4/mmm*.

The allure of the diffractogram presents evidence of a structural refinement and grain growth illustrated by the narrowing of the peaks line width and moreover, there is a splitting of the (200) peak of the cubic phase into the (200) and (002) peaks of the tetragonal phases.

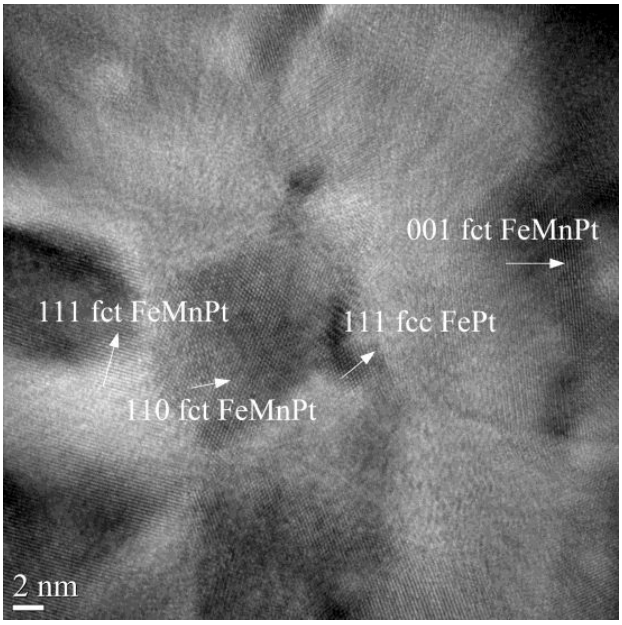

Fig. 2. *Grain structure showing fct FeMnPt regions separated by small fcc FePt patches in $Fe_{50}Mn_{10}Pt_{40}$ annealed at 550°C for 1h.*

In the case of annealed $Fe_{50}Mn_{10}Pt_{40}$ films, TEM and HREM images show a microstructure composed of large face centered tetragonal fct $L1_0$ grains, with an average size of about 15 – 20 nm, and also of some small *f*cc grains, with average sizes between 5 and 8 nm (**Fig. 2**). These results are in agreement with the XRD results where predominant tetragonal $L1_0$ phase is found in both annealed samples. Well-ordered $L1_0$ fct FeMnPt grains that are identified by the superlattice reflections (001) and (110) are visible, separated by rather small (5 nm) FePt fcc patches.

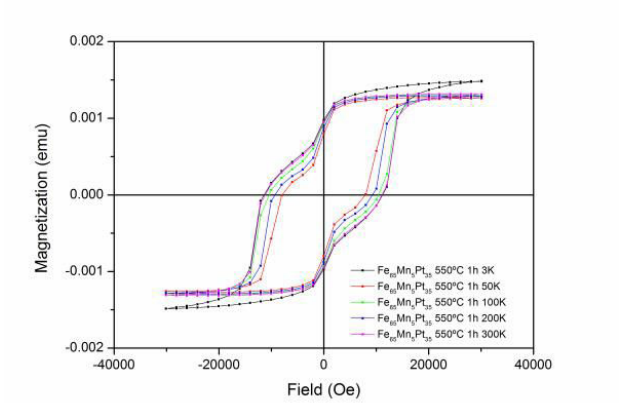

Fig. 3. *VSM hysteresis loops recorded at various temperatures from 3K to 300K for the sample $Fe_{60}Mn_5Pt_{35}$ annealed at 550°C for 1h*

Magnetic hysteresis loops, recorded from 3K to 300K, are depicted in **Fig. 3**. There is a significant coercivity observed for all investigated temperatures. All the loops exhibit inflection points on the demagnetization curves (quadrant IV of the hysteresis loops). These inflection points show unambiguously that there are two magnetic phases present in the samples, one with lower coercivity and another with a very high coercivity. These different phases are assigned as follows: a) the small soft magnetic component is related to the presence of disordered regions rich in fcc FePt, consistent with the results observed in HREM, b) a predominant hard magnetic component with high coercivity that belongs to the tetragonal $L1_0$ phases. Such strong coercivity is promising on one hand for potential applications as permanent magnets and on the other hand, the co-existence of soft and hard magnetic components creates premises for obtaining FePt-based exchange spring nanocomposite magnets.

References

[1] O. Crisan, et al. "Structure and magnetic properties of highly coercive $L1_0$ nano-composite FeMnPt thin films", Mater. Charact. 152 (2019) 245-252

Rhodium-Catalyzed Annulation of ortho-Alkenyl Anilides with Alkynes

C. Comanescu*
(in collaboration with Centro Singular de Investigación en Química Biolóxica e Materiais Moleculares (CIQUS) and Departamento de Química Orgánica, Universidade de Santiago de Compostela, Spain)

C-C, C-H and C-heteroatom bond activation by transition metal complexes [1] had evolved from purely theoretical proposal, to scarce laboratory examples and now to being a versatile tool in organic chemistry, that provides access to functionalization and oxidative annulation reactions.[2] The current report demonstrates that oalkenyl-*N*-triflylanilides can react with alkynes in presence of Cp*Rh(III) catalyst, to yield naphtalene adducts, by a combined dehydrogenative carboannulation process. [3]

This process can lead to variable amounts of a rearranged isomeric product, formed by a formal migration of the alkenyl group, a reaction outcome that is essentially unreported so far. (**Fig. 1**)

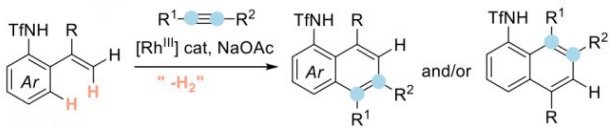

Fig. 1 *Annulation of o-alkenylanilides with alkynes to new naphthalene adducts, as isomeric, separable mixtures. [1]*

The reaction scope has been studies with respect to both alkyne (Table 1), and anilide partner.

The catalytic precursor of Rh(III) used was $[Cp^*RhCl_2]_2$, but mechanistic investigations caried out mainly by C. Comanescu showed some interesting aspects of the catalytic cycle, including the isolation of an elusive reaction intermediate: the Rh(III)-containing metal complex formed that is active in the catalytic oxidative annulation reaction. From the solvents surveyed, it was observed that reaction generates high (more than 80%) yields when run in THF (tetrahydrofurane) at 66 °C, which also reduces the energy consumption compared to solvents like toluene or DMF (that require over 105 °C to reach boiling). The *triflate* (-T*f*) group on amidic -*N* was however essential for the reaction to proceed to any meaningful products. Interestingly, the reaction also proceeds under Ar, therefore the presence of an internal oxidant (like Na^+ or Cu^{2+} acetates) in not a requirement for the reaction, which also points out to either a non-inocent ligand behaviour, or to a Rh(III)/Rh(I) catalytic mediation.

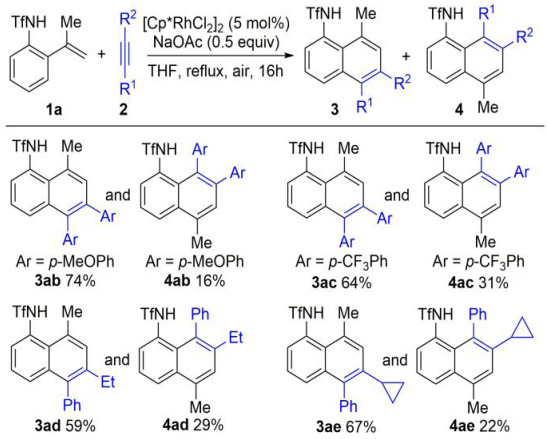

Table 1. Reaction scope with respect to the alkyne coupling partner.

Moreover, the acetate amount could also be reduced to 0.5 equivalents of NaOAc, with no negative impact on the overall yield. Even Rh(I) complex [Cp*Rh(COD)] displays catalytic activity, albeit much lower (18% yield), which again point out to a possible Rh(III)/Rh(I) catalytic cycle. Both symmetrical and asymmetrical acetylenes, either electron-rich or electron-poor, are well tolerated (up to 95% overall yield).

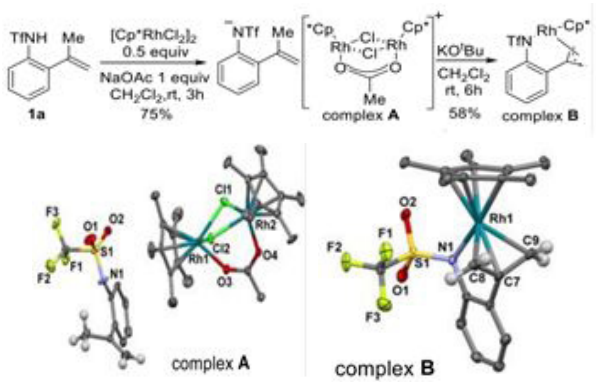

Scheme 1. *Procedure for isolation of complexes A and B that were characterized by single crystal -Xray diffraction.*

Formation and isolation of **B** was suggestive of its presence in the catalytic cycle, and indeed, by using **B** as catalyst we obtained similar yields as to Cp*Rh(III) precursor. The precursor would easily convert to intermediate **A** by deprotonation and rearrangement, while further deprotonation on a CMD-fashion would yield complex **B**. (Scheme 1) DFT computations performed on the C-H activation step shed some light on the energetics of this process. (**Scheme 2**)

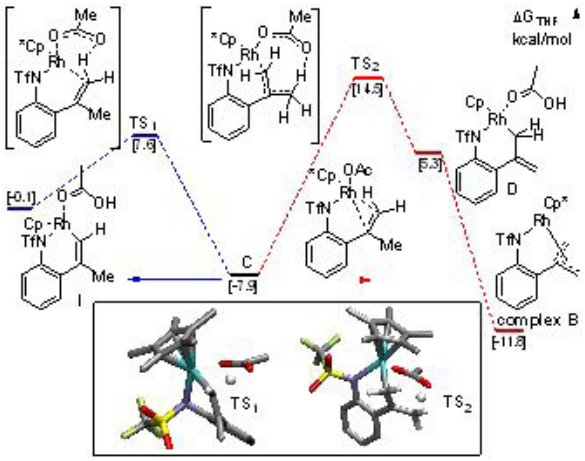

Scheme 2. *DFT calculations on the C-H activation stage.*

These DFT results imply that cycloaddition requires activation of alkenyl C-H bond, that occurs by a concerted CMD mechanism (ΔG=15.5 kcal/mol), favoured by the presence of a N-containing group (triflyl, -Tf), more electron-donating. In this context, isolation of **B** is explained by the higher stability of the π-allyl complex **B**. ($\Delta\Delta G‡$ (TS_2-TS_1) =+6.9 kcal/mol)

This work led to new rhodium-catalyzed oxidative annulation processes, that are atomeconomical, highly regioselective and present a broad synthetic scope, suitable to organic chemistry applications and cycle manipulation with various well-tolerated substituents. The reaction can successfully be scaled up to mmol scale.

The catalytic cycle involves a reoxidation step, as evidenced by the usage of a Rh(III) hydride catalyst. (yield: 62%, **Scheme 3**)

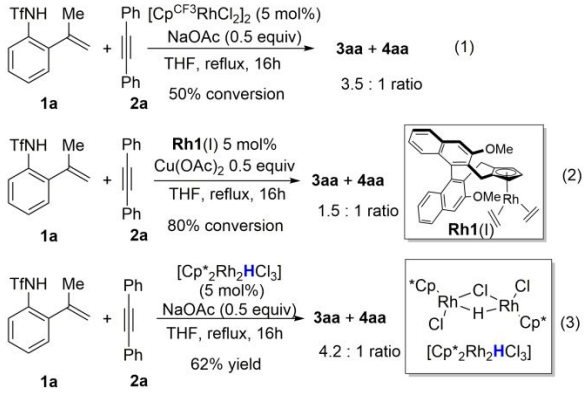

Scheme 3. *Involvement of well-defined Rh(III) hydride complex (^{1}H-NMR evidence) in the reoxidation step.*

The mechanistic investigations conducted reveal an unprecedented rearrangement process requiring the cleavage and formation of C-C bonds of great importance for organic and organometallic chemistry alike.

References

[1] A. Seoane, C. Comanescu, N, Casanova, R. Garcia- Fandino, X. Diz, J. L. Mascarenas, M. Gulias, Rhodiumcatalyzed annulation of ortho-alkenylanilides with alkynes: Formation of unexpected naphthalene adducts, Angew. Chem. Int. Ed. 2019, 131 (6), 1714-1718, DOI: 10.1002/ange.201811747 (IF=12.257, AIS=3.4).

[2] T. Gensch, M, N. Hopkinson, F. Glorius, J. WencelDelord, Chem. Soc. Rev. 2016, 45, 2900-2936.

[3] N. Umeda, H. Tsurugi, T. Satoh, M. Miura, Angew. Chem. Int. Ed. 2008, 120, 4083-4086. *Contact: cccomanes@gmail.com (C. Comanescu).

Effect of the process control agent in the ball-milled powders and SPS-consolidation temperature on the grain refinement, density and Vickers hardness of Fe14Cr ODS ferritic alloys

V. Mihalache, I. Mercioniu, A. Velea, P. Palade

The outstanding stability to heat of the microstructure and the mechanical properties of nanostructured oxide dispersion-strengthened ferritic stainless steels, ODSFS, provide an attractive cost-performance ratio for production of components and structural materials to be exposed to elevated or high temperatures. Reduced activation ODSFS are under intense development as structural materials that can provide irradiation tolerance (e.g. resistance to irradiation-induced swelling) along with superior high temperatures mechanical properties that are relevant for applications in future fusion and fission power reactors. Ti-, Y- and O-enriched nano-scale features in combination with nanostructuring induced by mechanical alloying (MA) enhance the high temperature mechanical properties (e.g., strength, hardness, long-term creep, resistance to fatigue, etc.) of ferritic steels. In particular, they act as a sink for the He and H generated by high-energy fusion neutrons. Process control agent, PCA, used in MA by ball milling can considerably influence the powder morphology and particle size, thereby affecting their densification behaviour. An advantage of milling with PCA [1,2] as opposed to dry milling [3, 4] is that finer particles with more homogeneous size distribution can be obtained as well as shorter milling time is required to reach the desired ultrafine crystallite size. MA (or mechanical milling) in combination with SPS is regarded as an efficient route for the production of fine grained structures in Fe-Cr-based alloys.

We produced Fe-14Cr-0.4Ti-0.25Y_2O_3 ferritic steels by varying the amount of residual process control agent (up to 30 wt%), PCA (ethanol), in the ball-milled (for 23 h) powders and changing the spark-plasma-sintering, SPS, temperature (550°C-1100°C). Unlike the majority of the reports found in literature, where the quantity of PCA was varied at milling stage leading to MA powders of different quality, we used the same (high) amount of 30 wt.% PCA in the milling process. In such MA powder the residual PCA can be easily removed. The powders with deferent amounts of PCA were obtained by applying different post-milling storage conditions.

Our investigation and results on the role of PCA in ball-milled powders for grain refinement, densification and hardening during SPS-consolidation and post - consolidation annealing of Fe14Cr ODS ferritic steels can be resumed as follows.

1.The contamination with carbon and oxygen appears a disadvantage of wet milling as compared to dry milling. However, the milling media well-balanced by relatively short time milling (23 h) with a high quantity of PCA (30 wt.%) resulted in a powder which was not reacted with the steel matrix, with ultrafine crystallite size, ~10nm, and with a large number of dislocations and nano-scale features (**Fig. 1**).

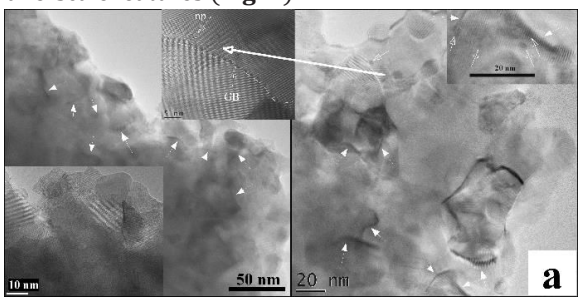

Fig. 1. *Microstructure characteristics of as-milled powder with a low amount of residual PCA. HRTEM images: left – low magnification, right – high magnification. Some defects and nanofeatures are marked by arrows as follows: dislocations (lines, pile-ups, staking-faults) - white filled arrows; nanoparticles - white unfilled arrows. Bottom inset: a magnified detail confirming that the average Fe14Cr ODS crystallite size is about 10 nm. Top left inset: a magnified detail showing a nanoparticle (np) at a grain boundary (GB). Top right inset: a magnified detail showing the ultrafine (< 5 nm) nanoparticles at dislocations.*

2. SPS-consolidation preserved fine structure of the as-milled powders, the average crystallite size not exceeding 53 nm. Higher temperatures reached at the particle - particle contact points and at the particle surface in products with lower amounts of residual PCA improved the densification rate (reducing the porosity) (**Fig. 2**), the PCA dissolution and the local carbon incorporation resulting in higher density and Vickers hardness.

3. The carbon traces resulted from the decomposition of survived PCA fragments in Fe14Cr alloys: (a) induced thermally activated processes observed in DTA between 900°C and 1270°C, which can also develop at the neck/particle surface during SPS consolidation at much lower nominal temperatures and facilitate the formation of metal - metal sintering contacts, improve the plastic deformation and accelerate the densification (improving density). (b) promoted a bcc α - fcc γ transformation registered in DTA heating curve at ~ 850 °C; the processes associated with phase transformations during rapid cooling from the carbon-enriched austenitic region resulted in sudden increase of Vickers hardness, density and additional grain refinement (from 53 at 770°C nm to 26.4 nm at 870 °C) (**Fig. 3**).

4. The high stability of refined ferrite grain size and hardness upon heating above the α→γ transition could be due to the pining of dense GB network by high concentration of stable nano-scale features (presumably rich in Y, Ti and O).

5. The optimum combination of SPS-consolidation (1100°C) and post-SPS treatment allowed for effective reduction (at least under the sensibility limit of XRD measurements) of $(Fe,Cr)_2O_3$ and carbides (Cr7C3) traces preserving high hardness (501.0 VH), fine ferrite grain size (36.2 nm) and high density (99.15%) of final steel.

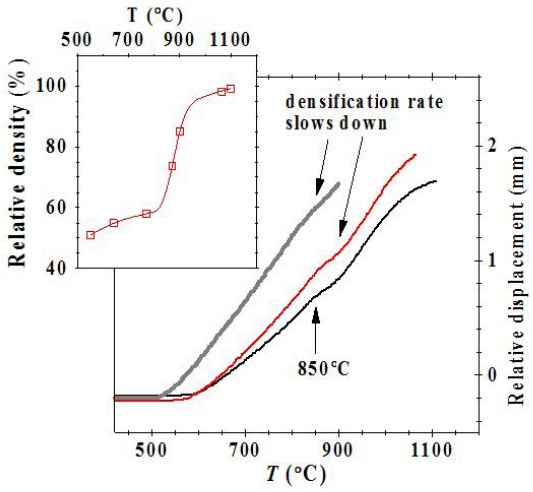

Fig. 2. *The relative punch displacement vs. T for the alloys SPS sintered at 900°C, 1065°C and 1100°C. Inset: the relative density vs. T of Fe14Cr ODS steels consolidated from the powders with a low amount of residual PCA.*

6. The processing route (**Fig. 3**) described in this work (which can be further optimized, e.g. by introduction of an efficient degassing step prior to compaction, etc.) could be an alternative for the production of highly stable Fe14Cr ODS ferritic steels offering the potential for elevated/high-temperature applications.

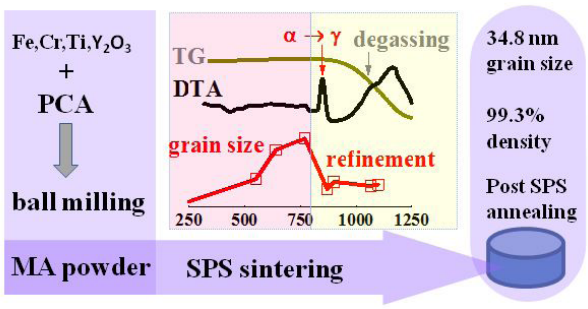

Fig. 3. *The sketch of the processing route of ODSFSs.*

The carbon traces resulted from the decomposition of survived PCA fragments in Fe14Cr alloys upon heating promoted bcc α - fcc γ transformation resulting in an grain refinement (in addition to the grain refinement induced by high energy milling with ethanol).

Acknowledgments: EC/EFDA (project WP13-MAT), Core Program: project PN18-110101 and PN-III-P1-1.2-PCCDI-2017-0871: project 47PCCDI/2018.

References

[1] V. Mihalache1, G. Aldica, I. Pasuk1, I. Mercioniu1, J Therm Anal Calorim 138 (2019) 2515.

[2] V. Mihalache, I. Mercioniu, A. Velea, P. Palade, Powder Technology Volume 347 (2019) 103.

[3] V. Mihalache, I. Mercioniu, G. Aldica G, I. Pasuk, J Therm Anal Calorim 134 (2018) 463.

[4] V. Mihalache, M. Walter, I. Mercioniu, N. Ordas, Metallurgical and Materials Transactions A 50 (2019) 3282.

ADVANCED MATERIALS FOR APPLICATIONS

SELECTED RESULTS

Palladium/palladium oxide coated electrospun fibers for wearable sweat pH-sensors

Victor C. Diculescu, Mihaela Beregoi, Alexandru Evanghelidis, Raluca F. Negrea, Nicoleta G. Apostol, Ionut Enculescu

Nowadays, an important breakthrough in personalized healthcare is the development of portable medical devices which provide the wearer's continuous real-time health status information. Biomarkers from sweat (like ions (H^+, Na^+, K^+, Cl^-), peptides, small molecules (glucose, uric acid, lactate, etc.) or small proteins) could provide valuable health information about physiological processes (sweat rate, dehydration, etc.) and vital signs, sweat analysis thus being a handy monitoring and diagnostic tool. Some wearable (bio)sensors for monitoring transcutaneous oxygen and humidity, pH, Na^+, lactate, K^+, Cl^- or glucose have been reported in scientific literature [1,2], others are already available on the market [3]. However, skin placed (bio)sensors which can read temperature, electrical signals, sweat composition, etc. are not simple to manufacture. In this context, flexible electrodes such as printed circuits, polymer foils, metallic fibre meshes and/or nanowire networks represent the great pylon of wearable electronics. In particular, metallic fibre meshes could be excellent candidates for a skin patch (bio)sensor that properly work because of good electrical features, flexibility, biocompatibility, are light-weight, low production costs, etc. The electrospinning technique is the most used method for in mass submicronic polymer fibre nets fabrication that can be easily metalized and attached on flexible substrates, behaving as (bio)sensor electrical interface.

Sweat pH-sensor fabrication

The fabrication of the sweat pH sensor implies several steps as described: first, electrospun fibre meshes were obtaining by using a 10% poly(methyl methacrylate) (PMMA) solution in optimized experimental conditions (solution flux of 0.5 mL/h, 15 kV applied voltage, 15 cm distance between collector and spinneret, collection time of about 10 min); second, the PMMA fibres were coated with about 200 nm Au layer by magnetron sputtering; next, Au coated PMMA fibres were thermally attached (heating at 150˚C) onto poly(ethylene terephthalate) (PET) foils; for preparing the working electrode, a sensing Pd layer was electrochemically deposited on Au coated nets attached on PET by using a 3 mM $PdCl_2$ in 0.1 M HCl solution at an applied potential of +0.10 V for 2 h, subsequently the ensemble being annealed in air for 4 h at 150°C in order to oxidize the Pd layer; a reference electrode was also produced by half-covering the Au coated meshes with a thin Ag layer by thermal evaporation, further the fibres being attached on PET substrates and anodized in 0.1 M HCl at +1.00 V during 2 min. In order to demonstrate the functionality of the sweat pH-sensor at epidermal level, a proof of concept device was thus manufactured (**Fig. 1**(a,b)): the substrates with Pd-PdO coated fibres were placed on top of the reference electrode in anti-parallel configuration in order to ensure a good electrical contact with the potetiostat, separated by a PET spacer to overcome any short-circuit; an aperture was created in the working electrode and spacer to allow the communication between the working and reference electrode; at the end, the sensor was covered with polyacrylamide (PAAm) hydrogel aqueous solution (containing 5% acrylamide, N,N-methylenebisacrylamide used as crosslinker and 0.8% Irgacure 2959-photoinitiator), this being irradiated with a UV lamp for the polymerization to take place; the obtained hydrogels were washed with deionized water and dried overnight in air at room temperature.

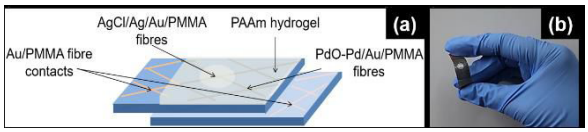

Fig. 1. *(a) Schematic representation of sweat pH-sensor component layers and (b) digital photo of the proof of concept device.*

The sensor response was investigated by registering the open circuit potential (OCP) variation with time and pH when 100 µL of artificial sweat was dropped on the PAAm-covered sensor. The response was compared with that obtained for Pd-PdO covered fibres.

Results and discussions

The prepared fibre meshes were morphologically characterized after each coverage step. Fig. 2 displays the SEM images at different magnifications of (a,a') Au coated PMMA fibres and of (b,b') those electrochemically covered with Pd and thermally treated.

The Au layer fully covers the PMMA fibres being smooth and continuous, displaying an average diameter of about 0.5 μm. After the Pd-PdO coverage, the fibres were homogeneous, wrapped in flake-like structures with acicular extremities, increasing the fibre diameter of about 1 μm.

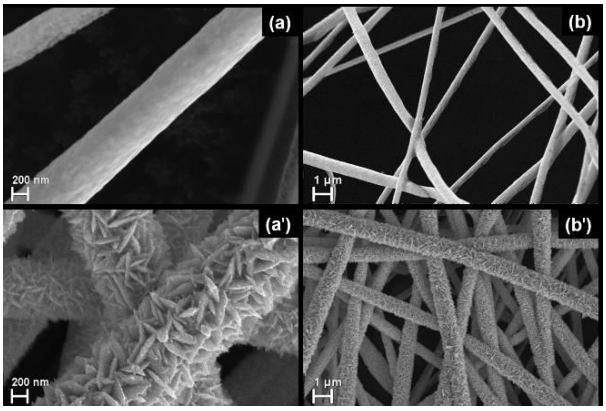

Fig. 2. *SEM images of (a, a') metalized and (b, b') Pd-PdO coated fibres.*

The sensitivity of the Pd-PdO coated fibres (**Fig. 3**(a,b)) and hydrogel embedded pH-sensor (**Fig. 3**(e,f)) was measured by registering the OCP in buffer solutions and/or artificial sweat with a pH between 4.5 and 9.2, at various time intervals. For Pd-PdO coated fibres, when buffer solutions were used, the slope of the line was -59.3 mV/pH unit, a response close to the theoretical prediction. When artificial sweat with different pH was used, the slope of the line was -59.7 mV/pH unit which also confirmed the theoretical prediction. For pH-sensor covered with a hydrogel layer, the measurements were performed by incubating the sensor in artificial sweat with different pH values. The slope of the line was -18.0 mV/pH unit, a response below the theoretical prediction because of artificial sweat complexity and hydrogel low mobility. The sensitivity temperature dependence, the minimum volume to which the sensor works and mechanical resistance were also determined

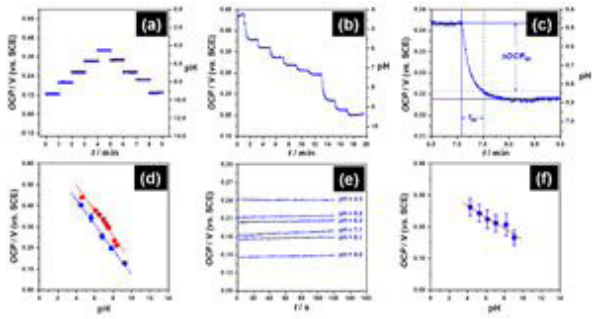

Fig. 3. (*a) OCP of PdO-Pd coated fibres as function of time recorded in electrolytes with different pH; (b) Same as (a) in artificial sweat; (c) Analysis of transition between pH 6.44 and 6.84 in artificial sweat; (d) Variation of OCP with the pH of the (•) electrolyte or of (•) artificial sweat; (e) Variation of OCP of the hydrogel covered sensor in artificial sweat with different pH as function of time; (f) Variation of OCP of the hydrogel covered sensor with the pH of the artificial sweat.*

Conclusions

This work proposes a new flexible sweat pH-sensor configuration based on electrospun fibre meshes electrochemically coated with Pd-PdO and PAAm hydrogel. The fabricated sensor was tested in artificial sweat, being found that it has a sensitivity of up to -18.0 mV/pH unit, volume detection of about 250 nL and mechanical resistance to bending and a temperature dependence of aprox. 1 mV/°C.

Acknowledgments

All authors acknowledge Romanian Ministry of Research and Innovation through Operational Programme Competitiveness 2014–2020, Projects: NANOBIOSURF-SMIS 103528 and PN16-480101-Phenomena and physico-chemical processes in complex nanometric systems, surfaces and interfaces - 12/2018 PFE project for financial support.

References

[1] Gao, W. *et al.* Fully integrated wearable sensor arrays for multiplexed in situ perspiration analysis. Nature 529, 509–514 (2016).

[2] Diculescu, V.C. *et al.* Palladium/palladium oxide coated electrospun fbers for wearable sweat pH-sensors. Sci. Rep. 9, 8902 (2019).

[3] Kim, J., Campbell, A., Esteban-Fernández de Ávila, B. & Wang, J. Wearable biosensors for healthcare monitoring. Nat. Biotechnol. 37, 389–406 (2019).

Direct Immobilization of Biomolecules through Magnetic Forces on Ni Electrodes via Ni Nanoparticles
Applications in Electrochemical Biosensors

M. M. Barsan, T. A. Enache, N. Preda, G. Stan, N. G. Apostol, E.Matei, A. Kuncser, V. C. Diculescu

Nanostructured materials have been extensively used in bioanalytical devices. Among these, metal nanoparticles (MeNPs) make use of their increased electroactive surface, electron conductivity, and catalytic properties, to tailor new biosensor architecture with superior sensitivity and selectivity.

In the present work, a new procedure for the magnetic immobilization of biomolecules is proposed, based on magnetic Ni electrodes at which magnetic MeNPs are directly attracted by magnetic forces [1]. Both magnetic electrodes and MeNPs were obtained by simple and cost-effective preparation methods, Ni electrodes by electroplating, and Ni nanoparticles (NiNPs) by the chemical reduction of a Ni salt. Ni, NiNP and NiNP/Ni were investigated using structural, magnetic and electrochemical methods.

X-ray diffraction results showed that NiNp patterns are featured by broader Ni maxima compared to Ni, characteristic for a nanocrystalline material.

Scanning electron microscopy (SEM) images recorded at NiNP/Ni, **Fig. 1A**, revealed globular structures with sizes between 50 and 200 nm with tendency to aggregate and form large NiNP islands.

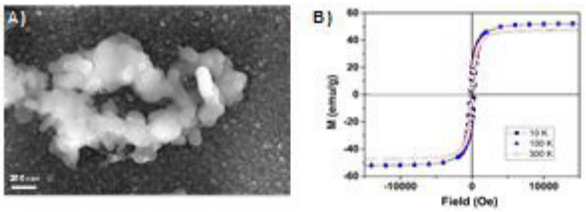

Fig. 1 A) *SEM micrographs and B) Magnetic hysteresis loops of NiNPs.*

Magnetic characterization and micromagnetic simulations (**Fig 1B**) results revealed that the magnetic force $F_z = m_z \frac{\partial Bz}{\partial z}$ acting on a NiNP at 30 nm from the Ni surface is in the range of 10^{-11} N, 7 order of magnitude higher than the gravitational component.

X-ray photoelectron spectroscopy spectra recorded on energy ranges corresponding to Ni 2p showed that after the deposition of NiNP on Ni electrode, the peaks of Ni^{2+} and Ni^{3+} overpass the peaks of metallic Ni, which are predominant at bare Ni electrodes.

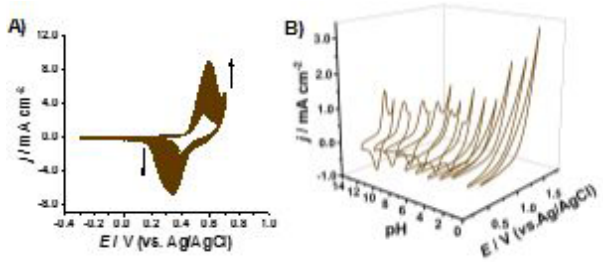

Fig. 2. *CVs at Ni electrodes in A) 0.1 M NaOH (200 scans at 0.5 $V^{s-1)}$ and B) Britton-Robinson buffer with pH values from 13 to 3 (0.1 V^{s-1}).*

The potential window of Ni electrodes in neutral media is between -0.5 to +1.0 V vs. Ag/AgCl. In basic media **(Fig. 2A**), the reversible pair of redox peaks corresponds to the oxidation of either one of the Ni^{2+} forms, NiO or Ni(OH)2, to a Ni^{3+} species such as NiOOH, as presented in the Eq. (1) and (2).

The CV response of Ni electrodes was recorded in Britton-Robinson buffer going from pH values from 13.0 to 3.0 (Fig. 2B), allowing the formation of NiOOH in basic media. No faradaic currents were for pH values below 6.0, due to the consumption of the NiOOH.

$$NiO_{(s)} + HO^- \rightarrow NiOOH_{(s)} + 1e^- (1)$$

$$Ni(OH)_{2(aq)} + HO^- \rightarrow NiOOH_{(s)} + H_2O + 1e^- (2)$$

On the other hand, electrochemical impedance spectra of Ni electrodes in neutral media were fitted using an equivalent circuit consisting in RΩ in combination with two RCs, the first representing the $Ni/Ni(OH)_2$ interface, and the second to the $Ni(OH)_2$/ electrolyte interface (**Fig. 3**).Further, Ni electrodes played dual role: as transducers and as support for the immobilization of biomolecules via NiNPs. First, the performance of Ni electrodes as electrochemical sensors for hydrogen peroxide was investigated by cyclic voltammetry and fixed potential amperometry.

The fixed potential amperometric response to H_2O_2 was tested over the potential range -0.50 V and +0.50 V, with reduction and oxidation of the analyte at the electrode surface for negative and positive potential values, respectively.

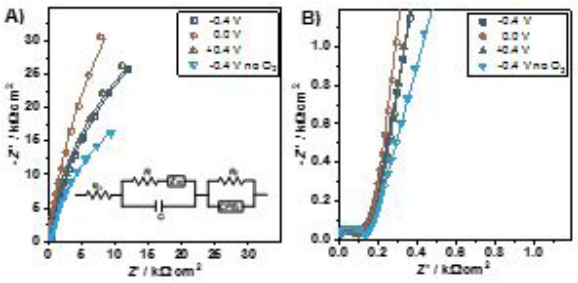

Fig. 3. *Nyquist plots recoded at Ni electrodes in neutral media A) in the frequency range 0.1 Hz-100 kHz and B) in the high frequency range only; inset in* ***Fig*** *3A is the equivalent circuit used to fit the spectra.*

Best analytical performance of the sensor was obtained at -0.4 V with a typical chronoamperometric response displayed in **Fig. 4A** and corresponding calibration plot in **Fig. 4B**. The sensitivity value at -0.4 V was 4.85 ±0.30 μA cm^{-2} mM^{-1}, with a limit of detection of 3.2 μM.

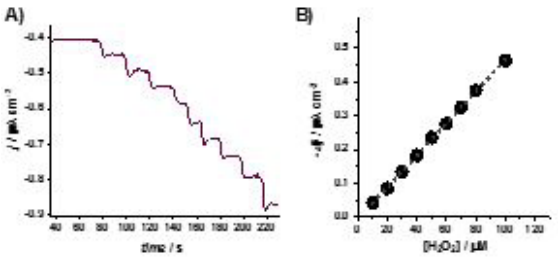

Fig. 4. *A) Fixed potential chronoamperometric response recorded at -0.4 V vs. Ag/AgCl with Ni electrodes upon injection of* H_2O_2 *and B) corresponding calibration plots.*

Next, Ni electrodes were used as substrates for the biosensor construction, which was done in two steps: i) first, the model enzyme glucose oxidase (GOx) was attached to the surface of the magnetic NiNP by incubating the enzyme solution and NiNP at 20 ˚C for different time intervals (24, 48. 72 and to 96 h) at 1500 rpm; ii) in the second step, Ni electrodes were immersed during 3 min in the solution prepared in the first step to get GOx-NiNP/Ni biosensors by the direct immobilization of the enzyme through magnetic forces. The biosensor with best analytical performance was obtained for 72 h incubation of GOx solution and NiNP and a typical fixed potential amperometric response is presented in **Fig 5A**, with the corresponding calibration plot in **Fig. 5B**.

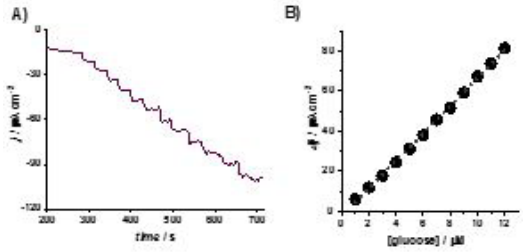

Fig. 5. A) *Fixed potential chronoamperometric response at -0.4 V vs. Ag/AgCl recoded with GOx-NiNP/Ni biosensors upon injection of glucose and B) corresponding calibration plots.*

Biosensors with no NiNP or Ni electrodes lack an amperometric signal, confirming that the immobilization of GOx through NiNP on Ni electrodes is based purely on magnetic forces.

The amperometric response upon glucose injection was a cathodic change in current at negative potential values (see **Fig. 4A**) and an anodic signal in the positive range, indicating that the working principle of the biosensor is based on H2O2 detection produced during the enzymatic reaction:

$$glucose + O_2 \xrightarrow{GOx} gluconic\ acid + H_2O_2 \quad (3)$$

Under optimum conditions, the biosensor had a sensitivity of 6.92 ±0.39 μA cm^{-2} mM^{-1} and a detection limit of 0.42 mM, with no interferences observed from manose, galactose, xylose, ascorbic, uric and citric acid.

Funding from NANOBIOSURF-SMIS 103528 and Core Program PN19-03 (contract no. 21 N/08.02.2019).

References

[1] M.M. Barsan, T.A. Enache, N. Preda, G. Stan, N.G. Apostol, E. Matei, A. Kuncser, V.C. Diculescu, "Direct immobilization of biomolecules through magnetic forces on Ni electrodes via Ni nanoparticles: Applications in electrochemical biosensors", ACS Applied Materials & Interfaces 11 (22) (2019) 19867-19877.

UV photodetector based on n-p heterojunction of individual ZnO-Cu_xO nanowire

A. Costas, C. Florica, N. Preda, N. Apostol, A. Kuncser, A. Nitescu, I. Enculescu

Recently, core-shell nanowires have attracted great scientific interests, due to their unique physical properties and advanced functionalities, having multiple applications in the next generation of optoelectronic devices. Combining two semiconductors, ZnO an n type semiconductor with a band gap of 3.3 eV and CuO wich is a p-type semiconductor with a band gap of 1.2 eV, into core-shell radial heterojunction nanowires, one can obtain a good control of the separation and recombination of the charge carriers at the interface between the two semiconductors.

In this work ZnO-Cu_xO core-shell radial heterojunction nanowire arrays were fabricated combining two simple preparation methods: thermal oxidation in air of zinc foils and radio frequency (RF) magnetron sputtering. Individual ZnO-Cu_xO core-shell nanowires were contacted using photolithography, electron beam lithography and thin film deposition techniques in order to evaluate their electrical and photoelectrical properties. The XRD pattern, photoluminescence spectrum and the Kubelka-Munk representation (**Fig. 1** (a, b)) performed on the ZnO-Cu_xO core-shell nanowire arrays revealed only the typical signature for ZnO core.

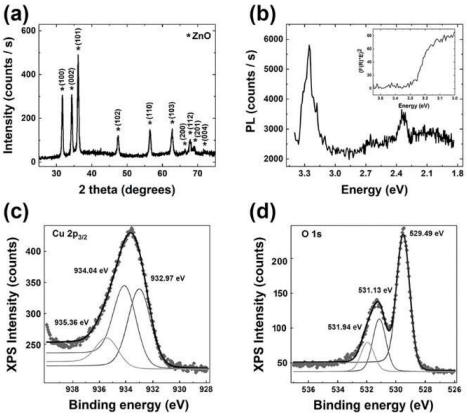

Fig. 1. *(a) XRD pattern, (b) photoluminescence spectrum, Inset: Kubelka-Munk representation, (c) and (d) XPS spectra of Cu 2p3/2 and O 1s levels for the ZnO-Cu_xO nanowire arrays.*

Accordingly, a hexagonal wurtzite phase, two emission bands: one in the UV region due to band-to-band transitions and the second one in the visible range is associated with deffects and a band gap around 3.28 eV. The absence of the Cu_xO shell into the XRD pattern can be explained by taking into account the amorphous nature of the film deposited by RF magnetron sputtering. In order to prove the existence of the Cu_xO shell and its oxidation state, XPS measurements were employed (**Fig. 1** (c, d)), demonstrating the presence of the Cu_xO layer formed by a mixture of CuO and Cu_2O with a mixture of 1:1.

The FESEM images of the as prepared ZnO-Cu_xO core-shell nanowire arrays (**Fig. 2** (a, b)) evidence a high density of cylindrical nanowires covering the zinc foil with lengths up to 30 μm and the diameters around 60 nm. The STEM image and the EDX elemental mapping of a single ZnO-Cu_xO core-shell heterojunction nanowire (**Fig. 2** (c, d)) confirms the diameter of about 60 nm estimated from the FESEM investigations and a thickness of about 15 nm for the Cu_xO shell. Also, the EDX analysis validate the formation of a radial heterojunction in the core-shell ZnO-Cu_xO nanowires with Zn K present only in the core area, Cu K to the edges of the nanowire and O K along the entire length and width of the nanowire.

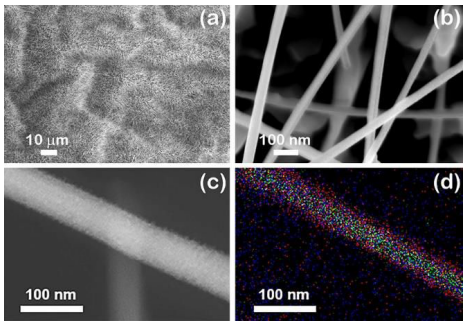

Fig. 2. *(a), (b) FESEM images at two different magnifications of the ZnO-Cu_xO core-shell nanowire arrays (c) STEM image and (d) EDX elemental mapping of a single ZnO-Cu_xO core-shell heterojunction nanowire.*

Fig. 3 (a) evidence a SEM image of a single ZnO-Cu_xO core-shell nanowire contacted by EBL with Pt metallic electrodes. The electrical properties performed in a cleanroom environment exhibit that the current-voltage characteristic of a single ZnO-Cu_xO radial heterojunction nanowire (**Fig. 3** (b)) contacted by electron beam lithography and thin film deposition techniques with platinum have a non-linear shape with a rectifying behaviour, which is typical for a ZnO-Cu_xO n-p diode. In the Inset, the EDS line profile analysis by STEM display a ZnO-Cu_xO nanowire partially uncovered by the Cu_xO shell at one end of the nanowire due to the process of nanowires harvesting in an alcoholic solution, explaining the rectifying behaviour of the single nanowire.

A direct-reverse ratio of approximatively 10^3 was calculated from the semilogarithmic representation of the current-voltage characteristic of an individual ZnO-Cu_xO radial heterojunction nanowire.

The current-voltage characteristic experimental data (black squares) was fitted (**Fig. 3** (b)) with a theoretical model (red line) considering an ideal diode and a parasitic series resistance coming from the individual ZnO-Cu_xO core-shell nanowire resistance, in order to estimate the ideality factor of about 1.3.

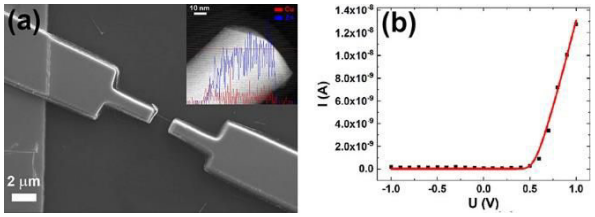

Fig. 3 *(a) SEM image, Inset: EDS Line profile analysis by STEM mode and (b) I-U characteristic (black squares) and theoretical fitting (red curve) of a single ZnO-Cu_xO core-shell nanowire contacted by EBL.*

Fig. 4 (a) revealed the current-voltage characteristics carried out on an n-p diode based on an individual ZnO-Cu_xO core-shell nanowire in dark (black dots) and under UV illumination at 405 nm (magenta dots) and 365 nm wavelengths (purple stars). All three characteristics have the same asymmetric shape due to the n-p heterojunction (**Fig. 4** (a Inset)) formed at the interface between the two semiconductors.

The increase in photocurrent under UV illumination is owed to the staggered gap heterojunction (type II band alignment) assembled between ZnO-Cu_xO which improves the charge separation efficiently at ZnO-Cu_xO interface. The current-time characteristic for an individual ZnO-Cu_xO core-shell nanowire-based photodetector under UV illumination (365 nm wavelength) reveals a rise and decay time of 43 s and a photocurrent gain of 17 nA. Taking into account the illuminated area (10^{-9} cm_2) and the incident light power of 4.55 mW/cm_2, at an applied bias of 1 V, key parameters for a photodetector, like responsivity, the external quantum efficiency and the detectivity, were estimated to be: 43.95 A/W, 149.3 % and 75.51 x 10^9 Jones. These results attest the potential application of the n-p diodes based on individual ZnO-Cu_xO core-shell nanowires as UV photodetectors.

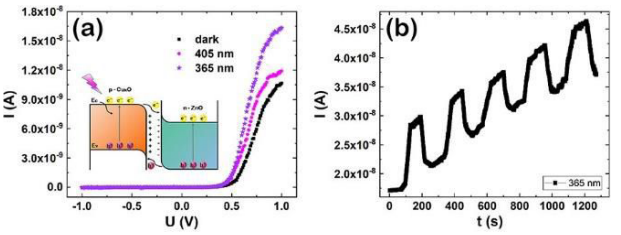

Fig. 4 *(a) I-U characteristics under dark (black dots), 405 nm UV illumination (magenta dots) and 365 nm UV illumination (purple stars), Inset: band diagram of a ZnO-Cu_xO heterojunction under UV illumination and (b) I-t characteristic under 365 nm UV illumination of a n-p ZnO-Cu_xO diode.*

Radial heterojunction ZnO-Cu_xO core-shell nanowires can be implemented as single components in n-p diodes acting as UV photodetectors, which can easily find applications in fields like flame detection, ozone sensing, leak detection, radiation detection, biological analysis, advanced communications and many others.

Funding from Core Program, contract No. PN18-11; PN-III-P2-2.1-PED-2016-1249; IDEI 124/2017.

References

[1] A. Costas, C. Florica, N. Preda, N. Apostol, A. Kuncser, A. Nitescu, I. Enculescu, "Radial heterojunction based on single ZnO-Cu_xO core-shell nanowire for photodetector applications", Scientific Reports 9, 5553 (2019).

Electrochemical Sensor for Carbonyl Groups in Oxidized Proteins

Teodor Adrian Enache, Elena Matei, and Victor Constantin Diculescu

Within a normal metabolism, the human body produces free radicals, mainly oxygen and nitrogen reactive species. At the same time, specific mechanisms with an important role in the prevention of aging process and pathophysiology of age-related diseases neutralize these radicals and maintain the balance between free radicals and antioxidants. The imbalance between production and accumulation of radical species in cells and the ability of the body to neutralize these reactive products results in oxidative stress which affects all cellular components, including DNA and proteins.

The interaction between proteins and reactive oxygen species results in protein oxidative damages such as the formation of carbonyl groups, which represents a type of oxidative stress biomarker. The objective of this research was to vdevelop an electrochemical sensor for the detection of carbonyl groups in proteins exposed to oxidative stress. [1].

Although proteins can be detected directly by voltammetric methods, **Fig. 1**, due to the electroactive residues, the quantification of carbonyl groups request specific recognition elements such as. dinitrophenylhidrazyne (DNPH), with high affinity for carbonyl moieties and with redox properties, **Fig. 2**.

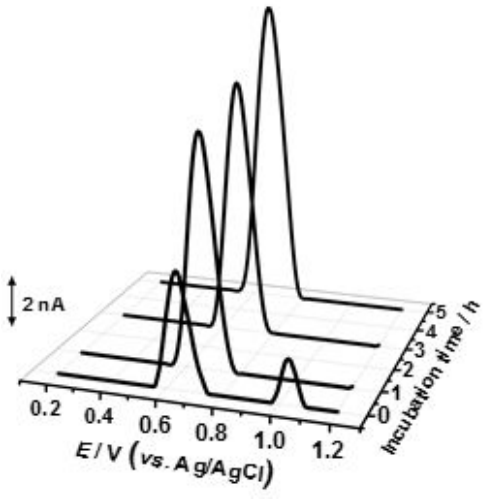

Fig. 1. *DP voltammograms recorded with the GC electrode for 0.5 mg mL^{-1} BSA after interaction with Fenton reagents during different times (BSAox).*

The differential pulse (DP) voltammogram recorded at GC electrode for 0.5 mg mL^{-1} bovine serum albumin (BSA), **Fig. 1**, showed two oxidation peaks at 0.65 V and 1.1 V, corresponding to the oxidation of tyrosine and tryptophan residues.

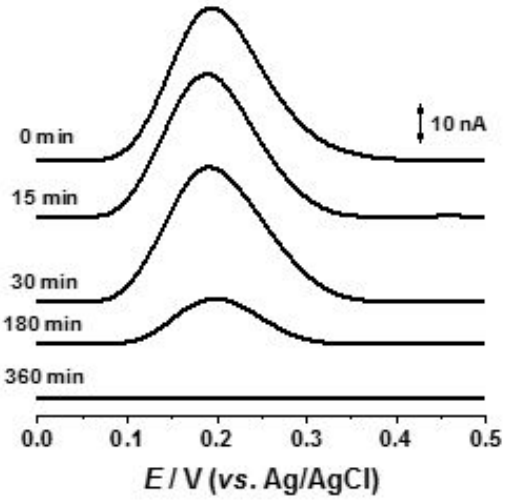

Fig. 2. *DP voltammograms recorded at GC electrode for 50 μM DNPH incubated with 0.5 mg mL^{-1} BSAox during different times*

The incubation of BSA with Fenton reagents induce oxid ative damage of BSA amino acid residues and formation of carbonyl groups (BSAox). From DP voltammograms recorded for BSAox solutions it was observed that the first oxidation peak increase with the incubation time while the second one disappeared, **Fig. 1**. This behaviour can be explained by taking into account the fact that the oxidation of BSA by Fenton reagents induces structural changes into secondary structure of BSA and increases the number of electroactive residues available for electrochemical oxidation. The DNPH molecule contains an electroactive hydrazine moiety, **Fig. 2**, and has the ability to covalently link to the carbonyl groups of BSAox. However, the reaction product DNPHBSAox is not electroactive and increasing the incubation time of DNPH with BSAox results in the decrease of free electroactive DNPH molecules. This phenomenon was pointed out by recording DP voltammograms in a solution containing DNPH and BSAox at different periods of time. It was observedthat the oxidation peak of DNPH decreases with the increase of incubation time and disappeared after 360 min of incubation, meaning that the conjugation reaction of DNPH with carbonyl groups of BSAox is completed and no free DNPH exists in solution.

These experiments showed that electrochemical methods can be used for the detection and quantification of oxidative damage in proteins.

In order to decrease the time of analysis while maintaining the advantages of voltammetric methods, an electrochemical sensor for detection of carbonyl groups in oxidized proteins based on the immobilization of DNPH at the GC electrode surface was proposed.

The immobilization procedure consisted on electrode surface modification with a polymer matrix as follows: 2 μL of 5% Nafion:4- styrenesulfonic acid (v:v) were deposited on the top of the electrode and allowed to dry, after which immersed for 3 min in a solution containing 500 μL DNPH. The obtained sensor was used for analytical quantification of BSAox using DP voltammetry.

Prior to electrochemical measurements, after each step of preparation of the sensor scanning electron microscopy (SEM) images were recorded. The images obtained revealed different morphologies ranging from a compact homogeneous surface with cluster structures, for Nafion-SS/GC to interconnected filaments and porous appearance decorated with globular structures, for DNPH/Nafion-SS/GC which becomes thicker and surface smoother after incubation in BSAox, **Fig. 3**.

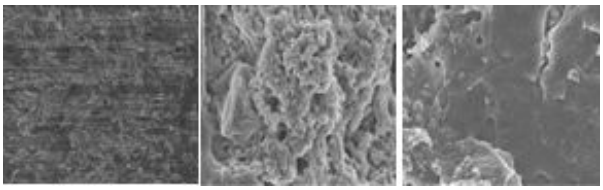

Fig. 3. *SEM images of A) SS-nafion/GCE B) DNPH/SS-nafion/GCE, and C) after interaction with 100 μg mL^{-1} BSAox*

Nevertheless, the formation of the immobilization matrix, as well as the DNPH sensing element and their selectivity for BSAox were proved by SPR experiments, Fig. 4.

The SPR signal obtained after injection of BSAox was about four times higher than that in the case of BSA, proving the working principle of the DNPH/SS-nafion sensor and the selectivity of the DNPH against carbonyl groups.

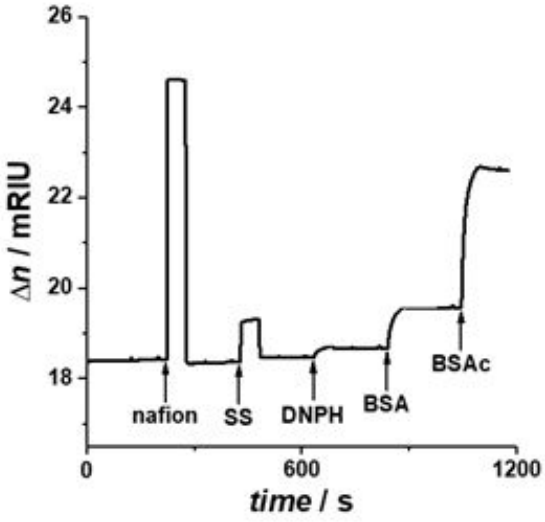

Fig. 4. *SPR signal recorded after consecutive injections of nafion, SS, and DNPH followed by 100 μg mL^{-1} BSA and BSAox*

Finally, the electrochemical sensor was tested against different concentrations of BSAox at a fixed incubation time of 20 s by DP voltammetry.

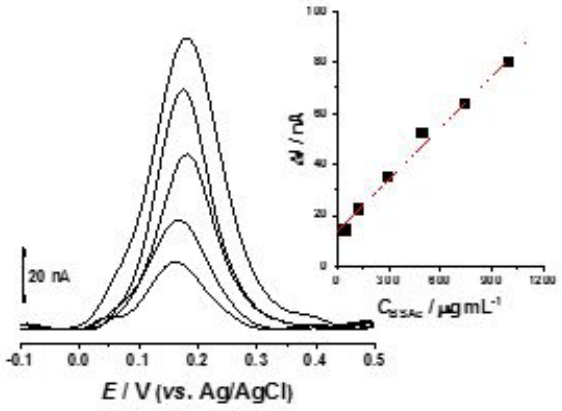

Fig. 5. *DP voltammograms and calibration curve btained for concentrations of BSAox between 50 and 1000 μg mL^{-1} during 20 s incubation.*

The sensitivity achieved was 0.015 nmol carbonyl per mg of oxidized protein with LOD of 0.75 pmol carbonyls.

References

[1] T.A. Enache, E. Matei, V.C. Diculescu, Anal. Chem. 2019, 91, 1920−1927.

Reticulated Mesoporous TiO_2 Scaffold, Fabricated by Spray Coating, for Large-Area Perovskite Solar Cells

A. G. Tomulescu, V. Stancu, C. Beşleagă, M. Enculescu, M. Florea, V. Dumitru, L. Pintilie, I. Pintilie, L. Leonat
In collaboration with
Assistant Prof. G. A. Nemneş, Faculty of Physics MDEO Research Center, University of Bucharest, Magurele 077125, Romania and
University of Bucharest, Faculty of Physics, 077125, Magurele, Ilfov, Romania

Lead halide perovskites are the new solar harvester materials. Currently they are studied as small area devices at the laboratory scale. A major challenge is to adapt the fabrication techniques to large scale manufacturing while maintaining high efficiency. The most efficient certified perovskite solar cells (PSCs) still use the "standard" mesoscopic structure where the electron selective part consists of a transparent stack of conducting oxides (TCOs)/TiO_2 compact (TiO_2c) and an additional TiO_2 mesoporous (TiO_2m) scaffold.

Most of the layers in a PSC are typically fabricated at the laboratory scale using spin coating, which cannot enable large-area thin-film fabrication. We report a simple deposition method for mesoporous TiO_2 applicable on large surfaces by adapting the spray-coating method in ambient atmosphere [1]. We used a computer-controlled system, assembled in-house

Fig. 1, with a pneumatic atomizing nozzle connected to a carrier gas source and a reservoir for precursor solution.

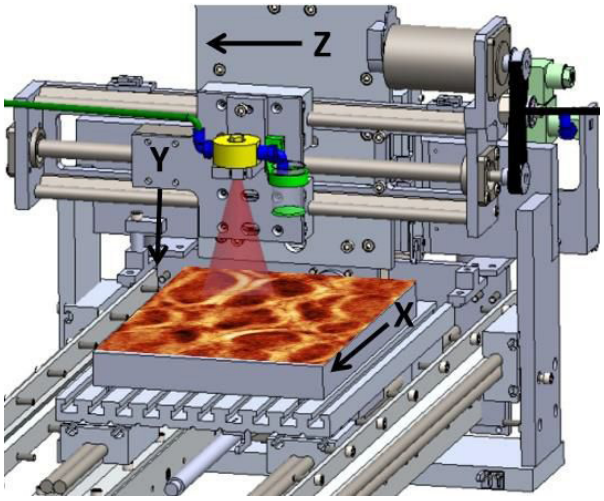

Fig. 1. *Scheme of the large-area spray deposition system*

Spray-deposition for TiO_2m induces the formation of a specific "reticulated" structure with oval-shaped cavities due to the overlapping of the droplets on the heated surface.

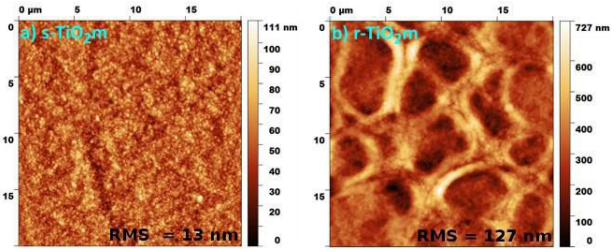

Fig. 2. *AFM images of the mesoporous TiO_2 layer fabricated by a) spin coating and b) spray coating.*

As depicted in the AFM images in **Fig 2**, the cavities have irregular dimensions, with diameters in the range of 3–7 μm and average height of 350 nm, an overall increase in roughness of one order of magnitude, compared with the spin-coated mesoporous (s-TiO_2m). The thickness of TiO_2c and TiO_2m was evaluated from cross-sectional SEM images, **Fig. 3**.

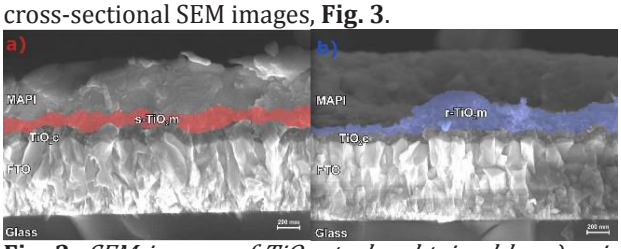

Fig. 3. *SEM images of TiO_2 stacks obtained by a) spin coating and b) spray coating with the perovskite layer deposited on top.*

TiO_2c is relatively thin, in the range of 90–110 nm. However, for the mesoporous, s-TiO_2m shows a quite uniform thickness of 200–250 nm, whereas for the reticulated mesoporous (r-TiO_2m) the thickness ranges from 70 to 350 nm. Consequently, when the perovskite (MAPI) was spun on top of the mesoporous, the sample with s-TiO_2m hosts a perovskite layer of ~400 nm thickness, whereas for r-TiO_2m, the perovskite thickness varies in a wider range, from 400 to 700 nm, due to the reticulated surface hosting. Approximately 30% (by volume) of the total 350 nm thick sprayed mesoporous film is represented by the cavities of the reticulated structure. The quantity of MAPI accommodated by these cavities is equivalent to an additional

100 nm-thick layer of active material. To evaluate the influence of the reticulated structure, we fabricated 42 solar cells, 21 with s-TiO_2m and 21 with r-TiO_2m. J–V characteristics for champion devices are shown in **Fig. 4**.

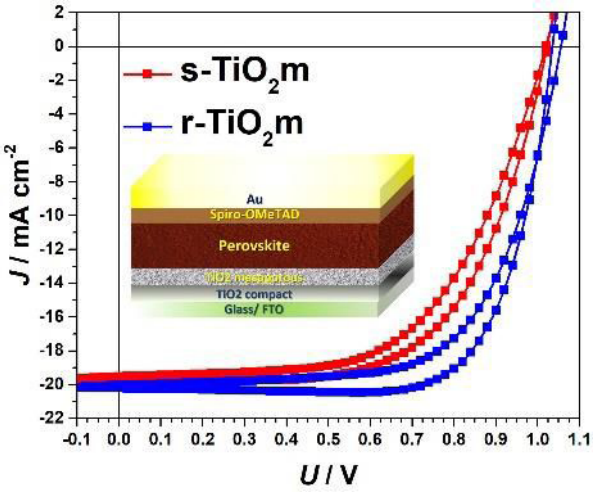

Fig. 4. *Electrical measurements of champion solar cells, insert – schematic structure of the solar cell*

A general improvement in all photovoltaic parameters for r-TiO_2m samples is observed. All parameters are shown in Table 1. The highest efficiency was obtained for the cell with the r-TiO_2m 14.53% revealing a 22% increase in efficiency of r-TiO_2m cells compared with s-TiO_2m PSCs.

		Active area (cm^2)	Voc (V)	Jsc (mA/cm^2)	FF (%)	PCE (%)
s-TiO_2m	C*	**0.09**	**1.021**	**19.6**	**61**	**12.14**
	A**	0.09	0.993	16.5	60	9.81
		1	0.971	12.6	45	5.89
r-TiO_2m	C*	**0.09**	**1.045**	**20.1**	**69**	**14.53**
	A**	0.09	1.046	17.8	64	11.95
		1	0.957	14.6	49	6.80

Table 1. Photovoltaic parameters as average between forward and reverse values for each parameter.

***Champion cell;** **Average values

Large-area devices follow the same trend where PCE is improved by over 15% for the devices with r-TiO_2m. The highest efficiency is 7.14% for r-TiO_2m and 6.65% for s-TiO_2m. Some aspects may justify this improvement for the r-TiO_2m: i) TiO_2/MAPI interface length is increased, subsequently the collection of photogenerated charges is increased; ii) r-TiO_2m is substantially thinner at the bottom of the cavities, which reduces charge losses within the most resistive component layer of the solar cell; iii) the cavities host an additional quantity of perovskite, providing better adhesion both on the bottom of the cavities as well as to the walls and inducing the formation of a compact homogeneous coverage with less pin-holes.

In conclusion, we find that spray deposition of mesoporous TiO_2 induces the formation of a specific reticulated, crystalline surface with considerably increased roughness, substantially thinner at the bottom of the cavities but with walls as high as hundreds of nm. In solar cells, we observed an improvement in all photovoltaic parameters for the samples with r-TiO_2m, resulting in an overall improvement in average PCE from 10% to 12% for small area devices. The same improvement is valid for large-area devices.

This entire spray-deposition assembly can be easily integrated into an automatic industrial equipment, due to its simple construction and operation, thus completing the printing technologies used for the other layers in a PSC (MAPI and hole transporter), making the full scale-up of PSCs very feasible.

Acknowledgements

Romanian Ministry of Research and Innovation and UEFISCDI for financial support through projects Core Program PN19-03, PN-III-16-48-01, and PN III-IDEI- 177/2017 and PN-III-P1-1.1-PD-2016-0703, respectively. The authors acknowledge that the fee for open-access publication was supported from the project DEXMAV, code 12PFE/2018, funded by the Romanian Ministry of Research and Innovation.

Reference

[1] A.G. Tomulescu, V. Stancu, C. Beşleagă, M. Enculescu, G.A.Nemneş, M. Florea, V. Dumitru, L. Pintilie, I. Pintilie, L. Leonat "Reticulated Mesoporous TiO_2 Scaffold, Fabricated by Spray Coating, for Large-Area Perovskite Solar Cells", Energy Technology vol. 8, issue 1, ian 2020, 1900922, available online from 26 September 2019 https://doi.org/10.1002/ente.201900922.

Evaluating the biological potential of some new cobalt(II) complexes with acrylate and benzimidazole derivatives

Ioana Dorina Vlaicu, in collaboration with:
R. Olar, C. Maxim, M. Badea
Department of Inorganic Chemistry, Faculty of Chemistry, University of Bucharest, 90- 92 Panduri Str, 050663 Bucharest, Romania;
M.-C. Chifiriuc
Department of Microbiology, Faculty of Biology, University of Bucharest, 1- 3 Aleea Portocalelor Str, 60101 Bucharest, Romania;
C. Bleotu, Stefan S Nicolau
Institute of Virology, 285 Mihai Bravu Ave, Bucharest, Romania;
N. Stănică
Romanian Academy, 'Ilie Murgulescu' Physical Chemistry Institute, 202 Splaiul Independentei, 77208 Bucharest, Romania;
G. Vasile Scăeţeanu
Department of Soil Sciences, University of Agronomical Sciences and Veterinary Medicine, 59 Mărăşti Str., Sector 1, 011464 Bucharest, Romania;
C. Dulea
Pharma Serv. International SRL, 52 Sabinelor Str., Sector 5, 050853 Bucharest, Romania;
S. Avram
Department of Anatomy, Animal Physiology and Biophysics, Faculty of Biology, University of Bucharest, 91- 95 Splaiul Independentei, Bucharest, Romania

Several studies previously reported revealed that metal complexes with mixed ligands (e.g. acrylate and imidazole derivatives) are promising candidates for further in-depth studies concerning their *in vitro* antimicrobial activity or their *in vivo* cytotoxic properties [1-3]. In the flow of these studies, four new cobalt complexes have been synthesized and subjected to structural and biological characterization. Predictive pharmacokinetic (ADME), toxicity and druglikeness profiles were evaluated for these Co(II) complexes.

The new Co(II) complexes have been obtained following the procedure described in Scheme 1 and they contain mixed ligands: acrylate ion (acr) and benzimidazole/ benzimidazole derivatives. Based on the elemental and mass spectrometry data they were formulated with the general formula $[Co(L)_2(acr)_2]\cdot nH_2O$, where L and n are as follows: [(1) L: benzimidazole (HBzIm), n: 0.5; (2) L: 2-methylbenzimidazole (2- MeBzIm), n: 0.5; (3) L: 5-methylbenzimidazole (5- MeBzIm), n: 0; (4) L: 5,6-dimethylbenzimidazole (5,6- Me2BzIm), n: 0].

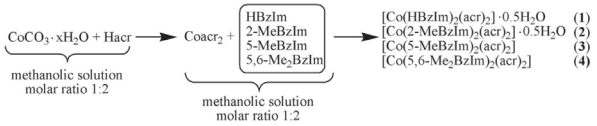

Scheme 1. *Synthesis procedure described for complexes (1) – (4).*

Fourier transform- infrared data indicate both unidentate and chelate coordination modes of the acrylato ligands in all four Co(II) complexes.

Benzimidazoles coordinate to the cobalt ion in a unidentate fashion by pyridine-type nitrogen atoms. The trigonal bipyramid geometry of cobalt ion in Co(II) complexes was assigned by data correlation of UV–Vis-NIR spectra and magnetic moments measurements.

Single- crystal X- ray diffraction reveals a mononuclear structure with a pentacoordinated cobalt(II) ion, connected to two acrylato coordinated in different modes and two unidentate 5,6-dimethylbenzimidazole ligands for compound (4) (**Fig. 1**).

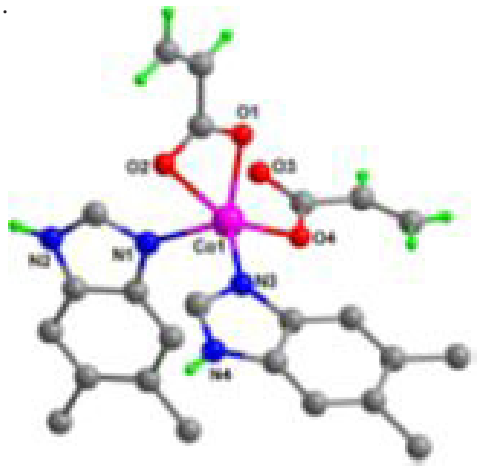

Fig. 1. The asymmetric unit for (4) along with the atoms numbering scheme

Thus, the single crystal X-ray diffraction confirmed the other experimental observations which lead to the proposed coordination for the other three Co(II) complexes (**Fig. 2**).

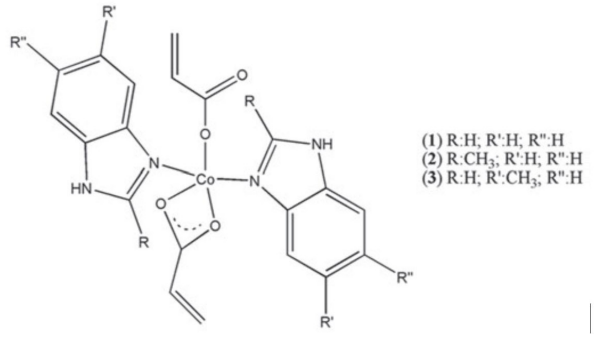

Fig. 2. *Proposed coordination for cobalt complexes (1)–(3).*

The biological tests were performed against several microbial strains. Thus, microbiological assays indicated that Co(II) complexes present a very good to good activity against Candida albicans 1760, Enterococcus faecium E5, Bacillus subtilis ATCC 6683 and Escherichia coli ATCC 25922.

The cytotoxicity was evaluated on HCT8 cellular lines (**Fig. 3**) and the cell cycle analysis was performed on HT29 cellular lines.

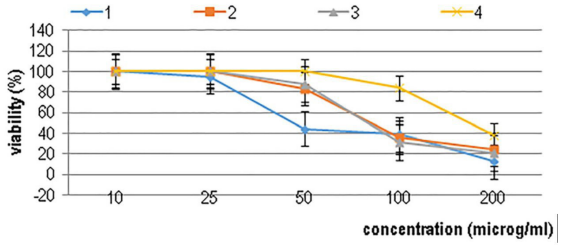

Fig. 3. *The Co(II) complexes effect on HCT8 cells [complex (1) – blue curve; complex (2) – orange curve; complex (3) – gray curve; complex (4) – yellow curve].*

The MIC (minimal inhibitory concentration) values were correlated with computational results regarding the molecular features, and it was found that complex (4) presents good activity against C. *albicans,* S. *aureus*, B. *subtilis* and *E. coli*, meanwhile complex (3) efficiently inhibits growth of S. aureus.

The evaluation of the drug-likeness profiles for all Co(II) complexes revealed that these compounds present a good drug-like profile and all compounds respected the Lipinski and Veber rules. Besides, Co(II) complexes presented a high bioavailability, being good drug candidates in oral administration.

The predictive ADMET profiles of Co(II) compounds were evaluated and the results revealed that Co(II) compounds present a high intestinal absorption and relatively less absorption at Caco-2 permeability. Distribution results indicated that complexes (1) and (2) present a low BBB penetration, meanwhile complexes (3) and (4) present a high BBB permeability. Interestingly, the central nervous system (CNS) permeability varies from −3.99 (for (1) to −3.60 for (4)) and, consequently, the risks for the occurrence of CNS side-effects are reduced.

Regarding the toxicity profiles, from predicted ADMET profiles it could be seen that all Co(II) compounds presented a low toxicity for humans, but high toxicity for fish and *T. pyriformis.* All subjected Co(II) complexes presented no carcinogen or mutagen features (AMES test negative). Also, it is important to mention that for complexes (1)–(4) non-hepatotoxicity and no skin sensitization were predicted, in correlation with a weak skin permeability.

Our results highlight that these four Co(II) complexes depicted in the present study are suitable to be used as efficient pharmacological agents.

References

[1] M. Badea, I.D. Vlaicu, R. Olar, M. Constand, C. Bleotu, M.C. Chifiriuc, L. Marutescu, V. Lazar, M.N. Grecu, D. Marinescu, Therm. Anal. Calorim. 118, 1119 (2014).

[2] I.D. Vlaicu, G. Borodi, G. Vasile Scăeţeanu, M.C. Chifiriuc, L. Măruţescu, M. Popa, M. Ştefan, I.F. Mercioniu, M. Maurer, C. Daniliuc, R. Olar, M. Badea, Molecules 23, 3253 (2018).

[3] I.D. Vlaicu, R. Olar, G. Vasile Scăeţeanu, L. Silvestro, M. Maurer, N. Stănică, M. Badea, J. Therm. Anal. Calorim. 134, 503 (2018).

[4] I.D. Vlaicu, R. Olar, C. Maxim, M.-C. Chifiriuc, C. Bleotu, N. Stănică, G. Vasile Scăeţeanu, C. Dulea, S. Avram, M. Badea, Appl. Organometal Chem. 33, e4976 (2019).

FastOs®BG-derived alkali-free bioactive glasses enclosing ZnO and/or SrO as joint coefficient of thermal expansion modulators and therapeutic agents

A.C. Popa, M. Cioangher, V. Dumitru, G.E. Stan
in cooperation with
M. Necsulescu
Army Centre for Medical Research, 020012 Bucharest, Romania
H.R. Fernandes, J.M.F. Ferreira
Department of Materials and Ceramics Engineering, CICECO, University of Aveiro, 3810-193 Aveiro, Portugal
C. Luculescu
National Institute for Lasers, Plasma and Radiation Physics, 077125 Magurele, Romania
B.W. Stuart, D.M. Grant
Faculty of Engineering, University of Nottingham, NG7 2RD, UK

Silica-based bioactive glasses (SBGs) possess the highest indicators of bioactivity known today, which are directly reflected in their ability to generate a fast and strong bond with hard tissues. Thereby, there is no surprise that SBGs are considered the forefront candidate materials for osseointegrative implant and bone regeneration applications. However, as the deficient treatments enabled bacterial strains to undertake genome mutations and attain an increased resistance to classical antibiotics. As the first bacterial strains resistant to all available antibiotics in medicine have been identified, we are fast-forwarding into the "post-antibiotic era". Consequently, an effective bone implant should be also equipped with pertinent defence features against bacterial infection.

The antibacterial effect is desirable and crucial in the case of temporary trauma associated with scaffold and implant surgery procedures, as in such situations in which the local immune response of the human body is weakened and incapable of a proper defence. Nowadays, one ubiquitous challenge is to develop implant coating materials combining high antimicrobial efficiency against both Gram-positive and Gram-negative resilient bacterial strains, good viability and proliferation of human mesenchymal stem cells, controlled degradation and high mechanical adhesion to the substrate. Yet, the significant thermal expansion coefficients (CTE) mismatch between commercial SBG systems (~14–17×10^{-6}×°C^{-1}) and titanium (Ti) and its super-alloys (~8.5–9.6×10-6×°C^{-1}), the prominent implant materials, is currently impeding the successful implementation of SBGs implant coatings due to the risk of high internal stresses resulting in poor adhesion. Alkali-free SBGs, such as FastOs®BG, are starting to be recognised for their noteworthy biological performances, among one can emphasize the: (i) lower degradation rate with respect to alkali-rich SBGs; (ii) lack of cytotoxic and genotoxic effects; (iii) high biomineralization capacity; and (iv) osteoconductivity and osteoinductivity [1].

***Table 1**: Oxide concentration (in mol %) of the as-synthesized SBG powders, with and without ZnO and/or SrO doping.*

SBG sample code	Oxide concentration (mol %)						
	SiO_2	CaO	P_2O_5	MgO	CaF_2	ZnO	SrO
Z0S0 (FastOs®BG)	38.5	36.1	5.6	19.2	0.6	–	–
Z4S0	38.5	36.1	5.6	15.2	0.6	4.0	–
Z6S0	38.5	36.1	5.6	13.2	0.6	6.0	–
Z0S6	38.5	30.1	5.6	19.2	0.6	–	6.0
Z4S4	38.5	32.1	5.6	15.2	0.6	4.0	4.0
Z6S4	38.5	32.1	5.6	13.2	0.6	6.0	4.0
Z6S6	38.5	30.1	5.6	13.2	0.6	6.0	6.0

Moreover, the decrease of a glass CTE could be achieved by the reduction/elimination of its alkali oxides content, which makes alkali-free SBGs highly appealing. Having these critical challenges in mind, in the framework of this study series of six alkali-free silica-based bioactive glasses (SBG) with ZnO and/or SrO additives (containing 0 – 12 mol%) were derived from the FastOs®BG system and synthesized by melt-quenching (see Table 1). They were subjected to a multi-parametrical structural (*X-ray diffraction, Fourier transform infrared and micro-Raman spectroscopy*), dilatometry, and biological (*ion release studies by inductively coupled plasma mass spectrometry, antimicrobial suspension inhibition and agar diffusion tests against Staphylococcus aureus and Escherichia coli strains, and human mesenchymal stem cells (hMSCs) cytocompatibility assays*) evaluation [2].

The combinative action of Zn and Sr antimicrobial agents incorporated in alkali-free SBG systems was investigated to optimise the composition such as to both (a) enable reduced differences in CTEs

between a potential coating and the Ti substrate and (b) hinder the development/prevent the adaptability of microorganisms.

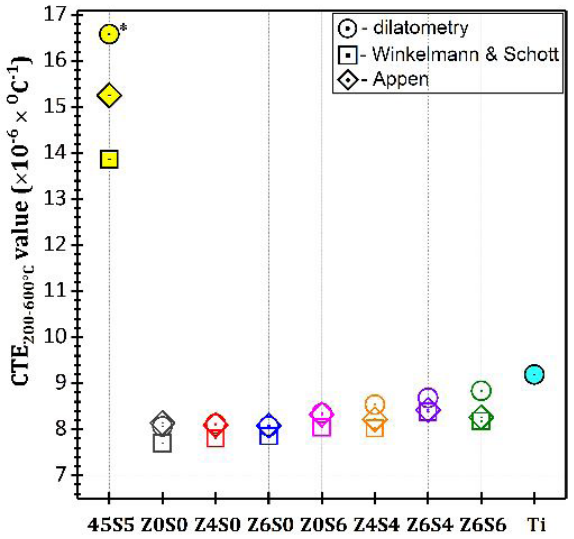

Fig. 1. *CTE (200 – 600°C) values obtained by dilatometry measurements (circles) and estimated on the basis of the empirical coefficients αi proposed by Wilkelmann and Schott (squares) or Appen (diamonds).*

By elimination of alkali oxides from the SBG composition, a significant reduction of the CTE values was achieved (**Fig. 1**), with a closer match to the CTE of Ti when both ZnO and SrO were incorporated into the glass. Subsequently, good prospects for the fabrication of low mechanical stress implant coatings using deposition methodologies such as magnetron sputtering could emerge from the development of such SBG formulations.

The biological tests evidenced that the new SBG formulations did not induce cytotoxic effects in hMSCs cultures, but were active against both Gram-positive and Gram-negative pathogens. A higher antibacterial activity was observed in the case of the materials that combine the two antimicrobial agents (ZnO and SrO), thus advancing these SBG formulations as solid coating variants for osseous implants.

Overall, the interpolation of the physico-chemical and biological results, suggested the Z6S4 formulation (mol%: SiO_2–38.49, CaO–32.07, P_2O_5–5.61, MgO–13.24, CaF_2–0.59, ZnO–6.0, SrO–4) as the best candidate for the future development of biofunctional glass coatings, as it possessed a coefficient of thermal expansion (~$8.68\times10^{-6}\times°C^{-1}$) matching well that of Ti and its medical alloys, whilst enabling a remarkable antimicrobial activity and minimal cytotoxic effect (**Fig. 2**).

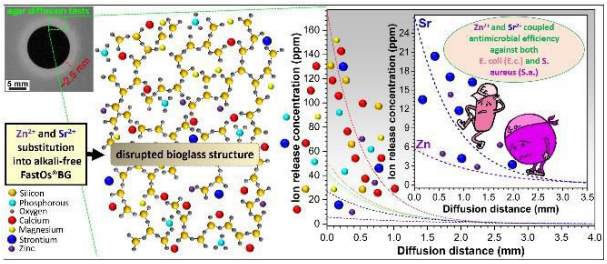

Fig. 2. *Synopsis: The structural and compositional features of the Z6S4 bioactive silica-based glass formulation, enables the release of Zn and Sr therapeutic ions in doses of ~6 mg/L and ~30 mg/L, respectively, which consequents into a strong antimicrobial effect against both Gram-positive (S. aureus) and Gram-negative (E. coli) bacterial strains.*

This research was funded by the Romanian Ministry of Research and Innovation, CCCDI-UEFISCDI, in the framework of projects PN-II-RU-TE-2014-4-0180, PN-III-P1-1.1-TE-2016-1501, and Core Programme PN18-110101.

References

[1] A. Goel, S. Kapoor, R.R. Rajagopal, M.J. Pascual, H.W. Kim, J.M.F. Ferreira, Acta Biomater. 8 (2012) 361–372.
[2] A.C. Popa, H.R. Fernandes, M. Necsulescu, C. Luculescu, M. Cioangher, V. Dumitru, B.W. Stuart, D.M. Grant, J.M.F. Ferreira, G.E. Stan, Ceram. Int. 45 (2019) 4368–4380.

MgB_2 superconductor: machinable material for magnetic shielding applications and textured bulk for performance enhancement

P. Badica*, G. Aldica, M. Burdusel, M.A Grigoroscuta, A.M. Ionescu, M. Enculescu, I. Pasuk, A. Kuncser, V. Sandu
in collaboration with
University Politehnica of Bucharest, Romania
National Institute for Materials Science, Tsukuba, Japan
Polytechnic University of Turin, National Institute Nuclear Physics, Turin, University of Turin, Italy

Research is focused on fabrication of high quality superconducting materials based on MgB_2 for magnetic shielding and permanent magnets applications. MgB_2 presents attractive features such as low cost, light weight, and long coherence length.

Fabrication of parts with complex shapes [1] and performance enhancement are important issues. We continue studies in this direction. In our Lab., dense bulk samples of MgB_2 (relative density above 95%) are obtained by Spark Plasma Sintering (SPS) from MgB2 commercial powders.

A machinable cylinder [2] of MgB_2 was obtained by adding hexagonal BN. The additive allows shaping the cylinder on a lathe machine into a tube with inner and external radius of $R_i = 7$ mm and $R_e = 10.15$ mm, respectively (**Fig. 1*a, inset***). Hall sensors were placed inside the tube at different positions as presented in **Fig. 1a, b** and the magnetic field was measured. The ratio between the applied magnetic field and the measured field defines the shielding factor (**Fig. 1 *c, d***). Despite a height/radius aspect ratio of only 1.75, shielding factors (**Fig. 1 c**) for the arrangement from **Fig. 1a**, location z1, are higher than 150 and 75 at T = 20 K and in axially-applied magnetic fields $\mu_0 H_{appl}$ of 0.1 and 1.0 T, respectively. For the unfavorable arrangement from **Fig. 1b**, at location y1, shielding factors are still above 4 at T=20-35 K and for a magnetic field of 0.1 T (**Fig. 1d**).

Texturing [3] of materials with anisotropy as for MgB_2 is very attractive for performance enhancement. MgB_2 has a hexagonal crystal structure with a different magnetic susceptibility in the (*ab*)-plane and along the *c*-axis.

To obtain (001) textured bulks, slip casting under a high magnetic field of 12 T (**Fig. 2*a***) was employed to obtain partially oriented green MgB_2 compacts. The texture degree as determined from the X-ray diffraction was 3.5 % and it is further enhanced to ~21 % during subsequent SPS of the green compacts (**Fig. 2c**).

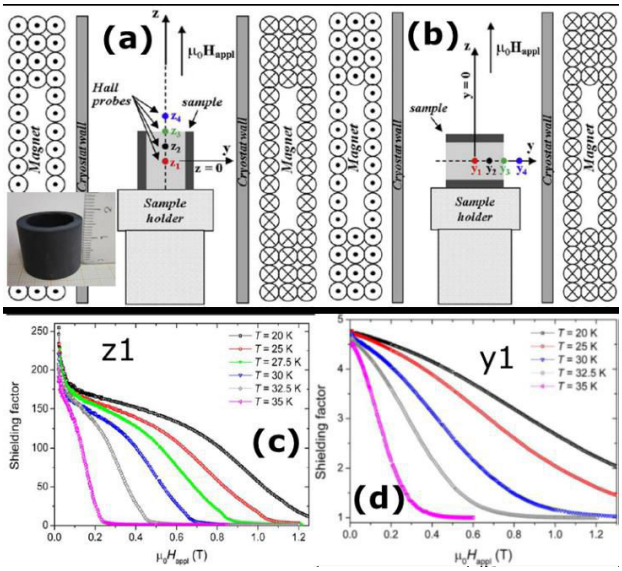

Fig. 1. ***(a) and (b)*** *- Measurement arrangements for determination of the shielding factors; (c) and (d) – Shielding factors as a function of applied magnetic field for measurements with the Hall sensor positioned at z1 and y1. Inset to (a) shows the MgB_2 tube obtained by SPS and machining.*

The critical current density Jc displays anisotropy relative to the orientation of the measuring magnetic field (**Fig. 2*b*, Fig. 3**). One also observes that at high magnetic fields and at 20 K, the critical current density of the oriented sample 'd' (**Fig. 2*c*, Fig. 3**) is higher than for the randomly oriented SPSed reference sample (***sample 'b' in* Fig. 2 *c***). Work demostrates the possibility of (001) textured MgB_2 bulk fabrication and performance enhancement.

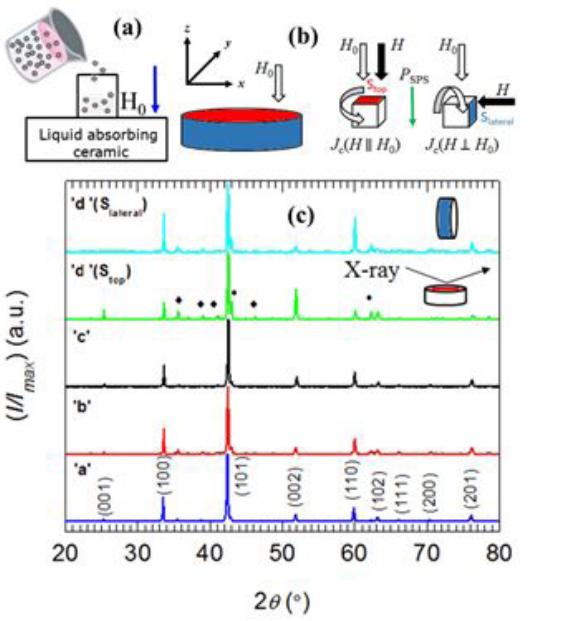

Fig. 2. ***(a)*** *– Schematics of slip casting under 12 T; (b) – Measurement setup (in XRD from* ***Fig. 2*** *c and in magnetic measurement from* ***Fig. 3****) of as-processed MgB_2 green and SPSed samples; (c) XRD patterns of MgB_2 samples: 'a'— raw MgB_2 powder; 'b'— reference randomly oriented sample obtained by SPS, 'c'— green body after 12 T slip casting, and 'd'— sample obtained by SPS using the green body 'c' (XRD was measured on S_{top} and on $S_{lateral}$, see* ***Fig2*** *b).*

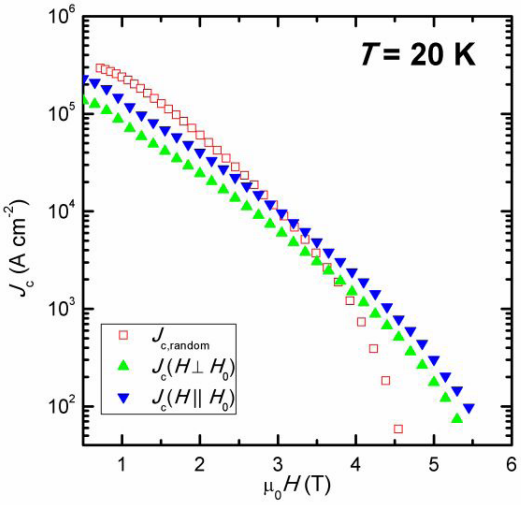

Fig. 3. ***(c)*** *Curves of $J_c(H)$ at 20 K for partially oriented SPSed sample 'd' (denoted $J_c(H//H_0$; $J_c(H \perp H_0)$) and for randomly oriented SPSed reference sample 'b'.*

References

[1] G.V. Aldica, M. Burdusel, M. Cioca, P. Badica, Machinable superconducting material and field concentrator/storer made of a material based on MgB_2, machinable by chip removable, Patent Number RO130252-A2.

[2] L. Gozzelino, R. Gerbaldo, G. Ghigo, F. Laviano, D. Torsello, V. Bonino, M. Truccato, D. Batalu, M.A. Grigoroscuta, M. Burdusel, G.V. Aldica, P. Badica, Passive magnetic shielding by machinable MgB_2 bulks: measurements and numerical simulations Supercond. Sci. Technol. 32 (2019) 034004 (DOI: 10.1088/1361-6668/aaf99e) (IF=2.489; AI=0.8).

[3] M.A. Grigoroscuta, V. Sandu, A. Kuncser, I. Pasuk, G. Aldica, T.S. Suzuki, O. Vasylkiv, P. Badica, Superconducting MgB_2 textured bulk obtained by ex situ spark plasma sintering from green compacts processed by slip casting under a 12 T magnetic field, Supercond. Sci. Technol. 32 (2019) 125001 (DOI: 10.1088/1361-6668/ab4620) (IF=2.489; AI=0.8).

$SrTiO_3$ single crystals without macrodefects for substrates used in thin films growth

P. Badica*, A. M. Vlaicu, L. Nedelcu, N. Preda, M. Secu, A.C Kuncser
in collaboration with
INOE 2000, Magurele, Romania
Fuuruchi Chemical Co., Tsukuba, Japan
Kanazawa Insitute of Technology, Hakusan, Japan
National Institute for Materials Science, Tsuka, Japan

The $SrTiO_3$ (STO) crystals are commercially produced by the flame fusion method, also named *Verneuil process*. Substrates for thin films growth are the main application of the STO crystals. At the moment, STO is also explored as an active material for novel devices in the power, energy and microelectronics fields.

Growth of large crystals is considered challenging. Usually, the commercial STO substrates are obtained with a diameter of 10-20 mm. Furthermore, the quality of the commercial STO crystals seems unacceptable for fabrication of the mentioned new devices. Literature presents different attempts to grow top quality STO crystals by other methods. Some of these methods are not convenient for commercial production due to small sizes, small growth rates, or low yield.

Regardless of the growth method, usually bulk STO crystals are obtained with a significant amount of oxygen vacancies. The dislocation density varies also depending on processing. Their color is black and they are conductive. Oxygenation is the next processing step, so that vacancies are removed, the crystal is insulating and the color becomes transparent white. The size of the crystal is defined in the crystal growth step, while the final quality will strongly depend also on the oxygenation treatment.

In our work [1, 2] we performed a complex optimization process of the growth by Verneuil method and characterization of the STO crystals to assess their quality. The target was to obtain STO single crystals of 30 mm in diameter. Growth is limited to approximately 4.75 h, i.e. to one production shift. Experiments are realized at the Furuuchi plant under industrial environment.

During typical industrial growth, conditions are not constant and at the end of the growth in the crystal there will form a region with macrodefects such as bubbles, cracks, and others. Among the difficult issues of the crystal growth are melt control and evaporation of Sr-oxide raw material. The length of the bubble region is D (**Fig. 1**).

Desirable is to obtain crystals with D = 0 mm and with as large as possible effective length, EL. Effective length is the length that can be used for fabrication of commercial substrates or for other applications (**Fig. 1**).

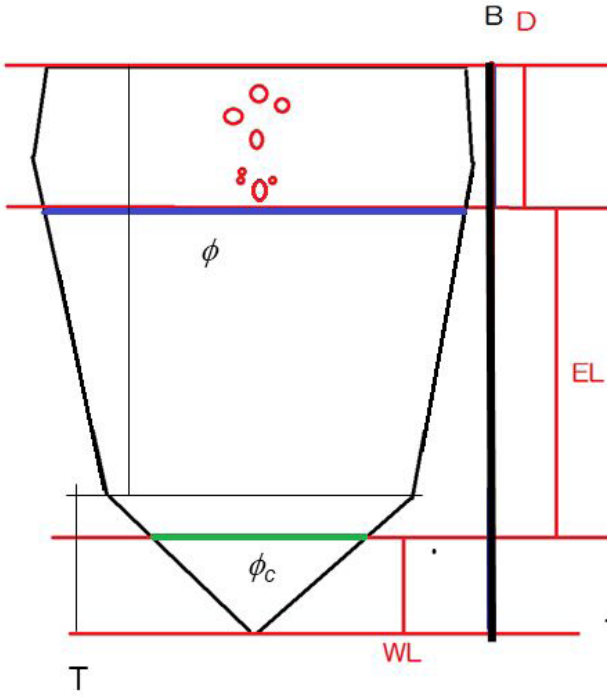

Fig. 1. *Schematic drawing of a STO crystal obtained by Verneuil method (growth starts from the bottom end). The crystal size parameters of interest are: B=length of the as-grown crystal, D= length of the region with bubbles, EL = (effective) length of the commercial product, WL= waste (tip) length, ϕ= maximum diameter of the (effective) commercial product, ϕ_C = designed (minimum) diameter of the (effective) commercial product, T= tip length.*

In the growth, there are employed source materials such as Sr and Ti oxides. The Sr oxide powder is mixed with $SrCO_3$ additive powder up to 5 wt. %. There are two flows of H_2, inner and outer, one of oxygen. Pulling rate and the rotation speed of the seed are controlled.

The optimum growth conditions for which the length of the region with bubbles D is zero and the effective length EL (i.e. the crystal length of commercial value) is maximized are for the amount of $SrCO_3$ additive of ~3 wt. % and for H_2 outer flow rate of ~35 l/min. The amount of $SrCO_3$ and the H_2 outer flow rate show the strongest influence on the growth. The influence on growth of other growth parameters (H_2 inner flow rate, O_2 flow rate increase, rotation speed) is also investigated and optimum values are established.

After growth and oxygenation, selected STO single crystals are characterized by X-ray diffraction, microscopy, photoluminiscence, Raman, and THz spectroscopy. They are compared with a commercial substrate and with crystals reported in literature. The as-grown crystals of 30mm in diameter (**Fig. 2**) without macrodefects (D = 0 mm) are of similar quality with the commercial substrate of 10 mm x 10 mm x 0.5 mm. Noticed differences were discussed in relation to oxygen vacancies.

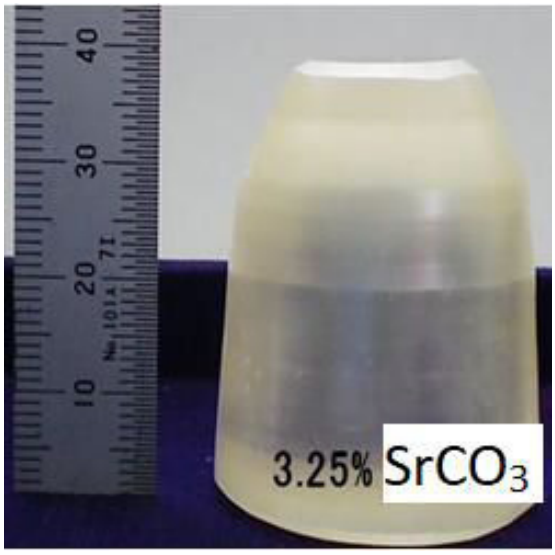

Fig. 1. *STO crystal obtained by Verneuil method grown for 3.25 wt % $SrCO_3$ additive, H_2 inner flow rate = 5 L/ min, H_2 outer flow rate = 35 L/min, oxygen-flow-rate-increase = 0.07 L/min2, rotation speed = 15 rpm, growth time = 4.75 h, and pulling rate = 10 mm/h.*

This work opens the possibility for the industrial growth of large $SrTiO_3$ single crystals and commercialization of large area substrates for thin films growth.

References

[1] Y. Tateno, K. Endo, S. Arisawa, A. M. Vlaicu, L. Nedelcu, N. Preda, M. Secu, R. Iordanescu, A.C. Kuncser, P. Badica, Growth of $SrTiO_3$ single crystals with a diameter of about 30 mm by the Verneuil Method, Crystal Growth and Design 19 (2019) 604-612 (IF=4.153, AI=0.9).

[2] P. Badica, Bubble-free $SrTiO_3$ crystals 30 mm in diamter by flame-fusion method, Science Trends (https://sciencetrends.com/bubble-free-srtio3-crystals-30-mm-in-diameter-by-flame-fusion-growth-method/)

*Contact: badica2003@yahoo.com (P. Badica)

Efficient catalytic materials for CH_4 oxidation

Florentina Neațu, Ștefan Neațu, Corneliu Ghica, Mihaela Florea
in collaboration with
Simona Somacescu[1], Nicoleta Cioatera[2], Petre Osiceanu[1], Jose Maria Calderon-Moreno[1], Georgeta Postole[3], Adriana Urdă[4], Laurence Massin[3], Patrick Gélin[3]
1. "Ilie Murgulescu" Institute of Physical Chemistry, Romanian Academy, Spl. Independentei 202, 060021, Bucharest, Romania
2. University of Craiova, Department of Chemistry, Calea Bucuresti 107i, 200478, Craiova, Romania
3. Univ. Lyon, Universite Claude Bernard Lyon 1, IRCELYON, Villeurbanne, France
4. University of Bucharest, Faculty of Chemistry, B-dul Regina Elisabeta 4-12, 030018 Bucharest, Romania

Methane transformation presents an increased interest due to its multiple uses like: (i) partial oxidation to methanol or formaldehyde, (ii) ethylene formation by oxidative coupling, (iii) syngas formation by steam reforming (MSR, eq.1) followed by water-gas shift (WGS) reactions with CO_2 formation (eq.2):

$CH_4 + H_2O \leftrightarrow CO + 3H_2$ (1)

$CO + H_2O \leftrightarrow CO_2 + H_2$ (2)

or by catalytic methane partial oxidation (CPOM)

$CH_4 + O_2 = CO + 2H_2$ (3)

Indirect transformation of CH_4 (by MSR or CPOM) in H_2 is an important reaction that takes place at the anode of solid oxide fuel cells (SOFCs) further allowing its transformation into electrical current. Thus, using CH_4 as fuel in SOFC can be an alternative to the currently hydrogen implemented technologies. Moreover, there is a constant need to develop new materials that rends SOFC working temperature to decrease from 800^{0}C–1000°C to 600^{0}C–800°C. Since indirect CH_4 transformation implies CO and CO_2 formation, the materials used as anode in SOFC must be tolerant to C deposition, reoxidation and S-poisoning. In this report we are emphasizing two types of materials an ABO_3 perovskite – $La_{0.75}Sr_{0.25}XO_3$ (X = Fe, Mn or Cr) and a modified yttria stabilized zirconia (YSZ) –$NiO/CeO_{2-\delta}$-YSZ that are able to perform MSR and CPOM, respectively. Both materials ABO_3 perovskite and modified yttria stabilized zirconia (YSZ) were synthesized by an easy and cost-efficient method preparation like citrate method or hydrothermal synthesis route, respectively.

The insertion of Fe, Mn and Cr (namely LSF, LSM and LSC, respectively) in $La_{0.75}Sr_{0.25}O_3$ perovskites as B cation has different contribution in the CH_4 steam reforming with or without H_2S. One of the most important behaviour of these catalysts is the substantial improvement of the CH_4 conversion in the first minutes when H_2S is added. Moreover, if LSF and LSM activity slowly decrease after the first minutes, LSC activity stabilizes at higher values when H_2S is present (**Fig. 1**). This special behavior can be explained by the gradual O^{2-} substitution with S^{2-}, which promotes the CH_4 steam reforming. In the case of LSF and LSM, S^{2-} substitution leads to the sulfites/sulfates formation at the catalyst surface, which in time deactivates the catalysts. The LSC material's good activity in time could be associated with its high ability to create O^{2-} vacancies, which are stabilized by S^{2-} insertion at the surface, therefore the presence of H_2S is beneficial. In contrast with LSF and LSM, LSC present no sulfur-containing phase as revealed by XRD, which can suggest that S^{2-} migration into the bulk proceeds very slowly limiting the deactivation process. Therefore, the LSC exhibit high resistance to C deposition and S tolerance.

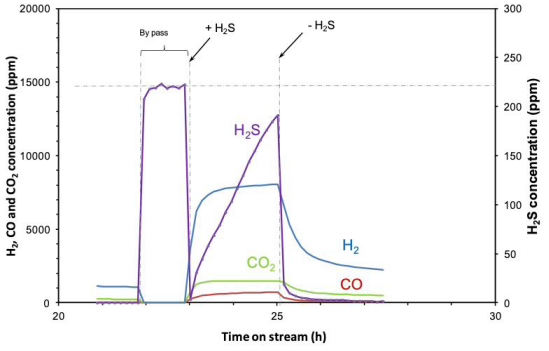

Fig. 1. *H_2, CO, and CO_2 formation rates as a function of time during CH_4/H_2O reactions (50 vol. % CH4/ 5 vol. % H2O, N_2 balance) at 750 °C with/without H_2S (220 ppm) over LSC. Total flow rate 7 $_{LNTP}hr^{-1}$; 100 mg catalyst.*

The second series of anodes $NiO/CeO^{2-\delta}$-YSZ with different amounts of Ni (5, 10 and 15 mol%) and

20% of Ce (named further N1, N2 and N3, respectively) presents also a high carbon tolerance in CPOM. Regarding the structure of the materials prepared, they present bimodal mesopores, and in the case when only 5% of Ni was used, Ni was entirely incorporated in the YSZ matrix, as revealed by XRD and HRTEM. An increase of Ni content leads to a secondary phase formation NiO, which segregates from the YSX lattice.

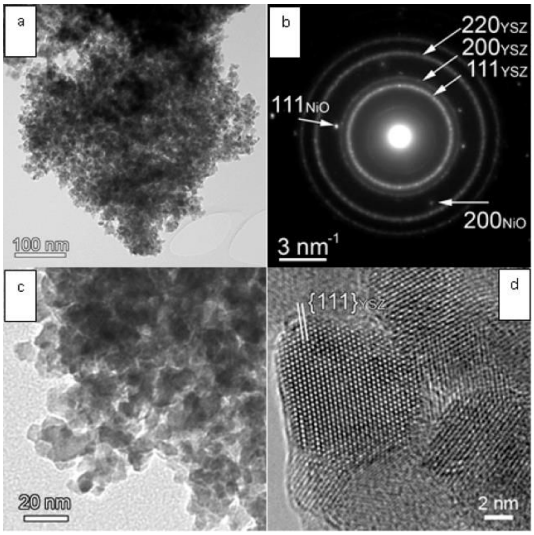

Fig. 2. ***(a)*** *Low-magnification TEM image showing nanostructured agglomerate from the sample N3. (b)*

Associated SAED pattern proving the formation of cubic YSZ as prevailing structural phase and traces of cubic NiO as secondary phase. (c) TEM image showing the morphology of the N3 powder nanograins. (d) HRTEM image of cubic N3 powder nanograins.

As shown by electrochemical impedance spectroscopy, the presence of the NiO phase and Ce^{3+} in high amounts has an enhancement effect over the electrical conductivity and also over the catalytic activity. Syngas formation through partial CH_4 oxidation takes place at higher temperature (550^0C) with high selectivity and activity on N1-3. The key features of these materials for the high catalytic conversion of CH_4 and CO selectivity consist in: (i) the presence of Ni^{2+} species and a high Ni/Ce ratio, as assessed by XPS analysis, and (ii) an improved reducibility of Ce^{3+} as highlighted by TPR, which generate oxygen vacancies. All these findings together with the increase in oxygen mobility in the YSZ matrix, by a transfer of oxygen from ceria to the nickel interface, are responsible for the high stability of the material, by oxidizing the C deposition from the surface. Moreover, there are evidences that Ni^0 has a high affinity for coke formation, while the Ni species with a good interaction with the support are C tolerant. In conclusion N3 sample, has all the features to perform CPOM with suitable C tolerance.

References

[1] M. Florea, S. Somacescu, G. Postole, A. Urdă, F. Neaţu, Ş. Neaţu, L. Massin, P. Gélin, Catal. Sci. Technol. 9, 2351-2366 (2019).

[2] S. Somacescu, N. Cioatera, P. Osiceanu, J. M. Calderon-Moreno, C. Ghica, F. Neaţu, M. Florea, Appl. Catal. B: Environ. 241, 393-406 (2019).

Enhanced photoresponse of SiGe nanocrystals in SiO_2 driven by hydrogen plasma annealing

Ionel Stavarache, Constantin Logofatu, Toma Stoica, Valentin Serban Teodorescu and Magdalena Lidia Ciurea
in collaboration with
Muhammad Taha Sultan[1], Andrei Manolescu[1], Jon Tomas Gudmundsson[2], Kristinn Torfason[1], Halldór Guðfinnur Svavarsson[1],
1 School of Science and Engineering, Reykjavik University, Iceland
2 Department of Space and Plasma Physics, School of Electrical Engineering and Computer Science, KTH-Royal Institute of Technology, Sweden; Science Institute, University of Iceland, Iceland
George Alexandru Nemnes
3 Faculty of Physics, University of Bucharest

Films of SiGe nanocrystals (NCs) in SiO_2 present both advantages of using the well-known amorphous SiO_2 matrix and embedded SiGe NCs. SiGe NCs allow the thermodynamic stability of SiGe alloy in NCs in respect to Ge NCs (having fast diffusion) as well as the tuning of SiGe NCs bandgap by varying SiGe composition and size, and consequently, the electrical and optical properties. These films have to be used in near-infrared (NIR) sensors fabrication for replacing the toxic and expensive III-V-based sensors in the market.

Our group together with the Icelandic group have prepared in the frame of M-Era.NET PhotoNanoP project / 2016-18, films and multilayers (MLs) of SiGe NCs embedded in oxides with enhanced photoresponse in NIR and short-wave IR (SWIR) [1–4].

We present SiO_2/SiGe/SiO_2/Si MLs deposited by magnetron sputtering (MS), namely SiO_2 by reactive dcMS and SiGe layer by co-deposition of Si by dcMS and Ge by high-power impulse MS (HiPIMS). After ML and Al contacts deposition, these samples were annealed in H_2/Ar (~70/30 %) mixture in an oven subjected to RF generator, at room temperature (RT). The hydrogenated MLs present improved photoresponse in VIS-SWIR in respect to those annealed in N_2 at different temperatures (rapid thermal annealing – RTA) [1,2].

We investigated the structure by taking grazing incidence XRD (GiXRD) diffractograms, the GiXRD pattern measured on as-deposited MLs (subtracted background) being shown in **Fig. 1**. From the SiGe (111) peak position results the composition of SiGe NCs of 50:50. SiGe NCs are small as it is revealed by the SiGe (111) peak aspect (full width at half maximum).

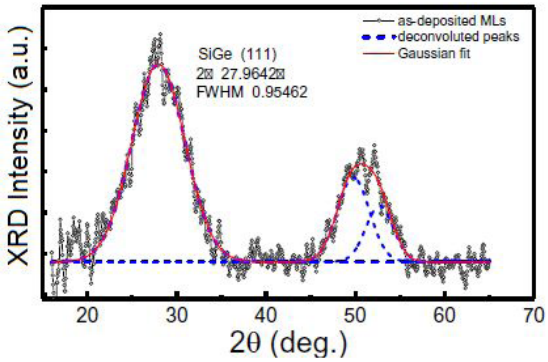

Fig. 1. *GiXRD pattern measured on as-deposited MLs (subtracted background). The SiGe (111) peak position corresponds to a SiGe composition of 50:50.*

We studied the photoresponse of hydrogenated MLs in respect to as-deposited ones. For this we measured current-voltage characteristics and photocurrent spectra in VIS-SWIR, at RT.

In **Fig. 2a** are given photocurrent spectra for as-deposited and hydrogenated MLs, the hydrogenation being made in 10 min intervals. **Fig. 2b** shows the dependence of peak B intensity on hydrogenation time. One can see a clear increase of the photoresponse after hydrogenation.

The peak-B intensity practically increases linearly up to about 70 min hydrogenation and then saturates.

The hydrogenated MLs are stable proven by the results reproducibility after 5 weeks spectra measurements.

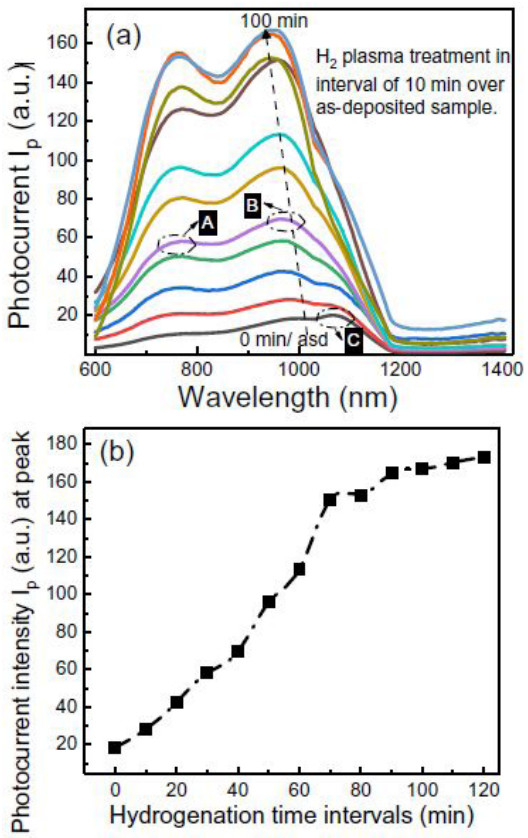

Fig. 2. *(a) Photocurrent spectra (1 V bias) taken on as-deposited and hydrogenated SiO_2/SiGe/SiO_2 MLs; hydrogenation is made in 10 min intervals; the dotted line shows hydrogenation intervals from 0 (asd) to 100 min. (b) The peak B intensity vs. hydrogenation time.*

The role of hydrogenation in the photoresponse increase is the healing of defects (by Si-H bonds formation) located at both SiGe NCs / SiO_2 interface and inside SiO_2 matrix by H and H^+ ions resulting from dissociation in plasma of H_2 (sometimes via H^{2+}, H^{3+} that in turn go to H and H^+) [2].

We also studied the effect of pressure of the H_2:Ar mixture (70:30 ratio) on the photoresponse spectra during 10 min hydrogenation. **Fig. 3** shows that by increasing the pressure from 0.6 to 20 mTorr, the photocurrent intensity increases up to more than 2 times. We attribute the photocurrent increase with pressure increase to the dominant presence of H^{2+} and H^{3+} ions in plasma at high pressure. In pure H_2 plasma, the efficiency to create H^{2+} is small due to small ionization cross- section of H^2.

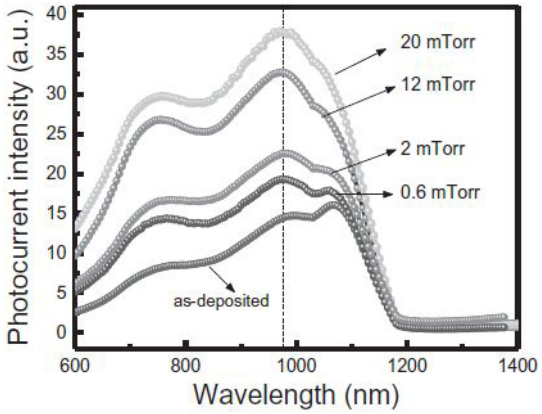

Fig. 3. *Effect of H_2:Ar (70:30 ratio) pressure on photocurrent spectra (1 V bias) of MLs. The hydrogenation was made for 10 min.*

In conclusion, we prepared SiO_2/SiGe/SiO_2/Si MLs with enhanced photoresponse in VIS-SWIR driven by hydrogenation in H_2/Ar (~70/30 %) plasma.

The ML were deposited by using dcMS and HiPIMS, and then they were subjected to hydrogenation for enhancing the photoresponse intensity. The photoresponse intensity increases with the increase of hydrogenation time and pressure. This is explained by healing of defects by H and H^+ ions present in plasma. The defects are healed and the SiGe NCs / SiO_2 interface is passivated by Si-H bond formation.

References

[1] M.T. Sultan, A. Manolescu, J.T. Gudmundsson, K. Torfason, G.A. Nemnes, I. Stavarache, C. Logofatu, V.S. Teodorescu, M.L Ciurea, H.G. Svavarsson, Appl. Surf. Sci. 469, 870 (2019).

[2] M.T. Sultan, J.T. Gudmundsson, A. Manolescu, T. Stoica, M.L Ciurea, H.G. Svavarsson, Appl. Surf. Sci. 479, 403 (2019).

[3] M.T. Sultan, V.S. Teodorescu, J.T. Gudmundsson, A. Manolescu, M.L. Ciurea, H.G. Svavarsson, Beilstein J. Nanotech. 10, 1873 (2019).

[4] M.T. Sultan, J.T. Gudmundsson, A. Manolescu, V. Teodorescu, M.L. Ciurea, H.G. Svavarsson, Nanotechnology 30, 365604 (2019).

Publications

Nr.	Title	Journal	Authors	FI	AIS	DOI	Q
1	Bulks of Al-B-C obtained by reactively spark plasma sintering and impact properties by Split Hopkinson Pressure Bar	SCIENTIFIC REPORTS,9,19484 (2019)	Vasylkiv, O; Borodianska, H; Demirskyi, D; Li, P; Suzuki, TS; Grigoroscuta, MA; Pasuk, I; Kuncser, A; Badica, P	4.011	1.286	10.1038/s41598-019-55888-z	Q1
2	Enhancement of the supercapacitive properties of laser deposited graphene-based electrodes through carbon nanotube loading and nitrogen doping	PHYSICAL CHEMISTRY CHEMICAL PHYSICS,21, pp.25175-25186 (2019)	del Pino, AP; Lopez, MR; Ramadan, MA; Lebiere, PG; Logofatu, C; Martinez-Rovira, I; Yousef, I; Gyorgy, E	3.567	0.942	10.1039/c9cp04237g	Q1
3	Influence of Sintering Strategy on the Characteristics of Sol-Gel Ba1-$_x$Ce$_x$Ti1-x/4O$_3$ Ceramics	NANOMATERIALS,9,1675 (2019)	Stanciu, CA; Pintilie, I; Surdu, A; Trusca, R; Vasile, BS; Eftimie, M; Ianculescu, AC	4.034	0.704	10.3390/nano9121675	Q1
4	Animal Origin Bioactive Hydroxyapatite Thin Films Synthesized by RF-Magnetron Sputtering on 3D Printed Cranial Implants	METALS,9,1332 (2019)	Chioibasu, D; Duta, L; Popescu-Pelin, G; Popa, N; Milodin, N; Iosub, S; Balescu, LM; Galca, AC; Popa, AC; Oktar, FN; Stan, GE; Popescu, AC	2.259	0.361	10.3390/met9121332	Q1
5	Core-shell nanowire arrays based on ZnO and CuxO for water stable photocatalysts	SCIENTIFIC REPORTS,9,17268 (2019)	Florica, C; Costas, A; Preda, N; Beregoi, M; Kuncser, A; Apostol, N; Popa, C; Socol, G; Diculescu, V; Enculescu, I	4.011	1.286	10.1038/s41598-019-53873-0	Q1
6	Structure and low field magnetic properties in phosphate-tellurite glasses	JOURNAL OF NON-CRYSTALLINE SOLIDS,524,UNSP 119651 (2019)	Polosan, S	2.6	0.414	10.1016/j.jnoncrysol.2019.119651	Q1
7	Synthesis and characterization of biocompatible polymer-ceramic film structures as favorable interface in guided bone regeneration	APPLIED SURFACE SCIENCE,494, pp.335-352 (2019)	Dascalu, CA; Maidaniuc, A; Pandele, AM; Voicu, SI; Machedon-Pisu, T; Stan, GE; Cimpean, A; Mitran, V; Antoniac, IV; Miculescu, F	5.155	0.671	10.1016/j.apsusc.2019.07.098	Q1

8	PCL-ZnO/TiO_2/HAp Electrospun Composite Fibers with Applications in Tissue Engineering	POLYMERS,11,1793 (2019)	Jinga, SI; Zamfirescu, AI; Voicu, G; Enculescu, M; Evanghelidis, A; Busuioc, C	3.164	0.592	10.3390/polym11111793	Q1
9	Electronic Structure of a Graphene-like Artificial Crystal of $NdNiO_3$	NANO LETTERS,19, pp.8311-8317 (2019)	Arab, A; Liu, XR; Koksal, O; Yang, WB; Chandrasena, RU; Middey, S; Kareev, M; Kumar, S; Husanu, MA; Yang, ZZ; Gu, L; Strocov, VN; Lee, TL; Minar, J; Pentcheva, R; Chakhalian, J; Gray, AX	12.279	4.018	10.1021/acs.nanolett.9b03962	Q1
10	Designing functional ferroelectric interfaces from first-principles: dipoles and band bending at oxide heterojunctions	NEW JOURNAL OF PHYSICS,21,113005 (2019)	Dorin, R; Filip, LD; Pintilie, L; Butler, KT; Plugaru, N	3.783	1.489	10.1088/1367-2630/ab4d8b	Q1
11	Fluorescent coumarin-modified mesoporous SBA-15 nanocomposite: Physico-chemical characterization and interaction with prokaryotic and eukaryotic cells	MICROPOROUS AND MESOPOROUS MATERIALS,288,UNSP 109583 (2019)	Tudose, M; Culita, DC; Voicescu, M; Musuc, AM; Kuncser, AC; Bleotu, C; Popa, M; Marutescu, L; Chifiriuc, MC; Nicolescu, M; Deleanu, C	4.182	0.67	10.1016/j.micromeso.2019.109583	Q1
12	Orthorhombic HfO_2 with embedded Ge nanoparticles in nonvolatile memories used for the detection of ionizing radiation	NANOTECHNOLOGY,30,445501 (2019)	Palade, C; Slav, A; Lepadatu, AM; Stavarache, I; Dascalescu, I; Maraloiu, AV; Negrila, C; Logofatu, C; Stoica, T; Teodorescu, VS; Ciurea, ML; Lazanu, S	3.399	0.744	10.1088/1361-6528/ab352b	Q1
13	Low value for the static background dielectric constant in epitaxial PZT thin films	SCIENTIFIC REPORTS,9,14698 (2019)	Boni, GA; Chirila, CF; Hrib, L; Negrea, R; Filip, LD; Pintilie, I; Pintilie, L	4.011	1.286	10.1038/s41598-019-51312-8	Q1
14	Optical properties of folic acid in phosphate buffer solutions: the influence of pH and UV irradiation on the UV-VIS absorption spectra and photoluminescence	SCIENTIFIC REPORTS,9,14278 (2019)	Baibarac, M; Smaranda, I; Nila, A; Serbschi, C	4.011	1.286	10.1038/s41598-019-50721-z	Q1

15	Bi1-xEuxFeO$_3$ Powders: Synthesis, Characterization, Magnetic and Photoluminescence Properties	NANOMATERIALS,9,1465 (2019)	Surdu, VA; Trusca, RD; Vasile, BS; Oprea, OC; Tanasa, E; Diamandescu, L; Andronescu, E; Ianculescu, AC	4.034	0.704	10.3390/nano9101465	Q1
16	Thermal, structural, magnetic and magneto-optical properties of dysprosium-doped phosphate glass	JOURNAL OF NON-CRYSTALLINE SOLIDS,521,UNSP 119545 (2019)	Elisa, M; Stefan, R; Vasiliu, IC; Rusu, MI; Sava, BA; Boroica, L; Sofronie, M; Kuncser, V; Galca, AC; Beldiceanu, A; Volceanov, A; Eftimie, M	2.6	0.414	10.1016/j.jnoncrysol.2019.119545	Q1
17	Internal and external surface features of newly developed porous ceramics with random interconnected 3D channels by a fibrous sacrificial porogen method	APPLIED SURFACE SCIENCE,489, pp.226-238 (2019)	Mocanu, AC; Miculescu, M; Machedon-Pisu, T; Maidaniuc, A; Ciocoiu, RC; Ionita, M; Pasuk, J; Stan, GE; Miculescu, F	5.155	0.671	10.1016/j.apsusc.2019.05.354	Q1
18	Imaging dopant distribution across complete phase transformation by TEM and upconversion emission	NANOSCALE,11, pp.16743-16754 (2019)	Avram, D; Colbea, C; Florea, M; Lazar, S; Stroppa, D; Tiseanu, C	6.97	1.591	10.1039/c9nr04345d	Q1
19	Cu$_X$CeMgAlO mixed oxide catalysts derived from multicationic LDH precursors for methane total oxidation	APPLIED CATALYSIS A-GENERAL,586,117215 (2019)	Al-Aani, HMS; Iro, E; Chirra, P; Fechete, I; Badea, M; Negrila, C; Popescu, I; Olea, M; Marcu, IC	4.63	0.77	10.1016/j.apcata.2019.117215	Q1
20	Synthesis and thermal, emission and dielectric properties of liquid crystalline Eu(III), Sm(III) and Tb(III) complexes based on mesogenic 4-pyridone ligands functionalized with cyanobiphenyl groups	JOURNAL OF MOLECULAR LIQUIDS,290,UNSP 111184 (2019)	Chiriac, LF; Ganea, PC; Manaila-Maximean, D; Pasuk, I; Circu, V	4.561	0.58	10.1016/j.molliq.2019.111184	Q1
21	Backaction effects in cavity-coupled quantum conductors	PHYSICAL REVIEW B,100,125416 (2019)	Moldoveanu, V; Dinu, IV; Manolescu, A; Gudmundsson, V	3.736	1.089	10.1103/PhysRevB.100.125416	Q1
22	Manipulating the Optical Properties of Carbon Dots by Fine-Tuning their Structural Features	CHEMSUSCHEM,12, pp.4480-4486 (2019)	Luo, H; Papaioannou, N; Salvadori, E; Roessler, MM; Ploenes, G; van Eck, ERH; Tanase, LC; Feng, JY; Sun, YW; Yang, Y; Danaie, M; Jorge, AB; Sapelkin, A; Durrant, J; Dimitrov, SD; Titirici, MM	7.804	1.625	10.1002/cssc.201901795	Q1

23	Probing single-unit-cell resolved electronic structure modulations in oxide superlattices with standing-wave photoemission	PHYSICAL REVIEW B,100,125119 (2019)	Yang, W; Chandrasena, RU; Gu, M; dos Reis, RMS; Moon, EJ; Arab, A; Husanu, MA; Nemsak, S; Gullikson, EM; Ciston, J; Strocov, VN; Rondinelli, JM; May, SJ; Gray, AX	3.736	1.089	10.1103/PhysRevB.100.125119	Q1
24	Efficacy of annealing and fabrication parameters on photo-response of SiGe in TiO_2 matrix	NANOTECHNOLOGY,30,365604 (2019)	Sultan, MT; Gudmundsson, JT; Manolescu, A; Teodorescu, VS; Ciurea, ML; Svavarsson, HG	3.399	0.744	10.1088/1361-6528/ab260e	Q1
25	Photoluminescent Hydroxylapatite: Eu_{3+} Doping Effect on Biological Behaviour	NANOMATERIALS,9,1187 (2019)	Andronescu, E; Predoi, D; Neacsu, IA; Paduraru, AV; Musuc, AM; Trusca, R; Oprea, O; Tanasa, E; Vasile, OR; Nicoara, AI; Surdu, AV; Iordache, F; Birca, AC; Iconaru, SL; Vasile, BS	4.034	0.704	10.3390/nano9091187	Q1
26	Synthesis, Characterization, and Antimicrobial Activity of Magnesium-Doped Hydroxyapatite Suspensions	NANOMATERIALS,9,1295 (2019)	Predoi, D; Iconaru, SL; Predoi, MV; Stan, GE; Buton, N	4.034	0.704	10.3390/nano9091295	Q1
27	Conductance Model for Single-Crystalline/Compact Metal Oxide Gas-Sensing Layers in the Nondegenerate Limit: Example of Epitaxial SnO_2(101)	ACS SENSORS,4, pp.2420-2428 (2019)	Simion, CE; Schipani, F; Papadogianni, A; Stanoiu, A; Budde, M; Oprea, A; Weimar, U; Bierwagen, O; Barsan, N	6.944	1.462	10.1021/acssensors.9b01018	Q1
28	The influence of UV light on the azathioprine photodegradation: New evidences by photoluminescence	RESULTS IN PHYSICS, 14,102443 (2019)	Smaranda, I; Nila, A; Manta, CM; Samohvalov, D; Gherca, D; Baibarac, M	3.042	0.368	10.1016/j.rinp.2019.102443	Q1
29	Cavity-Photon-Induced High-Order Transitions between Ground States of Quantum Dots	ANNALEN DER PHYSIK 531,1900306 (2019)	Gudmundsson, V; Abdullah, NR; Tang, CS; Manolescu, A; Moldoveanu, V	3.276	1.151	10.1002/andp.201900306	Q1
30	Formation peculiarities and optical properties of highly-doped (Y(0.86) La(0.09)Vb(0.05)) (2)O-3 transparent ceramics	CERAMICS INTERNATIONAL,45, pp.16002-16007 (2019)	Kryzhanovska, OS; Baumer, VN; Parkhomenko, SV; Doroshenko, AG; Yavetskiy, RP; Balabanov, AE; Tolmachev, AV; Skorik, SN; Li, J; Kuncser, A	3.45	0.454	10.1016/j.ceramint.2019.05.111	Q1

31	Nanoclustered Pd decorated nanocrystalline Zn doped SnO_2 for ppb NO_2 detection at low temperature	SENSORS AND ACTUATORS B-CHEMICAL,294, pp.148-156 (2019)	Somacescu, S; Ghica, C; Simion, CE; Kuncser, AC; Vlaicu, AM; Stefan, M; Ghica, D; Florea, OG; Mercioniu, IF; Stanoiu, A	6.393	0.824	10.1016/j.snb.2019.05.033	Q1
32	Spectroscopic investigations of Pr_{3+} ions doped CNGG and CLNGG single crystals	JOURNAL OF ALLOYS AND COMPOUNDS,799, pp.288-301 (2019)	Hau, S; Gheorghe, C; Gheorghe, L; Voicu, E; Greculeasa, M; Stanciu, G; Broasca, A; Enculescu, M	4.175	0.601	10.1016/j.jallcom.2019.05.154	Q1
33	Memcomputing and Nondestructive Reading in Functional Ferroelectric Heterostructures	PHYSICAL REVIEW APPLIED 12,024053 (2019)	Boni, GA; Filip, LD; Chirila, C; Iuga, A; Pasuk, I; Hrib, L; Trupina, L; Pintilie, I; Pintilie, L	4.532	1.832	10.1103/PhysRevApplied.12.024053	Q1
34	Nanostructured palladium doped nickel electrodes for immobilization of oxidases through nickel nanoparticles	ELECTROCHIMICA ACTA,315, pp.102-113 (2019)	Barsan, MM; Matei, E; Enculescu, M; Costescu, R; Preda, N; Enache, TA; Enculescu, I; Diculescu, VC	5.383	0.81	10.1016/j.electacta.2019.04.143	Q1
35	Adsorption of 1,4-phenylene diisothiocyanate onto the graphene oxide sheets functionalized with polydiphenylamine in doped state	SCIENTIFIC REPORTS,9,11968 (2019)	Baibarac, M; Daescu, M; Fejer, SN	4.011	1.286	10.1038/s41598-019-48314-x	Q1
36	Mineralization-Inspired Synthesis of Magnetic Zeolitic Imidazole Framework Composites	ANGEWANDTE CHEMIE-INTERNATIONAL EDITION,58, pp.13550-13555 (2019)	Terzopoulou, A; Hoop, M; Chen, XZ; Hirt, AM; Charilaou, M; Shen, Y; Mushtaq, F; del Pino, AP; Logofatu, C; Simonelli, L; de Mello, AJ; Doonan, CJ; Sort, J; Nelson, BJ; Pane, S; Puigmarti-Luis, J	12.257	3.243	10.1002/anie.201907389	Q1
37	Nitrogen-doped graphene as metal free basic catalyst for coupling reactions	JOURNAL OF CATALYSIS,376, pp.238-247 (2019)	Candu, N; Man, I; Simion, A; Cojocaru, B; Coman, SM; Bucur, C; Primo, A; Garcia, H; Parvulescu, VI	7.723	1.561	10.1016/j.jcat.2019.07.011	Q1
38	Dramatic impact of pressure and annealing temperature on the properties of sputtered ferroelectric HZO layers	APL MATERIALS,7,081109 (2019)	Bouaziz, J; Romeo, PR; Baboux, N; Negrea, R; Pintilie, L; Vilquin, B	4.296	1.409	10.1063/1.5110894	Q1

39	Fabrication of graphene-based electrochemical capacitors through reactive inverse matrix assisted pulsed laser evaporation	APPLIED SURFACE SCIENCE,484, pp.245-256 (2019)	del Pino, AP; Ramadan, MA; Lebiere, PG; Ivan, R; Logofatu, C; Yousef, I; Gyorgy, E	5.155	0.671	10.1016/j.apsusc.2019.04.127	Q1
40	3D hybrid structures based on biomimetic membranes and Caryophyllus aromaticus - "green" synthesized nano-silver with improved bioperformances	MATERIALS SCIENCE & ENGINEERING C-MATERIALS FOR BIOLOGICAL APPLICATIONS,101, pp.120-137 (2019)	Barbinta-Patrascu, ME; Badea, N; Bacalum, M; Ungureanu, C; Suica-Bunghez, IR; Lordache, SM; Pirvu, C; Zgura, I; Maraloiu, VA	4.959	0.751	10.1016/j.msec.2019.03.069	Q1
41	Physical properties of the ferroelectric capacitors based on Al-doped HfO_2 grown via Atomic Layer Deposition on Si	APPLIED SURFACE SCIENCE,483, pp.324-333 (2019)	Vulpe, S; Nastase, F; Dragoman, M; Dinescu, A; Romanitan, C; Iftimie, S; Moldovan, A; Apostol, N	5.155	0.671	10.1016/j.apsusc.2019.03.166	Q1
42	Ge nanoparticles in SiO_2 for near infrared photodetectors with high performance	SCIENTIFIC REPORTS,9,10286 (2019)	Stavarache, I; Teodorescu, VS; Prepelita, P; Logofatu, C; Ciurea, ML	4.011	1.286	10.1038/s41598-019-46711-w	Q1
43	Effect of Zn content on structural, morphological and magnetic behavior of Zn_xCo_1-xFe2O_4/SiO_2 nanocomposites	JOURNAL OF ALLOYS AND COMPOUNDS,792, pp.432-443 (2019)	Dippong, T; Deac, IG; Cadar, O; Levei, EA; Diamandescu, L; Borodi, G	4.175	0.601	10.1016/j.jallcom.2019.04.059	Q1
44	Impact on Ferroelectricity and Band Alignment of Gradually Grown Au on $BaTiO_3$	PHYSICA STATUS SOLIDI-RAPID RESEARCH LETTERS 13,1900077 (2019)	Popescu, DG; Husanu, MA; Chirila, C; Pintilie, L; Teodorescu, CM	3.729	0.79	10.1002/pssr.201900077	Q1
45	Evaluating the biological potential of some new cobalt (II) complexes with acrylate and benzimidazole derivatives	APPLIED ORGANOMETALLIC CHEMISTRY,33,e4976 (2019)	Vlaicu, ID; Olar, R; Maxim, C; Chifiriuc, MC; Bleotu, C; Stanica, N; Scaeteanu, GV; Dulea, C; Avram, S; Badea, M	3.259	0.334	10.1002/aoc.4976	Q1
46	The Quality of Fe-14Cr ODS Powder Alloys During Milling and Upon Heating and Its Impact on the Mechanical Properties of Consolidated Steels	METALLURGICAL AND MATERIALS TRANSACTIONS A-PHYSICAL METALLURGY AND MATERIALS SCIENCE,50A, pp.3282-3294 (2019)	Mihalache, V; Walter, M; Mercioniu, I; Ordas, N	1.985	0.533	10.1007/s11661-019-05264-3	Q1

47	Electrochemical assay for 20S proteasome activity and inhibition with anticancer drugs	TALANTA,199, pp.32-39 (2019)	de Jesus, CSH; Chiorcea-Paquim, AM; Barsan, MM; Diculescu, VC	4.916	0.762	10.1016/j.talanta.2019.02.052	Q1
48	The influence of the nanocrystals size and surface on the Yb/Er doped LaF_3 luminescence properties	JOURNAL OF ALLOYS AND COMPOUNDS,791, pp.1098-1104 (2019)	Secu, CE; Matei, E; Negrila, C; Secu, M	4.175	0.601	10.1016/j.jallcom.2019.03.267	Q1
49	Enhanced photoconductivity of embedded SiGe nanoparticles by hydrogenation	APPLIED SURFACE SCIENCE,479, pp.403-409 (2019)	Sultan, MT; Gudmundsson, JT; Manolescu, A; Stoica, T; Ciurea, ML; Svavarsson, HG	5.155	0.671	10.1016/j.apsusc.2019.02.096	Q1
50	Multilayer protective coatings obtained by pulsed laser deposition	APPLIED SURFACE SCIENCE,479, pp.1124-1131 (2019)	Ion, V; Scarisoreanu, ND; Bonciu, A; Moldovan, A; Ghenescu, V; Ghenescu, M; Banciu, MG; Andrei, A; Dinescu, M	5.155	0.671	10.1016/j.apsusc.2019.02.186	Q1
51	Direct Immobilization of Biomolecules through Magnetic Forces on Ni Electrodes via Ni Nanoparticles: Applications in Electrochemical Biosensors	ACS APPLIED MATERIALS & INTERFACES,11, pp.19867-19877 (2019)	Barsan, MM; Enache, TA; Preda, N; Stan, G; Apostol, NG; Matei, E; Kuncser, A; Diculescu, VC	8.456	1.65	10.1021/acsami.9b04990	Q1
52	Effect of high gamma radiations on physical properties of In2S3 thin films grown by chemical bath deposition for buffer layer applications	RESULTS IN PHYSICS,13,102115 (2019)	Souli, M; Bensalem, Y; Secu, M; Bartha, C; Enculescu, M; Mejri, A; Kamoun-Turki, N; Badica, P	3.042	0.368	10.1016/j.rinp.2019.02.051	Q1
53	Structure and magnetic properties of highly coercive L1(0) nanocomposite FeMnPt thin films	MATERIALS CHARACTERIZATION,152, pp.245-252 (2019)	Crisan, O; Vasiliu, F; Crisan, AD; Mercioniu, I; Schinteie, G; Leca, A	3.22	0.74	10.1016/j.matchar.2019.04.028	Q1
54	Hybrid layered double hydroxides-curcumin thin films deposited via Matrix Assisted Pulsed Laser Evaporation-MAPLE with photoluminescence properties	APPLIED SURFACE SCIENCE,478, pp.754-761 (2019)	Andrei, F; Vlad, A; Birjega, R; Tozar, T; Secu, M; Urzica, I; Dinescu, M; Zavoianu, R	5.155	0.671	10.1016/j.apsusc.2019.02.011	Q1
55	Effect of nickel content on structural, morphological and magnetic properties of $NixCo_1$-xFe_2O_4/SiO_2 nanocomposites	JOURNAL OF ALLOYS AND COMPOUNDS,786, pp.330-340 (2019)	Dippong, T; Levei, EA; Cadar, O; Deac, IG; Diamandescu, L; Barbu-Tudoran, L	4.175	0.601	10.1016/j.jallcom.2019.01.363	Q1

56	CO_2 methanation catalyzed by oriented MoS2 nanoplatelets supported on few layers graphene	APPLIED CATALYSIS B-ENVIRONMENTAL,245, pp.351-359 (2019)	Primo, A; He, JB; Jurca, B; Cojocaru, B; Bucur, C; Parvulescu, VI; Garcia, H	14.229	1.918	10.1016/j.apcatb.2018.12.034	Q1
57	Highly -sensitive near infrared luminescent nanothermometers based on binary mixture	JOURNAL OF ALLOYS AND COMPOUNDS,785, pp.250-259 (2019)	Avram, D; Colbea, C; Florea, M; Tiseanu, C	4.175	0.601	10.1016/j.jallcom.2019.01.162	Q1
58	The hysteresis-free behavior of perovskite solar cells from the perspective of the measurement conditions	JOURNAL OF MATERIALS CHEMISTRY C,7, pp.5267-5274 (2019)	Nemnes, GA; Besleaga, C; Tomulescu, AG; Leonat, LN; Stancu, V; Florea, M; Manolescu, A; Pintilie, I	6.641	1.159	10.1039/c8tc05999c	Q1
59	La0.75Sr0.25XO3 (X = Fe, Mn or Cr) with coking tolerance for CH_4/H_2O reaction: effect of H_2S on catalytic performance	CATALYSIS SCIENCE & TECHNOLOGY,9, pp.2351-2366 (2019)	Florea, M; Somacescu, S; Postole, G; Urda, A; Neatu, F; Neatu, S; Massin, L; Gelin, P	5.726	1.131	10.1039/c9cy00065h	Q1
60	Tailoring the Dopant Distribution in ZnO:Mn Nanocrystals	SCIENTIFIC REPORTS,9,6894 (2019)	Ghica, D; Vlaicu, ID; Stefan, M; Maraloiu, VA; Joita, AC; Ghica, C	4.011	1.286	10.1038/s41598-019-43388-z	Q1
61	Dextran-Coated Zinc-Doped Hydroxyapatite for Biomedical Applications	POLYMERS,11,886 (2019)	Predoi, D; Iconaru, SL; Predoi, MV	3.164	0.592	10.3390/polym11050886	Q1
62	Pulsed Laser Fabrication of TiO_2 Buffer Layers for Dye Sensitized Solar Cells	NANOMATERIALS,9,746 (2019)	Lungu, J; Socol, G; Stan, GE; Stefan, N; Luculescu, C; Georgescu, A; Popescu-Pelin, G; Prodan, G; Girtu, MA; Mihailescu, IN	4.034	0.704	10.3390/nano9050746	Q1
63	Multiferroic (Nd,Fe)-doped $PbTiO_3$ ceramics with coexistent ferroelectricity and magnetism at room temperature	CERAMICS INTERNATIONAL,45, pp.9390-9396 (2019)	Craciun, F; Cordero, F; Cernea, M; Fruth, V; Atkinson, I; Stanica, N; Vasile, BS; Trusca, R; Iuga, A; Galizia, P; Galassi, C	3.45	0.454	10.1016/j.ceramint.2018.08.147	Q1
64	Deposition temperature influence on the wear behaviour of carbon-based coatings deposited on hardened steel	APPLIED SURFACE SCIENCE,475, pp.762-773 (2019)	Feldiorean, D; Cristea, D; Tierean, M; Croitoru, C; Gabor, C; Jakab-Farkas, L; Cunha, L; Barradas, NP; Alves, E; Craciun, V; Marin, A; Moura, C; Leme, J; Socol, M; Craciun, D; Cosnita, M; Munteanu, D	5.155	0.671	10.1016/j.apsusc.2019.01.028	Q1

65	Negative ion-induced deuterium retention in mixed W-Al layers co-deposited in dual-HiPIMS	SURFACE & COATINGS TECHNOLOGY,363, pp.273-281 (2019)	Dinca, P; Tiron, V; Velicu, IL; Porosnicu, C; Butoi, B; Velea, A; Grigore, E; Costin, C; Lungu, CP	3.192	0.512	10.1016/j.surfcoat.2019.02.019	Q1
66	Growth of Ag(111) on Si(111) with nearly flat band and abrupt interface	APPLIED SURFACE SCIENCE,473, pp.433-441 (2019)	Bocirnea, AE; Costescu, RM; Apostol, NG; Teodorescu, CM	5.155	0.671	10.1016/j.apsusc.2018.12.167	Q1
67	New electrochemical sensor based on CoQ(10) and cyclodextrin complexes for the detection of oxidative stress initiators	ELECTROCHIMICA ACTA,302, pp.441-448 (2019)	Barsan, MM; Diculescu, VC	5.383	0.81	10.1016/j.electacta.2019.02.060	Q1
68	Radial heterojunction based on single ZnO-CuxO core-shell nanowire for photodetector applications	SCIENTIFIC REPORTS,9,5553 (2019)	Costas, A; Florica, C; Preda, N; Apostol, N; Kuncser, A; Nitescu, A; Enculescu, I	4.011	1.286	10.1038/s41598-019-42060-w	Q1
69	Evaluation of Antibacterial Activity of Zinc-Doped Hydroxyapatite Colloids and Dispersion Stability Using Ultrasounds	NANOMATERIALS,9,515 (2019)	Predoi, D; Iconaru, SL; Predoi, MV; Motelica-Heino, M; Guegan, R; Buton, N	4.034	0.704	10.3390/nano9040515	Q1
70	Effect of the process control agent in the ball-milled powders and SPS-consolidation temperature on the grain refinement, density and Vickers hardness of $Fe_{14}Cr$ ODS ferritic alloys	POWDER TECHNOLOGY,347, pp.103-113 (2019)	Mihalache, V; Mercioniu, I; Velea, A; Palade, P	3.413	0.588	10.1016/j.powtec.2019.02.006	Q1
71	Spontaneous symmetry breaking in the laser transition	PHYSICAL REVIEW B,99,115313 (2019)	Gartner, P	3.736	1.089	10.1103/PhysRevB.99.115313	Q1
72	Next frontiers in cleaner synthesis: 3D printed graphene-supported CeZrLa mixed -oxide nanocatalyst for CO_2 utilisation and direct propylene carbonate production	JOURNAL OF CLEANER PRODUCTION,214, pp.606-614 (2019)	Middelkoop, V; Slater, T; Florea, M; Neatu, F; Danaci, S; Onyenkeadi, V; Boonen, K; Saha, B; Baragau, LA; Kellici, S	6.395	0.864	10.1016/j.jclepro.2018.12.274	Q1
73	Very large remanent polarization in ferroelectric Hf_1-x$ZrxO_2$ grown on Ge substrates by plasma assisted atomic oxygen deposition	APPLIED PHYSICS LETTERS, 114,112901 (2019)	Zacharaki, C; Tsipas, P; Chaitoglou, S; Fragkos, S; Axiotis, M; Lagoyiannis, A; Negrea, R; Pintilie, L; Dimoulas, A	3.521	0.866	10.1063/1.5090036	Q1

74	Efficient glucose dehydration to HMF onto Nb-BEA catalysts	CATALYSIS TODAY,325, pp.109-116 (2019)	Candu, N; El Fergani, M; Verziu, M; Cojocaru, B; Jurca, B; Apostol, N; Teodorescu, C; Parvulescu, VI; Coman, SM	4.888	0.852	10.1016/j.cattod.2018.08.004	Q1
75	Charge separation and ROS generation on tubular sodium titanates exposed to simulated solar light	APPLIED SURFACE SCIENCE,470, pp.1053-1063 (2019)	Preda, S; Anastasescu, C; Balint, I; Umek, P; Sluban, M; Negrila, CC; Angelescu, DG; Bratan, V; Rusu, A; Zaharescu, M	5.155	0.671	10.1016/j.apsusc.2018.11.194	Q1
76	Antibacterial efficiency of alkali-free bio-glasses incorporating ZnO and/or SrO as therapeutic agents	CERAMICS INTERNATIONAL,45, pp.4368-4380 (2019)	Popa, AC; Fernandes, HR; Necsulescu, M; Luculescu, C; Cioangher, M; Dumitru, V; Stuart, BW; Grant, DM; Ferreira, JMF; Stan, GE	3.45	0.454	10.1016/j.ceramint.2018.11.112	Q1
77	Enhanced photoconductivity of SiGe nanocrystals in SiO_2 driven by mild annealing	APPLIED SURFACE SCIENCE,469, pp.870-878 (2019)	Sultan, MT; Manolescu, A; Gudmundsson, JT; Torfason, K; Nemnes, GA; Stavarache, I; Logofatu, C; Teodorescu, VS; Ciurea, ML; Svavarsson, HG	5.155	0.671	10.1016/j.apsusc.2018.11.061	Q1
78	Do topology and ferromagnetism cooperate at the EuS/Bi_2Se_3 interface?	PHYSICAL REVIEW B,99,064423 (2019)	Krieger, JA; Ou, Y; Caputo, M; Chikina, A; Dobeli, M; Husanu, MA; Keren, I; Prokscha, T; Suter, A; Chang, CZ; Moodera, JS; Strocov, VN; Salman, Z	3.736	1.089	10.1103/PhysRevB.99.064423	Q1
79	Energy-enhanced deposition of copper thin films by bipolar high power impulse magnetron sputtering	SURFACE & COATINGS TECHNOLOGY,359, pp.97-107 (2019)	Velicu, IL; Ianos, GT; Porosnicu, C; Mihaila, I; Burducea, I; Velea, A; Cristea, D; Munteanu, D; Tiron, V	3.192	0.512	10.1016/j.surfcoat.2018.12.079	Q1
80	Highly transparent Yb:Y_2O_3 ceramics obtained by solid-state reaction and combined sintering procedures	CERAMICS INTERNATIONAL,45, pp.3217-3222 (2019)	Stanciu, G; Gheorghe, L; Voicu, F; Hau, S; Gheorghe, C; Croitoru, G; Enculescu, M; Yavetskiy, RP	3.45	0.454	10.1016/j.ceramint.2018.10.224	Q1
81	Electrochemical Sensor for Carbonyl Groups in Oxidized Proteins	ANALYTICAL CHEMISTRY,91, pp.1920-1927 (2019)	Enache, TA; Matei, E; Diculescu, VC	6.35	1.348	10.1021/acs.analchem.8b03969	Q1

82	Rhodium-Catalyzed Annulation of ortho-Alkenyl Anilides with Alkynes: Formation of Unexpected Naphthalene Adducts	ANGEWANDTE CHEMIE-INTERNATIONAL EDITION,58, pp.1700-1704 (2019)	Seoane, A; Comanescu, C; Casanova, N; Garcia-Fandino, R; Diz, X; Mascarenas, JL; Gulias, M	12.257	3.243	10.1002/anie.201811747	Q1
83	Laser Processed Antimicrobial Nanocomposite Based on Polyaniline Grafted Lignin Loaded with Gentamicin-Functionalized Magnetite	POLYMERS,11,283 (2019)	Visan, AI; Popescu-Pelin, G; Gherasim, O; Grumezescu, V; Socol, M; Zgura, I; Florica, C; Popescu, RC; Savu, D; Holban, AM; Cristescu, R; Matei, CE; Socol, G	3.164	0.592	10.3390/polym11020283	Q1
84	Growth of $SrTiO_3$ Single Crystals with a Diameter of about 30 mm by the Verneuil Method	CRYSTAL GROWTH & DESIGN,19, pp.604-612 (2019)	Tateno, Y; Endo, K; Arisawa, S; Vlaicu, AM; Nedelcu, L; Preda, N; Secu, M; Iordanescu, R; Kuncser, AC; Badica, P	4.153	0.762	10.1021/acs.cgd.8b01004	Q1
85	Voltammetric and mass spectrometry investigation of methionine oxidation	JOURNAL OF ELECTROANALYTICAL CHEMISTRY,834, pp.124-129 (2019)	Diculescu, VC; Enache, TA	3.218	0.488	10.1016/j.jelechem.2018.12.058	Q1
86	Stable Hall voltages in presence of dynamic quasi-continuum bands in poly (3,4-ethylene-dioxythiophene)	ORGANIC ELECTRONICS,65, pp.412-418 (2019)	Stadler, P; Leonat, LN; Menon, R; Coskun, H; van Frank, S; Rankl, C; Scharber, MC	3.495	0.573	10.1016/j.orgel.2018.12.001	Q1
87	Bimodal mesoporous NiO/CeO_2-delta-YSZ with enhanced carbon tolerance in catalytic partial oxidation of methane-Potential IT-SOFCs anode	APPLIED CATALYSIS B-ENVIRONMENTAL,241, pp.393-406 (2019)	Somacescu, S; Cioatera, N; Osiceanu, P; Calderon-Moreno, JM; Ghica, C; Neatu, F; Florea, M	14.229	1.918	10.1016/j.apcatb.2018.09.065	Q1
88	UV-vis light induced photocatalytic activity of TiO_2/graphene oxide nanocomposite coatings	CATALYSIS TODAY,321, pp.81-86 (2019)	Datcu, A; Mendoza, ML; del Pino, AP; Logofatu, C; Luculescu, C; Gyorgy, E	4.888	0.852	10.1016/j.cattod.2018.02.026	Q1
89	Theoretical and Experimental Study of $(Ba,Sr)TiO_3$ Perovskite Solid Solutions and $BaTiO_3$/$SrTiO_3$ Heterostructures	JOURNAL OF PHYSICAL CHEMISTRY C,123, pp.2031-2036 (2019)	Rusevich, LL; Zvejnieks, G; Kotomin, EA; Krzmanc, MM; Meden, A; Kunej, S; Vlaicu, ID	4.309	1.017	10.1021/acs.jpcc.8b09750	Q1
90	Complex exchange coupling mechanisms in SRO/BFO/Fe heterostructures	JOURNAL OF ALLOYS AND COMPOUNDS,773, pp.338-345 (2019)	Greculeasa, SG; Schinteie, G; Hrib, LM; Stancu, V; Pasuk, I; Kuncser, A; Kuncser, V	4.175	0.601	10.1016/j.jallcom.2018.09.208	Q1

91	Pd-Cu catalysts supported on anion exchange resin for the simultaneous catalytic reduction of nitrate ions and reductive dehalogenation of organochlorinated pollutants from water	APPLIED CATALYSIS A-GENERAL,570, pp.120-129 (2019)	Bradu, C; Capat, C; Papa, F; Frunza, L; Olaru, EA; Crini, G; Morin-Crini, N; Euvrard, E; Balint, I; Zgura, I; Munteanu, C	4.63	0.77	10.1016/j.apcata.2018.11.002	Q1
92	Unveiling the double-well energy landscape in a ferroelectric layer	NATURE,565, pp.464-+ (2019)	Hoffmann, M; Fengler, FPG; Herzig, M; Mittmann, T; Max, B; Schroeder, U; Negrea, R; Pintilie, L; Slesazeck, S; Mikolajick, T	43.07	22.404	10.1038/s41586-018-0854-z	Q1
93	Akermanite-based coatings grown by pulsed laser deposition for metallic implants employed in orthopaedics	SURFACE & COATINGS TECHNOLOGY,357, pp.1015-1026 (2019)	Negrea, R; Busuioc, C; Constantinoiu, I; Miu, D; Enache, C; Iordache, F; Jinga, SI	3.192	0.512	10.1016/j.surfcoat.2018.11.008	Q1
94	NiTi coated with oxide and polymer films in the in vivo healing processes	JOURNAL OF MATERIALS RESEARCH AND TECHNOLOGY-JMR&T,8, pp.914-922 (2019)	Batalu, D; Nastase, F; Militaru, M; Gherghiceanu, M; Badica, P	3.327	0	10.1016/j.jmrt.2018.06.015	Q1
95	Addition of carbon fibers into B_4C infiltrated with molten silicon	CERAMICS INTERNATIONAL,45, pp.168-174 (2019)	Solodkyi, I; Bezdorozhev, O; Vterkovskiy, M; Bogomol, I; Bolbut, V; Kruger, M; Badica, P; Loboda, P	3.45	0.454	10.1016/j.ceramint.2018.09.148	Q1
96	Structural, Compositional, and Mechanical Characterization of $WxCryFe_1$-x-y Layers Relevant to Nuclear Fusion, Obtained with TVA Technology	MATERIALS,12,4072 (2019)	Lungu, M; Porosnicu, I; Dinca, P; Velea, A; Baiasu, F; Butoi, B; Pompilian, OG; Staicu, C; Constantina, PA; Porosnicu, C; Lungu, C; Tiseanu, I	2.972	0.608	10.3390/ma12244072	Q2
97	The Effect of the Ionizing Radiation on Hydroxyapatite-Polydimethylsiloxane Layers	POLYMER ENGINEERING AND SCIENCE,59, pp.2406-2412 (2019)	Groza, A; Iconaru, SL; Jiga, G; Chapon, P; Gaiaschi, S; Verga, N; Beuran, M; Prodan, AM; Matei, M; Marinescu, SA; Trusca, R; Predoi, D	1.92	0.293	10.1002/pen.25247	Q2

98	Preparations of Silver/Montmorillonite Biocomposite Multilayers and Their Antifungal Activity	COATINGS,9,817 (2019)	Iconaru, SL; Groza, A; Stan, GE; Predoi, D; Gaiaschi, S; Trusca, R; Chifiriuc, CM; Marutescu, L; Tite, T; Stanciu, GA; Hristu, R; Ghegoiu, L; Badea, ML; Turculet, CS; Ganciu, M; Chapon, P	2.33	0.369	10.3390/coatings9120817	Q2
99	Biocompatible Layers Obtained from Functionalized Iron Oxide Nanoparticles in Suspension	COATINGS,9,773 (2019)	Predoi, D; Iconaru, SL; Predoi, MV; Buton, N; Megier, C; Motelica-Heino, M	2.33	0.369	10.3390/coatings9120773	Q2
100	Superconducting MgB2 textured bulk obtained by ex situ spark plasma sintering from green compacts processed by slip casting under a 12T magnetic field	SUPERCONDUCTOR SCIENCE & TECHNOLOGY,32,125001 (2019)	Grigoroscuta, MA; Sandu, V; Kuncser, A; Pasuk, I; Aldica, G; Suzuki, TS; Vasylkiv, O; Badica, P	2.489	0.746	10.1088/1361-6668/ab4620	Q2
101	Modelling J?V hysteresis in perovskite solar cells induced by voltage poling	PHYSICA SCRIPTA,94,125809 (2019)	Anghel, DV; Nemnes, GA; Pintilie, I; Manolescu, A	2.151	0.442	10.1088/1402-4896/ab347d	Q2
102	Nonvolatile resistance switching in monolayer transition metal dichalcogenides: an explanation	SEMICONDUCTOR SCIENCE AND TECHNOLOGY,34,125004 (2019)	Mihai, C; Velea, A; Sava, F	2.654	0.576	10.1088/1361-6641/ab4b85	Q2
103	Molecular dynamics in bulk and surface species of cyanophenyl alkyl benzoates with 2, 3 and 7 carbon atoms in the alkyl chain: comparison in the whole homologous series	LIQUID CRYSTALS,, pp.- ()	Frunza, S; Ganea, CP; Zgura, I; Frunza, L; Schonhals, A	3.078	0.32	10.1080/02678292.2019.1687768	Q2
104	Comprehensive In Vitro Testing of Calcium Phosphate-Based Bioceramics with Orthopedic and Dentistry Applications	MATERIALS,12,3704 (2019)	Albulescu, R; Popa, AC; Enciu, AM; Albulescu, L; Dudau, M; Popescu, ID; Mihai, S; Codrici, E; Pop, S; Lupu, AR; Stan, GE; Manda, G; Tanase, C	2.972	0.608	10.3390/ma12223704	Q2
105	Electronic phase separation at $LaAlO_3/SrTiO_3$ interfaces tunable by oxygen deficiency	PHYSICAL REVIEW MATERIALS,3,106001 (2019)	Strocov, VN; Chikina, A; Caputo, M; Husanu, MA; Bisti, F; Bracher, D; Schmitt, T; Granozio, FM; Vaz, CAF; Lechermann, F	2.926	1.022	10.1103/PhysRevMaterials.3.106001	Q2

106	Reticulated Mesoporous TiO_2 Scaffold, Fabricated by Spray Coating, for Large-Area Perovskite Solar Cells	ENERGY TECHNOLOGY,8,UNSP 1900922 (2020)	Tomulescu, AG; Stancu, V; Besleaga, C; Enculescu, M; Nemnes, GA; Florea, M; Dumitru, V; Pintilie, L; Pintilie, I; Leonat, L	3.163	0.615	10.1002/ente.201900922	Q2
107	Photoluminescence and thermoluminescence properties of the $Sr_3Al_2O_6:Eu^{3+}/Eu^{2+},Tb^{3+}$ persistent phosphor	JOURNAL OF LUMINESCENCE 214,116540 (2019)	Gingasu, D; Mindru, I; Ianculescu, A; Preda, S; Negrila, C; Secu, M	2.961	0.421	10.1016/j.jlumin.2019.116540	Q2
108	Graphitic carbon nitride based photoanodes prepared by spray coating method	INTERNATIONAL JOURNAL OF HYDROGEN ENERGY,44, pp.24430-24440 (2019)	Sima, M; Vasile, E; Sima, A; Preda, N; Logofatu, C	4.084	0.581	10.1016/j.ijhydene.2019.07.243	Q2
109	Photoluminescence and structural properties of the nitrogen doped TiO_2 and the influence of SiO_2 and Ag nanoparticles	JOURNAL OF PHYSICS-CONDENSED MATTER,31,375201 (2019)	Nila, A; Baibarac, M; Udrescu, A; Smaranda, I; Mateescu, A; Mateescu, G; Mereuta, P; Negrila, CC	2.711	0.846	10.1088/1361-648X/ab2692	Q2
110	Fabrication and characterization of Si1-xGex nanocrystals in as-grown and annealed structures: a comparative study	BEILSTEIN JOURNAL OF NANOTECHNOLOGY,10, pp.1873-1882 (2019)	Sultan, MT; Maraloiu, AV; Stavarache, I; Gudmundsson, JT; Manolescu, A; Teodorescu, VS; Ciurea, ML; Svavarsson, HG	2.269	0.633	10.3762/bjnano.10.182	Q2
111	Study of the Structure and Antimicrobial Activity of Ca-Deficient Ceramics on Chlorhexidine Nanoclay Substrate	MATERIALS,12,2996 (2019)	Pazourkova, L; Reli, M; Hundakova, M; Pazdziora, E; Predoi, D; Martynkova, GS; Lafdi, K	2.972	0.608	10.3390/ma12182996	Q2
112	Development of W-monoblock divertor components with embedded thermal barrier interfaces	FUSION ENGINEERING AND DESIGN,146, pp.1351-1354 (2019)	Galatanu, M; Cioca, M; Ighigeanu, A; Ruiu, G; Enculescu, M; Popescu, B; Galatanu, A	1.457	0.32	10.1016/j.fusengdes.2019.02.074	Q2
113	Sintering and irradiation of copper-based high entropy alloys for nuclear fusion	FUSION ENGINEERING AND DESIGN,146, pp.1824-1828 (2019)	Dias, M; Antao, F; Catarino, N; Galatanu, A; Galatanu, M; Ferreira, P; Correia, JB; da Silva, RC; Goncalves, AP; Alves, E	1.457	0.32	10.1016/j.fusengdes.2019.03.044	Q2
114	Thermophysical and mechanical properties of W-Cu laminates produced by FAST joining	FUSION ENGINEERING AND DESIGN,146, pp.2371-2374 (2019)	Galatanu, A; Galatanu, M; Enculescu, M; Reiser, J; Sickinger, S	1.457	0.32	10.1016/j.fusengdes.2019.03.193	Q2

115	3D Superparamagnetic Scaffolds for Bone Mineralization under Static Magnetic Field Stimulation	MATERIALS,12,2834 (2019)	Paun, IA; Calin, BS; Mustaciosu, CC; Mihailescu, M; Moldovan, A; Crisan, O; Leca, A; Luculescu, CR	2.972	0.608	10.3390/ma12172834	Q2
116	Physical properties of Cu and Dy co-doped ZnO thin films prepared by radio frequency magnetron sputtering for hybrid organic/inorganic electronic devices	THIN SOLID FILMS,685, pp.379-384 (2019)	Locovei, C; Coman, D; Radu, A; Ion, L; Antohe, VA; Vasile, N; Dumitru, A; Iftimie, S; Antohe, S	1.888	0.324	10.1016/j.tsf.2019.06.027	Q2
117	Crystallization processes in europium-doped $Bi_4Ge_3O_{12}$ glass materials	JOURNAL OF LUMINESCENCE,213, pp.235-240 (2019)	Polosan, S	2.961	0.421	10.1016/j.jlumin.2019.05.031	Q2
118	Carbon-based sprayed electrodes for pyroelectric applications	PLOS ONE 14,e0221108 (2019)	Chirila, C; Botea, M; Iuga, A; Tomulescu, AG; Balescu, L; Galca, AC; Boni, AG; Leonat, L; Pintilie, I; Pintilie, L	2.776	0.978	10.1371/journal.pone.0221108	Q2
119	Generalized Master Equation Approach to Time-Dependent Many-Body Transport	ENTROPY,21,731 (2019)	Moldoveanu, V; Manolescu, A; Gudmundsson, V	2.419	0.516	10.3390/e21080731	Q2
120	Rapid thermal annealing for high-quality ITO thin films deposited by radio-frequency magnetron sputtering	BEILSTEIN JOURNAL OF NANOTECHNOLOGY,10, pp.1511-1522 (2019)	Prepelita, P; Stavarache, I; Craciun, D; Garoi, F; Negrila, C; Sbarcea, BG; Craciun, V	2.269	0.633	10.3762/bjnano.10.149	Q2
121	Structural, electric and pyroelectric properties of up and down graded PZT multilayers	CURRENT APPLIED PHYSICS,19, pp.804-810 (2019)	Botea, M; Hrib, L; Pasuk, I; Iuga, A; Trupina, L; Negrea, R; Becherescu, N; Pintilie, L	2.01	0.374	10.1016/j.cap.2019.04.010	Q2
122	Effect of dilute doping and non-equilibrium synthesis on the structural, luminescent and magnetic properties of nanocrystalline Zn_1-xNixO (x=0.0025-0.03)	MATERIALS RESEARCH BULLETIN,115, pp.37-48 (2019)	Mihalache, V; Negrila, C; Bercu, V; Secu, M; Vasile, E; Stan, GE	3.355	0.412	10.1016/j.materresbull.2019.03.001	Q2
123	Gd3+ co-doping influence on the morphological, up-conversion luminescence and magnetic properties of LiYF4:Yb3+/Er3+ nanocrystals	JOURNAL OF PHYSICS AND CHEMISTRY OF SOLIDS,130, pp.236-241 (2019)	Secu, CE; Bartha, C; Matei, E; Negrila, C; Crisan, A; Secu, M	2.752	0.385	10.1016/j.jpcs.2019.03.003	Q2

124	On the relaxation time of interacting superparamagnetic nanoparticles and implications for magnetic fluid hyperthermia	BEILSTEIN JOURNAL OF NANOTECHNOLOGY,10, pp.1280-1289 (2019)	Kuncser, A; Iacob, N; Kuncser, VE	2.269	0.633	10.3762/bjnano.10.127	Q2
125	Structural Change in Ni-Fe-Ga Magnetic Shape Memory Alloys after Severe Plastic Deformation	MATERIALS,12,1939 (2019)	Gurau, G; Gurau, C; Tolea, F; Sampath, V	2.972	0.608	10.3390/ma12121939	Q2
126	Bulk Versus Surface Modification of Alumina with Mn and Ce Based Oxides for CH_4 Catalytic Combustion	MATERIALS,12,1771 (2019)	Neatu, S; Trandafir, MM; Stanoiu, A; Florea, OG; Simion, CE; Leonat, LN; Cobianu, C; Gheorghe, M; Florea, M; Neatu, F	2.972	0.608	10.3390/ma12111771	Q2
127	Peppermint Essential Oil-Doped Hydroxyapatite Nanoparticles with Antimicrobial Properties	MOLECULES,24,2169 (2019)	Badea, ML; Iconaru, SL; Groza, A; Chifiriuc, MC; Beuran, M; Predoi, D	3.06	0.62	10.3390/molecules24112169	Q2
128	The Influence of Heteroatom Dopants Nitrogen, Boron, Sulfur, and Phosphorus on Carbon Electrocatalysts for the Oxygen Reduction Reaction	CHEMPLUSCHEM,84, pp.457-464 (2019)	Preuss, K; Siwoniku, AM; Bucur, CI; Titirici, MM	3.441	0.575	10.1002/cplu.201900083	Q2
129	Phase Control in Hafnia: New Synthesis Approach and Convergence of Average and Local Structure Properties	ACS OMEGA,4, pp.8881-8891 (2019)	Cojocaru, B; Avram, D; Negrea, R; Ghica, C; Kessler, VG; Seisenbaeva, GA; Parvulescu, VI; Tiseanu, C	2.584	0.533	10.1021/acsomega.9b00580	Q2
130	Sub-lattice polarization states in anti-ferroelectrics and their relaxation process	CURRENT APPLIED PHYSICS,19, pp.651-656 (2019)	Vopson, MM; Tan, X; Namvar, E; Belusky, M; Thompson, SP; Kuncser, V; Plazaola, F; Unzueta, I; Tang, CC	2.01	0.374	10.1016/j.cap.2019.03.009	Q2
131	Enhancement in magnetic and dielectric properties of the ruthenium-doped copper ferrite(Ru - $CuFe_2O_4$) nanoparticles	JOURNAL OF MAGNETISM AND MAGNETIC MATERIALS,476, pp.18-23 (2019)	Manikandan, V; Kuncser, V; Vasile, B; Kavita, S; Vigneselvan, S; Mane, RS	2.683	0.433	10.1016/j.jmmm.2018.12.050	Q2
132	Epitaxial Non c-Axis Twin-Free $Bi_2Sr_2CaCu_2O^{8+}$ Thin Films for Future THz Devices	MATERIALS,12,1124 (2019)	Endo, K; Arisawa, S; Badica, P	2.972	0.608	10.3390/ma12071124	Q2
133	Presence and distribution of impurity defects in crystalline cubic boron nitride. A spectroscopic study	RADIATION MEASUREMENTS,123, pp.21-25 (2019)	Nistor, SV; Nistor, LC; Joita, AC; Vlaicu, AM	1.435	0.384	10.1016/j.radmeas.2019.02.003	Q2

134	Structure of defects in semiconductor crystalline cubic boron nitride. A microstructural and micro analytical investigation	RADIATION MEASUREMENTS,123, pp.78-82 (2019)	Nistor, LC; Vlaicu, AM; Nistor, SV	1.435	0.384	10.1016/j.radmeas. 2019.02.019	Q2
135	Prototype Orthopedic Bone Plates 3D Printed by Laser Melting Deposition	MATERIALS,12,906 (2019)	Chioibasu, D; Achim, A; Popescu, C; Stan, GE; Pasuk, I; Enculescu, M; Iosub, S; Duta, L; Popescu, A	2.972	0.608	10.3390/ma12060906	Q2
136	Fabrication and characterization of Ru-doped $LiCuFe_2O_4$ nanoparticles and their capacitive and resistive humidity sensor applications	JOURNAL OF MAGNETISM AND MAGNETIC MATERIALS,474, pp.563-569 (2019)	Manikandan, V; Tudorache, F; Petrila, J; Mane, RS; Kuncser, V; Vasile, B; Morgan, D; Vigneselvan, S; Mirzaei, A	2.683	0.433	10.1016/j.jmmm. 2018.11.072	Q2
137	Behavior of Molybdenum-Vanadium Mixed Oxides in Selective Oxidation and Disproportionation of Toluene	MATERIALS,12,748 (2019)	Mitran, G; Neatu, F; Pavel, OD; Trandafir, MM; Florea, M	2.972	0.608	10.3390/ma12050748	Q2
138	Coexisting spin and Rabi oscillations at intermediate time regimes in electron transport through a photon cavity	BEILSTEIN JOURNAL OF NANOTECHNOLOGY,10, pp.606-616 (2019)	Gudmundsson, V; Gestsson, H; Abdullah, NR; Tang, CS; Manolescu, A; Moldoveanu, V	2.269	0.633	10.3762/bjnano.10.61	Q2
139	Passive magnetic shielding by machinable MgB_2 bulks: measurements and numerical simulations	SUPERCONDUCTOR SCIENCE & TECHNOLOGY,32,034004 (2019)	Gozzelino, L; Gerbaldo, R; Ghigo, G; Laviano, F; Torsello, D; Bonino, V; Truccato, M; Batalu, D; Grigoroscuta, MA; Burdusel, M; Aldica, GV; Badica, P	2.489	0.746	10.1088/1361-6668/aaf99e	Q2
140	Laser-induced synthesis and photocatalytic properties of hybrid organic-inorganic composite layers	JOURNAL OF MATERIALS SCIENCE,54, pp.3927-3941 (2019)	Ivan, R; Popescu, C; del Pino, AP; Yousef, I; Logofatu, C; Gyorgy, E	3.442	0.558	10.1007/s10853-018-3144-0	Q2
141	Zinc Doped Hydroxyapatite Thin Films Prepared by Sol-Gel Spin Coating Procedure	COATINGS,9,156 (2019)	Predoi, D; Iconaru, SL; Predoi, MV; Buton, N; Motelica-Heino, M	2.33	0.369	10.3390/coatings9030156	Q2
142	N-Doped Defective Graphene from Biomass as Catalyst for CO_2 Hydrogenation to Methane	CHEMCATCHEM,11, pp.985-990 (2019)	Jurca, B; Bucur, C; Primo, A; Concepcion, P; Parvulescu, VI; Garcia, H	4.495	0.991	10.1002/cctc.201801984	Q2

143	Physical properties investigation of samarium doped calcium sulfate thin films under high gamma irradiations for space photovoltaic and dosimetric applications	SUPERLATTICES AND MICROSTRUCTURES,126, pp.103-119 (2019)	Souli, M; Reghima, M; Secu, M; Bartha, C; Enculescu, M; Mejri, A; Kamoun-Turki, N; Badica, P	2.385	0.342	10.1016/j.spmi.2018.12.021	Q2
144	Naturally-Derived Biphasic Calcium Phosphates through Increased Phosphorus-Based Reagent Amounts for Biomedical Applications	MATERIALS,12,381 (2019)	Mocanu, AC; Stan, GE; Maidaniuc, A; Miculescu, M; Antoniac, IV; Ciocoiu, RC; Voicu, SI; Mitran, V; Cimpean, A; Miculescu, F	2.972	0.608	10.3390/ma12030381	Q2
145	Spirobifluorene-based Porous Organic Polymers as Efficient Porous Supports for Pd and Pt for Selective Hydrogenation	CHEMCATCHEM,11, pp.538-549 (2019)	Trandafir, MM; Pop, L; Hadade, ND; Hristea, I; Teodorescu, CM; Krumeich, F; van Bokhoven, JA; Grosu, I; Parvulescu, VI	4.495	0.991	10.1002/cctc.201801247	Q2
146	Structural characterisation and thermal stability of SnSe\GaSb stacked films	PHILOSOPHICAL MAGAZINE,99, pp.55-72 (2019)	Sava, F; Borca, CN; Galca, AC; Socol, G; Grolimund, D; Mihai, C; Velea, A	1.855	0.515	10.1080/14786435.2018.1529442	Q2
147	Tailoring SP2/SP3 ratio in diamond-like carbon films via deposition parametres in a high voltage anodic vaccum plasma	ROMANIAN REPORTS IN PHYSICS,71,414 (2019)	Badulescu, M; Anghel, A; Surdu-Bob, CC; Logofatu, C; Luculescu, C	1.94	0.296		Q2
148	Photo-electrical properties of thin films with Ge nanoparticles embedded in TIO_2 matrix	ROMANIAN REPORTS IN PHYSICS,71,504 (2019)	Stavarache, I; Maraloiu, VA	1.94	0.296		Q2
149	Composite BNT-BT0.08/$CoFe_2O_4$ with core-shell nanostructure for piezoelectric and ferromagnetic applications	MATERIALS SCIENCE AND ENGINEERING B-ADVANCED FUNCTIONAL SOLID-STATE MATERIALS,240, pp.7-15 (2019)	Cernea, M; Vasile, BS; Ciuchi, IV; Surdu, VA; Bartha, C; Iuga, A; Galizia, P; Galassi, C	3.507	0.495	10.1016/j.mseb.2019.01.001	Q2
150	Pulsed Laser Deposition of Indium Tin Oxide Thin Films on Nanopatterned Glass Substrates	COATINGS,9,19 (2019)	Socol, M; Preda, N; Rasoga, O; Costas, A; Stanculescu, A; Breazu, C; Gherendi, F; Socol, G	2.33	0.369	10.3390/coatings9010019	Q2

151	Room temperature ferromagnetism and its correlation to ferroelectricity of manganese embedded in lead zirco-titanate	THIN SOLID FILMS,669, pp.440-449 (2019)	Bucur, IC; Apostol, NG; Abramiuc, LE; Tanase, LC; Tache, CA; Lungu, GA; Costescu, RM; Chirila, CF; Trupina, L; Pintilie, L; Teodorescu, CM	1.888	0.324	10.1016/j.tsf.2018.11.018	Q2
152	Antireflective coatings with high damage threshold prepared by laser ablation	APPLIED PHYSICS A-MATERIALS SCIENCE & PROCESSING,125,815 (2019)	Filipescu, M; Palla-Papavlu, A; Bercea, A; Rusen, L; Cernaianu, MO; Ion, V; Calugar, A; Nistor, LC; Dinescu, M	1.784	0.308	10.1007/s00339-019-3110-y	Q3
153	Charge Transfer from Alq(3)-5Cl to Graphene Oxide in Donor-Acceptor Heterostructures	JOURNAL OF ELECTRONIC MATERIALS,48, pp.- (2019)	Polosan, S; Ciobotaru, CC; Ciobotaru, IC	1.676	0.273	10.1007/s11664-019-07531-w	Q3
154	Experimental study of Terahertz response from some ferroelectric and dielectric materials	PROCEEDINGS OF THE ROMANIAN ACADEMY SERIES A-MATHEMATICS PHYSICS TECHNICAL SCIENCES INFORMATION SCIENCE,20, pp.353-360 (2019)	Banciu, MG; Nedelcu, L; Furuya, T; Hrib, L; Geambasu, DC; Trupina, L; Pantelica, D; Mihai, MD; Tani, M	1.402	0.24		Q3
155	k-resolved electronic structure of buried heterostructure and impurity systems by soft-X-ray ARPES	JOURNAL OF ELECTRON SPECTROSCOPY AND RELATED PHENOMENA,236, pp.1-8 (2019)	Strocov, VN; Lev, LL; Kobayashi, M; Cancellieri, C; Husanu, MA; Chikina, A; Schroter, NBM; Wang, X; Krieger, JA; Salman, Z	1.343	0.544	10.1016/j.elspec.2019.06.009	Q3
156	Effect of slow charged 90 keV Ne8+ ions on zinc ferrite nanoparticles	MATERIALS RESEARCH EXPRESS 6,095077 (2019)	Trandafir, EV; Caltun, OF; Ciocarlan, R; Pui, A; Hempelmann, R; Diamandescu, L; Cervera, S; Trassinelli, M; Vernhet, D	1.449	0.236	10.1088/2053-1591/ab3174	Q3
157	Structural and electronic properties of the alpha-GeSe surface	SURFACE SCIENCE,686, pp.17-21 (2019)	Jiao, Z; Yao, QR; Balescu, LM; Liu, QJ; Bin, T; Zandvliet, HJW	1.849	0.46	10.1016/j.susc.2019.03.007	Q3
158	Formation of a Bistable Interstitial Complex in Irradiated p-Type Silicon	PHYSICA STATUS SOLIDI A-APPLICATIONS AND MATERIALS SCIENCE 216,1900354 (2019)	Makarenko, LF; Lastovski, SB; Yakushevich, HS; Gaubas, E; Pavlov, J; Kozlovski, VV; Moll, M; Pintilie, I	1.606	0.371	10.1002/pssa.201900354	Q3

159	Tryptophan/Dextran70 Based-Fluorescent Silver Nanoparticles: Synthesis and Physicochemical Properties	JOURNAL OF FLUORESCENCE,29, pp.981-992 (2019)	Voicescu, M; Ionescu, S; Calderon-Moreno, JM; Teodorescu, VS; Anastasescu, M; Culita, DC	1.913	0.269	10.1007/s10895-019-02411-2	Q3
160	A Dyson Equation for Non-Equilibrium Green's Functions in the Partition-Free Setting	PHYSICA STATUS SOLIDI B-BASIC SOLID STATE PHYSICS 256,1800447 (2019)	Cornean, HD; Moldoveanu, V; Pillet, CA	1.454	0.413	10.1002/pssb.201800447	Q3
161	Photoconductive Behavior of the PPV/RGO Composites: Insights of Charge Transfer Process	PHYSICA STATUS SOLIDI B-BASIC SOLID STATE PHYSICS 256,1800392 (2019)	Ilie, M; Dragoman, D; Baibarac, M	1.454	0.413	10.1002/pssb.201800392	Q3
162	Annealing of preexisting defects in silicon single crystals by ion irradiation	NUCLEAR INSTRUMENTS & METHODS IN PHYSICS RESEARCH SECTION B-BEAM INTERACTIONS WITH MATERIALS AND ATOMS,450, pp.85-89 (2019)	Mihai, MD; Ionescu, P; Pantelica, D; Petrascu, H; Craciun, D; Craciun, V; Vasiliu, F; Vasile, BS; Mercioniu, I	1.21	0.362	10.1016/j.nimb. 2018.09.005	Q3
163	Structural and optical properties of ZnO thin films grown by rapid atmospheric mist chemical vapor technique	OPTICAL AND QUANTUM ELECTRONICS,51,210 (2019)	Derbali, S; Nouneh, K; Galca, AC; Touhami, ME; Secu, M; Matei, E; Leonat, LN; Pintilie, L; El Harfaoui, N; Fahoume, M	1.547	0.21	10.1007/s11082-019-1937-2	Q3
164	Interaction and Size Effects in Open Nano-Electromechanical Systems	PHYSICA STATUS SOLIDI B-BASIC SOLID STATE PHYSICS 256,1800443 (2019)	Tanatar, B; Moldoveanu, V; Dragomir, R; Stanciu, S	1.454	0.413	10.1002/pssb.201800443	Q3
165	Polarization branches and optimization calculation strategy applied to ABO(3) ferroelectrics	MODELLING AND SIMULATION IN MATERIALS SCIENCE AND ENGINEERING,27,045008 (2019)	Filip, LD; Plugaru, N; Pintilie, L	1.826	0.672	10.1088/1361-651X/ab146e	Q3
166	Vibrational and photoluminescence properties of polydiphenylamine doped with silicotungstic acid heteropolyanions and their composites with reduced graphene oxide	JOURNAL OF MOLECULAR STRUCTURE,1184, pp.25-35 (2019)	Baibarac, M; Stroe, M; Fejer, SN	2.12	0.244	10.1016/j.molstruc. 2019.02.014	Q3

167	Efficiency enhancement of iridium-based organometallic light emitting diodes	MATERIALS RESEARCH EXPRESS 6,055104 (2019)	Polosan, S	1.449	0.236	10.1088/2053-1591/ab0625	Q3
168	Coordination polymers and a dinuclear complex constructed from zinc(II) ions and fluorescein: iodine adsorption and optical properties	JOURNAL OF COORDINATION CHEMISTRY,72, pp.1222-1237 (2019)	Raduca, M; Ene, CD; Ionescu, S; Florea, M; Madalan, AM	1.685	0.166	10.1080/00958972. 2019.1605442	Q3
169	Novel anhydrous solid-state form of Azathioprine: The assessing of crystal structure by powder X-Ray diffraction, Infrared Absorption Spectroscopy and Raman scattering	JOURNAL OF MOLECULAR STRUCTURE,1178, pp.702-710 (2019)	Covaci, OI; Samohvalov, D; Manta, CM; Buhalteanu, L; Barbatu, A; Baibarac, M; Daescu, M; Matea, A; Gherca, D	2.12	0.244	10.1016/j.molstruc. 2018.10.065	Q3
170	Multiferroic (Nd,Fe)-doped $PbTiO_3$ thin films obtained by pulsed laser deposition	APPLIED PHYSICS A-MATERIALS SCIENCE & PROCESSING,125,113 (2019)	Dumitru-Grivei, M; Ion, V; Birjega, R; Moldovan, A; Craciun, F; Cernea, M; Galassi, C; Dinescu, M	1.784	0.308	10.1007/s00339-019-2403-5	Q3
171	Comparison between dielectric and pyroelectric properties of PZFNT and BST type ceramics	PROCESSING AND APPLICATION OF CERAMICS,13, pp.269-276 (2019)	Stancu, V; Amarande, L; Botea, M; Iuga, A; Leonat, LN; Tomulescu, AG; Cioangher, M; Balescu, LM; Pintilie, L	0.976	0.19	10.2298/PAC1903269S	Q3
172	Ferroelectric Field Effect Transistors Based on PZT and IGZO	IEEE JOURNAL OF THE ELECTRON DEVICES SOCIETY,7, pp.268-275 (2019)	Besleaga, C; Radu, R; Balescu, LM; Stancu, V; Costas, A; Dumitru, V; Stan, G; Pintilie, L	2	0.764	10.1109/JEDS. 2019.2895367	Q3
173	Investigation of the photoelectrochemical behavior of nanocarbon/mesoporous TiO_2 films	DIGEST JOURNAL OF NANOMATERIALS AND BIOSTRUCTURES,14, pp.935-941 (2019)	Sima, M; Vasile, E; Sima, A	0.638	0.105		Q4
174	Structural evolution of the NiTi/NiFeGa smart hybrid material during severe plastic deformation	DIGEST JOURNAL OF NANOMATERIALS AND BIOSTRUCTURES,14, pp.539-546 (2019)	Gurau, C; Gurau, G; Tolea, F; Sampath, V	0.638	0.105		Q4
175	Structural dielectric and pyroelectric properties of Nb and Fe doped PZT ceramics	DIGEST JOURNAL OF NANOMATERIALS AND BIOSTRUCTURES,14, pp.225-230 (2019)	Stancu, V; Amarande, L; Botea, M; Cioangher, M; Tomulescu, A; Iuga, A; Pintilie, L	0.638	0.105		Q4

176	Raman investigations on gamma irradiated iPP-VGCNF nanocomposites: The polymer's tale	SURFACES AND INTERFACES,17,UNSP 100351 (2019)	Chipara, DM; Secu, C; Lozano, K; Secu, M; Chipara, M	not available	not available	10.1016/j.surfin.2019.100351	not available
177	GeSn Nanocrystals in $GeSnSiO_2$ by Magnetron Sputtering for Short-Wave Infrared Detection	ACS APPLIED NANO MATERIALS,2, pp.3626-3635 (2019)	Slav, A; Palade, C; Logofatu, C; Dascalescu, I; Lepadatu, AM; Stavarache, I; Comanescu, F; Iftimie, S; Antohe, S; Lazanu, S; Teodorescu, VS; Buca, D; Ciurea, ML; Braic, M; Stoica, T	not available	not available	10.1021/acsanm.9b00571	not available
178	Particularities of trichloroethylene photocatalytic degradation over crystalline $RbLaTa_2O_7$ nanowire bundles grown by solid-state synthesis route	JOURNAL OF ENVIRONMENTAL CHEMICAL ENGINEERING,7,UNSP 102789 (2019)	Raciulete, M; Papa, F; Kawamoto, D; Munteanu, C; Culita, DC; Negrila, C; Atkinson, I; Bratan, V; Pandele-Cusu, J; Balint, I	not available	not available	10.1016/j.jece.2018.11.034	not available
179	$Fe_3O_4/BaTiO_3$ Composites with core-shell structure	UNIVERSITY POLITEHNICA OF BUCHAREST SCIENTIFIC BULLETIN SERIES B-CHEMISTRY AND MATERIALS SCIENCE,81, pp.171-180 (2019)	Tanasa, E; Andronescu, E; Cernea, M; Oprea, OC	not available	not available		not available
180	Capatanii/Parang Mountains: Polovragi Cave-Oltetului Gorge Karst Area	CAVE AND KARST SYSTEMS OF ROMANIA,, pp.83-91 (2019)	Ponta, GML; Aldica, GV; Dumitru, R	not available	not available	10.1007/978-3-319-90747-5_12	not available
181	Mehedinti Mountains: Martel and Lazului Caves	CAVE AND KARST SYSTEMS OF ROMANIA,, pp.157-163 (2019)	Ponta, GML; Aldica, GV; Tulucan, T	not available	not available	10.1007/978-3-319-90747-5_19	not available

Conferences

Nr. Crt.	Scientific event (name, period, location)	Presentation title	Authors (name and surname)	Presentation type (invited, oral, poster)
Participations and financially supported presentations from project 12PFE / 2018, Phases 2 and 3 of 2019				
1	EMN Epitaxy, Amsterdam June 17th -21st , 2019, Holland	New functionalities and findings in epitaxial ferroelectric structures	Georgia A. Boni, Lucian D. Filip, Cristina Chirila, Alin Iuga, I. Pasuk, Luminita Hrib, Lucian Trupina, Ioana Pintilie, Lucian Pintilie	Invited
2	EMN Epitaxy, Amsterdam June 17th -21st , 2019, Holland	Strain driven defects in epitaxial thin films: HRTEM quantification and nanoscale mapping	Corneliu Ghica, Raluca Negrea, Valentin Teodorescu, Cristina Chirila, Nicu Scarisoreanu, Lucian Pintilie	Invited
3	E-MRS 2019 Conference, May 26th-June 1st 2019, Nice, France	About hysteresis, dielectric constant and negative capacitance in PZT capacitors	Lucian Pintilie*, Andra Georgia Boni, Cristina Chirila, Luminita Hrib, Lucian Trupina, Lucian Dragos Filip	Invited
4	RomCat Conference 2019, June 7th -12th , 2019, Bucharest, Romania	Fast photoelectron spectroscopy follow-up of the efficiency of ferroelectric substrates for CO reduction / oxidation: the case of Pb(Zr,-Ti)O3(001) decorated with gold nanoparticles	Nicoleta G. Apostol1, Marius A. Huşanu1, Daniel Lizzit2, Ioana A. Hristea1,3, Cristina F. Chirilă1, Lucian Trupină1, Cristian M. Teodorescu1*	Invited
6	SIPS Conference 2019, October 23rd -27th, 2019, Pafos, Cipru	Recent results and new functionalities in ferroelectric based structures	L. Pintilie, A. G. Boni, C. Chirila, L. Hrib, L.D. Filip, N. Plugaru, I. Pasuk, L. Trupina, R. Negrea, C. Istrate, L. Balescu, C. Besleaga, G. Stan, I. Pintilie,	Invited
7	35th International Conference on Mossbauer Effect Applications, ICAME 2019, September 1st -6th, 2019 Dalian, China	Mössbauer spectroscopy explaining specific magneto-functionalities in RE-Fe amorphous thin films	V. Kuncser,A.E. Stanciu, A. Kuncser, C. Locovei, G. Schinteie, N. Iacob, N. Plugaru, O. Crisan	Invited
8	European Advanced Materials Congress, August 11th -14th, 2019, Sweden , Stockolm	Organometallics for OLED and OPV: fundamentals and applications	S. Polosan	Invited
9	RomCat Conference 2019, June 7th -12th , 2019, Bucharest, Romania	Lead photo-reduction from $Pb(Zr,Ti)O_3(001)$ investigated by photoelectron spectro-microscopy	Laura E. Abramiuc[1,2], Liviu C. Tănase[1], Cristina F. Chirilă[1], Alexei Barinov[3], Cristian M. Teodorescu[1]	Oral presentation
10	SPR summer school, June 6th -11th , 2019, Tampere, Finland	Surface charge and pH influence on BSA adsorption on Polyelectrolyte layers	Anca Aldea, Dominik Söder, Jari Väliaho	Oral presentation

11	World Congress on Functional Materials and Nanotechnology May 13th -14th , 2019, Valencia, Spain	Mesoporous TiO_2 scaffold engineering in hybrid perovskite solar cells	Andrei Gabriel Tomulescu[1,2], Viorica Stancu[1], Cristina Beşleagă[1], Monica Enculescu[1], Mihaela Florea[1], Viorel Dumitru[1], Lucian Pintilie[1], Ioana Pintilie[1] and Lucia Leonat[1]	Oral presentation
12	Superconductivity meets Molecular Spins, March 22nd , Lisbon, Portugal, 2019	Ways toward multifunctionalityin systems of biomolecules	Bogdana Borca	Oral presentation
13	RomCat Conference 2019, June 7th -12th, 2019, Bucharest, Romania	Coupling ferroelectric PZT(001) surfaces with noble metals (Ag) for dissociation of adsorbed molecules (CO)	Adela Nicolaev, Nicoleta G. Apostol, Ruxandra M. Costescu, Amelia E. Bocîrnea, Ioana A. Hristea, Cristina F. Chirilă, Cristian M. Teodorescu	Oral presentation
14	E-MRS 2019 Conference, May 26th-June 1st 2019, Nice, France	ZnO-CuOcore-shell radial heterojunction nanowires: synthesis, properties and optoelectronic applications	Andreea Costas, Camelia Florica, Nicoleta Preda, Nicoleta Apostol, Andrei Kuncser, Ionut Enculescu	Oral presentation
15	World Congress on Functional Materials and Nanotechnology May 13th -14th , 2019, Valencia, Spain	Properties of electrochemically grown Cd-Tenanowires	Melania Loredana Onea1,2, Elena Matei 1, Monica Enculescu 1, Ionut Enculescu 1	Oral presentation
16	9th International Conference of the Chemical Societies of the South-East European Countries May 8th- 11th , 2019 Valahia University of Targoviste	La_2O_3-doped alumina supported cerium–manganese mixed oxides for CH_4 catalytic combustion	Mihaela M. Trandafir,[a] Ştefan Neaţu,[a] Florentina Neaţu,[a] Adelina Stănoiu,[a] Ovidiu G. Florea,[a] Cristian E. Simion,[a] Cornel Cobianu,[b] Marin Gheorghe,[b] Lucia N. Leonat,[a] Mihaela Florea[a]	Oral presentation
17	9th Edition of the International Conference on Chemistry Science and Technology & 11th International Conference & Expo on Chromathography Techniques", April 21st- 24th, 2019, Dublin, Ireland	Indium Tin Oxide Thin Films Deposited by Pulsed Laser Deposition on Nanopaterned Glass Substrates.	C. Breazu	Oral presentation

18	RomCat Conference 2019, June 7th -12th, 2019, Bucharest, Romania	CO adsorption, photodesorption and associated charge transfer on atomically clean graphene synthesized on atomically clean Pt(001)	Cristina Bucur, Nicoleta G. Apostol, George A. Lungu, Cristian A. Tache, Cristian M. Teodorescu	Oral presentation
19	GraFox Summer School, June 03rd -9th 2019, Milano, Italy	Ge Nanocrystals in TiO-2Films for Near Infrared Optical Sensors	Ovidiu Cojocaru, Ioana Dascalescu, Catalin Palade, Adrian Slav	Oral presentation
20	GraFox Summer School, June 03rd -9th 2019, Milano, Italy	Graphene-like carbon layers grown on ferroelectric Pb(Zr,Ti) O_3(001)	Nicoleta G. Apostol[1], Adrian Lungu[1], Cristina Dragoi[1], Daniel Lizzit[2], Paolo Lacovig[2], Silvano Lizzit[2], Lucian Pintilie[1], Cristian M. Teodorescu[1]	Oral presentation
21	GraFox Summer School, June 03rd -9th 2019, Milano, Italy	Low Field Dielectric Properties of Sol-Gel Derived Ferroelectric Oxides With Perovskite Structure	Roxana E. Patru[1*], Paul Ganea[1], Catalina-Andreea Stanciu[2], Vasile-Adrian Surdu[2], Adelina-Carmen Ianculescu[2], Ioana Pintilie[1] and Lucian Pintilie[1]	Oral presentation
22	F2CP2 Joint Conference, July 13th -20th, 2019, Switzerland / Lausanne	Ferroelectric multilayered thin films structures for new storing and/or computing concepts	Georgia A. Boni, Lucian D. Filip, Cristina Chirila, Alin Iuga, I. Pasuk, Luminita Hrib, Lucian Trupina, Ioana Pintilie, Lucian Pintilie	Oral presentation
27	International Conference on Magnetism and Magnetic Materials, August 19th -20th, 2019, London, UK	Structural, magnetic and magneto-transport study of epitaxial LSMO films of different thicknesses deposited on STO	Simona G. Greculeasa[1], Aurel Leca[1,2], Andrei Kuncser[1], Luminita Hrib[1], Iuliana Pasuk[1], Victor Kuncser[1]	Oral presentation
28	MECAME-GFSM 2019, May 19th – 23th , 2019, France / Montpellier	Magnetostriction effects in RE-Fe-B ribbons investigated by Mössbauer spectroscopy	C. Locovei, A. Alexandru, G. Schinteie, N. Iacob, A. Stanciu, S.Greculeasa, M. Sofronie, F. Tolea, C. Bartha and V. Kuncser	Poster
29	E-MRS 2019 Conference, May 26th-June 1st 2019, Nice, France	Effect of ITO electrode patterning on the properties of MAPLE prepared organic heterostructures based on non-fullerene acceptor	A. Stanculescu, C. Breazu, M. Socol and others	Poster
30	E-MRS 2019 Conference, May 26th-June 1st 2019, Nice, France	Hybrid organic-inorganic heterostructures deposited by MAPLE Section: Laser interaction with materials: from fundamentals to application.	M. Socol, N. Preda, A. Costas, C. Breazu and others	Poster

31	E-MRS 2019 Conference, May 26th-June 1st 2019, Nice, France	Water stable photo-catalysts based on zinc oxide and copper oxide core-shell nanowires	Camelia Florica, Andreea Costas, Nicoleta Preda , Mihaela Beregoi, Andrei Kuncser, Nicoleta Apostol, Cristina Popa, Gabriel Socol, Victor Diculescu and Ionut Enculescu	Poster
32	E-MRS 2019 Conference, May 26th-June 1st 2019, Nice, France	Studies of the epitaxial $PbZr_{0.2}Ti_{0.8}O_3$ thin films capacitor structures deposited on Si substrate	G. A. Boni[1], C. Chirila[1], L. D. Filip[1], A. Iuga[1], I. Pasuk[1], L. Hrib[1], L. Trupina[1], A.M. Husanu[1], C. Istrate[1], Gwenael Le Rhun[2], I. Pintilie[1], L. Pintilie[1]	Poster
33	GraFox Summer School, June 03rd -9th 2019, Milano, Italy	Optoelectronic Properties of Heterojunction ZnO-CuxOCore-Shell Nanowires	Andreea COSTAS,* CameliaFLORICA,NicoletaPREDA, NicoletaAPOSTOL, Andrei KUNCSER, Andrei NITESCUand IonutENCULESCU1	Poster
34	GraFox Summer School, June 03rd -9th 2019, Milano, Italy	Properties of Cd-Tenanowires contacted on a SiO2/Si substrate	Melania Loredana ONEA, Elena Matei , Monica Enculescu , Ionut Enculescu	Poster
35	International Summer School on Nanoscience and Nanotechnologies & International Conference on Nanoscience and Nanotechnologies (ICNN), June 28th –July 6th 2019, Salonic, Greece	Nanoaggregates of impurities in superhard cubic boron nitride crystals	A. C. Joita*1,2, S. V. Nistor 1,2, L. C. Nistor 1, R. F. Negrea 1	Poster
36	International Summer School on Nanoscience and Nanotechnologies & International Conference on Nanoscience and Nanotechnologies (ICNN), June 28th –July 6th 2019, Greece/ Salonic	On the thermal stability of mesoporous metal oxide systems decorated with metallic nanoparticles for gas sensing applications	M. C. Istrate[1], V. A. Maraloiu[1], C. Radu[1], I. D. Vlaicu[1], S. Somacescu[2], A. Kuncser[1], C.Ghica[1]	Poster
37	ICSON – 2019, August 19th-21st, 2019, Spain / Barcelona	Optical properties of the polystyrene / graphene oxide composites	M. Stroe1, M. Cristea1, E. Matei1, L. C. Cotet2, L. Pop2, L. Baia3, M. Baibarac 1	Poster
38	NANOTECH France – 2019, June 26th -29th, 2019, Paris, France	Composites based on poly(2, 2'-bithiophene) and TiO_2 nanoparticles: from chemical synthesis to optical properties and their applications in the leather and textile materials field	I. Smaranda[1*], M. Stroe[1], A. Radu[1], R. Cercel[1], C. Gaidau[2], L. Chirila[2], M. Baibarac[1]	Poster

39	9th International Conference on Amorphous and NanostructuredChalcogenides-Fundamentals and Applications June 30th – July 4th , 2019, Chisinau, Republic of Moldova	Nonvolatile resistance switching in monolayer transition metal dichalcogenides: an explanation	C. Mihai, A. Velea, F. Sava*, A.T. Buruiana	Poster
40	IBWAP 2019, July 16th -20th 2019, Constanta, Romania	Optical and conductive properties of the composites based on iron oxide and carbon nanotube	M. Daescu [1], A. Udrescu[1], P. Ganea[1], I. Mercioniu[1], N. Iacob[1], V. Kuncser [1], M. Baibarac[1]	Poster
41	F2CP2 Joint Conference, July 13th -20th, 2019, Switzerland / Lausanne	Ferroelectric switching dynamic and negative capacitance regimes in epitaxial $PbZr_{0.2}Ti_{0.8}O_3$ based thin film capacitor	G. A. Boni[1], C. Chirila[1], L. D. Filip[1], A. Iuga[1], I. Pasuk[1], L. Hrib[1], L. Trupina[1], I. Pintilie[1], L. Pintilie[1]	Poster
42	F2CP2 Joint Conference, July 13th -20th, 2019, Switzerland / Lausanne	Optimization strategy for Berry phase polarization calculations	Lucian D. Filip, Neculai Plugaru and Lucian Pintilie	Poster
43	International Conference for Physics Students, August 10th -17th , 2019, Cologne, Germany	Te-based chalcogenide materials for selector applications	A.T. Buruiană[a], A. Velea[a,b], K. Opsomer[b], W. Devulder[b],	Poster
44	50th General Assembly & 47thIUPAC World Chemistry Congress, July 5th -12th, 2019, Paris, France	Mn-silica hollow spheres for ethanol transformation	Mihaela M. Trandafir, Ştefan Neaţu, Mihaela Florea, Florentina Neaţu	Poster
45	International Conference on Magnetism and Magnetic Materials, August 19th -20th, 2019, London, UK	Exchange interactions and associated magnetic and magneto-resistive properties of amorphous Fe-RE (RE = Gd, Dy) thin films	A.E. Stanciu[1], G. Schinteie[1], A. Kuncser[1], N. Iacob[1], V. Kuncser[1]	Poster
Participations in conferences in 2019 financially supported from other sources, but which contribute to the fulfillment of the INCDFM development plan for the 2018-2020 period				
1	19th International Balkan Workshop on Applied Physics and Materials Science, July 16th –19th , 2019, Constanta, Romania	Coloring and dielectric properties of phosphotellurite glasses	Silviu Polosan, Andrei Nitescu, Mihai Secu	Invited
2	2nd Edition of CERIC Satellite Event at the NESY Winterschool & Symposium 2019, March 4th -8th, 2019, Altaussee, Austria	Seeing with electrons -Introduction to electron microscopy	Ghica Corneliu	Invited

3	16th International Conference on Nanosciences & Nanotechnologies, (NN), perioada July 2nd – 5th, 2019, Thessaloniki, Greece	Origin of the collective magnetism in cubic ZnS quantum dots doped with Mn2+ ions. From myths to the harsh reality.	Sergiu V. Nistor	Invited
4	Magnetic nanoparticles and their applications in medicine, April 4th -5th, 2019, Belgrade , Serbia	Engineering and optimization of specific absprption rates of Fe oxides nanoparticles in magnetic hyperthermia	V.Kuncser, N.Iacob, A.Kuncser, P.Palade, C.Comanescu, R.Turcu, G.Schinteie	Invited
5	5th Mediterranean Conference on the Applications of the Mossbauer Effect MECAME-GFSM 2019, May 19th -23rd, 2019, Montpellier, France	Mossbauer Spectroscopy-a powerful tool in explaining particularities of Specific Absorption Rates of Fe oxide nanoparticles in magnetic hyperthermia	V.Kuncser, N.Iacob, P.Palade, C.Comanescu, A.Kuncser, G.Schinteie	Invited
6	Network of the Hungarian Mossbauer Laboratories	On the capability of Mossbauer Spectroscopy to reveal various magneto-functionalities in layered nanosized systems	V.Kuncser	Invited
7	20th International Union of Materials Research Societies International Conference in Asia (IUMRS-ICA 2019), September 22nd -26th, 2019, Perth, Australia	Development of MgB2-based composites for superconducting applications	P. Badica	Invited
8	VI International Conference of Technical Chemistry from Theory to Praxis, May 21st -23rd , 2019, Perm, Russia	MgB2-based materials for different applications	P. Badica	Invited
9	Electron correlation in superconductors and nanostructures (ECSN 2019), October 6th -10th , 2019, Odessa, Ukraine	State of the art in development of Spark Plasma Sintered MgB2 superconductor	P. Badica	Invited
10	15th International Workshop on Magnetism & Superconductivity at Nanoscale, June 30th-July 6th 2019, Coma-Ruga, Spain	“Influence of the structural vortex-phase transition on the second magnetization peak in BaFe2(As1−xPx)2 single crystals”	Lucica Miu, Adrian Crisan	Invited
11	Materials Research Meeting (MRM 2019), December 10th -14th 2019, Yokohama, Japan	Development of MgB2-based materials towards different superconducting applications	P. Badica	Invited

12	COST Workshop on Nanoscale Imaging of quantun devices, February 17th -20th, 2019, Eilat, Israel	Dynamic Liquid-like Vortex Phase and Pinning Potential in Bi:2212 Films in Low Magnetic Fields Probed by Scanning Hall Probe Microscopy	A. Crisan, S. Bending	Invited
13	Superstripes International Conference 2019, June 22nd -30th , Ischia, Italy	Disappearance of the second magnetization peak in La2-xSrxCuO4 single crystals in the presence of static stripe order	Adrian Crisan, Alina Ionescu, Lucica Miu	Invited
14	15th International Workshop on Magnetism and Superconductivity at nanoscale, June 30th-July 6th, Coma-Ruga, Spain	Models of current-dependent pinning potential in nanostructured YBa2Cu3O7 superconducting films	Adrian Crisan, Ion Ivan, Lucica Miu	Invited
15	International Union of Materials Research Societies – International Conference in Asia, September 20th -28th, 2019, Perth, Australia	Vortex matter and dynamics in YBa2Cu3O7 superconducting films with correlated and synergetic pinning centres	Adrian Crisan, Ion Ivan, Lucica Miu	Invited
16	Electron Correlations in Superconductors and Nanostructures International Conference, October 6th -11th, 2019, Odessa, Ukraine	AC susceptibility, DC magnetization and magnetic relaxation studies of YBa2Cu3O7 films with synergetic pinning centres grown by PLD	Adrian Crisan, Ion Ivan, Lucica Miu	Invited
17	International Conference on Condensed Matter and Materials Science, October 13th -20th, 2019, Adana, Turkey	Multi-harmonic Susceptibility Response and Steep Vortex Melting Line in Iron-based Superconducting Single Crystal CaKFe4As4	Adrian Crisan, Lucica Miu	Invited
18	The 11th International Conference on Materials Science and Engineering – BraMat, March 13th –16th, 2019, Brasov, Romania	Effect of processing parameters on the morphology, surface and mechanical properties of sintered ceramics prepared from fish bone	A. Maidaniuc, M. Miculescu, T.M. Butte, L.M. Boldu, R.C. Ciocoiu, F. Miculescu, G.E. Stan, T. Machedon-Pisu	Oral presentation
19	The 11th International Conference on Materials Science and Engineering – BraMat, March 13th –16th, 2019, Brasov, Romania	Internal and external surface features of newly developed porous ceramics with random, interconnected 3D channels by fibrous sacrificial porogen method	A.C. Mocanu, M. Miculescu, T. Machedon-Pisu, A. Maidaniuc, S.I. Voicu, R.C. Ciocoiu, A.M. Pandele, M Ionita, G.E. Stan, F. Miculescu	Oral presentation

20	The 11th International Conference on Materials Science and Engineering – BraMat, March 13th –16th, 2019, Brasov, Romania	Synthesis and characterization of biocompatible polymer-ceramic film structures as favorable interface in guided bone regeneration	C.A. Dascălu, A. Maidaniuc, I.V. Antoniac, F. Miculescu, A.M. Pandele, S.I. Voicu, T. Machedon-Pisu, G.E. Stan, A. Cîmpean, V. Mitran	Oral Presentation
21	E-MRS 2019 Spring Meeting, 27-31 mai 2019, Nisa, Franta	$GeSnSiO_2$ layers with embedded GeSn nanocrystals for sensing in SWIR	A. Slav, C. Palade, C. Logofatu, I. Dascalescu, A. M. Lepadatu, I. Stavarache, S. Iftimie, V. Braic, S. Antohe, S. Lazanu, V. S. Teodorescu, D. Buca, M. L. Ciurea, T. Stoica, M. Braic	orala
22	3rd Edition of International Congress on Catalysis and Chemical Science, February 18th -26th, 2019, Singapore	Recent development of Ni based composite as electrocatalysts for proton exchange membrane fuel cells	F. Neaţu, M. M. Trandafir, S. Neaţu, S. Somacescu, M. Florea	Oral presentation
23	Annual session of the "Vasile Pârvan" Institute of Archeology "Method, theory and practice in contemporary archeology", March 27th -29th, 2019, Bucharest, Romania	Physico-chemical characterization of the white pigments used in the decoration of late Bronze pottery from southern Romania (approx. 1550–150 BC BC), Preliminary study	N. Palincaş, M. Straticiuc, D. Mirea, A.M. Vlaicu, G. Stan, M.-M.Manea, C.A. Simion, A. Velea, L. Trache	Oral presentation
24	3rd Edition of International Congress on Catalysis and Chemical Science, February 18th -26th, 2019, Singapore	Europium-doped $CH_3NH_3Pb_{1-x}Eu_xI_3$ for perovskite based solar cell application	S. Derbali, F. Neatu, S. Neatu, A. C. Galca, L. N. Leonat, A. G. Tomulescu, V. Stancu, V. Toma, I. Pintilie, M. Florea	Oral presentation
25	4th Edition of International Workshop of Materials Physics, May 28th -29th, 2019, Magurele, Romania	Cost efficient oxygen generation through alkaline water electrolysis using Ni on SnO_2 mesoporous support-based electrocatalysts	S. Neatu, F. Neatu, V. C. Diculescu, M. M. Trandafir, N. Petrea, S. Somacescu, M. Florea	Oral presentation
26	4th Edition of International Workshop of Materials Physics, May 28th -29th, 2019, Magurele, Romania	Photoelectron spectromicroscopy: revealing the stability of ferroelectric surfaces with respect to irradiation and contamination	L. E. Abramiuc, D. G. Popescu, M. A. Husanu, L. C. Tanase, N. G. Apostol, C. A. Tache, I. C. Bucur, A. Barinov, J. Avila, C. F. Chirila, L. Trupina, C. M. Teodorescu	Oral presentation
27	4th Edition of International Workshop of Materials Physics, May 28th -29th, 2019, Magurele, Romania	Carbon monoxide adsorption, dissociation and oxidation on ferroelectric surfaces decorated with nanoparticles of noble metals	A. Nicolaev, M. A. Husanu, N. G. Apostol, R. M. Costescu, A. E. Bocirnea, I. A. Hristea, D. Lizzit, C. F. Chirila, L. Trupina, C. M. Teodorescu	Oral presentation
28	4th Edition of International Workshop of Materials Physics, May 28th -29th, 2019, Magurele, Romania	The use of three-component composites in the photocatalytic water splitting reaction	S. Neatu, F. Neatu, M. Florea, L. E. Abramiuc, C.M. Teodorescu	Oral presentation

29	IEEE International Semiconductor Conference – IEEE CAS, October 9th -11th, 2019, Sinaia, Romania	Controlling SWIR photosensitivity limit by composition engineering: from Ge o GeSi nanocrystals embedded in TiO_2	I. Dascalescu, O. Cojocaru, I. Lalau, C. Palade, A. Slav, A. M. Lepadatu, S. Lazanu, T. Stoica, M. L. Ciurea	Oral presentation
30	19th International Balkan Workshop on Applied Physics – IBWAP, July 16th -19th, 2019, Constanta, Romania	Extension of short-wave infrared detection by Sn alloying of Ge nanocrystals	I. Dascalescu, A. Slav, C. Palade, C. Logofatu, A. M. Lepadatu, F. Comanescu, S. Iftimie, S. Lazanu, V. S. Teodorescu, M. L. Ciurea, M. Braic, T. Stoica	Oral presentation
31	BES2019 – XXV International Symposium on Bioelectrochemistry and Bioenergetics, May 26th -30th, 2019 , Limerick, Ireland	Magnetic Electrodes and Nanoparticles for Direct Immobilization of Biomolecules through Magnetic Forces	Victor Diculescu, Madalina Barsan, Monica Enculescu, George Stan, Nicoleta Preda, Nicoleta Apostol, Ruxandra Costescu	Oral presentation
32	ISE2019 – 70th Annual Meeting of the International Society of Electrochemistry, August 4th -9th, Durban, South Africa	Antibody-based Electrochemical Biosensors for 20S Proteasome	Victor Diculescu, Madalina Barsan	Oral presentation
33	19th International Balkan Workshop on Applied Physics and Materials Science, June 16th –19th , 2019, Constanta, Romania	Effect of Additives on the Properties of Electrodeposited CZTS Thin Films	M.Y. Zaki, K. Nouneh, M. Ebn Touhami, A.C. Galca, M. Enculescu, M. Baibarac, L. Pintilie	Oral presentation
34	9th International Conference on Amorphous and Nanostructured Chalcogenides (ANC9), June 30th –July 4th, 2019, Chisinau, Republic of Moldova	Optical properties of binary and ternary chalcogenides	A.C. Galca, F. Sava, I.D. Simandan, G. Socol, A. Velea	Oral presentation
35	70th Annual Meeting of the International Society of Electrochemistry (ISE); August 4th -9th , 2019; Durban, South Africa	Redox Mechanism of Azathioprine and its Interaction with DNA	TA. Enache, M. Enculescu and VC. Diculescu	Oral presentation
36	5th Conference of the Serbian Society for Ceramic Materials: 5CSCS-2019, June 11th -13th, 2019, Belgrade, Serbia.	Microstructure control in multiferroic composites	Carmen Galassi, Pietro Galizia, Marin Cernea, Elisa Mercadelli, Claudio Capiani, Floriana Craciun,	Oral presentation
37	3rd Conference of the Romanian Electron Microscopy Society, October 23rd -25th, 2019, Poiana Brasov, Romania	Atomic-resolution structural and analytical characterization of layered precipitates in special alloys for high-temperature applications	Ghica Corneliu, Solís Cecilia, Munke Johannes, Stark Andreas, Gehrmann Bernd, Bergner Marie, Rösler Joachim, Gilles Ralph	Oral presentation
38	3rd Conference of the Romanian Electron Microscopy Society, October 23rd -25th, 2019, Poiana Brasov, Romania	Analytical HRTEM/ STEM study of impurity defects in cubic boron nitride crystals	Leona C. Nistor	Oral presentation
39	3rd Conference of the Romanian Electron Microscopy Society, October 23rd -25th, 2019, Poiana Brasov, Romania	Pd cluster organization in nanostructured SnO2	Andrei C. Kuncser, Ioana D. Vlaicu, Corneliu Ghica, Simona Somacescu, Cristian Radu	Oral presentation

40	University of Bucharest, Faculty of Physics, Annual Scientific Conference 2019, June 21st -22nd ,2019, Bucharest, Romania	Effect of Mn substitution on the structural, magnetic and magnetostrictive properties of Fe-Pd ferromagnetic shape memory alloy prepared as ribbons	M. Sofronie, F. Tolea M. Enculescu, A.D. Crisan	Oral presentation
41	University of Bucharest, Faculty of Physics, Annual Scientific Conference 2019, June 21st -22nd ,2019, Bucharest, Romania	Interplay of magneto-strictive and magneto-transport properties of Fe-Dy ribbons	C. Locovei, A.E. Stanciu, G.Schinteie, N.Iacob, A.Leca, M.Sofronie, V. Kuncser	Oral presentation
42	University of Bucharest, Faculty of Physics, Annual Scientific Conference 2019, June 21st -22nd ,2019, Bucharest, Romania	Physical characterization of Dy and Cu co-doped ZnO thin films grown by radio-frequency magnetron sputtering	Claudiu Locovei, Diana Coman, Adrian Radu, Lucian Ion, Vlad A. Antohe, Nicoleta Vasile, Marilena Colt, Marina Manica, Anca Dumitru, Sorina Iftimie, Stefan Antohe	Oral presentation
43	International Conference on the Applications of the Mossbauer Effect, ICAME 2019, September 1st -6th, 2019 2019, Dalian, China	Mossbauer Spectropscopy Explaining Specific Magneto-functionalities in RE-Fe Amorphous Thin Films	V.Kuncser, A.E.Stanciu, A.Kuncser, C.Locovei, G.Schinteie, N.Iacob, N.Plugaru, O.Crisan	Oral presentation
44	4th edition of the International Workshop of Materials Physics (IWMP), May 28th -29th, 2019, Magurele, Romania	Thermoelectric nano-composite from double filled skutterudite and carbides	B. Popescu, M. Galatanu, A. D. Crisan, C. Bartha, M.Enculescu, A. Galatanu	Oral presentation
45	4th edition of the International Workshop of Materials Physics (IWMP), May 28th -29th, 2019, Magurele, Romania	Development of thermal barriers materials with application in energy	M. Galatanu, B. Popescu, M. Enculescu, A. Galatanu	Oral presentation
46	19th International Balkan Workshop on Applied Physics and Materials Science, July 15th -20th, 2019, Constanta, Romania	Improved W-monoblock with embedded functionally graded thermal barriers for the DEMO divertor	M. Galatanu, B. Popescu, M. Enculescu, A. Galatanu	Oral presentation
47	19th International Balkan Workshop on Applied Physics and Materials Science, July 15th -20th , 2019, Constanta, Romania	Development of W-W laminates: Fighting against W brittleness	A, Galatanu, M. Galatanu, M. Enculescu, J. Reiser	Oral presentation
48	21st Romanian International Conference on Chemistry and Chemical Engineering (RICCCE), September 4th -7th, 2019, Mamaia, Romania	Correlation of hyperthermia and magnetic measurements in nanosized cobalt ferrite systems	Cezar Comanescu, Nicusor Iacob, Petru Palade, Victor Kuncser	Oral presentation
49	The 10th Pacific Rim International Conference on Advanced Materials and Procesing (PRICM 10) August 18th -22nd , 2019, Xi'an, China	New composites for additive manufacturing	D. Batalu, A. Bunescu, P. Badica, Z. Xiang, W. Lu	Oral presentation

50	2nd European ONE HEALTH Conference, June 21st -22nd, 2019, Bucharest, Romania	MgB2 based materials for the improvement of life quality	P. Badica , M. Burdusel, MA Grigoroscuta, G Aldica, DN Batalu, M Bucur, C Chifiriuc	Oral presentation
51	4th Edition of International Workshop of Materials Physics, May 28th -29th, 2019, Magurele, Romania	Improved performance of a Si-solar cell by up-conversion in Yb/Er doped CeO2 thin films	MA Grigoroscuta, M. Secu, L. Trupina, M. Enculescu, C. Besleaga, I. Pintilie, P. Badica	Oral presentation
52	11th International Workshop on Processing and Applications of Superconducting Bulk Materials (PASREG 2019) August 29th - 30th , Prague, Czech Republic	Passive magnetic shielding by machinable MgB2 bulks and its modulation by Fe shield addition	L. Gozzelino, R. Gerbaldo, G. Ghigo, F. Laviano, D. Torsello, V. Bonino, M. Truccato, D. Batalu, M. A. Grigoroscuta, M. Burdusel, G. V. Aldica, P. Badica	Oral presentation
53	22nd International Conference on Composite Materials ICCM22, August 12th – 16th, 2019, Melbourne, Australia	RE-FREE EXCHANGE COUPLED NANOCOMPOSITE MAGNETS	O. Crisan	Oral presentation
54	3rd International Conference on Applied Surface Science – ICASS, June 17th -20th, 2019, Pisa, Italy	Germanium nanocrystals embedded in oxide matrix for new memories devices applications	M. L. Ciurea, I. Stavarache, A. Slav, C. Palade, A.-M. Lepadatu, I. Dascalescu, I. Lalau, O. Cojocaru, V. S. Teodorescu, A. V. Maraloiu, S. Lazanu, T. Stoica	Poster
55	EuroNanoForum 2019 (NANOTECHNOLOGY AND ADVANCED MATERIALS PROGRESS UNDER HORIZON2020 AND BEYOND), June 12th -14th , 2019, Bucharest, Romania	New advanced materials based on SiGeSn nanocrystals in oxides for SWIR phototodetectors and non-volatile memory devices	C. Palade, I. Stavarache, A. M. Lepadatu, A. Slav, S. Lazanu, T. Stoica, V. S. Teodorescu, M. L. Ciurea, F. Comanescu, A. Dinescu, R. Muller, G. Stan, A. Enuica, M. T. Sultan, A. Manolescu, H. G. Svavarsson	Poster
56	E-MRS 2019 Spring Meeting, May 27th -31st , 2019, Nisa, France	Ge nanocrystals in TiO_2 with enhanced spectral photosensitivity by photo-effects in semiconductor substrate	I. Dascalescu, A.-M. Lepadatu, A. Slav, C. Palade, O. Cojocaru, I. Lalau, M. Enculescu, S. Iftimie, S. Lazanu, V. S. Teodorescu, T. Stoica, M. L. Ciurea	Poster
57	ISE2019 – 70th Annual Meeting of the International Society of Electrochemistry, August 4th -9th, Durban, South Africa	Synthesis and Properties of CdTe nanowires fabricated electrochemically via template method	Melania Loredana Onea, Elena Matei, Monica Enculescu, Ionut Enculescu	Poster
58	Conference of the Romanian Electron Microscopy Society (conference) October 23rd -25th, 2019, Poiana Brasov, Romania	Integration of electrochemically fabricated CdTe nanowires in functional devices using electron beam lithography	Melania Loredana Onea, Elena Matei, Monica Enculescu, Ionut Enculescu	Poster
59	ISE2019 – 70th Annual Meeting of the International Society of Electrochemistry, August 4th -9th, Durban, South Africa	Influence of electrodeposition parameters and electrochemical bath composition on the electrical properties of multichannel ZnO nanowire field effect transistors	Elena Matei, Enculescu Monica, Victor Diculescu, Andreea Costas, Melania Onea, Ionut Enculescu	Poster

60	19th International Balkan Workshop on Applied Physics and Materials Science, July 16th –19th , 2019, Constanta, Romania	Terahertz Characterization of (Ba,Sr)TiO3 Ferroelectric Films Grown By PLD And RF Magnetron Sputtering	L. Nedelcu, C. Chirila, G.E. Stan, A.C. Galca, L. Hrib, L. Trupina, C.D. Geambasu, M.G. Banciu	Poster
61	19th International Balkan Workshop on Applied Physics and Materials Science, July 16th –19th , 2019, Constanta, Romania	Effect of Europium Substitution on the Structural and Optical Properties of CH3NH3PbI3 Perovskite Films	S. Derbali, M. Florea, A.C. Galca , F. Neatu, S. Neatu, L.N. Leonat, M. Secu, A.G. Tomulescu, V. Stancu, K. Nouneh, L. Pintilie	Poster
62	9th International Conference on Amorphous and Nanostructured Chalcogenides (ANC9), June 30th –July 4th, 2019, Chisinau, Republic of Moldova	Comparative study between CZTS1-xSex and ABX3 based solar cells	S. Derbali, K. Nouneh, A.C. Galca, M. Florea, F. Neatu, A.G. Tomulescu, L.N. Leonat, M. Secu, V. Stancu, L. Pintilie	Poster
63	9th International Conference on Amorphous and Nanostructured Chalcogenides (ANC9), June 30th –July 4th, 2019, Chisinau, Republic of Moldova	Characterization of CZTS thin films obtained by magnetron co-deposition from binary sputtering targets	O. Diagne, A.C. Galca, F. Sava, I.D. Simandan, A. Velea	Poster
64	9th International Conference on Amorphous and Nanostructured Chalcogenides (ANC9), June 30th –July 4th, 2019, Chisinau, Republic of Moldova	Study of Electrodeposited Cu2ZnSnS4 Thin Film Properties by a Modified Sulfurization Process	S. Azmi, E.M. Khoumri, M. Nohair, A.C. Galca, M. Dabala	Poster
65	9th International Conference on Amorphous and Nanostructured Chalcogenides (ANC9), June 30th –July 4th, 2019, Chisinau, Republic of Moldova	Enhancing the stoichiometry of sequentially electrodeposited CZTS thin films	M.Y. Zaki, K. Nouneh, M. Ebn Touhami, A.C. Galca, E. Matei, L. Pintilie	Poster
66	9th International Conference on Amorphous and Nanostructured Chalcogenides (ANC9), June 30th –July 4th, 2019, Chisinau, Republic of Moldova	Structural and optical properties of amorphous GeTe films	I.D. Simandan, A.C. Galca, F. Sava, C. Bucur, V. Dumitru, C. Porosnicu, C. Mihai, A. Velea	Poster
67	12th European Congress of Chemical Engineering (ECCE12), September 15th-19th ,2019, Florence, Italy	Synthesis, electronic polarizability and optical basicity of a novel zinc phospho-tellurite glass	L. Boroica, B.A. Sava, M. Elisa, R.C. Stefan, I.C. Vasiliu, S.M. Iordache, A.C. Galca, V. Kuncser	Poster
68	European Congress and Exhibition on Advanced Materials and Processes (EUROMAT 2019), September 1st -5th, 2019, Stockholm, Sweden	Novel magnetic field sensor based on zinc phospho-tellurite glass for Faraday rotators	M. Elisa, C.R. Stefan, I.C. Vasiliu, S.M. Iordache, B.A. Sava, L. Boroica, A.C. Galca, V. Kuncser	Poster
69	XXV International Symposium on Bioelectrochemistry and Bioenergetics (BES 2019); May 26th -31st, 2019; Limerick, Ireland	Redox Mechanisms of Proteasome Inhibitors	Teodor Adrian Enache, Victor Constantin Diculescu	Poster
70	70th Annual Meeting of the International Society of Electrochemistry (ISE); August 4th -9th , 2019; Durban, South Africa	Polyhydrazide Architectures for (bio)Sensing Applications	Daniel N Crisan, Teodor A Enache, Victor C Diculescu	Poster

71	IUPAC Chemistry Congress" (IUPAC 2019)	Surface studies on the PEDOT:PSS films modified with Triton-X 100 surfactant	Lucia Leonat	Poster
72	9th International Balkan Workshop on Applied Physics and Materials Science", July 16th - 20th, 2019 , Constanta, Romania 2019	Structural, ferroelectric and cytotoxic properties of barium titanate-hydroxyapatite composite ceramics	Luminita AMARANDE, George STAN, Corneliu Florin MICLEA, Marius CIOANGHER, Lucian TRUPINA, Iuliana PASUK, Elena MATEI, Tudor SAVOPOL, Mihaela Georgeta MOISESCU, Luminita Claudia MICLEA	Poster
73	The 7th International Workshop on Far-Infrared Technologies 2019 (IW-FIRT 2019), March 5th -7th, 2019	Investigation s on some dielectric materials in sub-Terahertz and Terahertz beams	Banciu Marian Gabriel, Furuya Takashi, Hrib Luminita, Nedelcu Liviu, Trupina Lucian, Pantelica Dan, Mihai M. Dana, Tani Masahiko	Poster
74	EMRS 2019 Spring Meeting, May 27th – 31st 2019, Nice, France	Terahertz and optical properties of Ba0.6Sr0. 4TiO3 thick films grown by PLD	Nedelcu L., Annino G., Chirila C., Trupina L., Galca A.C., BanciuM. G.	Poster
75	EMRS 2019 Spring Meeting, May 27th – 31st 2019, Nice, France	Dielectric properties of BNT-BT ferroelectric thin films in microwave and millimeter waves	Stancu V., Trupina L., Nedelcu L., Mihalache V., Banciu M. G., Huitema L., Ghalem A., Crunteanu A., Contantinescu C., Dumas-Bouchiat F., Champeaux C.	Poster
76	20th International Balkan Workshop onApplied Physics and Materials Science, July 14th -17th, 2019, Constanta, Romania	Terahertz characterization of (Ba,Sr)TiO3 ferroelectric films grown by PLD and RF magnetron sputtering	Nedelcu L., Chirila C., Stan G., Galca A.C., Hrib L., Trupina L., GeambasuC. D.,Banciu M. G.	Poster
77	EMN Rome Meeting 2019, May 13th -17th May 2019 Rome, Italy	Antibacterial cerium doped hydroxyapatite nanopowders for biomedical applications	D. Predoi, S.L. Iconaru, A.M. Prodan, M. Matei, M. Beuran, C.M. Chifiriuc, R.V.Ghita	Poster
78	5th International Conference on Mechanics of Composites (MECHCOMP5), July 1st -4th 2019, Lisbon, Portugal	Biological properties of iron oxide-hydroxyapatite biocomposites	Alina Mihaela Prodan, Simona Liliana Iconaru, Mihai Valentin Predoi, Mikael Motelica-Heino, Regis Guegan, Olivera Lupescu, Mihai Matei, Daniela Predoi	Poster
79	5th International Conference on Mechanics of Composites (MECHCOMP5), July 1st -4th 2019, Lisbon, Portugal	Biological studies of zinc doped hydroxyapatite synthetized at low concentrations	Alina Mihaela Prodan, Simona Liliana Iconaru, Mihai Valentin Predoi, Nicolas Buton, Mircea Beuran, Olivera Lupescu, Adrian Costescu, Nicoleta Vineticu, Daniela Predoi	Poster
80	6th International Congress on Microscopy and Spectroscopy (INTERM), May 12th -18th 2019, Istanbul, Turkey	Electron microscopy: a useful tool for the characterization of novel nanostructures with new architectures	Bogdan S. Vasile, Otilia R. Vasile, Roxana Trusca, Marin Cernea	Poster

81	13th International Summer School on Nanosciences and Nanotechnologies, Organic Electronics and Nanomedicine, June 29th – July 6th, 2019, Thessaloniki, Greece	Complex morpho-structural characterization of mezoporous metal oxide systems for chemo-resistive gas sensors	Cătălina Mihalcea, Andrei Kuncser, Ionel Mercioniu, Aurel Mihai Vlaicu, Simona Somăcescu, Corneliu Ghica	Poster
82	16th International Conference on Nanosciences & Nanotechnologies, (NN), perioada July 2nd – 5th, 2019, Thessaloniki, Greece	Nanostructured impurities in superhard crystalline cubic boron nitride	Leona C. Nistor, Sergiu V. Nistor, Alexandra C. Joita	Poster
83	3rd Conference of the Romanian Electron Microscopy Society, October 23rd -25th, 2019, Poiana Brasov, Romania	Nanometric morpho-structural characterization of mesoporous metal oxide semiconductors for chemo-resistive gas sensors	Cătălina Mihalcea, Andrei Kuncser, Ionel Mercioniu, Aurel Mihai Vlaicu, Simona Somăcescu, Corneliu Ghica	Poster
84	3rd Conference of the Romanian Electron Microscopy Society, October 23rd -25th, 2019, Poiana Brasov, Romania	SEM investigations of Fe-doped ZnO powders	Roxana Trusca, Marian Cernea, Monica Enculescu, Adrian-Ionut Nicoara, Traian Popescu, Corneliu Trisca-Rusu	Poster
85	3rd Conference of the Romanian Electron Microscopy Society, October 23rd -25th, 2019, Poiana Brasov, Romania	Atomic impurity defects in crystalline cubic boron nitride semiconductor	Sergiu V. Nistor, Leona C. Nistor, Alexandra C. Joita	Poster
86	3rd Conference of the Romanian Electron Microscopy Society, October 23rd -25th, 2019, Poiana Brasov, Romania	Tailoring the Dopant Distribution in ZnO:Mn Nanocrystals	Daniela Ghica, Ioana D. Vlaicu, Mariana Stefan, Valentin A. Maraloiu, Alexandra C. Joita, Corneliu Ghica	Poster
87	3rd Conference of the Romanian Electron Microscopy Society, October 23rd -25th, 2019, Poiana Brasov, Romania	Microstructural Characterization of Ferroelectric Oxides Thin Films Based on Hafnia	Cristian Radu, Corneliu Ghica	Poster
89	ECCE12, The 12th European Congress of Chemical Engineering, September 15th -19th , 2019, Florence, Italy	Synthesis, electronic polarizability and optical basicity of a novel zinc phospho-tellurite glass,	L. Boroica, B. A. Sava, M. Elisa, R.C. Stefan, I. C. Vasiliu, S. M. Iordache, A. C. Galca, V. Kuncser	Poster
90	19th International Balkan Workshop on Applied Physics and Materials Science, July 15th -20th, 2019, Constanta, Romania	FAST-based route to produce improved DEMO divertor monoblocks	M. Galatanu, G. Ruiu, M. Cioca, A. Ighigeanu, M. Enculescu, A. Galatanu	Poster
91	14th International Symposium on Fusion Nuclear Technology, September 22nd -27th, 2019, Budapesta, Hungary	W2C-Reinforced Tungsten: A Promising Candidate for High-Heat-Flux Material	P. Jenuš, M. Kocen, A. Abram, A.S. Zavašnik, A. Galatanu, E. Tejado, J.Y. Pastor, M. Wirtz, G. Pintsuk, S. Novak	Poster

92	The 19th International Conference on Fusion Reactor Materials (ICFRM-19), October 27th – November 1st, 2019 La Jolla, California, SUA	W-W laminates processed by FAST	M, Galatanu, M. Enculescu, A. Galatanu, J. Reiser	Poster
93	The 19th International Conference on Fusion Reactor Materials (ICFRM-19), October 27th – November 1st, 2019 La Jolla, California, SUA	WC as reinforcement for tungsten or matrix material for DEMO divertor	S. Novak, P. Jenuš, M. Kocen, A. Abram, A. Šestan Zavašnik, S. Markelj, M. Kelemen, A. Galatanu, E. Tejado, J.Y. Pastor, G. Pintsuk	Poster
94	14th European Conference on Applied Superconductivity (EUCAS 2019), September 1st -5th, 2019, Glasgow, UK	Magnetic shielding by machinable MgB2 and superimposed MgB2/Fe bulks	L. Gozzelino, R. Gerbaldo, G. Ghigo, F. Laviano, D Torsello, V. Bonino, M. Truccato, M. Burdusel, M.A. Grigoroscuta, D. Batalu, G. Aldica, P. Badica	Poster
95	14th European Conference on Applied Superconductivity (EUCAS 2019), September 1st -5th, 2019, Glasgow, UK	Microwave investigation of pinning and flux-flow in Te- and cubic-BN- added MgB2	A. Alimenti, K. Torokhtii, M. Grigoroscuta, P. Badica, A. Crisan, E Silva, N. Pompeo	Poster
96	5th Central and Eastern European Conference on Thermal Analysis and Calorimetry & 14th Mediterranean Conference on Calorimetry and Thermal Analysis, August 27th -30th 2019, Rome, Italy	Thermal analysis on Ga or In acetylacetonate powders	G.V Aldica, D. Batalu, P. Badica	Poster
97	Materials Research Meeting (MRM 2019), December 10th -14th 2019, Yokohama, Japan	Superconducting Thin Films of Bi2Sr2CaCu2O8+δ for Future THz Planar Devices	K. Endo, S. Arisawa, P. Badica	Poster
98	The 5th Central Eastern European Conference on Thermal Analysis and Calorimetry & 14th Mediterranean Conference on Thermal Analysis and Calorimetry (CEEC-TAC5 & MEDICTA2019), August 27th – 30th , 2019, Rome, Italy	Thermal analysis of Ga and In acetylacetonate powders	Aldica Gheorghe Virgil	Poster
99	17th International Workshop on Vortex Matter in Superconductors, May 19th -26th, 2019, Antwerpen, Belgium	Vortices in YBCO thin films with complex pinning structure investigated by AC susceptibility measurements	Adrian Crisan, Ion Ivan, Lucica Miu	Poster
100	11th European Exhibition of Creativity and Innovation EUROINVENT, May 16th -18th, 2019, Iasi, Romania	Powders sintered bodies and MgB2 coatings resistant to microbial colonization and microbial biofilm efficacy and method of its use	P Badica, D. Batalu, M Grigoroscuta, M Burdusel, G Aldica, M Popa, M Chifiriuc	Poster

101	17th International Exhibition of Research, Innovation and inventions PROINVENT, March 20th -22nd, 2019, Cluj Napoca, Romania	Pulberi, corpuri sinterizate si acoperiri pe baza de MgB2 rezistente la colonizarea microbiana si cu eficienta impotriva biofilmelor microbiene si metoda de folosire a acestuia	P Badica, D Batalu, M. Grigoroscuta, M. Burdusel, Gh. Aldica, M. Popa, M. Chifiriuc	Poster
102	5th International Conference on Applications of Mossbauer Effect ICAME 2019, September 1st – 6th , 2019, Dalian, China	Structure and magnetism of l10 nanocomposite fe-mn-pt thin films	O. Crisan	Poster
103	10th International Conference on Materials for Advanced Technologies ICMAT2019, June 24th – 28th, 2019, Singapore	Novel RE-free L10 phase Nanocomposite Magnets in Magnetic and Spintronic Materials and Devices	O. Crisan	Poster
104	European Materials Research Society (E-MRS) Conference – Spring Meeting, May 27th –31st , 2019, Nice, France	Synergetic antibacterial effect in alkali free bio glasses incorporated with ZnO and/or SrO as therapeutic agents	A.C. Popa, T. Tite, I.M. Bogdan, H.R . Fernandes, M. Necsulescu, C. Luculescu, M. Cioangher, V. Dumitru, B.W. Stuart, D.M. Grant, J.M.F. Ferreira, G.E. Stan	Poster
105	European Materials Research Society (E-MRS) Conference – Spring Meeting, May 27th –31st , 2019, Nice, France	Tuning the structure and biological response of sputtered phosphate bioglass films by the deposition pressure	T. Tite, A.C. Popa, A.C. Galca, L.M. Balescu, I.M. Bogdan, B.W. Stuart, G. Pelin-Popescu, G.E. Stan	Poster
106	European Materials Research Society (E-MRS) Conference – Spring Meeting, May 27th –31st , 2019, Nice, France	Investigation of morphological, structural changes and biological performance of Zinc or Magnesium substituted hydroxyapatite with dopant concentration	I.M. Bogdan, T. Tite, L.M. Balescu, S. Iconaru, C.S. Ciobanu, D. Predoi, A.C. Popa, L. Albulescu, C. Tanase, S. Nita, G.E. Stan	Poster
107	European Materials Research Society (E-MRS) Conference – Spring Meeting, May 27th –31st , 2019, Nice, France	Investigation of morphological, structural and biological performance in Strontium or Cerium substituted hydroxyapatite at low concentration	I.M. Bogdan, T. Tite, L.M. Balescu, A.C. Popa, L. Albulescu, C. Tanase, S. Nita, G.E. Stan	Poster
108	European Materials Research Society (E-MRS) Conference – Spring Meeting, May 27th –31st , 2019, Nice, France	Comparative structural and dielectric properties of pure and Li-doped synthetic and bovine bone-derived hydroxyapatite in both bulk and thin film form	T. Tite, I.M. Bogdan, L.M. Balescu, G.E. Stan, I. Pasuk, G. Boni, L. Hrib	Poster
109	42ndInternational Semiconductor Conference CAS 2019, October 9th –11th 2019, Sinaia, Romania	Replacing Pb with Sb in Halide Perovskite for Field Effect Thin Film Transistors	C. Besleaga, V. Stancu, C. Ciobotaru, S. Polosan, H. Saidi, G. Stan, L. Pintilie	Poster

110	EuroNanoForum, June 12th –14th, 2019, Bucharest, Romania	Functional performance of bioactive silica-based glass implant coatings deposited by magnetron sputtering onto dental screws	G.E. Stan, A.C. Popa, V.M.F. Marques, A.C. Galca, C. Ghica, M.A. Husanu, M. Enculescu, C. Tanase, D.U. Tulyaganov, J.M.F. Ferreira	Poster
111	6th Nano Today Conference, June 16th -20th June 2019, Lisbon, Portugal	Dielectric relaxations studies of ternary nanocomposite of vinyl resin matrix reinforced with carbon nanotubes and microcrystalline celluloses	L. Kreit, A.C. Galca, A. Zyane, P. Ganea, C. Bartha, G.E. Stan, M. Enculescu, L. Pintilie, M. El Hasnaoui, M.E. Achour, A. Belfkira	Poster
112	19th International Balkan Workshop on Applied Physics and Materials Science, July 16th –19th , 2019, Constanta, Romania	Terahertz Characterization of (Ba,Sr)TiO3 Ferroelectric Films Grown By PLD And RF Magnetron Sputtering	L. Nedelcu, C. Chirila, G.E. Stan, A.C. Galca, L. Hrib, L. Trupina, C.D. Geambasu, M.G. Banciu	Poster
113	19th International Balkan Workshop on Applied Physics, July 16th -19th 2019, Constanta, Romania	"Interchangeable metasurfaces for immunofluorescent staining sensor and spectroscopical system"	Costel Cotirlan-Simioniuc, Catalin Constantin Negrila, Constantin Logofatu	Poster
114	19th International Balkan Workshop on Applied Physics, July 16th -19th 2019, Constanta, Romania	"Metasurfaces with available characteristics for polarization state analyzers, superlens or electro-optical modulators"	Costel Cotirlan-Simioniuc, Catalin Constantin Negrila, Constantin Logofatu	Poster
115	9th International Conference of the Chemical Societies of the South-East European Countries (ICOSECS9), May 8th- 10, 2019, Târgovişte, Romania	Hybride organic-inorganic perovskite ($CH_3NH_3Pb_{1-x}Eu_xI_3$) for solar cell applications	F. Neatu, S. Derbali, S. Neatu, A. C. Galca, L. N. Leonat, A. G. Tomulescu, V. Stancu, V. Toma, I. Pintilie, M. Florea	Poster
116	47th IUPAC World Chemistry Congress, July 5th -12th, 2019, Paris, France	Synthesis and properties of $C_3N_2H_5PbI_3$ powders as precursors for hybride perovskite based solar cells	M. Florea, F. Neaţu, S. Neaţu, S. Derbali, A. C. Galca, V. Toma, C. Bartha, L. N. Leonat, A.G. Tomulescu, V. Stancu, I. Pintilie	Poster
117	IEEE International Semiconductor Conference – IEEE CAS, October 9th -11th, 2019, Sinaia, Romania	High performance NIR photosensitive films of Ge nanoparticles in Si_3N_4	I. Stavarache, P. Prepelita, I. Lalau, O. Cojocaru, V. S. Teodorescu, M. L. Ciurea	Poster

International collaborations

Large projects

Pintilie I
CERN RD50 "Radiation hard semiconductor devices for very high luminosity colliders"
(http://rd50.web.cern.ch/rd50/): 48 research institutions from 27 countries around the world
Scientific coordonator of the workpackage **"Defect/Material Characterization"**

H2020 and EURATOM
Galatanu A
EUROfusion and WPMAT, GA633053 "Romanian participation in the EUROfusion WPMAT and complementary research"
2014-2020
Galatanu A
H2020 "Accelerator Research and Innovation for European Science and Society (ARIES)", GA730871
2017-2021

Pintilie L
H2020 "Energy efficient Embedded Non-volatile Memory Logic based on Ferroelectric Hf(Zr)O2" GA780302
2018-2021

Romania-Bulgaria Projects
Galatanu A
"**D-EMERSYS** Rapid intervention force in case of chemical, biological, radiological and nuclear emergency on the Danube river" Interregrobg Cod e-MS ROBG - 123 INCDFM coord
2016-2018, implementation 2018-2022

Galatanu A
"**JEROME** Capabilities and interoperability for Romanian-Bulgarian, specialized intervention, at chemical-biological-radiological-nuclear-explosive event", Interregrobg Cod e-MS ROBG - 121 INCDFM coord
2016-2018, implementation 2018-2022

SEE, Norwegian funding
Rasoga O
Project EEA GRANTs, **„Elastomeric tunable metasurfaces for efficient spectroscopic sensors for plastic detection"**
Coordinator: National Institute of Materials Physics
Partners: University of Bucharest, National Institute for Research and Development in Microtechnologies and SINTEF, Trondheim – Norway
2019-2023

Projects COST

Crisan A

COST CA16218 Nanoscale Coherent Hybrid Devices for Superconducting Technologies (NANOCOHYBRI).

Main representative of Romania in the management committee

Coordinator: Dr. Herman Suderow, Spain

Project ERA-NET

Trupina L

Integration of new and improved materials for smart millimeter-wave sensors

Project **M-ERA.NET**

French partner: University from Limoges, AirMems (SME)

2016 – 2019

Stoica TS

Project **M-ERA NET Call 2015**

GESNAPHOTO (Nano-structured GeSn coatings for photonics)

Partners from Romania (INOE-2000, OPTOELECTRONICA- 2001 S.A) and Germany (Forschungszentrum Jülich, Peter Grünberg Institute PGI-9, nanoplus Nanosystems and Technologies GmbH)

2016-2019

Vlaicu ID

Project **M-ERA NET**

Innovative nano-materials and architectures for integrated piezoelectric energy harvesting applications (HarvEnPiez)

Coordinator: Iosef Stefan Institute din Ljubljana, Slovenia

Partners: Institute of Solid State Physics, University of Latvia (ISSP UL), Latvia; National Institute of Materials Physics (NIMP), Romania; Faculty of Electrical Engineering, Power Engineering and Information Technology, (Intelectro Iasi SRL), Romania; Technical University Iasi (TU Iasi), Romania

2016-2019

Badica P

COFUND M-ERA.NET II / Contract 74/2017,

BIOMB, Advanced biodegradable materials based on MgB_2 resistant to microbial colonization

Coordinator: NIMP, Partners: UPB, UB, U. Torino

2017-2020

Velea A

M-ERA.NET project

Functional 2D materials and heterostructures for spintronic-memristive devices

Coordinator: National Institute of Materials Physics

Partners: Catalan Institute of Nanoscience and Nanotechnology (ICN2) – Spain,

Institute of Optical Materials and Technologies (IOMT-BAS) – Bulgaria,

Institute of Solid State Physics (ISSP-BAS) - Bulgaria 2019-2022

Baibarac M
Project ID: **MNET18/ADMA3454**
4D printed energy harvesting devices based on innovative printable conductive elastomers
Coordinator: National Institute of Materials Physics
Partners: All Green SRL, Intelectro Iasi SRL and Izertis Ltd.
2019-2021

C-ERIC

Ghica C
Graphene for Water in Life Science,
CERIC Grant
Coordinator: Elettra Sincrotrone Trieste
Partners: Technical University Graz (Austria), Charles University Prague (Czech Republic), NIMP (Romania)

Other international projects

Predoi D
Nanoparticles for remedy of contaminated soils
Project **PICS**
French partner: Institut des Sciences de la Terre d'Orléans.

Chirila C
Optimised pyroelectric elements on Si wafers for sensing and energy harvesting
Project **IFA-CEA**
French partner: CEA Grenoble Laboratory of components for micro actuators
2016-2019

Crisan O
Programme Hubert Curien PHC Brancusi
Novel RE-free permanent magnet systems for automotive applications
Partner: Faculte des Sciences, Universite du Maine, le Mans, France
2019-2020

Zgura I
Project **JINR-RO**
Investigations of biocomposite materials wwith bio-medical applications by means of neutron scattering and complementary methods
Romanian Partner: National Institute of Materials Physics
Foreign Partner: Frank Laboratory of Neutron Physics (FLNP)
2019

Bilateral agreements

Crisan O
Project **Romania France PN-III-P3-3.1-PM-RO-FR-2019-0327**
Project Director 2019-2020

Ghica C
Romania-France bilateral cooperation project PN-III-P3-3.1-PM-RO-FR-2019-0219
The structure-functionality interdependence in the case of nanostructured materials for gas sensors by electron tomography and TEM operando
Project Director

Kuncser V
Associate partner in the REISESEE
Project funded by the European Institute of Technology, RawMaterials,
2018-2020

Badica P
Romania (INCDFM + UPB) - Ukraine (National Technical University of Ukraine, "Kiev Politechnical Institute"), Bilateral Cooperation PN3-P3-127.3BM / 2016, New hard ceramic composite materials for cutting tools, duration 2016-2017.

Grigoroscuta M
INCDFM - NIMS, cooperation through NIMS 'MSc, PhD internship program, Textured ceramics (c-axis oriented MgB2 bulks by high magnetic field), Tsukuba, Japan,
11 Sept-1 Dec. 2017

Badica P
INCDFM-NIMS, cooperation through NIMS 'advanced researchers visits' program, Tsukuba, Japan, Composites for special conditions: 2019; 2020.

Badica P
INCDFM-Kanazawa Inst. Technology, Associate Partner in Kakenhi type project (Materials for direct connection) funded by JST, Japan: 2019-2020

Burdusel M
(**INCDFM + UPB**) - Tongi Univ. Shanghai China; Magnets without rare earths; the program "Silk Road" funded by China: 2020-2021

Stan GE
University of Aveiro, Portugal
Development of a new generation of highly biocompatible dental titanium implants functionalized by sputtering techniques with novel bioactive glass materials
2016 – 2020

Stanculescu A
University of Angers- Photonics Laboratory, France
Accord de coopération scientifique dans le domaine des films minces notamment sur les thématiques suivantes: structures multicouches organiques à basse dimension et composantes or oganiques et hybrides.

Stanculescu A
University of Western Cape, Departament of Chemistry, SensoLab, South Africa
Polymeric single/multilayer heterostructures for photovoltaic and electronic applications; polymeric field effect transistors for sensing applications; organic and hybrid devices (realisation, characterization)

Badica P
Tohoku University, Japan
Joints of superconducting tapes: fabrication and characterization
Proiect: **ICC-IMR** Visiting Prof. collaboration and exchange of researchers/students
INCDFM- HFSLM-Tohoku University

Baibarac M
Institut des Materiaux Jean Rouxel, Nantes, France
Surface plasmons enhancement of optical properties of SWNTs, highly separated in metallic and semiconducting components, electrochemically functionalized with conjugated polymers.

Cooperations with research institutions from abroad

Galatanu A
European Energy Research Alliance, in the frame of Joint Programme on Nuclear Materials, collaboration, expertise exchanges, R&D project proposals

Galatanu A
SINTEF Industry (Norway), Dept. Sustainable Energy Technology, in the field of " Thermoelectric materials for sensors, cooling and utilizing waste heat", samples' exchange, R&D project proposals

Ghica D
University of Bologna – Department BiGeA - Astrobiology and Geomicrobiology Laboratory, Prof. Barbara Cavalazzi Microstructural analysis of samples for paleo-antropology research area

Crisan A
The University of Tokyo, AIST Tsukuba, Japan, Vortex dynamics in multicomponent iron-based superconductors

Crisan A, Badica P
Roma 3 University, Italy, Microwave investigations of pinning in MgB_2

Crisan A
University of Oslo, Norway, Channeling of Magnetic Flux in $YBa2Cu_3O7-\delta$ Superlattices

Ciurea ML
Department of Physics and Astronomy, University of Catania, CNR-IMM, Catania, Italy
Ge-based nanostructures for applications as photodetectors or transparent electrodes for photovoltaic cells

Ciurea ML, Lepadatu AM
Istituto Nazionale di Fisica Nucleare-Laboratori Nazionali di Frascati, Frascati, Italy
Nanostructures based on Ge nanoparticles immersed in oxidic matrices for optical sensors applications

Ciurea ML
Reykjavik University, School of Science and Engineering, Iceland
GeSi nanocrystals in oxides with targeted photoconductive properties in VIS-NIR

Kuncser V
Laboratory of Applied Materials, Portsmouth University, UK,
Asoc. Prof. Melvin M. Vopson

Crisan O
Swiss Federal Laboratory for Materials Research & Technology, EMPA, Thun, Switzerland
Prof. Patrik Hoffman

Crisan O
John Dalton Institute, Manchester Metropolitan University, Manchester, UK
Prof. John Colligon

Crisan O
Institut des Materiaux et Molecules du Mans I3M, Fac. Des Sciences, Universite du Maine, Le Mans, France
Prof. N. Randrianantoandro

Crisan O
Department of Renewable Energy, University of Sharjah, United Arab Emirates
Prof. Hamid al-Naimyi

Miclea CF
Los Alamos National Laboratory, Los Alamos, NM. USA.
Measurements, co-publication, specimen exchange

Miclea CF
Max Planck Institute for Chemical Physics of Solids, Dresden, Germany
Measurements, co-publication, specimen exchange

Nedelcu L
Research Center for Development of Far-Infrared Region, University of Fukui, Japan
Measurements, specimen exchange

Nistor SV
Institute of Physics, Czech Academy, Prague
Investigation by magnetic electronic resonance techniques and optical spectroscopy of the semiconducting II-VI materials optically activated with transitional ions

Nistor SV
Physics Department, Antwerp University, Belgium
Development of new advanced multifunctional materials containing defects

Pintilie L
UMP CNRS-Thales, Palaiseau, France and Université Paris-Sud
Measurements, specimen exchange

Pintilie L, Pintilie I
University of Oulu, Finland
Ferroelectric measurements

Pintilie L
Darmstadt University of Technology, Germany
Specimen exchange, co-publication

Pintilie I
Oslo University, Norway
Specimen exchange, working stages

Preda N
Yildiz Technical University, Turkey
Learning Agreement for Traineeships within the ERASMUS Program

Predoi D
Institut de Chimie de la Matière Condensée de Bordeaux CNRS-UPR 9048 France
Elemental analysis, hydrogen storage

Predoi D
Universite Bordeaux, EA 4592 Géoressources&Environnement, ENSEGID, France
Collaboration project IFA CEA C2-06, TEM, environment tests

Predoi D
Marcoule Institute for Separative Chemistry, France
Predoi D Technical University Ostrava, Czech Republic

Predoi D
Institute of Life Sciences Research and Technologies:
Laboratory of Chemistry and Biology of Metals (LCBM) Grenoble, France
Collaboration project IFA CEA C4-05- biological tests

Predoi D
Institut des Sciences de la Terre d'Orléans, France
Raman, ICP, magnetic measurements

Predoi D
Université du Havre, France
Ultrasound studies

Predoi D
Horiba Jobin Yvon S.A., France
Zeta potential, DLS, photoluminescence

Predoi D
University of Dayton, Research Institute, USA
Carbon nanotubes

Stoica T
Peter Grünberg Institute, Forschungszentrum Jülich, Germany
2D materials based on chalcogenides of transition metals, 2D-TMD

Simion C.E
University College London, Department of Chemistry, UK
Prof. Chris Blackman
Fundamental and applications with chemoresistive gas sensors.

Stanoiu A
Gas Sensors Research Group in cadrul Institut für Physikalische und Theoretische Chemie,
Eberhard Karls Universität Tübingen, Germany
Prof. Dr. Nicolae Barsan
Academic and applied reasearch devoted to chemical gas sensors.

Stefan M
University of Bologna – Department BiGeA - Astrobiology and Geomicrobiology Laboratory,
Prof. Barbara Cavalazzi
EPR investigation of materials for astrobiology

Teodorescu CM
Elettra Trieste (Italy)
CoSMoS
Combined Spectroscopy and Microscopy operating at SuperESCA

Visitors
Invited within the C-ERIC consortium

WORKING VISITS	
Marcin LAPINSKI Gdansk University of Technology, POLAND Au-Si plasmonic platforms: mechanism of formation Consortium C-ERIC, Lab. 50 electron microscopy group (invitation Dr. C. Ghica)	26-27.02.2019
Stefano LETTIERI CNR- Institute of Applied Science and Intelligent Systems, ITALY Investigating structural and electronic fingerprints of enhanced photocatalytic efficiency in TiO2/graphene and N-doped TiO2 nanostructures. Consortium C-ERIC, Lab. 50 electron microscopy group (invitation Dr. C. Ghica)	02-05.04.2019
Sebastian WACHOWSKI Gdansk University of Technology, POLAND Structural defects, cation ordering and phase transitions in triple conducting BaLnCo2O6 double perovskites Consortium C-ERIC, Lab. 50 electron microscopy group (invitation Dr. C. Ghica)	06-13.05.2019
Nico Hempel Technische Universität Braunschweig, GERMANY Analysis of microstructural evolution in high-alloy steels due to welding and plastic deformation at high temperatures Consortium C-ERIC, Lab. 50 electron microscopy group (invitation Dr. C. Ghica)	18-21.11.2019

Jose da Silva Universidade do Minho, PORTUGAL Understating interfacial effects on p-n junctions for thermoelectric generator devices Consortium C-ERIC, Lab. 50 electron microscopy group (invitation Dr. C. Ghica)	04-06.11.2019
Jose da Silva Universidade do Minho, PORTUGAL Evaluation of the interface quality in ferroelectric-dielectric structures for energy storage capacitors Consortium C-ERIC, Lab. 50 electron microscopy group (invitation Dr. C. Ghica)	09-13.12.2019
GENERAL SEMINARS	
Jacques WERCKMANN Instituto de Ciências Biomédicas, Universitade Federal de Rio de Janeiro, Brasil (invitation Dr. C. Ghica)	22.05.2019
Prof. Ana SANCHEZ University of Warwick, UK La0.7Sr0.3MnO3/PbTiO3 ferroelectric tunnel junctions: Domain con-Figuration and interface characterization (invitation Dr. C. Ghica)	22.10.2019
Dr. Richard BEANLAND University of Warwick, UK Femtometre resolution using electron diffraction (invitation Dr. C. Ghica)	22.10.2019

Work placements (foreign students or researchers who came to work in INCDFM)

Ricardo Leote (PhD)
Project Contract: No. 27/01.09.2016
Date of employment: October 24th, 2018.

Dr. Hamza SAIDI (researcher, Eugen Ionescu – AUF/MAE)Monastir University, Tunise)
Work placement in Laboratory 40 (06.05- 03.08.2019)
Research topic: Study of load transport properties in organic structures based on NO2-BMN

Sara AZMI (PhD, Eugen Ionescu scholarship – AUF/MAE)
Hassan II University, Casablanca, Morocco
Work placement in Laboratory 10 (10.05- 07.08.2019)
Research topic: Electrodeposition of kesterite films for photovoltaic applications

Khaled BELFAA (PhD, Eugen Ionescu scholarship – AUF/MAE)
University from Gabes, Tunise
Work placement in Laboratories 30 and 10 (06.05- 03.08.2019)
Research topic: Elaboration and characterization of nanocrystals and thin films of pure TiO2 doped with noble metals

Dr. Larbi FILALI (researcher, Eugen Ionescu scholarship – AUF/MAE)
Ahmed Ben Bella Es Sénia Oran 1 University, Oran, Algeria
Work placement in Laboratories 10 and 40 (06.05- 03.08.2019)
Research topic: Study of the effect of molecular hydrogen in silicon nanostructures for the detection of biomolecules at the solid / liquid interface

Sarah DERBALI (PhD, Eugen Ionescu scholarship – AUF/MAE)
Ibn Tofail University, Kenitra, Morocco
Work placement in Laboratory 10 - Heterostructures Group (15.05- 12.08.2019) Research topic: Obtaining and characterizing new halogenated organic perovskites

Marwa HATTAB (PhD student, Eugen Ionescu scholarship - AUF / MAE)
El Manar University, Tunis, Tunisia
Work placement in Laboratories 10 and 50 (06.05-03.08.2019)
Research topic: Corrosion study of ceramic coatings developed by the sol-gel method on magnesium and its alloys for use in biomedical applications

Ilhame ASSAHSAHI (PhD student, Eugen Ionescu scholarship - AUF / MAE)
Ibn Tofail University, Kenitra, Morocco
Work placement in Laboratory 20 - Magnetism Group (07.05-04.08.2019)
Research topic: Thermoelectric materials for energy recovery applications

Mohamed Yassine ZAKI (PhD student, Eugen Ionescu Scholarship - AUF / MAE)
Ibn Tofail University, Kenitra, Morocco
Work placement in Laboratory 10 (15.05- 12.08.2019)
Research topic: Obtaining and characterizing Cu2ZnSnS4 films for photovoltaic applications

Mohammed GUERBOUB (PhD student, Eugen Ionescu scholarship - AUF / MAE)
Sidi Mohammed Ben Abdellah University, Fès, Morocco
Work placement in Laboratory 10 - Heterostructures Group (05.05-02.08.2019)
Research topic: Study of defects induced by irradiation in detectors

Ousmane DIAGNE (PhD student, Eugen Ionescu scholarship - AUF / MAE)
Cheikh Anta Diop
University, Dakar, Senegal
Work placement in Laboratories 40 and 10 (07.05-04.08.2019)
Research topic: Development and characterization of thin films of Cu2ZnSnS4 (CZTS) for photovoltaic applications

Oussama AITMELLAL (PhD student, CNRST Morocco scholarship)
Sultan Moulay Slimane University, Béni Mellal, Morocco
Work placement in Laboratories 40, 30 and 50 (09.05- 06.08.2019)
Research topic: Obtaining and studying the properties of luminescent materials with potential applications in the field of energy

Sara AIT BOUZID (PhD student, CNRST scholarship Morocco)
Sultan Moulay Slimane University, Béni Mellal, Morocco
Work placement in Laboratories 20, 10 and 50 (09.05- 06.08.2019)
Research topic: Synthesis and characterization of new magnetocaloric materials

Abdelbassat KENANE (PhD student, PNE scholarship awarded by the Algerian government)
Mustapha Stambouli University, Mascara, Algeria
Work placement in Laboratories 10 and 40 (22.10.2018 - 30.04.2020)
Research topic: Synthesis and characterization of new polymer / clay hybrid materials

Events

First Announcement

4th edition of the International Workshop of Materials Physics

28th -29th May 2019

The National Institute of Materials Physics (NIMP) announces the organization of the 4th edition of the International Workshop of Materials Physics (IWMP). The topic for 2019 edition is dedicated to energy, with special focus on topics such as: photovoltaics (novel photo-effects, halide perovskites, new architectures for solar cells, etc.), energy harvesting (piezo, pyro, thermoelectric), fusion, energy storage, energy transport, and other similar topics. Aspects related to modeling, fabrication, characterization will be presented and discussed.

Similar to the first three editions, the 4th edition of IWMP is organized on invitation only.

The aim is to attract well known researchers in the field, the final purpose being to establish new collaborations concretized in common publications, projects and exchange of personnel.

Young researchers willing to present their latest results on topics related to the main topic of the workshop are invited to submit a 2 page abstract (A4, Times New Roman 11, single spacing, 2 cm margins, including Figures and references) to the organizers (pintilie@infim.ro). The best abstracts will be selected for oral presentations during the workshop.

The workshop will take place at NIMP premises located in Magurele, Romania.

The topics for the next two editions:

2020-Materials and structures for bio-applications

2021-Recent developments in the field of ferroelectrics and multiferroics

IWMP, 28th -29th May 2019

28th of May

8:15-8:50 Registration
8:50-9:00 Opening

9:00-11:15 Session 1 (Enculescu, Pintilie)
9:00-9:30
Magdalena Titirici, Department of Chemical Engineering, Imperial College London, UK
Going green with black: On Biomass, Carbon and Clean Energy
9:30-10:00
Vladimir Matolin, Charles University, Czech Republic
PEM Based Ordered Superstructures as a Durable Support for Fuel Cell Catalyst.
10:00-10:30
Ifan Stephens, Imperial College London, UK
Power-to-X: the role of catalysis in advancing the electrochemical synthesis of our most coveted chemicals
10:30-11:15
M. Florea
Cost efficient oxygen generation through alkaline water electrolysis using Ni on SnO2 mesoporous support-based electrocatalysts
A. Nicolaev
Carbon monoxide adsorption, dissociation and oxidation on ferroelectric surfaces decorated with nanoparticles of noble metals
S. Neatu
The use of three-component composites in the photocatalytic water splitting reaction

11:15-11:30 Coffee break

11:30-13:00 Session 2 (Pintilie, Florea)

11:30-12:00
Joe Briscoe, Queen Mary University London, UK
Sustainable energy devices using nanostructured polar materials
12:00-12:30
Andrew Holmes, Imperial College London, UK
Piezoelectric Devices for Energy Harvesting from Motion and Flow
12:30-13:00
Sam Cooper, Imperial College London, UK
Multilength scale characterisation of materials, microstructures and performance of batteries and fuel cells.

13:00-14:30 Lunch

14:30-16:30 Session 3 (Polosan)

14:30-15:00
Marin Alexe, University of Warwick, UK
Bulk- and Flexo-Photovoltaic effects
15:00-15:30
G. A. Nemnes
Measurement protocols for a reliable electrical characterization of perovskite solar cells
15:30-16:00
Anca Duta, Transilvania University Brasov
VIS-active photocatalytic composites for advanced wastewater treatment
16:00-16:30
L. Leonat
Reticulated mesoporous TiO2 scaffold for hybrid perovskite solar cells
M. Grigoroscuta Improved performance of a Si-solar cell by up-conversion in Yb/Er doped CeO2 thin films
16:30-18:00
Visit to NIMP facilities
18:00 departure for dinner

29th of May
9:00-11:15 Session 4 (Andrei Galatanu)

9:00-9.30
Andrei.V. Kovalevsky, CICECO – Aveiro Institute of Materials, Department of Materials and Ceramic Engineering, University of Aveiro, Portugal
Selected approaches for designing oxide thermoelectrics
9:30-10:00
Andres Sotelo, ICMA-CSIC-Universidad de Zaragoza, Spain
Very high thermoelectric performances in Sr-doped textured Ca3Co4O9. Costs optimization of unileg thermoelectric generator fabrication.
10:00-10:30
Ernst Bauer, Technische Universität Wien, Austria
Bulk and thin film Heusler alloys as promising thermoelectric materials
10:30-11:15
B. Popescu
Thermoelectric nano-composite from double filled skutterudite and carbides
I. Mercioniu
On the adherence of ceramic layers for thermal barriers coatings
M. Galatanu
Development of thermal barriers materials with application in energy

11:15-11:30 Coffee break

11:30-13:15 Session 5 (Ghica, Polosan)

11:30-12:00
Mihai A. Gîrţu, Department of Physics and Electronics, Ovidius University of Constanţa, Constanţa, Romania
DFT Calculations of Structure and Electronic Properties of TiO2 Nanoclusters, of Dye-Nanocluster and Dye-Electrolyte Systems for Modeling Hybrid Photovoltaic and Photocatalytic Applications
12:00-12:30
Chris Chikere, School of Pharmacy and Life Sciences, Robert Gordon University, Aberdeen, UK
New Electrode Materials for Energy Storage Devices-Battery Applications
12:30-13:15
O. Rasoga
Tryphenylamine and carbazol oligomers for photovoltaic applications
S. Polosan
Organometallic compounds for photovoltaic applications
M. Baibarac
Composites based on carbon nanotubes and polydiphenylamine: from the functionalization process to applications in the energy storage field

13:15-14:45 Lunch
14:45-17:00 Session 6 (Teodorescu)

14:45-15:15
Ibrahim Burc Misirlioglu, Sabanci Univeristy Istanbul, Turkey
Functionality from ferroelectric superlattices: Designing a phase transition and its implications for applications
15:15-15:45
Andrei Manolescu, University of Reykjavik, Iceland
Excitons in core-shell nanowires with polygonal cross section
15:45-16:15
L. Abramiuc
Photoelectron spectromicroscopy: revealing the stability of ferroelectric surfaces with respect to irradiation and contamination
A. Crisan
Nanotechnology of Pinning Centres in Superconducting Films for Clean Energy-saving Power Applications
16:15-16:30 Closing
16:45 departure for some sightseeing and dinner

Awards

EUROINVENT 2019 (Iassy, May 2019)

1. Installation for obtaining substrates of fibrils from biopolymers through electrospinning
Authors: Mihai Cioca, Gabriel Dobrescu, Adelina Ighigeanu, Alexandru Evanghelidis, Elena Matei, Ionut Enculescu
Award: Diploma of GOLD MEDAL

2. Mesoporous layer for perovskite solar cells and the fabrication method
Authors: Ioana Pintilie, Andrei-Gabriel Tomulescu, Lucia Nicoleta Leonat, Viorica Stancu, Cristina Besleaga Stan, Vasilica Toma, Viorel-Georgel Dumitru, Lucian Pintilie
Award: Diploma of SILVER MEDAL

3. Process for obtaining one-dimensional zinc oxide nanostructures by the thermal oxidation of zinc foils
Authors: C. Florica, N. Preda, A. Costas, A. Evanghelidis, M. Oancea, M. Enculescu, E. Matei, I. Enculescu
Award: Diploma of EXCELLENCE

4. Process for obtaining a photodetector based on nanowire matrixes of copper-zinc oxide-zinc oxide core made of interdigitated metallic electrodes
Authors: A. Costas, C. Florica, N. Preda, A. Evanghelidis, C. Besleaga, M. Beregoi, M. Enculescu, E. Matei, V. Diculescu, A. Enache, M. Ignat-Barsan, M. Onea, A. Aldea, M. Apostol, M. Bunea, D. Crisan, O. Constantinescu, I. Enculescu
Award: Diploma of SILVER MEDAL

5. Procedure for obtaining doped LYF4 luminophores with rare earths (Yb, Er) with luminescent properties under the influence of infrared radiation
Authors: Mihail Secu, Corina-Elisabeta Secu
Award: Diploma of BRONZE MEDAL

6. Capacitive matrix for non-volatile memory based on germanium nanocrystals immersed in hafnium dioxide and process for making it
Authors: A. Slav, C. Palade, A.-M. Lepadatu, S. Lazanu, M.L. Ciurea – INCDFM in collaboration with D. Vasilache, M. Dragoman – IMT Bucharest
Award: Diploma of EXCELLENCE

7. Powders, sintered bodies and MgB2 coatings resistant to microbial colonization and microbial biofilm efficacy and method of its use
Authors: Petre Bădică, Dan Nicolae Batalu, Mihai Alexandru Grigoroşcută, Mihail Burdușel, Gheorghe Virgil Aldica, Marcela Popa, Mariana Carmen Chifiriuc
Award: Diploma of GOLD MEDAL

8. Development of DEMO divertor components with embedded functionally graded thermal barriers
Authors: Magdalena Galatanu, Mihai Cioca, Adelina Ighigeanu, George Ruiu, Monica Enculescu, Bogdan Popescu, Andrei Galatanu
Award: Diploma of BRONZE MEDAL

PROINVENT 2019 (Cluj, March 2019)
1. Installation for obtaining substrates of fibrils from biopolymers through electrospinning
Authors: Mihai Cioca, Gabriel Dobrescu, Adelina Ighigeanu, Alexandru Evanghelidis, Elena Matei, Ionut Enculescu
Award: Diploma of EXCELLENCE and GOLD MEDAL

2. Mesoporous layer for perovskite solar cells and the fabrication method
Authors: Ioana Pintilie, Andrei-Gabriel Tomulescu, Lucia Nicoleta Leonat, Viorica Stancu, Cristina Besleaga Stan, Vasilica Toma, Viorel-Georgel Dumitru, Lucian Pintilie
Award: Diploma of EXCELLENCE and PROINVENT MEDAL

3. Process for obtaining one-dimensional zinc oxide nanostructures by the thermal oxidation of zinc foils
Authors: C. Florica, N. Preda, A. Costas, A. Evanghelidis, M. Oancea, M. Enculescu, E. Matei, I. Enculescu
Award: Diploma of EXCELLENCE

4. Process for obtaining a photodetector based on nanowire matrixes of copper-zinc oxide-zinc oxide core made of interdigitated metallic electrodes
Authors: A. Costas, C. Florica, N. Preda, A. Evanghelidis, C. Besleaga, M. Beregoi, M. Enculescu, E. Matei, V. Diculescu, A. Enache, M. Ignat-Barsan, M. Onea, A. Aldea, M. Apostol, M. Bunea, D. Crisan, O. Constantinescu, I. Enculescu
Award: Diploma of EXCELLENCE and GOLD MEDAL

5. Procedure for obtaining doped LYF4 luminophores with rare earths (Yb, Er) with luminescent properties under the influence of infrared radiation
Authors: Mihail Secu, Corina-Elisabeta Secu
Award: Diploma of EXCELLENCE and PROINVENT MEDAL

6. Capacitive matrix for non-volatile memory based on germanium nanocrystals immersed in hafnium dioxide and process for making it
Authors: A. Slav, C. Palade, A.-M. Lepadatu, S. Lazanu, M.L. Ciurea – INCDFM in colaborare cu D. Vasilache, M. Dragoman – IMT Bucuresti
Award: Diploma of EXCELLENCE and PROINVENT MEDAL

7. Powders, sintered bodies and MgB2 coatings resistant to microbial colonization and microbial biofilm efficacy and method of its use
Authors: Petre Bădică, Dan Nicolae Batalu, Mihai Alexandru Grigoroșcută, Mihail Burdușel, Gheorghe Virgil Aldica, Marcela Popa, Mariana Carmen Chifiriuc
Award: Diploma of EXCELLENCE and PROINVENT MEDAL

Romanian Academy Awards (awarded in 2019 for articles published in 2017)
Radu GRIGOROVICI Award

George Stan

Contributions to the development and promotion of new conceptual solutions for the in vitro manufacturing and testing of biomimetic of the implantological structures of volume (porous scaffolds) or of small dimensionality (thin layers), having superior performances and low manufacturing costs.

Nicoleta Apostol

Winner of the L'Oréal - UNESCO National scholarship "For Women in Science", 9th edition, 2018, in the field of Physical Sciences (the awards ceremony took place in November 2018, but the contract and scientific activity were carried out during 2019)

Nicoleta Apostol

1st prize at the "Rada Mihalcea" awards for young researchers in science and engineering, 5th edition (August 2019, Cluj-Napoca)

Cristina Besleaga Stan

3rd prize at the contest "Rada Mihalcea" for young researchers in science and engineering, 5th edition (August 2019, Cluj-Napoca)

Personnel (summary)

R&D	211
Auxiliary&Admin	83

R&D	
Senior researcher rank 1	42
Senior researcher rank 2	27
Senior researcher rank 3	50
Junior researcher	25
Assistant researcher	63
Development engineer rank 3	3
Development engineer	2

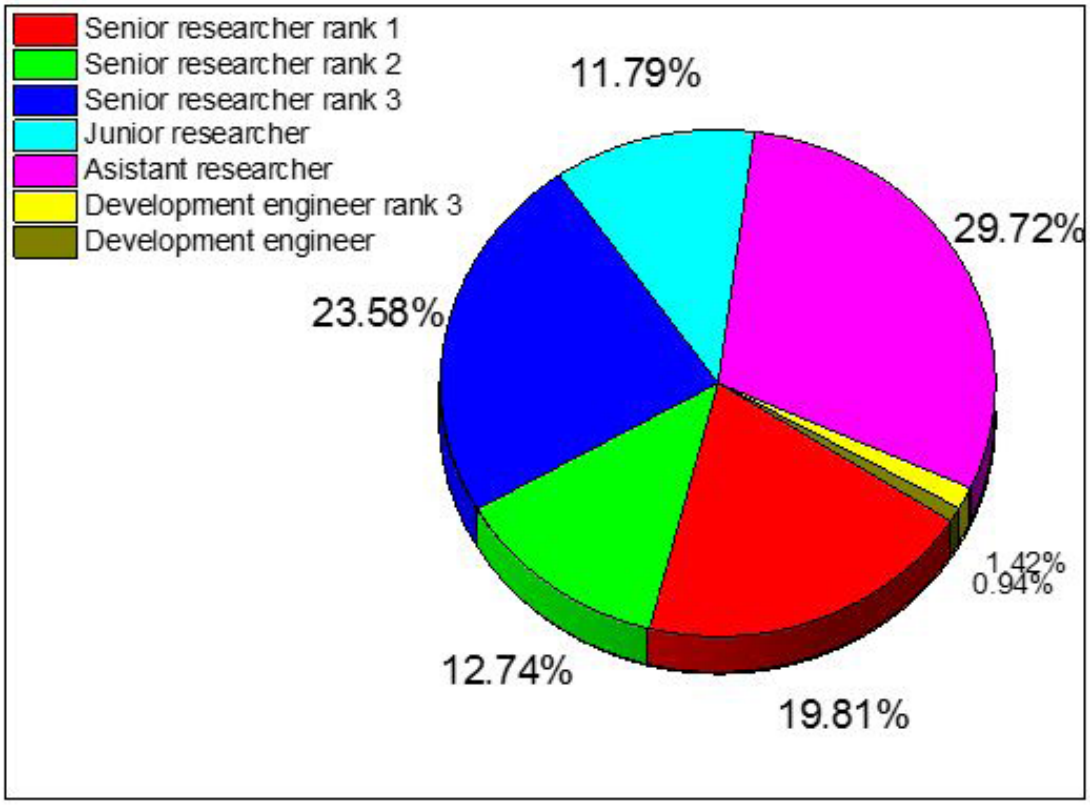

Financial summary (incomes, lei)

Core Program	25,469,744
Basic research	5,785,545.0
Strategic programs	2,198,283.0
International Projects	385,211.32
Human Resources	2,104,817.0
Support for infrastructure	542,235.00
Solutions	1,645,000.0
International Cooperation	839,915.37
Economic Contracts	1,359,715.0
Structural funds	12,888,516
Institutional performance	7,672,016.6

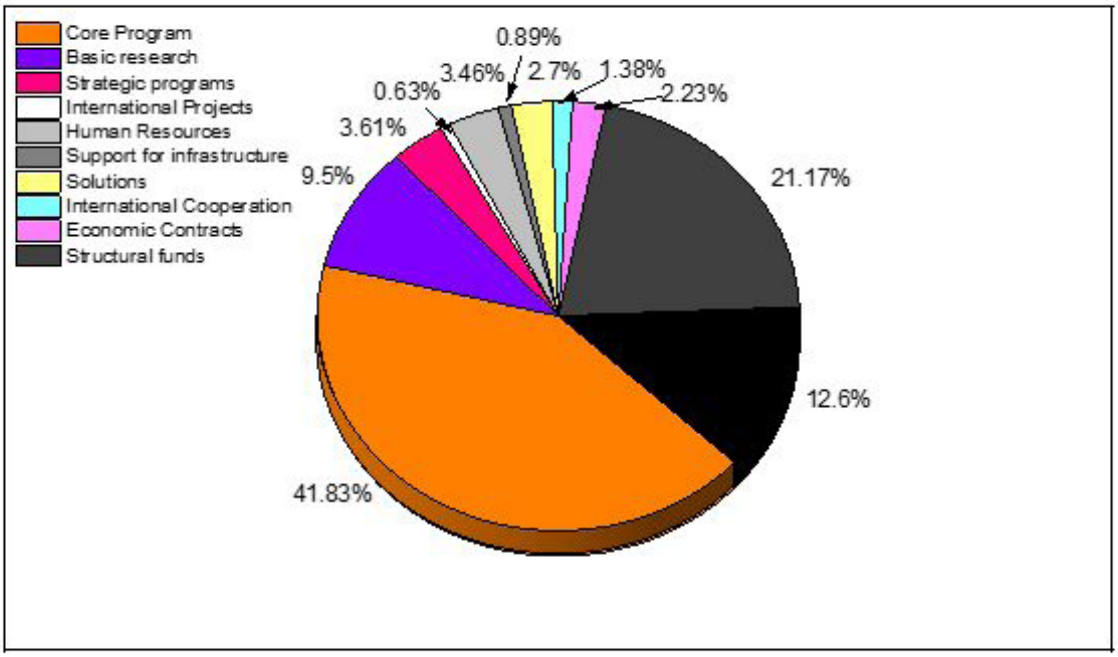

Scan the QR code,
for electronic version

2019

National Institute of Materials Physics
405A Atomistilor Street, 077125, P. O. Box: MG 7 Magurele, Ilfov, Romania
Phone: +4021 369 01 85, Fax: +4021 369 01 77, e-mail: director@infim.ro, www.infim.ro